Mixtures of superfluids

Marion Delehaye

ENS

Laboratoire Kastler Brossel
Physique quantique et applications

Département de Physique
École normale supérieure

THÈSE DE DOCTORAT
DE L'ÉCOLE NORMALE SUPÉRIEURE

Spécialité : Physique

École doctorale : "Physique en Île-de-France"

réalisée

au Laboratoire Kastler Brossel

présentée par

Marion Delehaye

pour obtenir le grade de :

DOCTEUR DE L'ÉCOLE NORMALE SUPÉRIEURE

Sujet de la thèse :

Mixtures of superfluids

soutenue le 8 Avril 2016

devant le jury composé de :

M.	Frédéric Chevy	Directeur de thèse
M.	David Guéry-Odelin	Rapporteur
M.	Takis Kontos	Examinateur
M^{me}	Anna Minguzzi	Rapportrice
M.	Christophe Salomon	Membre invité
M.	Sandro Stringari	Examinateur

THÈSE DE DOCTORAT
de l'Université de recherche
Paris Sciences Lettres –
PSL Research University

préparée à
l'École Normale Supérieure

Mélanges de superfluides

Mixtures of superfluids

par Marion Delehaye

École doctorale n°564
Spécialité: Physique
Soutenue le 08.04.2016

Composition du Jury :

M Takis Kontos
École Normale Supérieure
Président du Jury

Mme Anna Minguzzi
CNRS
Rapportrice

M David Guéry-Odelin
Université Paul Sabatier
Rapporteur

M Frédéric Chevy
École Normale Supérieure
Directeur de thèse

M Christophe Salomon
CNRS
Co-Directeur de thèse

M Sandro Stringari
Università di Trento
Membre du Jury

ENS ÉCOLE NORMALE SUPÉRIEURE
PSL RESEARCH UNIVERSITY PARIS

Contents

Remerciements

Le travail présenté dans cette thèse est le fruit des efforts de nombreuses personnes, à qui je souhaite exprimer toute ma gratitude.

En premier lieu, mes deux directeurs de thèse, Frédéric Chevy et Christophe Salomon. Ce sont les remarquables talents pédagogiques de Fred qui m'ont initialement poussée dans le monde des atomes froids et dont je ne suis plus ressortie. Il a en outre toujours su faire preuve de patience et de disponibilité dans les moments où nous avions besoin de ses précieux conseils. Sa capacité à décrire rapidement nos observations physiques par des modèles théoriques plus ou moins simples a contribué à la curiosité et à la persévérance nécessaires aux longues heures de prises de données. L'enthousiasme inébranlable de Christophe est particulièrement motivant et ses encouragements constants ainsi que sa grande connaissance des mécanismes expérimentaux ont éclairci à la fois le fonctionnement au jour le jour de l'expérience et les mécansimes subtils sur lesquels elle repose. Fred et Christophe m'ont accordé leur confiance dès le début de la thèse, me permettant de lancer différents projets de rénovation de l'expérience, de m'intéresser à plusieurs aspects techniques des manips d'atomes froids et de continuer à apprendre au quotidien. Les discussions informelles, tant sur la montagne que sur la cuisine, ont participé au cadre chaleureux dans lequel j'ai pu réaliser ma thèse.

Je souhaite également remercier les membres de mon jury : mes rapporteurs Anna Minguzzi et David Guéry-Odelin, qui m'ont fait l'honneur d'accepter de relire ma thèse, Takis Kontos, qui a accepté de présider un jury de thèse dans un domaine différent du sien, et Sandro Stringari, qui a été un précieux collaborateur et dont les travaux, avec ceux de Tomoki Ozawa, ont soulevé de nombreuses questions de physique qui m'ont particulièrement intéressée.

Les travaux présentés dans cette thèse sont le fruit d'un travail d'équipe, et je tiens à souligner le rôle crucial qu'ont joué Igor Ferrier-Barbut et Sébastien Laurent dans l'obtention et l'analyse des données, ainsi que leur capacité remarquable à me supporter pendant toutes ces heures dans la salle de manip. Igor, ainsi que ses prédécesseur Benno Rem et Andrew Grier, ont su faire preuve de pédagogie et de patience pour m'apprendre le fonctionnement de "la manip lithium", tandis que Sébastien et plus tard Matthieu Pierce ont ensuite pris le relais et m'ont permis d'exercer ma pédagogie. Ensemble, nous avons pu contribuer au mythe de l'indestructabilité de l'ancienne manip lithium, qui après avoir vécu plusieurs péripéties lors de ses vies précédentes, a survécu avec nous à plusieurs fuites d'eau, au remplacement "à cœur ouvert" de l'une de ses bobines, et finalement à un début d'incendie. Merci à tous ceux qui ont permis de la maintenir à flot, en particulier aux ateliers électronique avec Lionel et Toufik,

capables de fixer toutes nos pannes en un temps record, informatique avec Jérémie, Mathilde et Frédéric, qui assurent la survie de nos ordinateurs, mécanique avec Jean-Michel, Matthieu, Allan, Saysavanh, José, Georges, Arnaud et Nabil, sources de bons conseils et capables de réaliser avec le sourire n'importe quelle pièce farfelue, au service administratif, avec Thierry, Dominique, Audrey et Delphine, d'une patience exemplaire face à mon incompétence pour les démarches administratives (et merci à Delphine pour le tango !), et à Didier, Célia et Catherine, qui ont réussi l'exploit de maintenir le bâtiment debout en dépit de tous les efforts de Bouygues. Merci également à Tarik pour ses commentaires très pertinents sur mon manuscrit.

Il est formidable de voir ses collègues devenir des amis, et je tiens à remercier les membres de l'équipe Fermix, Misha, Tom, Cédric, Diogo et tout particulièrement Daniel, pour leur soutien et leur entrain quotidien, les chocolats chauds et les bières, ainsi que PVG et Hanna qui ont permis de faire vivre le labo via les maintenant fameux Thirsday et Friday bars. J'ai eu la chance de partager mon enseignement avec Ombline, et ça a été l'occasion de passer d'excellents moments avec elle, Adrien et Claire. Bien que j'aie initialement rencontré Claude, Stéphanie, Johanna, Gabriel, Elsa, Hervé, Timothée, Mariane, Lucile, Alexandre, Hang Zhou dans les couloirs de l'ENS ou à proximité, nous avons partagé bien plus que des sciences, et les occasions de se retrouver sont toujours des moments joyeux et riches de découvertes et de discussions.

Merci également aux amis de toujours, Zoë, Aurélien, Florian, Floraine, Jérémy, à mes cousins Amélie, Jim, Pierre, Violaine et Thomas, à ma tante Isabelle, qui ont regardé mes excentricités physiciennes d'un œil bienveillant et m'ont fait le plaisir de venir à ma soutenance. Je tiens à remercier aussi la famille de Baptiste d'être venue aussi et de s'être autant intéressée à mes travaux de recherche.

Merci à ma famille de m'avoir soutenue quand j'ai embarqué pour ce beau voyage, mes frères qui m'ont toujours encouragée, mes parents qui m'ont appris la curiosité et le fameux bricolage, avec une mention spéciale à ma mère qui a eu la gentillesse de réaliser les dessins de cette thèse.

Enfin, merci à Baptiste d'avoir partagé la physique et le quotidien, de m'avoir entourée pendant cette belle aventure, d'être là tout simplement.

Introduction

"What kind of computer are we going to use to simulate physics?" Richard Feynman asked in 1982[1], before adding, about quantum mechanics, *"I want to talk about the possibility that there is to be an* exact *simulation, that the computer will do* exactly *the same as nature"*. It means that, to simulate accurately and efficiently quantum physics, one needs a quantum computer[2]. Those quantum computers are still under development[3], but the idea arose to use quantum simulators rather than quantum calculators, and to model quantum matter with quantum systems that share the same Hamiltonian. So far, such quantum systems are made of ultracold atoms[4] photons[5] or ions[6].

Even though cold atoms can be used to simulate long-elusive particles, such as the Higgs mode[7] or Weyl fermions[8], most of the quantum simulation is focused on aspects related to condensed matter, in which one of the most spectacular manifestation of quantum effects is superfluidity.

Superfluidity in quantum fluids

Superconductivity

The first superfluidity effects were discovered with the superconductivity of mercury in 1911. In superconductors, electrons feel effective attractive interactions mediated by phonons and form Cooper pairs, as was explained in Bardeen-Cooper-Schrieffer (BCS) theory[9]. The superfluid character of the Cooper pairs leads to the observed absence of electric resistance.

Helium

In 1937, Kapitza[10], Allen and Misener[11] discovered that the viscosity of helium 4 below the phase transition temperature of 2.2 K was exactly zero. This was interpreted[12] as the condensation predicted by Bose and Einstein of bosonic ^{4}He. Years later, in 1972, helium 3 was also found to undergo a phase transition, at a temperature of 2.6 mK,

[1] [Feynman, 1982]
[2] [Lloyd, 1996]
[3] [Ladd *et al.*, 2010]
[4] [Bloch *et al.*, 2012, Bloch *et al.*, 2008]
[5] [Aspuru-Guzik and Walther, 2012]
[6] [Blatt and Roos, 2012]
[7] [Endres *et al.*, 2012]
[8] [Suchet *et al.*, 2015]
[9] [Bardeen *et al.*, 1957]
[10] [Kapitza, 1938]
[11] [Allen and Misener, 1938]
[12] [Tisza, 1938, London, 1938, Landau, 1941, Tisza, 1947]

below which it was superfluid[13]. Here, the superfluidity was interpreted[14] as resulting from the formation of pairs of fermionic ^{3}He.

Ultracold atoms

For the new quantum fluids that ultracold gases were about fifteen years ago, with the first Bose-Einstein condensate in 1995[15] and the degenerate Fermi gas in 1999[16], evidences of superfluidity were searched intensively. Among the spectacular effects of superfluidity are phase coherence[17], the presence of vortices and the existence of a critical velocity for dissipation, and these effects attracted most efforts in the cold atom community. Vortices are due to the quantization of circulation in quantum fluids and can be seen via the presence of zero-density lines within the gas. The existence of a critical velocity is a completely different phenomenon and is based on Landau's criterion to create excitations in a quantum fluid flow that lead to dissipation. For Bose-Einstein condensates, both vortices[18] and critical velocity[19] were observed in the early 2000s. For fermions, the observation of vortices at MIT[20] provided indisputable proofs on the superfluidity of these systems for various interaction strengths. The critical velocity for fermions was also measured with different probing techniques[21]. It is also worth mentioning the recent realization of Bose-Einstein condensates of polaritons[22] and magnons[23], that are also superfluids.

Quantum simulation with ultracold atoms

Hubbard models

In was noticed in the early days of ultracold atoms that the high purity of their environment and their controllability made them systems of choice to simulate various condensed-matter Hamiltonians[24]. Observation of superfluidity in ultracold gases was a prelude to quantum simulation of environments that challenge it. Among them is the Hubbard model, that predicts a phase transition between a superfluid state and a Mott insulating state for particles in a lattice when varying the ratio between interaction energy and tunnel energy. The first realizations of the Bose-Hubbard Hamiltonian (with bosons in an optical lattice)[25] paved the way for theoretical and experimental studies of Fermi-Hubbard[26] and Bose-Fermi Hubbard[27] models. Cold atoms provide unique tools to explore their phase transitions, such as single site and single atom resolution[28] (that would correspond to imaging directly single electrons in a solid).

[13] [Osheroff *et al.*, 1972a, Osheroff *et al.*, 1972b]
[14] [Leggett, 1975]
[15] [Anderson *et al.*, 1995, Davis *et al.*, 1995a]
[16] [DeMarco and Jin, 1999]
[17] [Bloch *et al.*, 2000]
[18] [Matthews *et al.*, 1999, Madison *et al.*, 2000, Abo-Shaeer *et al.*, 2001]
[19] [Raman *et al.*, 1999, Onofrio *et al.*, 2000, Fedichev and Shlyapnikov, 2001]
[20] [Zwierlein *et al.*, 2005, Zwierlein *et al.*, 2006a]
[21] [Miller *et al.*, 2007, Weimer *et al.*, 2015, Delehaye *et al.*, 2015]
[22] [Amo *et al.*, 2009, Balili *et al.*, 2007]
[23] [Nikuni *et al.*, 2000, Demokritov *et al.*, 2006]
[24] [Fisher *et al.*, 1989, Jaksch *et al.*, 1998, Jaksch and Zoller, 2005]
[25] [Greiner *et al.*, 2002, Will *et al.*, 2010]
[26] [Köhl *et al.*, 2005, Strohmaier *et al.*, 2007, Jordens *et al.*, 2008, Schneider *et al.*, 2008]
[27] [Günter *et al.*, 2006, Ospelkaus *et al.*, 2006]
[28] [Bakr *et al.*, 2009]

The possibility to visualize directly single-site population gives access to the correlation functions and enables precise study of quantum phase transitions. Some controllable disorder[29] can also be added to the Hubbard models in various dimensions to study the localization of particles due to disorder, a phenomenon called Anderson localization.

Charged matter in magnetic fields

More recently, the challenge of simulating the behavior of charged matter in magnetic fields with neutral atoms was also addressed[30]. Since cold atoms are neutral, they are not accelerated by magnetic fields. It is thus required to apply so-called *artificial* gauge fields. One of the realization of artificial gauge fields consists in implementing a global rotation $\mathbf{\Omega}$ of the gas. The resulting Coriolis force $2M\mathbf{\Omega} \wedge \mathbf{v}$ (where M is the mass of the system and $\mathbf{v}$ its velocity) has the same mathematical structure as the Lorentz force $q\mathbf{v} \wedge \mathbf{B}$[31], where q is the charge of the particle. Another possibility to create artificial gauge fields is to apply a specific laser scheme, designed to imprint a Berry phase (similar to the phase acquired by a particle evolving in a magnetic field) on atoms in bulk phases[32] or in optical lattices[33]. This led for instance to the realization of the Hofstadter Hamiltonian[34]. These synthetic magnetic fields also offer the possibility to reach fractional quantum Hall regime for ultracold atoms under a strong artificial magnetic field.

Transport properties

Since the starting point of most cold atom experiments is a system at equilibrium in a trapping potential, one natural way to investigate transport properties is to modify the trapping potential and observe the response of the system to this perturbation[35]. However, one key observable of solid-state physics, electric conduction, can not be simulated with this technique because it requires two reservoirs and a channel connecting them. Conduction was observed by engineering such a system with optical potentials and realizing a population imbalance between the two reservoirs so that the particles would go from one to the other through the channel[36], both in the ballistic and diffusive regime.

Dipolar gases

The first atoms that were cooled to quantum degeneracy were alkali. They have negligible dipole magnetic moment and only interact with short-range contact interactions. One workaround to study the effect of long-range interactions is the use of Rydberg atoms[37]. Another one relies on dipolar gases, that exhibit long-range, anisotropic in-

[29] [Roati *et al.*, 2008, Billy *et al.*, 2008, Kondov *et al.*, 2011, Gurarie *et al.*, 2009, Schreiber *et al.*, 2015]
[30] [Bloch *et al.*, 2008, Dalibard *et al.*, 2011, Goldman *et al.*, 2014]
[31] [Madison *et al.*, 2000]
[32] [Lin *et al.*, 2009, Wang *et al.*, 2012, Cheuk *et al.*, 2012]
[33] [Aidelsburger *et al.*, 2011, Struck *et al.*, 2013, Miyake *et al.*, 2013]
[34] [Aidelsburger *et al.*, 2013]
[35] [Jin *et al.*, 1996, Ben Dahan *et al.*, 1996, Ott *et al.*, 2004, Sommer *et al.*, 2011, Schneider *et al.*, 2012]
[36] [Brantut *et al.*, 2012]
[37] [Schauß *et al.*, 2012, Weimer *et al.*, 2008, Pohl *et al.*, 2010]

teractions[38]. They may challenge the stability of a Bose-Einstein condensate[39], or lead to Rosensweig instability[40]. Antiferromagnetism can also be simulated[41].

Fermi gases with tunable interactions

Ultracold gases can also predict the properties of systems hard to reach experimentally, such as neutron stars for instance[42]. Neutron stars are strongly interacting Fermi systems at a temperature $T \sim 10^6 - 10^8\,\mathrm{K}$, well below their Fermi temperature $T_\mathrm{F} \sim 10^{12}\,\mathrm{K}$. Their behavior is similar to that of an ultracold strongly interacting Fermi gas, and the knowledge of the equation of state of the ultracold Fermi gas gives access to that of a layer of the neutron star. Strongly interacting Fermi gases are composed of several fermionic species (for instance, atoms in two different spin-states noted $\uparrow$ and $\downarrow$). Those two fermionic species may interact with each other, and interactions are characterized by the scattering length a_ff and the interaction strength $k_\mathrm{F}a_\mathrm{ff}$, where k_F is the Fermi wave-vector. For small values of $1/|k_\mathrm{F}a_\mathrm{ff}|$, the system is said strongly interacting, and the $1/|k_\mathrm{F}a_\mathrm{ff}| \to 0$ limit is called unitarity. For $1/k_\mathrm{F}a_\mathrm{ff} \gg 1$ ("BEC regime"), fermions form tightly-bound pairs with bosonic character that may undergo Bose-Einstein condensation, while for $1/k_\mathrm{F}a_\mathrm{ff} \ll -1$ ("BCS regime"), fermions form Cooper pairs. Superfluidity is possible in the whole BEC-BCS crossover, and is characterized by pairing between spin-$\uparrow$ and spin-$\downarrow$ fermions.

For fermions, the equation of state is thus a function of three parameters: the temperature, the interaction strength, and the ratio between the two spin-populations[1]. In three dimensions[2], it has been obtained as a function of temperature at unitarity[43], as a function of interaction strength at zero temperature[44], and as a function of spin imbalance. Indeed, when considering spin-imbalanced gases, one key parameter is the population imbalance above which superfluidity is lost. This issue, known as the Clogston-Chandrasekhar limit[45], has been investigated both theoretically[46] and experimentally[47].

For spin-imbalanced Fermi systems, several exotic, long-elusive phases have been predicted. Among them is the FFLO phase[48], characterized, with other properties,

[1] For bosons the equation of state is a function only of temperature and interaction strength. It has been measured as a function of temperature in three dimensions [Ensher *et al.*, 1996, Gerbier *et al.*, 2004b, Gerbier *et al.*, 2004a], in two dimensions [Hung *et al.*, 2011, Rath *et al.*, 2010, Yefsah *et al.*, 2011] and in one dimension [van Amerongen *et al.*, 2008, Armijo *et al.*, 2011]. The study of ultracold gases in more than three dimensions is now considered [Boada *et al.*, 2012, Celi *et al.*, 2014, Zeng *et al.*, 2015, Price *et al.*, 2015], by seeing the spin degrees of freedom of the atoms as a discrete extra dimension.

[2] In two dimensions, the equation of state of fermions has been measured recently [Boettcher *et al.*, 2016, Fenech *et al.*, 2016].

[38] [Lahaye *et al.*, 2009]
[39] [Lahaye *et al.*, 2007, Lahaye *et al.*, 2008, Ferrier-Barbut *et al.*, 2016]
[40] [Kadau *et al.*, 2016]
[41] [Simon *et al.*, 2011, Greif *et al.*, 2015]
[42] [Ho, 2004, Gezerlis and Carlson, 2008]
[43] [Thomas *et al.*, 2005, Stewart *et al.*, 2006, Luo *et al.*, 2007, Nascimbène *et al.*, 2010, Horikoshi *et al.*, 2010, Ku *et al.*, 2012]
[44] [Shin, 2008, Bulgac and Forbes, 2007, Navon *et al.*, 2010]
[45] [Clogston, 1962, Chandrasekhar, 1962]
[46] [Bausmerth *et al.*, 2009, Chevy, 2006, Lobo *et al.*, 2006]
[47] [Zwierlein *et al.*, 2006a, Navon *et al.*, 2010]
[48] [Fulde and Ferrell, 1964, Larkin and Ovchinnikov, 1964]

by Cooper pairs with non-zero momentum and a spatially varying order parameter. Despite intensive experimental effort, no irrefutable proof of their observation could be seen, even though some evidence have been put forward[49]. In three dimensions, they are predicted to appear only in a narrow range of parameters[50] (see Figure 0.1), so their signature is mainly smeared out when the system is trapped in a harmonic potential, as it is usually the case for ultracold gases[3]. The ongoing development of uniform trapping potentials is thus very promising for the observation of FFLO phases.

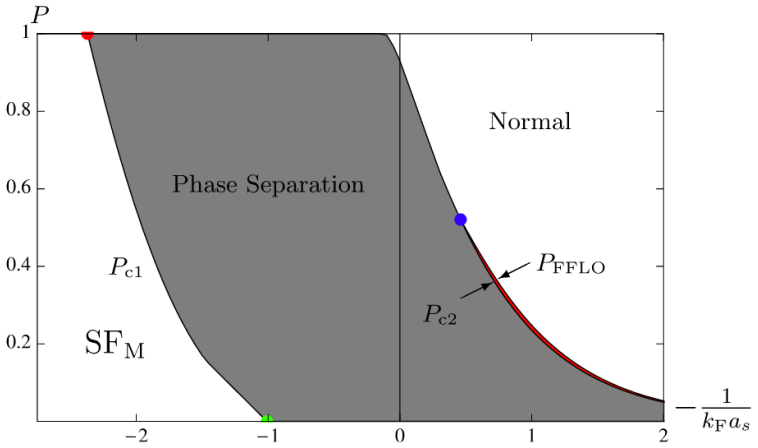

Figure 0.1: Mean-field phase diagram of imbalanced Fermi gases, as a function of inverse scattering length and local spin polarization imbalance P, showing regimes of magnetized (imbalanced) superfluid (SF_M), FFLO (in red, bounded by P_{FFLO} and P_{c2}) and normal Fermi liquid, taken from [Radzihovsky and Sheehy, 2010].

Uniform systems

Harmonic traps were very convenient to measure the equation of state of ultracold systems. Indeed, the atomic density varies spatially and explores a finite range on a single cloud, giving access to many points of the equation of state curve from a single experimental realization. However, the search for phases that appear in a narrow range of phase diagram (such as the above-mentioned FFLO phase) is made challenging, because they would appear only in a small portion of the cloud's volume. On the contrary, in box potentials, where the potential and hence the atomic density is constant on a finite volume (the "box"), it would be possible to "zoom in" into the parameter subspace of interest. Box potentials were initially reported in[51], then more recently in[52], where they have already provided the opportunity to study critical phenomena,

[3] In one dimensional systems, FFLO phase occupies a larger portion of the phase diagram[Liao *et al.*, 2010, Mizushima *et al.*, 2005, Orso, 2007, Hu *et al.*, 2007, Guan *et al.*, 2007, Parish *et al.*, 2007a, Feiguin and Heidrich-Meisner, 2007, Casula *et al.*, 2008, Kakashvili and Bolech, 2009], allowing possible experimental detection [Kinnunen *et al.*, 2006, Edge and Cooper, 2009].

[49] [Kontos *et al.*, 2001, Bianchi *et al.*, 2003]
[50] [Sheehy and Radzihovsky, 2007, Bulgac and Forbes, 2008, Parish *et al.*, 2007b]
[51] [Meyrath *et al.*, 2005]
[52] [Gaunt *et al.*, 2013, Corman *et al.*, 2014]

such as Kibble-Zurek mechanism[53].

Bose-Fermi mixtures

State of the art

After the discovery of superfluidity in ^{3}He, one natural question that arose was whether is was possible to make a mixture with the two known superfluids, ^{3}He and ^{4}He. It turns out that strong interactions between the two species downshift the critical temperature for superfluidity to about 50 µK, while the coldest temperature reached in mixtures of liquid helium is so far 100 µK[54]. That question thus remained open for about 50 years before we could realize such a Bose-Fermi superfluid mixture with cold atoms.

In cold atoms, many degenerate mixtures of bosons and fermions have been realized, also because one of the first methods to cool fermions was via sympathetic cooling with bosons. But none of the mixtures was showing simultaneously Bose and Fermi superfluidity: either the bosons were condensed but the fermions were not superfluid (for instance because there was only one fermionic spin-state, or because the critical temperature for superfluidity was too low), or the fermions were superfluid but the Bose gas not condensed (because of too few atoms for instance).

Mixtures		
Bosons	Fermions	Reference
^{7}Li	^{6}Li	[Schreck *et al.*, 2001b, Truscott *et al.*, 2001]
^{23}Na	^{6}Li	[Hadzibabic *et al.*, 2002]
^{87}Rb	^{40}K	[Roati *et al.*, 2002]
^{87}Rb	^{6}Li	[Silber *et al.*, 2005]
^{4}He*	^{3}He*	[McNamara *et al.*, 2006]
^{87}Rb	^{6}Li-^{40}K	[Taglieber *et al.*, 2008]
^{85,97}Rb	^{6}Li	[Deh *et al.*, 2008, Deh *et al.*, 2010]
^{84,86,88}Sr	^{87}Sr	[Tey *et al.*, 2010, Stellmer *et al.*, 2013]
^{174}Yb	^{6}Li	[Hara *et al.*, 2011, Hansen *et al.*, 2011]
^{170,174}Yb	^{173}Yb	[Sugawa *et al.*, 2011]
^{41}K	^{40}K-^{6}Li	[Wu *et al.*, 2011]
^{162}Dy	^{161}Dy	[Lu *et al.*, 2012]
^{23}Na	^{40}K	[Park *et al.*, 2012]
^{133}Cs	^{6}Li	[Repp *et al.*, 2013]

Reported degenerate Bose-Fermi mixtures

Superfluid mixture

Our experiment had already produced mixtures of a Bose-Einstein condensate and of a degenerate Fermi gas[55], and cold bosons in the presence of superfluid fermions[56]. In

[53] [Chomaz *et al.*, 2014, Navon *et al.*, 2015]

[54] [Tuoriniemi *et al.*, 2002, Rysti *et al.*, 2012]

[55] [Schreck *et al.*, 2001b]

[56] [Nascimbène *et al.*, 2010]

2014 we were able to achieve simultaneous superfluidity of bosonic ^{7}Li and fermionic ^{6}Li in a mixture by choosing the right combination of atomic states to make use of the ^{6}Li Feshbach resonance in a magnetic field range where the Bose-Einstein of ^{7}Li is stable[57].

The report of our superfluid mixture raised very fast new questions regarding the validity of Landau's argument in the case of a Bose-Fermi superfluid counterflow[58]. During my PhD, we addressed a few of them, such as the measurement of the critical velocity of the mixture or the effect of finite temperature.

In addition to these dynamic studies, we also exploited static properties, such as the possibility to create a flat bottom potential. Previously reported uniform potentials[59] use repulsive laser sheets to create a box for the atoms. The approach that we propose is completely different. It uses the repulsive interactions between bosons and fermions to compensate the curvature of the harmonic trap for the Fermi cloud. The flatness of the trap can be set by the precise tuning of Bose-Bose interactions through a Feshbach resonance. The effective trapping potential for the Fermi gas then has a flat bottom and opens the way to probe spin-imbalanced Fermi gases in homogeneous systems, hence Clogston-Chandrasekhar limit and FFLO phases.

Outline of this thesis

My first contribution to research within the group was to take data regarding the lifetime and three-body losses of the unitary Bose gas[60] (see Appendix C.5). After an interlude for the implementation a new cooling technique on lithium based of D_1 cooling[61] (see Appendix C.1) that led to the design and construction of a new lithium experiment, we turned to the production of a superfluid Bose-Fermi mixture[62] (see Appendix C.2) and the study of its properties[63] (see Appendix C.3). This forms the central part of my PhD work. Among the properties of this novel system, we have focused both on its superfluidity and critical velocity, and on the implementation of the flat bottom trap proposed in collaboration with the Trento group[64] (see Appendix C.2).

This thesis is organized the following way:

- **chapter 1** is dedicated to an introduction to the subject of superfluidity. It gives a brief overview of the major steps in history of superfluidity, then details some of its most spectacular physical manifestations. It then turns to the subject of quantum gases, and to the relation between their interactions and superfluidity.

- **chapter 2** describes the lithium machine on which all of the results given in this PhD were obtained. It was thoroughly described in several PhD theses from students before me[65], so I only go briefly over the different steps that lead to the realization of a Bose-Fermi superfluid mixture[66].

[57] [Ferrier-Barbut *et al.*, 2014]
[58] [Castin *et al.*, 2015, Abad *et al.*, 2015, Zheng and Zhai, 2014, Wen and Li, 2014, Shen and Zheng, 2015, Chevy, 2015]
[59] [Meyrath *et al.*, 2005, Gaunt *et al.*, 2013, Corman *et al.*, 2014]
[60] [Rem *et al.*, 2013, Eismann *et al.*, 2015]
[61] [Grier *et al.*, 2013]
[62] [Ferrier-Barbut *et al.*, 2014]
[63] [Delehaye *et al.*, 2015]
[64] [Ferrier-Barbut *et al.*, 2014]
[65] [Schreck, 2002, Tarruell, 2008]
[66] [Ferrier-Barbut *et al.*, 2014]

- **chapter 3** concerns the study of the Bose-Fermi counterflow. It details the initiation of the counterflow, its mean-field study, the measurement of the critical velocity in the BEC-BEC crossover, and the observation of an unexpected phase-locking of the two clouds at unitarity when increasing the temperature.
- **chapter 4** is dedicated to the study of imbalanced Fermi gases in a flat bottom trap. It explains the theoretical prediction and the conditions to implement it on our experiment. First results show evidence for a novel superfluid phase with a shell structure that topologically differs from the standard bulk Fermi superfluid produced so far.
- **chapter 5** describes the new lithium experiment, currently under construction. It gives details on the desired properties of the new experiment, as well as on its technical mechanical drawing, planned laser system and magnetic fields configurations.

Chapter 1

Superfluidity

1.1 Superfluids

1.1.1 Historical approach

The adventure of superfluidity began with the liquefaction of helium in 1908 by the Dutch physicist Heike Kamerlingh Onnes: via a succession of compressions and expansions of gaseous ^{4}He (^{3}He was still unknown back then), he managed to reach temperatures as low as 1.5 K, while ^{4}He undergoes liquefaction at 4.2 K. Having such a cold reservoir of liquid allowed him to cool down different kind of materials, and this is how he discovered the superconductivity of mercury in 1911: below a temperature of 4.2 K, the resistivity of mercury drops to exactly zero. In 1937, Kapitza [Kapitza, 1938], Allen and Misener [Allen and Misener, 1938] discovered that liquid ^{4}He underwent a phase transition at 2.2 K between type I helium (above 2.2 K) and type II helium (below 2.2 K), the viscosity of which was found to be zero. These absences of electric resistance and viscosity are deeply connected, and while superfluidity in ^{4}He was quickly associated to the Bose-Einstein condensation of bosonic ^{4}He atoms and a theory proposed by Tisza, London and Landau [Tisza, 1938, London, 1938, Landau,

1941, Tisza, 1947] in 1941, superconductivity relies on the creation of Cooper pairs between electrons, as detailed in Bardeen-Cooper-Schrieffer (BCS) theory. Years after, in 1972, Lee, Osheroff and Richardson [Osheroff *et al.*, 1972a, Osheroff *et al.*, 1972b] showed that ^{3}He becomes superfluid as well, for temperatures below 2.6 mK. Such a low transition temperature is due to the necessity to form pairs of fermionic ^{3}He so that it can become superfluid. A theory presented by Leggett [Leggett, 1975] adapted BCS theory to the p-wave pairing occurring in ^{3}He.

Along the years superconductivity was discovered in many different materials, with even some materials showing unconventional superconductivity, which is not perfectly understood yet. However, at the very low temperatures needed to reach superfluidity, most materials are solid, and no other superfluid was discovered until the first realization, in 1995, of Bose-Einstein condensates (BECs) in ultracold atoms [Anderson *et al.*, 1995, Davis *et al.*, 1995a]. During the past 20 years, intense experimental and theoretical efforts have been dedicated to the search in cold atoms for some of the most spectacular signatures of superfluidity, which are detailed below.

1.1.2 Properties of superfluid helium and superfluid atomic gases

Historically, the existence of superfluidity in helium was unexpected. It came out when Kapitza, Allen and Misener measured the viscosity of helium below 2.2 K through capillary tubes and found out it had a "non-viscous" character [Wilks and Betts, 1987]. A two-fluids model was proposed by Landau [Landau, 1941] and Tisza [Tisza, 1938], in which helium below 2.2 K was composed of two fluids, one is called the *normal* fluid and behaves like a Newtonian fluid, the other one is superfluid, has no viscosity and carries no entropy.

A number of very specific properties have been demonstrated for superfluid helium, some of which also have been observed in the field of ultracold gases:

- superfluid flow. The flow rate of liquid helium through capillary tubes tends to increase with decreasing temperature below 2.2 K. This is also the case for cold atoms superfluids: it is possible to build an experiment with two reservoirs connected by a small channel and measure the resistance of the flow through it [Stadler *et al.*, 2012]. A theory proposed by Landau [Landau, 1941] connects the superfluid flow to the fact that it is not possible to create excitations in the superfluid below a certain critical velocity. The existence of such a critical velocity has been demonstrated in [Onofrio *et al.*, 2000, Raman *et al.*, 1999], even though this evidence was more qualitative than quantitative, and will be the subject of our investigations in chapter 3. Landau's criterion will be demonstrated in subsection 3.3.2.

- siphon effect. Driven by surface tension, a fluid may wet the walls of its containers, and for normal fluids the velocity of the film is limited by viscosity. In the case of superfluids, since the viscosity is zero, the flow is much higher. Superfluid helium may thus escape an open container.

- phase coherence. Superfluids are described by a single macroscopic wave function $\psi(\boldsymbol{r})$. This single wave function implies phase coherence for the superfluid, and

this was evidenced by the interferences of condensates [Andrews *et al.*, 1997b, Bloch *et al.*, 2000].

- heat transport. Superfluid helium does not transport heat by conduction but only by convection. The superfluid component goes from cold places to hot places while the normal component goes the other way. This process is actually very efficient, leading to a high thermal conductivity. This results in the spectacular fountain effect: by blocking the flow of the normal component, any temperature gradient can be rapidly turned into a pressure gradient of the superfluid, that may form a fountain. Similar experiments, showing particle flow under a pressure gradient, have also been demonstrated in ultracold atoms [Brantut *et al.*, 2013].

- second sound. It is possible to create entropy waves, in which the density of the normal and superfluid components oscillate with opposite phases. These entropy waves are associated to temperature waves that lead to the specific heat transport described above. It is analogous to the conventional sound ('first sound') except that instead of being associated to an isentropic density wave, it is an isobaric entropy-wave, hence its name of 'second sound'. Evidence of first and second sound have been given in both ^{4}He and ^{3}He, but also in cold atom experiments [Andrews *et al.*, 1997a, Stamper-Kurn *et al.*, 1998, Hou *et al.*, 2013, Sidorenkov *et al.*, 2013].

- vortices. They are typical evidence for superfluidity. Indeed, the wave function that describes the superfluid can be separated into a module and a phase: $\psi(\boldsymbol{r}) = |\psi(\boldsymbol{r})|e^{i\phi(\boldsymbol{r})}$, and the velocity of the superfluid is proportional to the gradient of the phase ϕ:
$$\boldsymbol{v} = \frac{\hbar}{m}\boldsymbol{\nabla}\phi,$$
where m is the mass of the particles composing the superfluid. Since the phase cannot be multivalued, this leads to [Onsager, 1949, Feynman, 1953, Feynman, 1954]
$$\oint \boldsymbol{v}\cdot d\boldsymbol{l} = 2\pi n\frac{\hbar}{m},$$
where n is an integer. If the density is always strictly positive, the only possible value for n is zero. Having a non-zero value for n, which means having a non-zero circulation, necessarily implies the existence of lines of zero density, called vortices. The number of quanta n associated to each vortex is called its *charge*. Two vortices of equal charge repel each other, this is why vortices will arrange themselves into lattices called Abrikosov lattices. Vortices have been observed in the 1950's after their theoretical prediction in superfluid helium [Hall and Vinen, 1956a, Rayfield and Reif, 1964]. As an obvious proof for superfluidity, they were also sought for and evidenced in the early days of ultracold atoms [Matthews *et al.*, 1999, Madison *et al.*, 2000, Abo-Shaeer *et al.*, 2001, Zwierlein *et al.*, 2005], and it was demonstrated as well that vortices were quantized and arranged themselves in lattices.

I will now give more details on the nature of the particles that form the superfluids, and on the mechanisms at the origin of superfluidity.

1.2 Bosons and fermions

1.2.1 Quantum statistics

Particles that form our universe can be sorted into two categories: bosons and fermions. Fermions have a half-integer spin and are the building bricks of matter: protons, neutrons and electrons are fermions. Bosons have an integer spin and gauge bosons, such as the photon or the famous Higgs boson, mediate the interactions between particles. An assembly of fermions, like an atom composed of protons, neutrons and electrons, may either have a fermionic nature if its total spin is half integer, that is if it is composed of an odd number of fermions, or rather a bosonic nature if it is composed of an even number of fermions, leading to an integer spin. For instance, ^{4}He and ^{7}Li are bosons, while ^{3}He and ^{6}Li are fermions.

Bosons and fermions obey different statistics. Indistinguishable bosons will follow the Bose-Einstein statistics, where the population n_i in a state of energy ε_i with degeneracy g_i for an ensemble of indistinguishable bosons of chemical potential μ is given by:

$$n_i(\varepsilon_i) = \frac{g_i}{e^{(\varepsilon_i-\mu)/k_\mathrm{B}T} - 1},$$

where T is the temperature and k_B the Boltzmann's constant. On the other hand, indistinguishable fermions with the same chemical potential μ obey the Fermi-Dirac statistics and

$$n_i(\varepsilon_i) = \frac{g_i}{e^{(\varepsilon_i-\mu)/k_\mathrm{B}T} + 1}.$$

From this equation, we can see that $n_i \leq g_i$: two identical fermions cannot occupy the same energy state. This is a reformulation of Pauli principle that for example applies to electrons. In the high temperature or low-density limit, these two distributions lead to the same Maxwell-Boltzmann statistics:

$$n_i(\varepsilon_i) = \frac{g_i}{e^{(\varepsilon_i-\mu)/k_\mathrm{B}T}}.$$

The first implication of this result is straightforward: to observe the effect of the quantum nature of particles, it will be necessary to go to low temperature and relatively high atomic densities. Indeed, quantum effects start to appear when the interparticle distance $n^{-1/3}$ is on the order on the size of the wave packet describing each particle. The size of this wave packet is given by the thermal De Broglie wavelength $\lambda_{th} = \sqrt{\frac{\hbar^2}{2\pi m k_\mathrm{B} T}}$. When $n\lambda_{th}^3 \gtrsim 1$, the description in terms of independent particles is not relevant any more and one has to take into account quantum mechanics and quantum statistics as matter-waves start interfering.

1.2.2 Low-temperature behavior

At low temperature, bosons macroscopically accumulate in the lowest energy state and there is a phase transition towards a Bose-Einstein condensate (BEC). For a uniform

non-interacting system, the transition temperature is given by:

$$T_c = \frac{1}{(g_{3/2}(1))^{2/3}} \frac{2\pi\hbar^2}{m_\mathrm{b} k_\mathrm{B}} n_\mathrm{b}^{2/3},$$

where n_b is the density of bosons, m_b their mass and $g_n(z)$ is the polylogarithm $g_n(z) = \sum_{k=1}^{\infty} z^k/k^n$. When the system is not uniform but in a harmonic trap with average trap frequency $\bar{\omega}$ and total number of atoms N_b, this transition temperature is given by:

$$T_c = \frac{1}{(g_{3/2}(1))^{1/3}} \frac{\hbar\bar{\omega}}{k_\mathrm{B}} N_\mathrm{b}^{1/3}.$$

Fermion behavior is very different. At low temperature, identical fermions form a Fermi Sea, with one particle per energy state. Typical temperature at which Fermi statistics start to take over thermal effects is the Fermi temperature T_F. For a uniform non-interacting system, the Fermi temperature is given by:

$$T_\mathrm{F} = \frac{\hbar^2}{2k_\mathrm{B} m_\mathrm{f}} (3\pi^2)^{2/3} n_\mathrm{f}^{2/3},$$

with n_f the fermion density and m_f their mass. In a harmonic trap the Fermi temperature is given by

$$T_\mathrm{F} = \frac{\hbar\bar{\omega}}{k_\mathrm{B}} (6N_\mathrm{f})^{1/3}.$$

These different behaviors are summed up on Figure 1.1 for particles in harmonic traps.

In liquid bosonic ^{4}He, interactions are everything but negligible, but the transition towards superfluidity occurs at a temperature relatively close to the critical one for Bose-Einstein condensation for a system of non-interacting bosons with the same density (3.2 K). Indeed, the superfluidity of ^{4}He can be interpreted as a Bose-Einstein condensation of interacting bosons.

As for fermionic ^{3}He, the origin of its superfluidity is more complex. Indeed, ^{3}He is a fermion, and identical fermions cannot occupy the same energy state. However, two fermions that differ, by the value of their spin for example, can be paired up and form a composite boson. This is what happens for ^{3}He, and since the critical temperature for pair formation is much smaller than the critical temperature for condensation, this explains the very low temperature for superfluidity in ^{3}He (2.6 mK). For superconductivity, similar phenomenon is at play, and electrons pair up in momentum space to form Cooper pairs thanks to attractive interactions mediated by the phonons of crystalline structure.

The quantum nature of particles thus has an important role for explaining different behaviors and phenomena observed in condensed matter. However, one of the difficulties in the quantitative understanding and modeling of condensed matter is its density: strong interactions between particles lead to behaviors that are very complicated to predict theoretically. In addition, these interactions can also lead to demixion within the superfluid. For instance, while (as indicated above) both ^{3}He and ^{4}He have been successfully cooled down separately to superfluidity, this has not been the case so far for the mixture of ^{3}He and ^{4}He. Indeed, strong interactions between ^{3}He and ^{4}He lead to a phase separation of the system into two phases, one of pure ^{3}He, and the

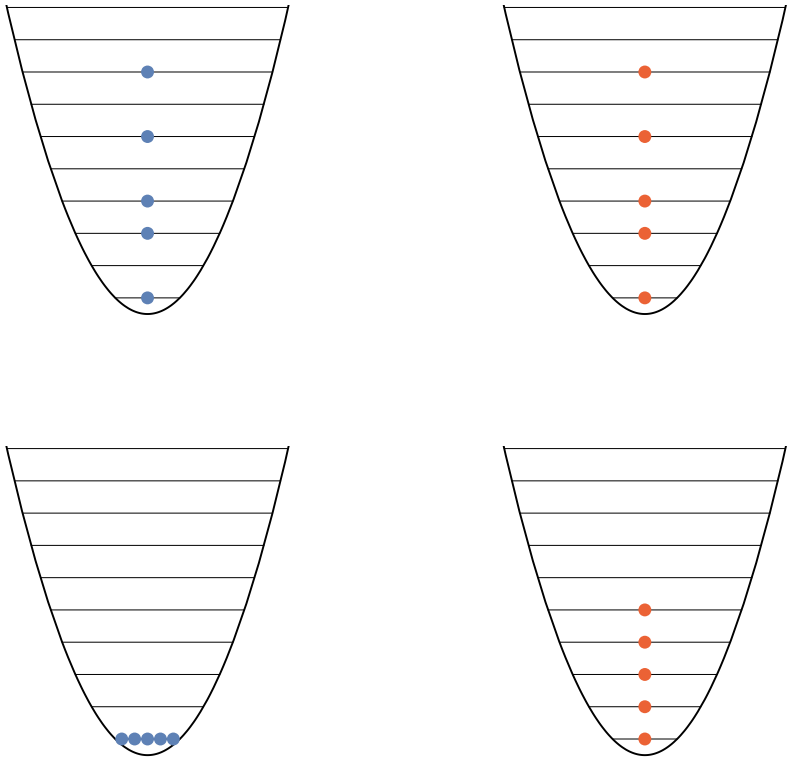

(a) Bosons (b) Fermions

Figure 1.1: (Top) high temperature and (bottom) low temperature behavior of the different classes of particles, according to their statistics. Here, the notion of "high" and "low" temperature is given with respect to the energy spacing $\hbar\omega$ between levels.

second one of a mixture and ^{4}He and only 6% of ^{3}He (see Figure 1.2) [Rysti *et al.*, 2012, Tuoriniemi *et al.*, 2002]. This demixion phenomenon is used for dilution refrigerators but the resulting low density of ^{3}He in the mixed phase has led to a decrease of the critical temperature for superfluidity down to an estimated temperature of $\sim 50\,\mu$K, while the coldest temperatures reached with liquid helium so far are $\sim 100\,\mu$K. No double Bose-Fermi superfluid mixture has been reported in condensed matter so far.

For the last 20 years, another kind of systems have shown quantum properties: ultracold gases. These systems have a very cold temperature (around or below $1\,\mu$K), associated with an atomic density high enough to show the effects of quantum statistics, but low enough to allow a simple description of interactions and prevent solidification. Their description will be the object of the next section.

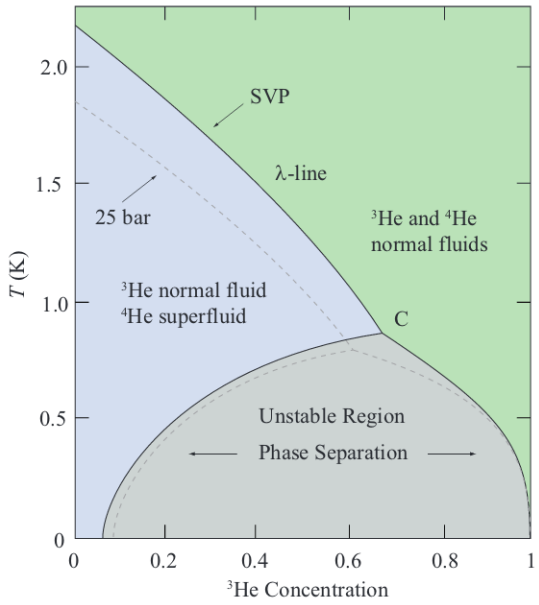

Figure 1.2: Phase diagram of helium mixtures taken from [Rysti, 2013], at the saturated vapor pressure (SVP) and at 25 bars. In the green area, both isotopes are in the normal phase, in the blue area, ^{4}He is superfluid while ^{3}He is normal. The λ line indicates the superfluid transition for ^{4}He. The gray area shows an instable region where phase separation occurs.

1.3 Superfluidity in ultracold atomic gases

1.3.1 Interactions and scattering length

The nature of superfluidity in ultracold gases is strongly related to the interactions between particles. For low density gases, the dominant interactions are two-body interactions. For neutral atoms, these are Van der Waals interactions. They are characterized by an energy U and a finite range r_0: when the distance r between two particles is much larger than r_0, their interaction energy decays as $1/r^6$, while it is in the order of $U < 0$ for distances $\lesssim r_0$ and infinitely repulsive at very short distances. In very dilute gases, when the typical interparticle distance is much larger than the interaction range $n^{-1/3} \gg r_0$, these interactions are modeled by contact interactions and can be described with a potential proportional to Delta function $\delta(r)$. A lot of details on this subject are given in [Walraven, 2012, Rem, 2013], so I will only recall the main results. For lithium, magnetic dipole-dipole interactions are negligible with respect to contact interactions, and will not be considered in the following.

Let us now consider a collision between two particles, in the center of mass frame defined by (r,θ,ϕ) the wave function of the systems obeys the Schrödinger equation, with m_r the reduced mass of the two particles and $E_k = \hbar^2 k^2/(2m_r)$ the energy of the system:

$$\left[-\frac{\hbar^2}{2m_r}\Delta_r + U(r) - \frac{\hbar^2 k^2}{2m_r}\right]\psi = 0.$$

This equation can be solved into

$$\psi = \psi^0 + f_k(\theta)\frac{e^{ikr}}{r},$$

where $f_k(\theta)$ is the scattering amplitude, equal to:

$$f_k(\theta) = \frac{1}{k}\sum_{l=0}^{\infty}\sqrt{4\pi(2l+1)}Y_l^0(\theta)e^{i\delta_l}\sin\delta_l,$$

with $Y_l^m(\theta,\phi)$ the spherical harmonics and δ_l a phase acquired by the wave function due to the interaction potential. δ_l is typically very dependent on the details of the interaction potential. l is a quantum number describing the scattering. For symmetry reasons, for identical bosons, l is necessarily even, while it is odd for identical fermions with in particular $\delta_0 = 0$. There are no restrictions on l for distinguishable particles. Different values of l correspond to different effective scattering potentials U_l, and for each potential U_l it is possible to define a classical turning point r_l, corresponding to the distance at which incoming classical particles with energy $E = \hbar^2k^2/(2m)$ would have a zero kinetic energy. We have:

$$r_l = \frac{\sqrt{l(l+1)}}{k}.$$

In the low energy limit, corresponding to the low-temperature limit, $k \to 0$, and particles scattering with $l > 0$ feel a repulsive barrier, so that the phase shift $\delta_{l>0}$ actually vanishes: $\delta_{l>0} = 0$. We will thus in the following only consider $l = 0$ scattering, also called *s*-wave scattering, according to spectroscopic vocabulary. For identical fermions, since $\delta_0 = 0$, there is no collision in the low temperature limit. For bosons or distinguishable particles, f_k is equal to

$$f_k(\theta) = \frac{1}{k}e^{i\delta_0}\sin\delta_0,$$

and we define the *scattering length* a as:

$$a = -\lim_{k\to 0} f_k = -\lim_{k\to 0}\frac{\delta_0}{k}.$$

It is the scattering length that accounts for most of the scattering properties. To the first order in k, the scattering amplitude can be expressed as:

$$f_k(\theta) = \frac{-a}{1+ika}.$$

The total scattering cross-section σ_k, equal to $\sigma_k = 2\pi\int_0^{2\pi} d\theta\,\sin\theta|f_k(\theta) + f_k(\pi-\theta)|^2$, can also be expressed in terms of k:

$$\sigma_k = 4\pi\frac{a^2}{1+k^2a^2}$$

for distinguishable particles, and

$$\sigma_k = 8\pi\frac{a^2}{1+k^2a^2}$$

for indistinguishable particles. In the limit of small scattering length, the interaction strength of the system can be written as:

$$g = \frac{2\pi\hbar^2 a}{m_r}.$$

Let us now discuss the different interaction cases:

- Between two identical fermions, only p-wave interaction occurs and the scattering cross-section drops to zero as T^2.
- Between two identical bosons, the scattering length a_{bb} can take any value. For small values of a_{bb}, the interaction energy is given by $g_{\mathrm{bb}} n_{\mathrm{b}}$ where $g_{\mathrm{bb}} = \frac{4\pi\hbar^2 a_{\mathrm{bb}}}{m_{\mathrm{b}}}$ is the interaction strength. For negative values of a_{bb}, interactions are attractive and may lead to a collapse of the gas for large atom number [Bradley *et al.*, 1997, Sackett *et al.*, 1999, Gerton *et al.*, 2000, Donley *et al.*, 2001, Roberts *et al.*, 2001]. Large values of a_{bb} correspond to strong interactions between bosons. This will not be discussed in this thesis, but at the beginning of my PhD we performed experiments relating the lifetime of a Bose gas with $a_{\mathrm{bb}} \to \infty$ to the temperature [Rem *et al.*, 2013, Eismann *et al.*, 2015, Rem, 2013]. In the regime of the diverging scattering length, called the unitary limit, some predictions were made by Efimov [Efimov, 1970] regarding the existence of a three-body bound state for specific values of the two-body scattering length [Kraemer *et al.*, 2006, Berninger *et al.*, 2011], with some log-periodic properties [Huang *et al.*, 2014, Tung *et al.*, 2014, Pires *et al.*, 2014].
- Between two distinguishable fermions, for example between two fermions with different spin states, the scattering length a_{ff} can take any value. The regime where $a_{\mathrm{ff}} \to \infty$ is also called the unitary regime, and the scattering cross-section takes its maximum value $8\pi/k^2$. For fermions, the case $a_{\mathrm{ff}} > 0$ corresponds to strong attraction between fermions and leads to the formation of molecules with binding energy $-\frac{\hbar^2}{m_{\mathrm{f}} a_{\mathrm{ff}}^2}$. Being formed of two fermions, these molecules have an integer spin and bosonic behavior. The case $a_{\mathrm{ff}} < 0$ corresponds to weak attraction between fermions, as in the Bardeen-Cooper-Schrieffer theory for superconductivity. The fermion-fermion interactions will be discussed with more details in subsection 1.3.3.
- It may also be relevant to consider interactions between a boson and a fermion. In this case, the two colliding particles are obviously distinguishable, and the scattering length a_{bf} may take any value.

Let us now look at the effects of interactions on low-temperature gases.

1.3.2 Bose-Einstein Condensates

Realizing a Bose-Einstein condensate (BEC) of ultracold atoms had been a longstanding goal in the atomic physics community. This requires to obtain a combination of temperature and densities such that $n\lambda_{th}^3 \gtrsim 1$. A Bose-Einstein condensate with condensed matter thus requires temperature on the order of 1 K. However, except for

helium, all other atomic elements undergo solidification at temperatures well above 1 K, preventing condensation. Realizing a gaseous BEC thus requires to go to very low densities, typically $10^{14} - 10^{15}\,\mathrm{cm}^{-3}$. At such low densities, the rate of inelastic collisions (proportional to n^2) is strongly suppressed, with a typical timescale on the order of a few seconds or minutes. The gas is thus chemically metastable. The rate of elastic collisions (proportional to n) is still high enough to ensure thermal equilibrium. The counterpart is that the Bose-Einstein condensation occurs at even lower temperatures, on the order of 1 µK. Advanced cooling and trapping techniques were developed over the years by the atomic physics community with notably the Nobel Prize in Physics of 1997 attributed to W.D. Phillips, S. Chu and C. Cohen Tannoudji "for development of methods to cool and trap atoms with laser light".

The first BECs were realized in 1995 in the teams of E.A. Cornell and C.E. Wieman, and of W. Ketterle, also awarded with the Nobel prize in 2001. They were prepared in harmonic traps, and evidence for the condensation was given by a narrow peak in the velocity distribution.

To obtain the density distribution in the general case (and for simplicity here in the $T = 0$ limit), one should integrate the Gross-Pitaevskii equation:

$$i\hbar\frac{d\psi}{dt} = -\frac{\hbar^2}{2m_\mathrm{b}}\Delta\psi + U(\boldsymbol{r})\psi + g_\mathrm{bb}|\psi|^2\psi,$$

where ψ is the wave-function of the BEC, and $g_\mathrm{bb} = 4\pi\hbar^2 a_\mathrm{bb}/m_\mathrm{b}$. The terms of the right-hand-side of the equation account respectively for kinetic energy, trapping energy, and interaction energy.

One has to make a distinction between two different regimes: the ideal-gas limit, and the Thomas-Fermi limit. In the ideal gas limit, interactions are negligible with respect to the trapping potential energies ($n_\mathrm{b} g_\mathrm{bb} \ll \hbar\omega_{x,y,z}$). If we call $U(\boldsymbol{r}) = \frac{1}{2}m_\mathrm{b}(\omega_x^2 x^2 + \omega_y^2 y^2 + \omega_z^2 z^2)$ the harmonic trapping potential, the system is described by the Schrödinger equation:

$$i\hbar\frac{d\psi}{dt} = -\frac{\hbar^2}{2m_\mathrm{b}}\Delta\psi + U(\boldsymbol{r})\psi$$

The BEC wave function is the ground state of the harmonic oscillator and

$$n_\mathrm{b}(\boldsymbol{r}) = \frac{N_\mathrm{b}}{\pi^{3/2}}\frac{e^{-x^2/l_{ho,x}^2}}{l_{ho,x}}\frac{e^{-y^2/l_{ho,y}^2}}{l_{ho,y}}\frac{e^{-z^2/l_{ho,z}^2}}{l_{ho,z}},$$

where $l_{ho,\alpha=x,y,z} = \sqrt{\frac{\hbar}{m\omega_\alpha}}$ is the harmonic oscillator length and N_b the atom number in the BEC. However, non-interacting BECs are difficult to produce because low collision rate leads to a poor thermalization, and in most cases interactions are not negligible.

In the limit of strong interactions, called the Thomas-Fermi limit, the kinetic energy term in Schrödinger equation is neglected, and the wave-function obeys:

$$i\hbar\frac{d\psi}{dt} = U(\boldsymbol{r})\psi + g_\mathrm{bb}|\psi|^2\psi.$$

The atomic density is then

$$n_\mathrm{b}(\boldsymbol{r}) = \frac{15}{8\pi}\frac{N_\mathrm{b}}{l_{TF,x}\,l_{TF,y}\,l_{TF,z}}\max\left(1 - \left(\frac{x^2}{l_{TF,x}^2} + \frac{y^2}{l_{TF,y}^2} + \frac{z^2}{l_{TF,z}^2}\right), 0\right),$$

where $l_{TF,\alpha=x,y,z} = \sqrt{\frac{2\mu_\mathrm{b}}{m\omega_\alpha^2}}$ is the Thomas-Fermi radius of the cloud and μ_b its chemical potential. The density distribution has a parabolic shape. This expression can be integrated and inverted to express μ_b as a function of the other parameters: $\mu_\mathrm{b}^{5/2} = \frac{15\hbar^2 m_\mathrm{b}^{1/2}}{2^{5/2}} N_\mathrm{b} \bar{\omega} a_\mathrm{bb}$, with $\bar{\omega} = (\omega_x\omega_y\omega_z)^{1/3}$ the geometric mean of the trapping frequencies. A common technique to image BECs is to release them from the trap, and let them expand for a few milliseconds of *time of flight* t_{tof} before imaging them. For cigar-shape harmonic traps as it is the case for our experiment, with $\omega_x \approx \omega_y \approx \omega_\rho \gg \omega_z$, the initial half-lengths of the BEC $x_0(t=0)$, $y_0(t=0)$, $z_0(t=0)$ are within a ratio $z_0(0) = \frac{\omega_\rho}{\omega_z} x_0(0) = \frac{\omega_\rho}{\omega_z} y_0(0)$ and evolve as:

$$\begin{aligned} x_0(t) &= x_0(0)\sqrt{1+\tau^2}, \\ y_0(t) &= y_0(0)\sqrt{1+\tau^2}, \\ z_0(t) &= z_0(0)\left(1 + \frac{\omega_z^2}{\omega_\rho^2}\left(\tau \arctan\tau - \ln\sqrt{1+\tau^2}\right)\right), \end{aligned} \tag{1.1}$$

where $\tau = \omega_\rho t_{tof}$. This leads to the inversion of the ellipticity of the clouds for long time of flights (typically $\sim 10 - 100\,\mathrm{ms}$), and allows to measure the velocity distribution of trapped clouds. In our experiments, we will only use very short time of flights ($\lesssim 5\,\mathrm{ms}$), so that the cloud does not have time to expand axially. We do not have access to the 3D local density distribution of atoms, but rather to the integrated density along one or two directions. The density distributions vary then as:

$$\tilde{n}(y,z) \propto \max\left(1 - \frac{y^2}{l_{TF,y}^2} - \frac{z^2}{l_{TF,z}^2}, 0\right)^{3/2},$$

for densities integrated along x direction, and

$$\bar{n}(z) \propto \max\left(1 - \frac{z^2}{l_{TF,z}^2}, 0\right)^{2},$$

for densities integrated along x and y.

Let us now discuss the influence of interactions on BECs. A BEC with attractive interactions ($a_\mathrm{bb} < 0$) is unstable and collapses on itself above a critical atom number, on the order of 1000 atoms [Bradley *et al.*, 1997, Sackett *et al.*, 1999, Gerton *et al.*, 2000, Donley *et al.*, 2001, Roberts *et al.*, 2001]. A purely non-interacting BEC is stable, but the absence of collisions prevents thermalization between particles. It is also not superfluid because its critical velocity for superfluidity vanishes. For weakly interacting BECs with $a_\mathrm{bb} > 0$, it was shown [Bogoliubov, 1947] that they have an excitation spectrum compatible with Landau's criterion for superfluidity and are thus superfluids. This was evidenced by numerous experiments, for instance with the existence of quantized vortices [Matthews *et al.*, 1999, Madison *et al.*, 2000, Abo-Shaeer *et al.*, 2001] and critical velocity [Raman *et al.*, 1999, Onofrio *et al.*, 2000] in a stirred BEC.

1.3.3 Fermi superfluids

The realization of Fermi degenerate gases[67] (1999) and Fermi superfluids[68] (2004) was achieved after the first BECs. Fermions are difficult to cool because Pauli principle forbids s-wave collisions, thus preventing thermalization between identical fermions at low temperature. Standard evaporative cooling techniques cannot be used. There are two usual workarounds for the last cooling stages: either by sympathetic cooling, for which a bosonic and a fermionic gas are hold in the same trap, and fermions thermalize with the bosons that are evaporatively cooled [Schreck *et al.*, 2001b]. The other option consists in trapping two fermionic states between which collisions are allowed [DeMarco and Jin, 1999]. At the unitary limit, this option has proven to be very efficient, since the scattering cross-section is large and unitary limited.

Two-component Fermi clouds can then be prepared at temperatures well below the Fermi energy. The question of whether they are superfluids then depends on the temperature and on the interaction parameter $k_\mathrm{F} a_\mathrm{ff}$, where k_F is the Fermi wave vector of the gas, defined as $\frac{\hbar^2 k_\mathrm{F}^2}{2m_\mathrm{f}} = E_\mathrm{F}$ and a_ff the scattering length.

For values of a_ff such that $\frac{1}{k_\mathrm{F} a_\mathrm{ff}} \gg 1$, the system is said to be on the BEC limit. Indeed, strong attraction between fermions lead them to form pairs that then have a bosonic behavior and can undergo Bose-Einstein condensation [Zwierlein *et al.*, 2003, Zwierlein *et al.*, 2004].

For values of a_ff such that $\frac{1}{k_\mathrm{F} a_\mathrm{ff}} \ll -1$, the system is said to be on the BCS limit. Indeed, weak attraction between fermions lead them to form Cooper-like pairs, as described by the Bardeen-Cooper-Schrieffer (BCS) theory. Pairing occurs in momentum space, between two particles with opposite momentum.

For values of a_ff such that $\left|\frac{1}{k_\mathrm{F} a_\mathrm{ff}}\right| \ll 1$, the system is said to be unitary. Since the scattering length, characteristic length for the interactions, diverges, the only relevant length left in the problem is the interparticle distance $n^{-1/3}$, and results obtained for such a system are applicable for any system with resonant interactions. This is how neutron stars and other complex systems can be simulated with ultracold atoms [Bloch *et al.*, 2012]. The equation of state of a unitary Fermi gas at finite temperature has been obtained in [Nascimbène *et al.*, 2010].

[67] [DeMarco and Jin, 1999]

[68] [Regal *et al.*, 2004b]

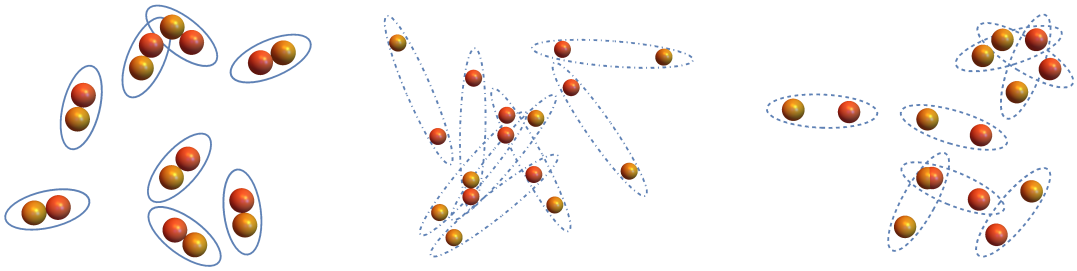

(a) BEC regime (b) BCS regime (c) Unitary regime

Figure 1.3: Representation of the three limit regimes of the BEC-BCS crossover. Fermionic pairs are circled in blue. On the BEC side, the typical pair size is smaller than the interparticle distance, while it is larger on the BCS side. At unitarity, both lengths are comparable.

These three regime span the so-called BEC-BCS crossover. They are represented on Figure 1.3. Superfluidity has been proven in the whole crossover, via the existence of vortices [Zwierlein *et al.*, 2005], and of a critical velocity [Miller *et al.*, 2007, Weimer *et al.*, 2015, Delehaye *et al.*, 2015]. The nature of the superfluid varies in the crossover, from tightly bound molecules to Cooper pairs [Veeravalli *et al.*, 2008]. A sketch of this is shown on Figure 1.3. The critical temperature for superfluidity varies as well as a function of $1/k_\mathrm{F}a_\mathrm{ff}$, from a roughly constant value on the BEC side to an exponentially small value on the BCS side, with a maximum close to $1/k_\mathrm{F}a_\mathrm{ff} = 0$ [Haussmann *et al.*, 2007].

In many experiments, fermions were mixed with bosons, that provided both a cooling agent and a convenient thermometer, but it was not until 2014 [Ferrier-Barbut *et al.*, 2014] that a Bose-Fermi superfluid mixture was produced in our group with ^{6}Li (fermions) and ^{7}Li (bosons) atoms. Other fermions involved in Bose-Fermi mixtures are ^{40}K, ^{87}Sr, ^{173}Yb, ^{161}Dy and ^{53}Cr, but so far Fermi superfluids were produced only with ^{6}Li and ^{40}K.

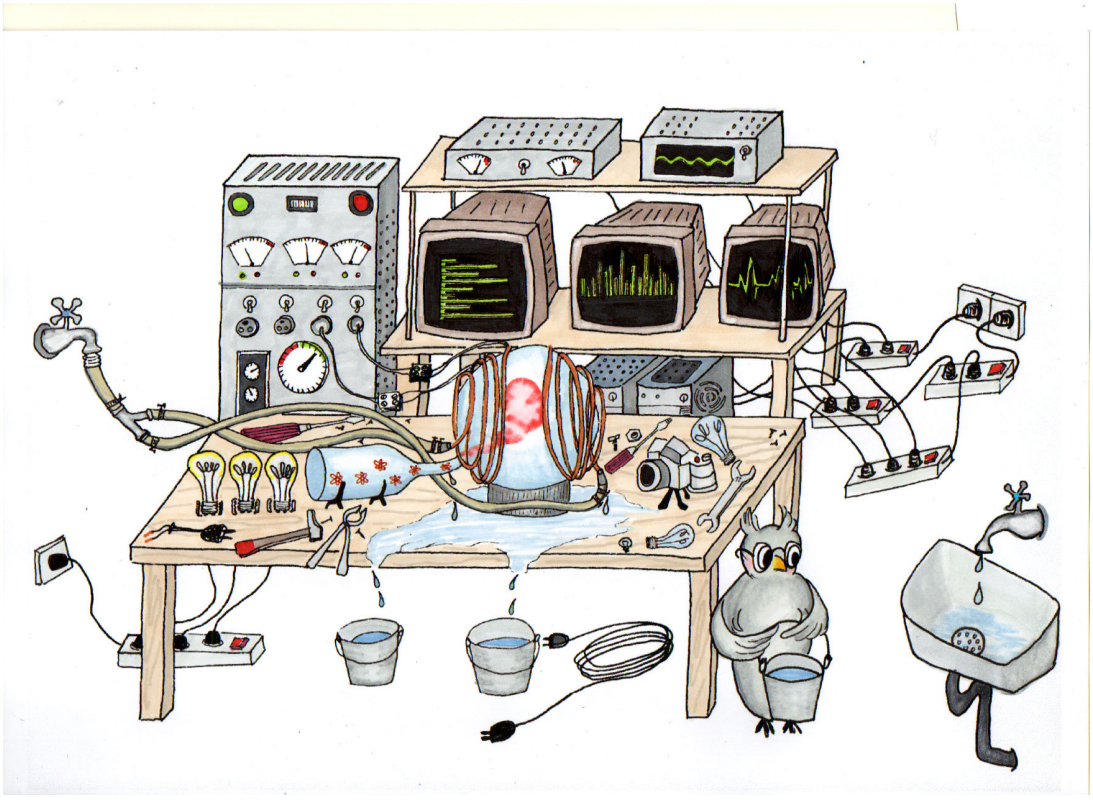

Chapter 2

Lithium Machine and Double Degeneracy

In this chapter I will present the historical machine that we use to produce ultracold gases of both fermionic and bosonic lithium (^{6}Li and ^{7}Li). It was built by Florian Schreck and Gabriele Ferrari in 1999 [Schreck, 2002] and rebuilt by Leticia Tarruell in 2004 [Tarruell, 2008]. All of the results described in this PhD have been obtained on this machine. Since it has already been described with great details in [Schreck, 2002, Tarruell, 2008, Nascimbène, 2010], and no major change to the experiment has been made since then, I will not go into deep details and refer the interested reader to the PhD theses cited above. First I will give a short overview of the main steps of the experiment, then present some specificities of lithium such as the existence of Feshbach resonances, before using these properties to describe the different steps of the experiment.

2.1 General description

For many cold-atom experiments, an initial Magneto-Optical Trap (MOT) stage is followed by direct loading of another trap, either optical or magnetic, where evaporative cooling can be performed. However, in the case of lithium, due to a small hyperfine splitting of the excited states, the temperature at the end of the MOT stage is usually[1] not low enough to load efficiently an optical dipole trap directly after the MOT. To overcome this issue, we transport the cloud to a small appendage allowing for strong magnetic gradients. Atoms are transfered in a magnetic Ioffe-Pritchard trap where we do a first evaporative cooling stage of ^{7}Li, that sympathetically cools down ^{6}Li. Atoms are then transfered into an optical dipole trap where some additional evaporative cooling stages are performed. ^{6}Li atoms are cooled down very efficiently and they sympathetically cool ^{7}Li. At the end of this second evaporative cooling stage, physics experiment are performed in a hybrid optical-magnetic trap. The different stages of the experiment are shown in Figure 2.1 and will be discussed later in this chapter.

2.2 Lithium

2.2.1 The atom of lithium

Lithium is an alkali with atomic number $Z = 3$. Its electronic ground state configuration is [He]$1s^1$. It has two natural isotopes: ^{6}Li (natural abundance 7.5%) and ^{7}Li (natural abundance 72.5%) and one artificial isotope, ^{8}Li with a half-life of 0.838 s. In the following, we will focus on ^{6}Li and ^{7}Li. Lithium is highly reactive with water and needs special care when manipulating. ^{6}Li has six nucleons and three electrons, it is thus a fermion, while ^{7}Li, with seven nucleons and three electrons, is a boson. Some of its physical properties are given in [Gehm, 2003].

[1] In the case of very large number of atoms and very powerful dipole trap this is however possible, as in the group of Chris Vale in Melbourne, Australia.

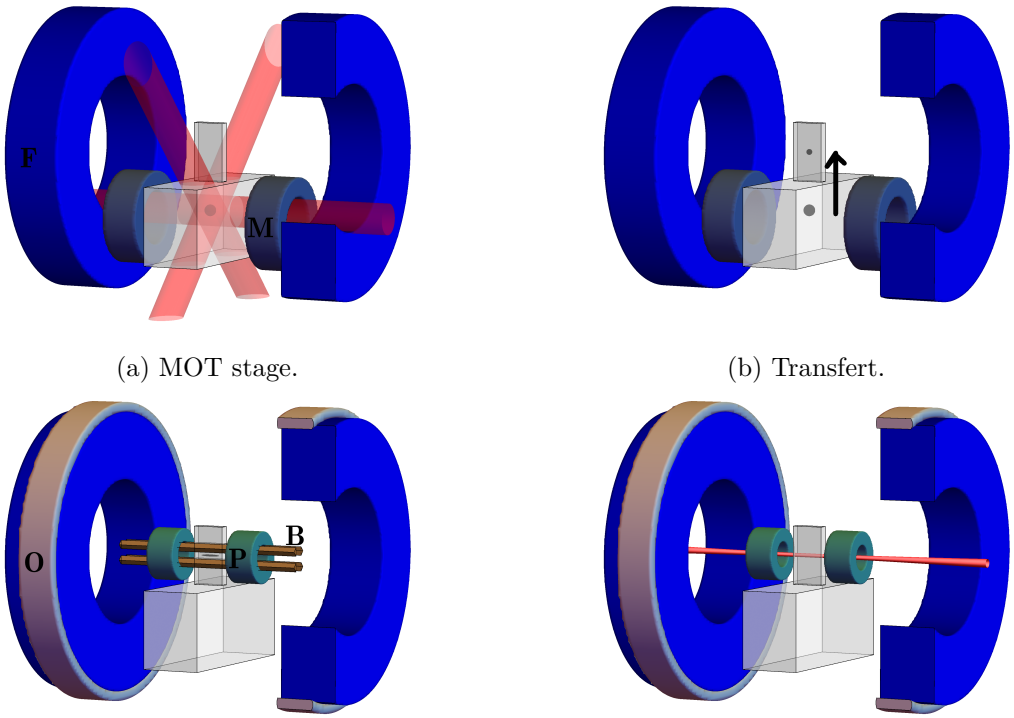

(a) MOT stage.

(b) Transfert.

(c) Ioffe-Pritchard trap.

(d) Dipole trap.

Figure 2.1: Experimental steps. (a) shows the MOT loading, with the two pairs of coils involved in this stage: the small MOT coils (M) generating the magnetic field gradient for the MOT, and the larger Feshbach coils (F), which are used at this stage to shift the MOT and locate it in front of the exit of the Zeeman slower. The red beams are the MOT beams. (b) shows the transfer of the atoms in the quadrupole trap from the MOT chamber to the appendage. Initially, the quadrupole trap is made by the MOT coils, but the current in the Feshbach coils in anti-Helmholtz configuration is progressively ramped up, displacing the minimum of the trap and the atoms accordingly. (c) shows the Ioffe-Pritchard trap. The bars (B) provide the radial confinement. The axial confinement is made by the greenish Pinch coils (P), while the magnetic field offset is adjusted by the blue Feshbach coils and can be tuned finely using the gray Offset coils (O). (d) shows the final configuration in the dipole trap. Radial trapping is made by a tightly focused far-detuned laser beam, while the Pinch coils make the axial confinement. The Feshbach and Offset coils are used to tune finely the magnetic field to the Feshbach resonance.

2.2.2 Atomic structure

Like all alkali atoms, since it only has one valence electron, the atomic structure of Li is quite simple. It is given in Figure 2.2. The ground state is $2^2S_{1/2}$, and its two lowest excited states are $2^2P_{1/2}$ and $2^2P_{3/2}$. The $2^2S_{1/2} \rightarrow 2^2P_{1/2}$ and the $2^2S_{1/2} \rightarrow 2^2P_{3/2}$ transitions are both in the red, at a wavelength of $\lambda = 671\,\text{nm}$. Reasonably high optical power at 671 nm is available from commercial sources. The next excited state, $3^2P_{3/2}$ (not shown in Figure 2.2), can be reached from the ground state with UV light at $\lambda = 323\,\text{nm}$ [Duarte *et al.*, 2011], though we do not use it in the experiment. The fine splitting between the $2^2P_{1/2}$ and the $2^2P_{3/2}$ is equal to 10.5 GHz, also equal to the isotopic shift. This results in a fortuitous coincidence between the D_1 lines of ^{7}Li and the D_2 lines of ^{6}Li that is used for the design of the laser system. The fine splitting (Δ_f) is indicated in Figure 2.2, as well as the hyperfine splitting Δ_{hf}. For the $2^2P_{3/2}$ (D_2 transition from ground state), the hyperfine states cannot be resolved because the width of all excited states is $\Gamma = 5.9\,\text{MHz}$.

Due to the Zeeman effect, the energy of these levels changes when varying the magnetic field B. For the $J = 1/2$ states, it is possible to solve the perturbated Hamiltonian exactly, and one obtains the Breit-Rabi formula [Breit and Rabi, 1931]:

$$E(m_F) = -\frac{\Delta_{hf}}{4} + \frac{g_I \mu_B}{\hbar} m_F B \pm \frac{\Delta_{hf}\left(I+\frac{1}{2}\right)}{2}\sqrt{1 + \frac{2\mu_B(g_I - g_J)}{\Delta_{hf}\hbar\left(I+\frac{1}{2}\right)^2} m_F B + \frac{\mu_B^2(g_I-g_J)^2}{\Delta_{hf}^2\hbar^2\left(I+\frac{1}{2}\right)^2}B^2}.$$

Here m_F is the magnetic moment $-F \leq m_F \leq F$, a_{hf} is the magnetic dipole moment for the ground state $2^2S_{1/2}$ and g_I (resp. g_J) are the nucleic (resp. electronic) Landé g-factor. Their values and other relevant quantities are shown in Table 2.1 for both isotopes.

Isotopic properties	^{6}Li	^{7}Li
Natural abundance	7.59%	92.4%
Mass	$9.99 \cdot 10^{-27}$ kg	$11.65 \cdot 10^{-27}$ kg
Total electronic spin S	1/2	1/2
Total nuclear spin I	1	3/2
Hyperfine coupling constant Δ_{hf}	152.14 MHz	401.75 MHz
Electronic g-factor for ground state g_S	2.0023010	2.0023010
Nuclear g-factor g_I	$-0.448 \cdot 10^{-3}$	$-1.182 \cdot 10^{-3}$
D_1 transition frequency	446.7896 THz	446.8001 THz
D_2 transition frequency	446.7996 THz	446.8102 THz
Excited state linewidth	5.9 MHz	5.9 MHz
Hyperfine splitting of ground state	228 MHz	803.5 MHz

Table 2.1: Some atomic properties of Li

This is used to calculate the evolution of the energy of the ground state $2^2S_{1/2}$ sub-

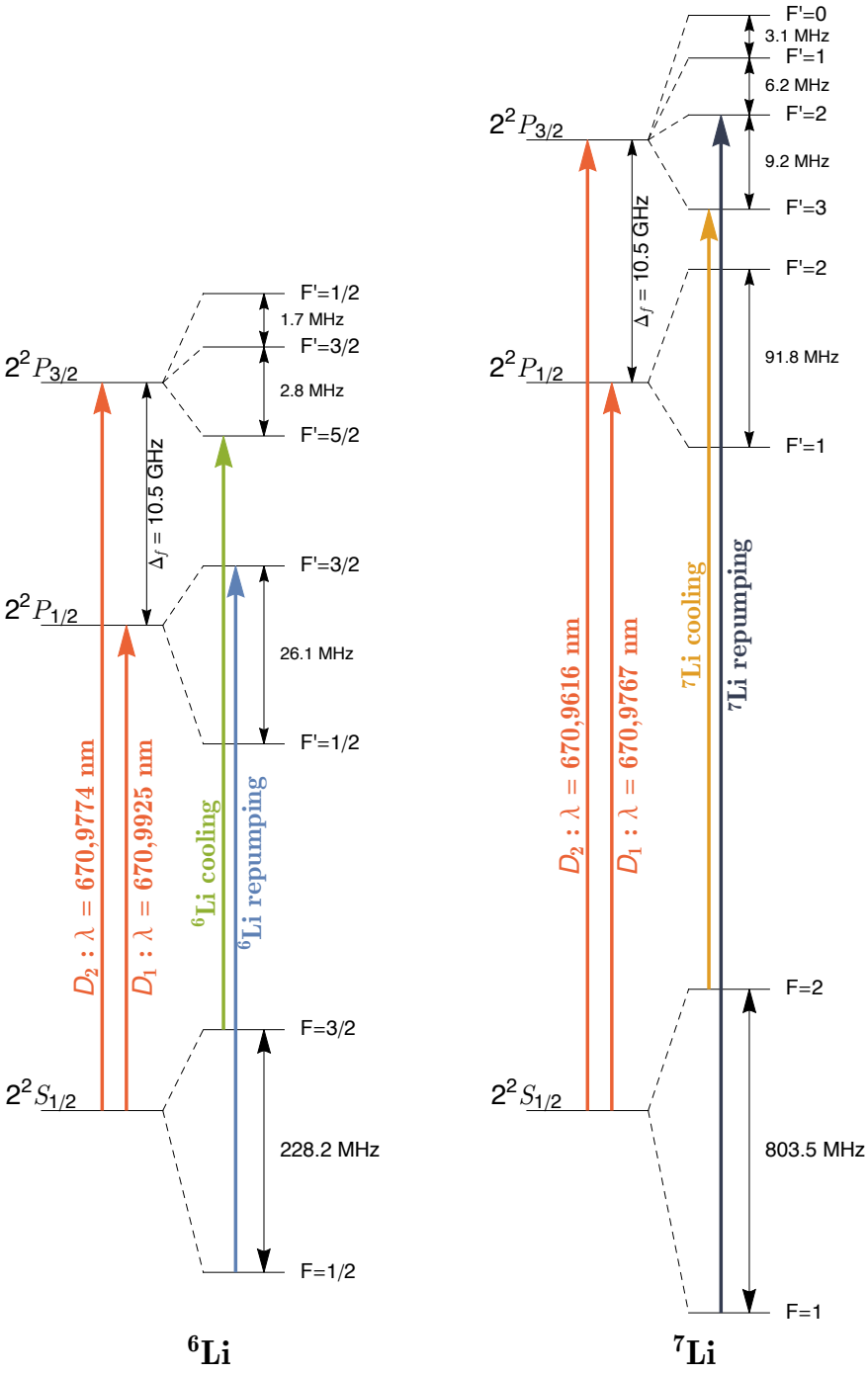

Figure 2.2: Schematic representation of ^{6}Li and ^{7}Li atomic structure. Only the first two excited states are shown. The excited state fine splitting is 10.5 GHz for both isotopes. The wavelengths for the atomic transitions are shown in red, and the green, blue, yellow and dark gray indicate the transitions used to cool the atoms with the Zeeman slower and the MOT. The color code for the cooling and repumping frequencies correspond to the one we use on the experiment, except that the 'white' is shown in dark gray here. The width of the excited states is 5.9 MHz.

levels for both ^{6}Li and ^{7}Li, as shown in Figure 2.3 and Figure 2.4[2]. Note that at zero magnetic field (as in Figure 2.2) the Zeeman sub-levels are degenerate. The notations introduced in Figure 2.3 and Figure 2.4 will be used in the following to refer to the atomic states. Atoms the energy of which decreases when increasing the magnetic field are called *high field seekers*, those the energy of which increases with magnetic field are called *low field seekers*.

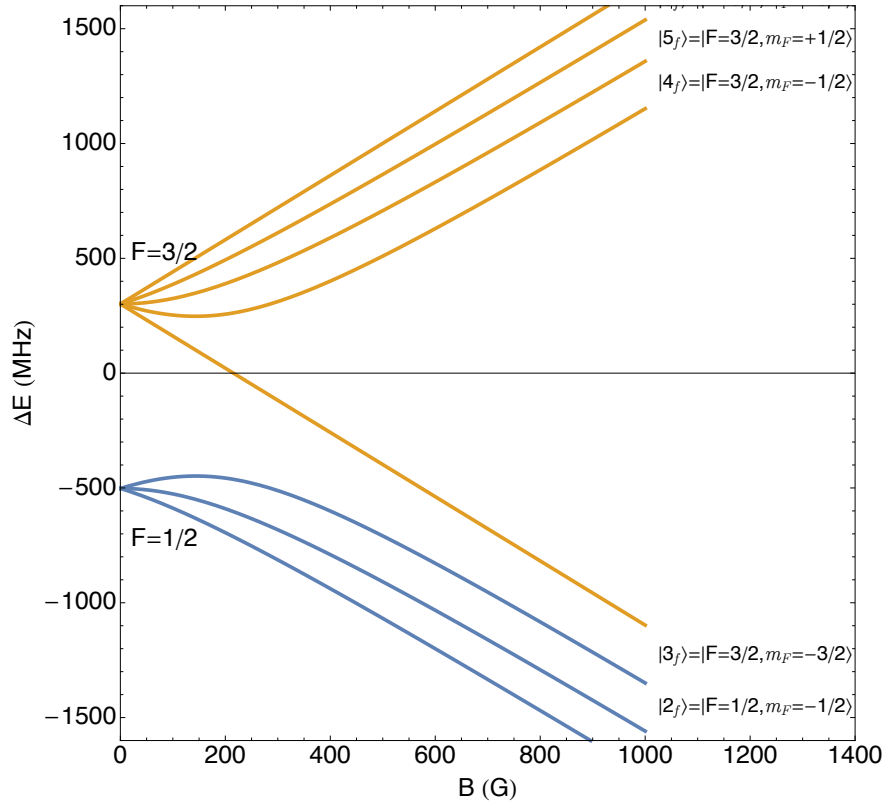

Figure 2.3: Energy of the Zeeman sub-levels of the ground state $2^2S_{1/2}$ of ^{6}Li as a function of magnetic field. The magnetic field vector is chosen as the quantization axis.

2.2.3 Feshbach resonances

The atom of lithium has a very important property: the interatomic interaction can be tuned via the use of Feshbach resonances. As indicated in chapter 1, low interactions between atoms are characterized at low energy by the scattering length a between these atoms. For atoms showing Feshbach resonances, the scattering length can be tuned simply by varying the magnetic field. This property is used both to cool efficiently the atoms and to probe strongly-interacting many-body physics.

The principle of the Feshbach resonances is the following [Walraven, 2012, Dalibard, 1999]: consider a collision between two atoms. Each atom has several internal states,

[2]Courtesy from Daniel Suchet

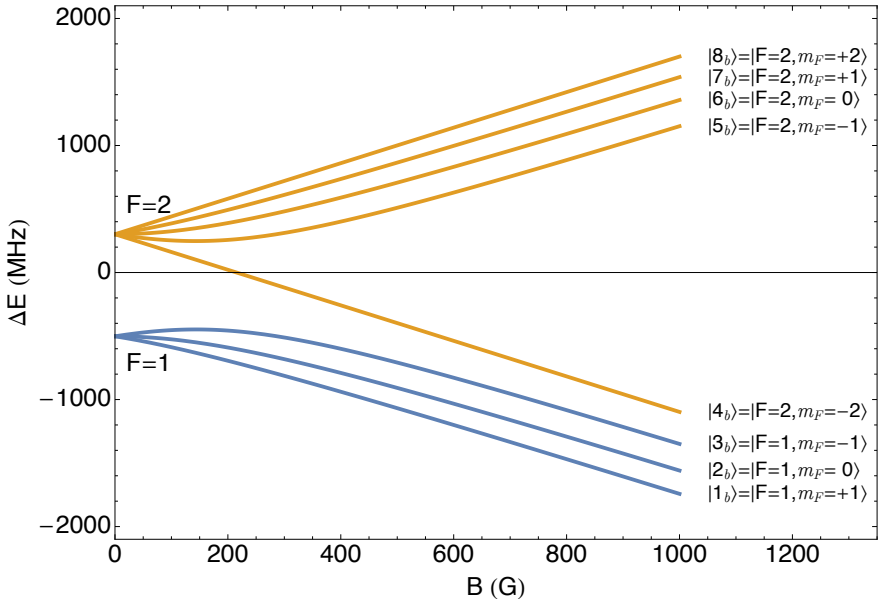

Figure 2.4: Energy of the Zeeman sub-levels of the ground state $2^2S_{1/2}$ of ^{7}Li as a function of magnetic field. The magnetic field vector is chosen as the quantization axis.

and each combination of states is associated to an interaction potential (displayed in Figure 2.5 in the center-of-mass frame). In the general case, the potentials may have bound states. If the only accessible states of a certain potential are bound states, then this potential is called a "closed channel". This is the case of the potential shown in blue in Figure 2.5. However, if scattering levels are accessible for this pair of atoms, the potential is called an "open channel",as it is the case for the potential shown in pink in Figure 2.5. Since the internal states of the particles may change during a collision, these potentials are coupled to each other. Now, in the low energy physics that apply with cold atoms, if two particles collide, they come from a scattering state from an open channel (then called the "entrance channel") with an energy E slightly higher than the dissociation limit of the entrance channel. They interact during the collision, and may go away again from each other. But if there was a level of the closed channel whose energy was very close to 0 (the energy of the colliding particles), its coupling to the open channel strongly affects the collisional properties of the system, such that the scattering length diverges.

And as it turns out, since the internal states depend on the magnetic field, for some atoms it is possible to tune the energy of the bound channel with respect to that of the open channel by varying the magnetic field. In other words, we can change the scattering properties and more particularly the scattering length with the magnetic field. This phenomenon is called a Feshbach resonance [Feshbach, 1958]. In the vicinity of the resonance, a good approximation for the scattering length is given by

$$a(B) = a_{bg}\left(1 + \frac{\Delta B}{B - B_{\text{res}}}\right)$$

where a_{bg} is the collisional background scattering length, ΔB the width of the reso-

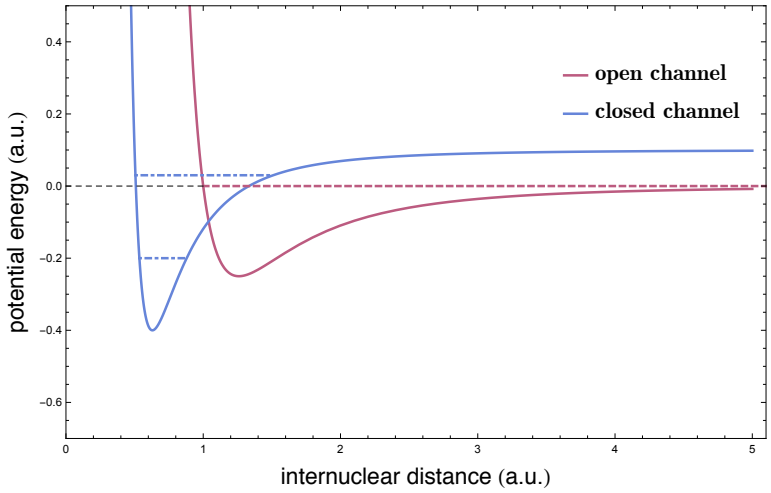

Figure 2.5: Schematic representation of the level crossing that leads to a Feshbach resonance. The blue curve represents a closed channel and its energy states, the pink curve an open channel with its energy states, in arbitrary units. We can see that the highest energy state of the closed channel is very close to zero, the dissociation energy of the open channel. If one of the potentials is sensitive to magnetic field (say the open channel for instance), it is possible to bring them to the same energy, and this results into a resonance phenomenon and a divergence of the scattering length. This phenomenon is known as a Feshbach resonance.

nance, and B_{res} the magnetic field at resonance.

This phenomenon of Feshbach resonance may appear between two identical bosons, as it is the case for ^{7}Li. ^{7}Li shows a number of Feshbach resonances, some of which are given in Table 2.2. They have been used in our group to vary the interactions within the gas, and to study beyond mean-field effects [Navon *et al.*, 2010], three-body losses and Efimov physics [Rem *et al.*, 2013, Eismann *et al.*, 2015]. For ^{6}Li, there is no s-wave collisions for identical fermions[3]. However, for fermions in two different spin states, the scattering length may also vary and encounter Feshbach resonances, as it is the case for ^{6}Li. Some of the relevant Feshbach resonances for ^{6}Li are given in Table 2.2. There also exists Feshbach resonances between ^{6}Li and ^{7}Li (see Table 2.3), and even though we do not exploit them in the current experiment, we plan to use them in the future[4]. For the whole range of magnetic fields that we used in the experiments described in this PhD, the scattering length between ^{6}Li and ^{7}Li is roughly equal for all spin states and its value is 40.8 a_0, where $a_0 = 52.9\,\text{pm}$ is the Bohr radius.

[3] And the colder the atoms, the more p-wave collisions can be neglected.

[4] Some of these resonances require to trap low-field seeking states, with a crossed-dipole trap for instance, currently not implemented in the experiment. The other resonances are around 400 G, but their narrowness (they are only a few mG wide) makes them challenging to study with the current experiment.

Atomic levels	$a_{bg}(a_0)$	B_{res} (G)	ΔB (G)
$\|1_b\rangle$	-20.98	738.2	171
$\|2_b\rangle$	-18.24	845.5	-4.52
		893.7	237.8
$\|1_f\rangle - \|2_f\rangle$	-1582	832.2	262.3
$\|1_f\rangle - \|3_f\rangle$	-1770	690.43	166.6
$\|2_f\rangle - \|3_f\rangle$	-1642	811.2	200.2

Table 2.2: List of Feshbach resonance parameters for the atomic states used in the experiment, with the notations for the Zeeman states defined in Figure 2.3 and Figure 2.4, from [Chin *et al.*, 2010].

Atomic levels	$\|1_f\rangle$	$\|2_f\rangle$	$\|3_f\rangle$	$\|4_f\rangle$	$\|5_f\rangle$	$\|6_f\rangle$
$\|1_b\rangle$	230	270	310	530	530	535
	550	578	610			
$\|2_b\rangle$	310	330	380	660	670	680
	600	610	660			
$\|3_b\rangle$	360	390	730	820		
	670	700				
$\|4_b\rangle$	450	800				
	770					
$\|5_b\rangle$	690	740				
$\|6_b\rangle$	750	805	860			
$\|7_b\rangle$	750	800	830			
$\|8_b\rangle$	700	750	810			

Table 2.3: Indications of the magnetic fields (in G) for the Feshbach resonances between the different states of ^{6}Li and ^{7}Li, with the notations for the Zeeman states defined in Figure 2.3 and Figure 2.4. The given magnetic fields are ± 10 G approximations. All of the resonances below 500 G have a width below 5 G. However, there are some relatively wide resonances between $|3_b\rangle$ and $|4_f\rangle$, $|5_f\rangle$, and between $|6_b\rangle$ and $|1_f\rangle$, $|2_f\rangle$. They are indicated in blue.

2.3 Loading the MOT

The first step of every cold atom experiment is to load a magneto-optical trap (MOT). This trap relies on the use of near-resonant laser beams that acts both as a molasses to slow down the atoms and as a trapping force so that they can be trapped in the local minimum of a potential created by a magnetic field. Atoms are thus trapped both in real space and in momentum space. The source of atoms is usually either an oven (as it is the case here) or a dispenser. They produce a hot atomic vapor that, depending on the atomic species, may be loaded directly into the MOT (for cesium for instance), or has to be slowed down (as for lithium). Here this is done by a Zeeman slower, but a 2D MOT [Dieckmann *et al.*, 1998] have been used successfully in other

experiments [Tiecke *et al.*, 2009].

2.3.1 Oven

Since lithium has a very low vapor pressure at room temperature, it is necessary to heat it up to about 500°C to have a strong enough atomic flux. A drawing of the oven used to heat up the atoms is given in Figure 2.6. It is composed of a vertical tube, with a CF40 flange on top, connected to the rest of the experiment through an horizontal tube. This provides a collimated atom beam. Several heating cables[5] and temperature sensors are wrapped around the oven in order to control its temperature accurately at different positions[6]. Currently the temperature at the bottom of the tube is at 510°C, and there is a decreasing temperature gradient from the oven to the experiment in order to recycle lithium atoms. The surface tension of liquid lithium decreases with temperature, so that it goes from cold to hot surfaces and returns to the oven. In addition, a thin grid[7] inserted in the horizontal tube increases the wetting of the surface by lithium. However, this recycling strategy is sometimes not efficient enough, and the tube may get clogged, as it happened a few times without us noticing it. To remove the clog, we had to heat up the horizontal tube at 600°C by increasing the current in the thermocoax cable while monitoring the fluorescence of the MOT. Important jumps in the fluorescence signal indicated the unclogging of drops from the tube. Running the experiment with the oven at 600°C would prevent the tube to clog, but leads to a important reduction of the trap lifetime, incompatible with the following steps of the experiment.

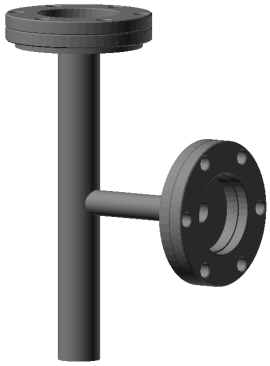

Figure 2.6: Drawing of the oven. The lithium is lying at the bottom of the vertical tube, which is heated up at 500°C.

2.3.2 Zeeman slower

When they exit the oven, the atoms have a thermal velocity of about $1700\,\mathrm{m.s^{-1}}$, while the capture velocity of the MOT is approximately $50\,\mathrm{m.s^{-1}}$. It is thus necessary to slow down the atoms. This is performed by shining a counter-propagating beam on

[5] Thermocoax SEI 10/50-25/2x CM10
[6] Temperature controller Omega CN76133
[7] Alpha Aesar 13477

atoms exiting the oven. But as soon as the atoms are slowed down, the Doppler effect brings them out of resonance for the laser beam. A Zeeman slower uses Zeeman effect to overcome this issue, and creates a magnetic field that compensates the change in resonance frequency of the atoms. To get a constant deceleration, the magnetic field has to vary with the square-root of the distance traveled by the atomic beam. Several designs can be used and in our case we have a *spin-flip* Zeeman slower, in which the magnetic field goes from +800 G at the entrance of the Zeeman slower to −200 G at the exit. This configuration ensures that the laser beams used in the Zeeman slower will be off-resonant for atoms in the MOT and reduces power consumption and heating.

Considering now the laser beams, here we have four frequencies mixed together: two principal and two repumpers.

- The principal light for ^{6}Li, on the D_2 line from $F = 3/2$ to $F' = 5/2$, slows down ^{6}Li atoms (shown in green in Figure 2.2).

- The repumper light for ^{6}Li is necessary to recycle the atoms falling into the $F = 1/2$ level of the ground state. This repumper light is on the D_1 line of ^{6}Li (shown in blue in Figure 2.2).

- The principal light for ^{7}Li, on the D_2 line from $F = 2$ to $F' = 3$ slows down ^{7}Li atoms (shown in yellow in Figure 2.2).

- A repumper is also needed for ^{7}Li, to recycle atoms that fell in the $F = 1$ level of the ground state, but we cannot use its D_1 lines because it would affect ^{6}Li. Repumping is thus made on the D_2 line, between $F = 1$ and $F' = 2$ (shown in gray in Figure 2.2).

All four laser frequencies are recombined on a single mirror just before being sent into the Zeeman slower tube. The detunings used in the experiment are given in Table 2.4. The detuning of the beams is very robust and almost never needs to be re-optimized[8].

^{7}Li Principal	-390 MHz
^{7}Li Repumper	-400 MHz
^{6}Li Principal	-390 MHz
^{6}Li Repumper	-375 MHz

Table 2.4: Detunings used for the Zeeman slower, with respect to the transitions indicated in Figure 2.2. The detunings are quite large because the magnetic field is varied from +800 G to −200 G between the two ends of the Zeeman slower and the beams are resonant with the atoms when they are in the area with $B \simeq 0$, where they still have a velocity of about 250 m.s^{-1}.

[8]Even though a small drift of the alignment may require some minor adjustments from time to time.

2.3.3 MOT

At the end of the Zeeman slower, atoms are slow enough to be captured in a magneto-optical trap. It is composed of three pairs of counter-propagating laser beams, orthogonal to each other, and of a magnetic field gradient. The combination of laser beams and of the magnetic field traps atoms in real and momentum space. A reading on optical molasses and magneto-optical traps was given by Jean Dalibard at Collège de France, year 2014-2015 (lecture notes are available in French). We have a dual-species MOT, and the laser frequencies used follow the same constraints as for the Zeeman slower. The four frequencies (Principal and Repumper for each isotope) are recombined on four beam-splitter cubes, resulting into four beams containing each of the four frequencies. Three of these beams are the MOT beams and are sent on the atoms, and the last one is sent on a Fabry-Perot for frequency monitoring. The magnetic field gradient is provided by a pair of coils called the MOT coils, and the MOT is shifted upward to be located in front of the exit of the Zeeman slower by another pair of coils called the Feshbach coils, see Figure 2.1a. We load the MOT for about one minute. At the end of the loading stage, we typically have $4 \cdot 10^7$ ^{6}Li atoms and 10^9 ^{7}Li atoms at a temperature of 3 mK. We then switch off the Feshbach coils (that brought the center of the magnetic trap in front of the Zeeman slower) to do the 'Shift MOT'. Then the MOT is compressed (CMOT) by bringing the lasers closer to resonance and reducing the repumper beam intensities. This increases atomic density and decreases temperature, ensuring an increase of the phase-space density and a better loading into the next trap, purely magnetic. Detunings and magnetic field gradients for MOT and CMOT stages are summed up in Table 2.5. The detunings have to be re-optimized from time to time due to slow drifts. After the CMOT, we have $N_\mathrm{b} \sim 10^9$, $N_\mathrm{f} \sim 4 \cdot 10^7$ atoms at a temperature of $T = 600\,\mu\mathrm{K}$.

	MOT	CMOT
^{7}Li Principal	-49 MHz	-30 MHz
^{7}Li Repumper	-38 MHz	-21 MHz
^{6}Li Principal	-35 MHz	-8 MHz
^{6}Li Repumper	-12 MHz	-7 MHz
Gradient	25 G/cm	25 G/cm

Table 2.5: Detunings and magnetic field gradients used for the MOT and CMOT. Values from May 2015. The detunings are given with respect to the transitions indicated in Figure 2.2.

2.3.4 Laser system

The frequencies are generated by three master lasers that are locked on atomic transitions. However, these master lasers produce a relatively low optical power which has to be amplified before being sent on the atoms. We use slave diodes[9] that are injected with a few hundreds of µW and output about 150 mW. These are low-cost diodes

[9]Hitachi HL6545MG, now available from Thorlabs

manufactured for DVD players, but their natural output wavelength is approximately 660 nm, so they have to be heated at 70°C to emit at 670 nm. The lifetime of these diode is rather short (a few months), so we use optical fibers to be able to replace them without realigning the rest of the experiment. We have one diode for each of the frequencies for both the Zeeman slower and the MOT, each of them delivering a total power of 40-50 mW on the atoms. We also have two more pre-amplifying slave diodes after the master laser on the D_2 of each isotope. In addition, since a high atom number of ^{7}Li turned out to be critical for the realization of a double-superfluid mixture, we thus had to increase the optical power at the ^{7}Li principal frequencies both for the MOT and the Zeeman slower using Tapered Amplifiers(TAs)[10]. They are seeded with 10-20 mW and produce up to 500 mW of output power, resulting in 100-150 mW of power available on the atoms[11]. This cascade of light sources ensures enough optical power to perform the experiment, at the price of a relatively poor shot-to-shot stability.

2.4 Magnetic trap, transport, and RF evaporation

2.4.1 Optical pumping

Before loading atoms into a magnetic trap, we have to prepare them in the right spin states: since Maxwell's equations prevent a local maximum of static magnetic field, we can only trap atoms polarized in low-field seeking states. Since we also want them to be stable against spin-exchange collisions, the only acceptable states are $|F = 2, m_F = +2\rangle$ for ^{7}Li and $|F = 3/2, m_F = +3/2\rangle$ for ^{6}Li (indicated as $|8_b\rangle$ and $|6_f\rangle$ in Figure 2.4 and Figure 2.3, respectively). However, at the end of the CMOT stage, atoms are in $F = 1/2$ (for ^{6}Li) and $F = 1$ (for ^{7}Li), and are evenly distributed in the Zeeman sub-levels $|1_f\rangle$, $|2_f\rangle$ and $|1_b\rangle$, $|2_b\rangle$, $|3_b\rangle$[12]. It is thus necessary to perform an optical pumping stage.

Optical pumping is realized with a beam with σ^+ light, with respect to a weak ($\sim$10 G) guiding magnetic field, in which two frequencies are mixed. One of the frequencies is used to transfer ^{7}Li from $F = 1$ to $F = 2$ *via* the $F' = 2$ state of the D_2 transition and realizes the so-called 'hyperfine' pumping for ^{7}Li. It is tuned to the $F = 1 \rightarrow F' = 2$ transition at zero magnetic field. The other frequency has two roles: first, it pumps the ^{7}Li atoms of the $F = 2$ manifold to $|F = 2, m_F = 2\rangle$ state through the $F' = 2$ state of the D_1 transition and realizes the 'Zeeman' optical pumping for ^{7}Li. The pumping is made on the D_1 transition in order not to disturb the hyperfine pumping. Second, it also pumps ^{6}Li atoms from the $F = 1/2$ to the $F = 3/2$ manifold, *via* the $F' = 3/2$ state of the D_2 transition, for the hyperfine pumping of ^{6}Li. The detuning for that frequency results from a compromise between these two roles, and simultaneous optimization of ^{6}Li and ^{7}Li atom numbers leads to a detuning of -45 MHz for the $F = 2 \rightarrow F' = 2$ D_1 transition for ^{7}Li and of $+25$ MHz for the

[10] We use TA chips from Toptica installed in a home-designed mount.

[11] 180 mW in the best conditions. The high fraction of lost power is due to a non-gaussian output mode of the Tapered Amplifier which makes its coupling into a polarization-maintaining single mode fiber challenging. In addition, the total output power slowly decays from 500 mW to 300 mW.

[12] During CMOT, the intensities of the repumpers are decreased to zero. Atoms thus accumulate in the $F = 1/2$ (for ^{6}Li) and $F = 1$ (for ^{7}Li) states.

$F = 1/2 \rightarrow F' = 3/2$ D_1 transition for ^{6}Li. There is no Zeeman optical pumping for ^{6}Li because the number of ^{6}Li atoms is not critical at that stage of the experiment. The full optical pumping sequence lasts 300 µs, long enough to give time to magnetic fields to stabilize, but short enough not to heat up the clouds. A summary of the optical pumping parameters is given in Table 2.6. Its efficiency is about $\sim 60\%$.

Isotope	Pumping type	Transition	Detuning (MHz)
^{7}Li	Hyperfine	D_2 $F = 1 \rightarrow F' = 2$	0
	Zeeman	D_1 $F = 1 \rightarrow F' = 2$	-45
^{6}Li	Hyperfine	D_2 $F = 1/2 \rightarrow F' = 3/2$	+25
	Zeeman		

Table 2.6: Parameters for the optical pumping. The detunings are given with respect to the transitions indicated in Figure 2.2.

2.4.2 Magnetic trap and transport

2.4.2.1 Magnetic trap

Once the atoms are prepared in the right magnetic states, they are loaded into a quadrupole magnetic trap. The trap is realized by the MOT coils with current in opposite directions (as in anti-Helmholtz configuration) and is ramped on in 2 ms. Since the same coils are used for the MOT stage and for the quadrupole trap, at the end of the MOT the atoms are already at the center of the quadrupole trap. We use the maximum available current of 500 A, leading to a magnetic field gradient of 335 G.cm^{-1}. The number of trapped atoms are $N_\mathrm{f} = 7 \cdot 10^7$ and $N_\mathrm{b} = 7 \cdot 10^8$ at a temperature of ~ 2 mK. Loading efficiency is about 60 %.

2.4.2.2 Magnetic transport

The clouds now have to be transported inside the appendage, an additional very thin part of the cell that allows the realization of very strong magnetic field gradients. This is done by moving the center of the magnetic trap: the Feshbach coils, the center of which is located inside the appendage, are ramped on in anti-Helmholtz configuration while the current of the MOT coils is decreased to zero in 500 ms. The current in the MOT coils is finally reversed to give a final push to the atoms and center them in the appendage. The overall efficiency of the transfer is about 40 %, mainly because part of the cloud is cut by the walls of the appendage. A scheme of this stage is given in Figure 2.1b.

2.4.3 Ioffe-Pritchard trap

The simplest magnetic trapping configuration is the quadrupole trap realized using anti-Helmholtz coils in which atoms are confined near the magnetic field zero. However, this design suffers from Majorana losses when temperature is decreased: close to a zero of magnetic field, atoms might undergo a spin flip and go from a *low-field seeking*

trapped state to a *high-field seeking* anti-trapped state... To overcome this issue, several possibilities have been used in the cold atom community:

- The Time Orbiting Potential (TOP) trap, where the minimum of the magnetic field is rotated fast enough so that the atoms don't notice, and see on average a non-zero magnetic field minimum [Petrich *et al.*, 1995, Anderson *et al.*, 1995].
- The plug, where the position of the magnetic field zero is plugged by a blue-detuned laser beam that repel the atoms from the center [Davis *et al.*, 1995a].
- The Ioffe-Pritchard trap, which have a non-zero minimum, and is the solution that was used in our experiment [Pritchard, 1983].

In our experiment, the Ioffe-Pritchard trap is made of four bars parallel to the z direction that realize a tight radial confinement and of a pair of coils called the *Pinch Coils* to realize the axial confinement. Another pair of coils (that turns out to be the Feshbach coils used for the magnetic transport) is used to tune the bias field, so that the bias field is high enough to prevent Majorana losses, and low enough not to reduce the radial confinement. It can be finely adjusted using a third pair of coils called *Offset* coils. A scheme of the trap is given in Figure 2.1c.

The loading of the Ioffe-Pritchard trap is not so straightforward due to the different shapes of the traps: the quadrupole trap at the end of the transport has an aspect ratio of 2, the axial direction z being more confined than the radial ones x and y, while the cloud in the Ioffe-Pritchard trap will have an elongated, cigar-like shape with a much higher aspect-ratio. To ensure good loading efficiency, the cloud is deformed at the end of the transport by switching on the current in the bars. This has to be done abruptly to avoid any cancellation of the confinement in one of the radial directions[13]. The pinch coils are then ramped up while decreasing the quadrupole to ensure that axial confinement is always present. The efficiency of the transfer in the Ioffe-Pritchard trap is hard to evaluate because we cannot count reliably the atoms at this stage: the clouds are too dense.

2.4.3.1 Doppler cooling

After the Ioffe-Pritchard trap loading, the atoms have a temperature of 3 mK. Unfortunately, the collisional scattering cross-section for ^{7}Li vanishes for a relative collision energy of 6 mK and at 3 mK it is still too low to ensure efficient evaporation. It is thus necessary to add another cooling stage of ^{7}Li.

A single beam with σ^+ polarization slightly red-detuned from the the D_2 transition $|F = 2, m_F = 2\rangle \rightarrow |F' = 3, m'_F = 3\rangle$ of ^{7}Li is thus sent on the atoms. This beam cools in one direction, and thermalization in the other directions is ensured by the collisions in the quadrupole trap [Suchet *et al.*, 2015]. Doppler cooling is made in two stages of 1 s, and the trap is re-compressed between the first and the second stage by increasing the bias field to optimize overall cooling. At the end of the Doppler cooling, the

[13] The 3D quadrupole made by the Feshbach coils have a magnetic field given by $\boldsymbol{B} = b'(-x\boldsymbol{e_x} - y\boldsymbol{e_y} + 2z\boldsymbol{e_z})$ while the 2D quadrupole made by the bars have a magnetic field given by $\boldsymbol{B} = G(x\boldsymbol{e_x} - y\boldsymbol{e_y})$, with b' and G positive. When increasing the bars' current, G increases, and when $G = b'$, there is no more confinement in the x direction.

temperature is about 300 μK, at the price of 25% atom loss, and the collision rate of about $\sim 15\,\mathrm{s}^{-1}$ is now sufficiently high to allow efficient evaporative cooling [Schreck *et al.*, 2001a]. The efficiency of the Doppler cooling is very sensitive to the detuning, which itself depends on the magnetic fields. In practice, the optimization is empirical and has to be redone daily.

2.4.4 RF evaporation

Evaporative cooling consists in removing the hottest atoms from an assembly of atoms and in letting the remaining atoms thermalize at a lower temperature [Ketterle and Druten, 1996]. Since the hot atoms are at the tail of the Maxwell-Boltzmann distribution, they carry a significant amount of energy, and this loss of hot atoms actually leads to an increase of phase-space density. There exist two main situations to perform evaporative cooling: either in a magnetic trap, where a finely tuned RF signal transfers the hot atoms from a trapped to an anti-trapped state [Hess, 1986, Masuhara *et al.*, 1988, Anderson *et al.*, 1995, Davis *et al.*, 1995a], or in an optical trap, where the depth of the potential can be lowered so that the hot atoms escape the trap. The latter will be used later in the experiment, and the former is the one used for this stage. This is the last cooling stage of ^{7}Li, that will sympathetically cool ^{6}Li: Pauli blocking prevents collisions between fermions in the same spin state, but collisions between ^{6}Li and ^{7}Li are allowed and are frequent enough to ensure good thermalization between ^{6}Li and ^{7}Li. This stage is realized in the Ioffe-Pritchard trap with a low bias field and radio-frequency (RF) field [Pritchard *et al.*, 1989, Davis *et al.*, 1995b] that transfer the hottest ^{7}Li atoms from the trapped $|F = 2, m_F = 2\rangle$ state to the anti-trapped $|F = 1, m_F = 1\rangle$ state. In the process, the remaining ^{7}Li atoms thermalize together and cool as well the ^{6}Li atoms. The evolution of the RF frequency with respect to time follows approximately a decaying exponential and goes from 1050 MHz down to 840 MHz in 22 s. At the end of this evaporation, the temperature is $T = 12\,\mu\mathrm{K}$, with $N_\mathrm{f} = 2 \cdot 10^6$ and $N_\mathrm{b} = 6 \cdot 10^5$, with a phase-space density of 10^{-1} for ^{6}Li and $2 \cdot 10^{-2}$ for ^{7}Li and it is possible to load the atoms into an optical dipole trap for the final cooling stages. The evolution of the RF frequency as a function of time during evaporation ramp is shown in Figure 2.7.

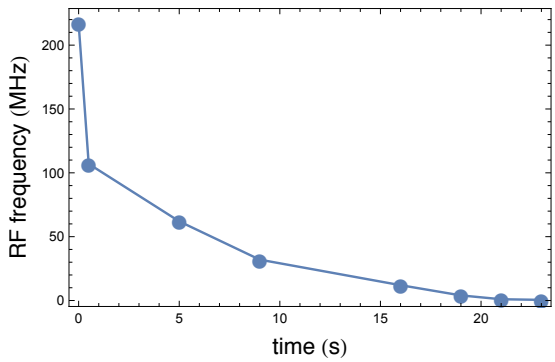

Figure 2.7: RF frequency as a function of time during radio-frequency (RF) evaporative cooling.

2.5 Optical trap

The final trap is a cigar-shaped trap composed of a far-detuned ($\lambda = 1070\,\text{nm}$) optical dipole trap[14] that provides the radial trapping, and of a magnetic trap that provides axial trapping. A bias field of about 800-1000 G is also applied to be in the vicinity of Feshbach resonances. This final trap is represented in Figure 2.1d.

2.5.1 Generalities on optical traps

In the presence of a laser beam with frequency close to an atomic transition, atoms experience an AC Stark Shift proportional to the laser's intensity, and this corresponds to a potential of

$$V(r) = \frac{\hbar\Gamma^2}{8\delta}\frac{I(r)}{I_s},$$

where Γ is the natural linewidth of the transition ($\Gamma = 5{,}9\,\text{MHz}$ in the case of Li), δ is the detuning of the laser with respect to the transition ($\delta = -2\pi \cdot 1.67 \cdot 10^{14}\,\text{Hz}$ for a $\lambda_0 = 1070\,\text{nm}$ laser beam for a transition at $\lambda = 670\,\text{nm}$), $I(r)$ is the laser beam intensity, and I_s is the saturation intensity (here for the D_2 line of Li the representative saturation intensity is $I_s = 2.5\,\text{mW.cm}^{-2}$). For a blue-detuned laser beam, atoms are attracted by low-optical-intensity areas, while they are attracted towards high-optical-intensities for red-detuned beams. For a TEM_{00} laser beam at the output of an optical fiber, the mode is Gaussian and

$$I(x,y,z) = \frac{2P}{\pi w_0^2(1+z^2/z_R^2)}\exp\left(-\frac{2(x^2+y^2)}{w_0^2(1+z^2/z_R^2)}\right),$$

where P is the total laser power, w_0 is the beam waist ($w_0 = 27(2)\,\mu\text{m}$ in our experiment), and $z_R = \pi w_0^2/\lambda_0$ is the Rayleigh range ($z_R = 2{,}1\,\text{mm}$ here). Close to the bottom of the trap, at the first-order approximation, the potential is harmonic with

$$V(x,y,z) = -U_0 + \frac{1}{2}m\omega_r^2(x^2+y^2) + \frac{1}{2}m\omega_z^2 z^2,$$

with

$$U_0 = \frac{\hbar\Gamma^2 P}{4\pi\delta I_s w_0^2},$$
$$\omega_r = \sqrt{\frac{4U_0}{m w_0^2}},$$
$$\omega_z = \frac{1}{2\pi}\frac{\lambda_0}{w_0^2}\omega_r.$$

2.5.2 Loading the hybrid trap

The geometry of the final hybrid optical-magnetic trap is similar to that of the Ioffe-Pritchard trap, so no sophisticated mode-matching preparation is needed here. We

[14] IPG laser 120 W

simply ramp up the optical trap power up to 40% of its maximum power while ramping down the current in the Ioffe-Pritchard bars. The loading efficiency is about 80%, with $N_\mathrm{f} = 1.8 \cdot 10^6$ and $N_\mathrm{b} = 5 \cdot 10^5$ after loading. The optical trap power is then about 8 W, with a waist of $w_0 = 27(2)\,\mu\mathrm{m}$, leading to trap frequencies of $\omega_r \simeq 2\pi \cdot 8\,\mathrm{kHz}$ for the radial direction and $\omega_z \simeq 2\pi \cdot 75\,\mathrm{Hz}$ for the axial direction[15]. At high laser power, the axial confinement provided by the dipole trap is sufficient to trap the atoms, but this is not the case any more at low trap power, where it falls below 1 Hz. Some extra axial confinement is needed, and this is realized *via* a magnetic trap. To axially trap atoms, there are two possibilities: either a global minimum of the magnetic field (to trap low-field seekers), or a saddle point with a maximum in the axial direction and a minimum in the radial direction (to trap high-field seekers if radial confinement is obtained by other means). The atomic levels that we want to use for ^{6}Li are high field seekers, so the second option is preferred: the radial confinement is made by the optical trap. It is thus possible to tune independently the radial and the axial confinement. To obtain such a saddle point, we use two pairs of coils: the curve coils (already used in the Ioffe-Pritchard trap) produce a magnetic curvature of $1.0\,\mathrm{G.(cm^2)^{-1}.A^{-1}}$ and a bias field of $2.28\,\mathrm{G.A^{-1}}$. The Feshbach coils, with current in the other direction, produce a bias field of $-2.28\,\mathrm{G.A^{-1}}$ and a very small curvature of $-0.080\,\mathrm{G.cm^{-2}.A^{-1}}$. By imposing a large current in the Feshbach coils, the minimum of magnetic field becomes negative, and becomes a maximum in amplitude, trapping the high-field seeking states. With this configuration, it is thus possible to trap high-field seekers states at a bias field of 832 G, in the vicinity of the Feshbach resonance.

2.5.3 Mixture preparation

Once the atoms are loaded into the optical dipole trap, we ramp up the optical trap power to its maximum value and transfer the atoms to the high-field seekers states, $F = 1$ for ^{7}Li and $F = 1/2$ for ^{6}Li. This is done using adiabatic passage. We apply two RF frequencies, of 827 MHz (for ^{7}Li) and 240 MHz (for ^{6}Li) and vary the bias magnetic field from 13 G to 4 G in 50 ms, crossing the resonance and transferring the atoms into the desired states. This RF transfer is very robust and never needs to be re-optimized.

Ultimately, we want to have ^{7}Li atoms in the $|2_\mathrm{b}\rangle$ state and the ^{6}Li atoms in a mixture of the $|1_\mathrm{f}\rangle$ and the $|2_\mathrm{f}\rangle$ state, while so far the atoms are in $|1_\mathrm{b}\rangle$ and $|1_\mathrm{f}\rangle$, respectively. We first prepare ^{7}Li. The transfer has to be done at a magnetic field below 738 G to avoid crossing of the Feshbach resonance of the $|1_\mathrm{b}\rangle$ state. We increase the current in the Feshbach coils up to a magnetic field of 656 G, and perform another adiabatic passage, but this time varying the RF frequency from 170.9 MHz tp 170.7 MHz, crossing again the resonance since the frequency of the transition $|1_\mathrm{b}\rangle \to |2_\mathrm{b}\rangle$ is 170.8 MHz at that magnetic field. The ramp is long enough (10 ms) to ensure a complete transfer of ^{7}Li atoms into the $|2_\mathrm{b}\rangle$ state. To prepare the ^{6}Li atoms into the desired states, the magnetic field is further ramped to 835 G, very close to the Feshbach resonance

[15] We have to operate the laser at full power to obtain a clean $\mathrm{TEM_{00}}$ output mode. To reduce this power to lower intensities, we first use a Brewster plate that reflects most of the laser power so that the maximum optical power that can be sent on the atoms is about 20 W. We finally adjust the power during the experimental sequence with a high-power Acousto-Optic Modulator (AOM).

at 832 G. We then perform a last RF sweep from 76.30 MHz and 76.25 MHz (around the transition frequency of $|1_f\rangle$ and $|2_f\rangle$), but instead of doing an adiabatic passage, we make a partial Landau Zener sweep: the sweep time is too short for a full transfer, only part of the atoms are transferred from $|1_f\rangle$ to $|2_f\rangle$. We can thus control the ratio of $|1_f\rangle$ with respect to $|2_f\rangle$ by varying the sweep time. The "fermionic polarization", or simply "polarization", is defined as

$$P = \frac{N_\uparrow - N_\downarrow}{N_\uparrow + N_\downarrow},$$

where $|\uparrow\rangle = |1_f\rangle$ or $|2_f\rangle$ is the atomic state with the highest number of atoms $N_\uparrow$ and $|\downarrow\rangle$ the one with the smallest atom number $N_\downarrow$. The transfer efficiency is subject to fluctuations and the sweep time has to be re-optimized from time to time. A summary of the different RF pulses is shown in Table 2.7.

Isotope	B (G)	ν_{RF} (MHz)	Action
^{7}Li	$13 \to 4$	827	$\|8_b\rangle \to \|1_b\rangle$
^{6}Li	$13 \to 4$	240	$\|6_f\rangle \to \|1_f\rangle$
^{7}Li	656	$170.9 \to 170.7$	$\|1_b\rangle \to \|2_b\rangle$
^{6}Li	835	$76.30 \to 76.25$	$\|1_f\rangle \to (\|1_f\rangle + \|2_f\rangle)$

Table 2.7: Summary of the RF sweeps performed to prepare the mixture.

2.5.4 Evaporation

After the mixture preparation, the magnetic field is held at 835 G and the optical evaporation is performed by ramping down the dipole trap power. We now have $N_b = 2 \cdot 10^5$ bosons and $N_f = 1.5 \cdot 10^6$ fermions. The unitary Fermi gas has there a very high collisional cross section and the evaporation is very efficient. The evaporation ramp lasts for 3.2 s, the evolution of the laser power as a function of time during evaporation is shown in Figure 2.8. At the end of the evaporation we have typically $N_b = 10 - 20 \cdot 10^3$, $N_f = 60 - 100 \cdot 10^3$ at a temperature $\lesssim 80$ nK. ^{7}Li is sympathetically cooled during the process. To ensure complete thermalization between ^{6}Li and ^{7}Li, one needs to wait about 1 s after the end of the evaporation before performing further experiments on the mixture.

When we want to perform experiments around 860 G with bosons in the $|2_b\rangle$ state, we have to evaporate at 860 G in order not to cross the ^{7}Li Feshbach resonance at 845 G with a cold cloud. The evaporation ramp is then slightly longer to allow for enough thermalization.

2.5.5 Summary

By means of different magnetic and optical traps, we are thus able to produce ultracold samples of bosons and fermions. A summary of atom numbers and temperatures at each step is given in Table 2.8. The bosons are condensed into a Bose-Einstein Condensate (BEC), as it is obvious from the clear peak in the density profiles. The

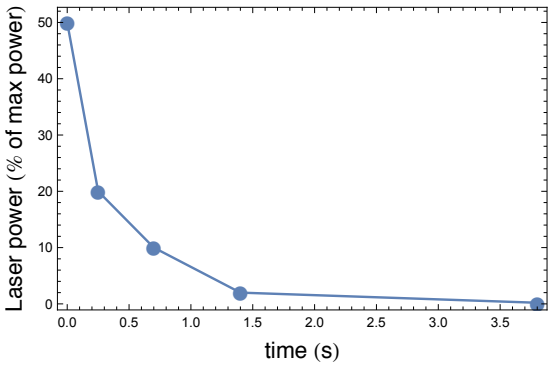

Figure 2.8: Laser power as a function of time during optical evaporative cooling.

superfluidity of the fermions is harder to demonstrate, but several proofs will be given in the following chapters (chapter 3 and chapter 4). The data obtained on the clouds are taken in the form of absorption images of the cloud. This technique will be described in the next section.

	MOT	CMOT	Quadrupole	RF evaporation (end)	optical evaporation (beginning)	optical evaporation (end)
N_b	10^9	10^9	$4 \cdot 10^8$	$6 \cdot 10^5$	$2 \cdot 10^5$	$20 \cdot 10^3$
N_f	$4 \cdot 10^7$	$4 \cdot 10^7$	$2 \cdot 10^7$	$6 \cdot 10^6$	$1.5 \cdot 10^6$	$200 \cdot 10^3$
T	3 mK	600 µK	2 mK	12 µK	40 µK	80 nK

Table 2.8: Summary of typical atom numbers and temperatures at the different stages of the experiment.

2.6 Imaging

2.6.1 Absorption imaging

We use standard *in situ* absorption imaging to image the clouds by shining on it resonant light. Atoms absorb the photons and the shadow of the cloud is captured by a camera ("absorption image"). The atoms that absorbed a photon are now excited and escape the trap. Another image is then taken after a wait time of 10-20 ms without the atoms ("reference image"). A scheme of the imaging process is shown in Figure 2.9.

If we note y the imaging direction, $I_a(x,z)$ the intensity of the absorption image in the $x-z$ plane, and $I_r(x,z)$ that of the reference image. The optical density $OD(x,z)$ is then given by

$$OD(x,z) = -\ln\left(\frac{I_a(x,z)}{I_r(x,z)}\right),$$

and the optical density is itself related to the number of atoms *via* the relation

$$OD(x,z) = \sigma \int dyn(x,y,z),$$

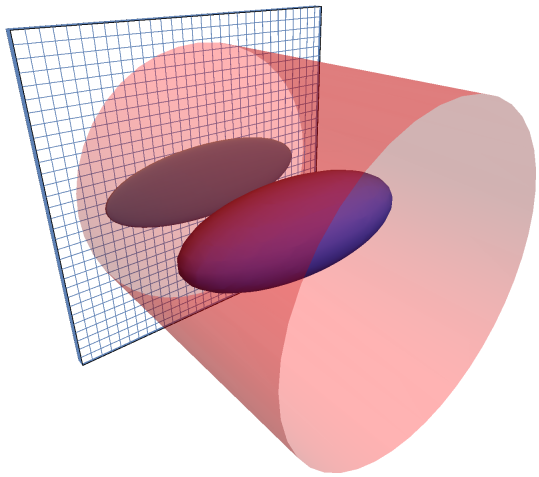

Figure 2.9: Imaging process: a resonant beam is shone on the atoms, their shadow is cast on a camera ("absorption image"), before a second image, without the atoms ("reference image") is taken. The cloud is shown here in purple, the CCD camera is the blue-and-white grid, and the imaging beam is shown in red.

where $n(x,y,z)$ is the atomic density of the cloud and σ the absorption cross-section of one atom. The cross-section at resonance is known as a function of Clebsch-Gordan coefficients and can be calculated. However, because of complex optical pumping-like phenomena and of some experimental difficulties (such as the relatively large spectral bandwidth of the laser, on the order of a few hundred kilohertz, some polarization fluctuations, or the acceleration of detected atoms increased by the lightness of lithium), the scattering cross-section is reduced and we have to calibrate it experimentally. This has been done by measuring the Thomas-Fermi radius for both bosons and fermions: the relation between the total atom number and the Thomas-Fermi radius is well known, and this procedure gives access to the imaging correction factor [Ferrier-Barbut, 2014]. We only image in the linear absorption regime, when the optical density is $\lesssim 1$, so that no additional correction to the atom number needs to be taken into account [Reinaudi *et al.*, 2007]. A consequence of this low-intensity imaging is that we cannot image very dense clouds. This can be circumvented using a short *time-of-flight*, as will be discussed below.

2.6.2 Imaging system

Our imaging system allows to image in two orthogonal directions. One of the imaging directions is along the dipole trap direction z, while the other one is along y. Imaging in the z direction requires some time of flight to reduce the optical density (typically on the order of 4 ms), while imaging in the y direction can be done *in situ*, even though we usually have a very short time of flight (on the order of 100 µs) to reduce the

optical density. However, the radial dimensions of the cloud are on the order of the imaging resolution, about 5 µm and no information is lost by integration also along the x direction. We thus have access to the doubly-integrated density $\bar{n}(z)$. The PixelFly cameras that we use can operate very fast. Each of these two cameras can take two images with a time separation as short as 3 µs. This allows to take quasi-simultaneous images of the two fermionic spin states, or of one fermionic spin state with the bosons. Cameras have a quantum efficiency of 40%, but the short imaging pulse duration that we use (10 µs) reduces the number of photons per pixel to typically one hundred. This combined with the relatively high readout noise of 7 electrons RMS makes the overall signal-to-noise ratio not very high. A scheme of the imaging system is given in Figure 2.10 for fast imaging in the radial direction of both fermionic spin states (time delay between both images of 10 µs) and time-of-flight imaging of bosons ($t_{tof} = 4$ ms here) in the axial direction from a single experimental realization.

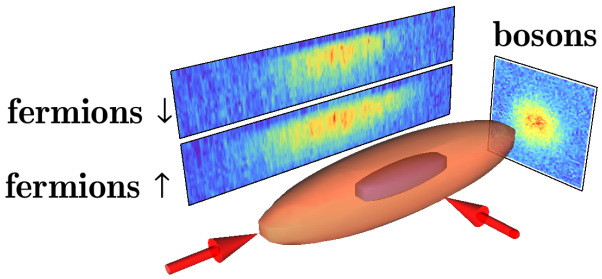

Figure 2.10: Typical imaging scheme. Here, we performed fast imaging of both fermionic spin states in the radial direction, and time-of-flight imaging of the bosons in the axial direction. The clouds are in red (fermions) and blue (bosons), imaging beam directions are shown with red arrows.

During my PhD, we used this system to take either simultaneous images of one fermionic spin state with the bosons (for dynamic studies of the mixture, see chapter 3), or simultaneous images of both fermionic spin states, with the bosons in time-of-flight, as shown in Figure 2.10 (for static studies of the mixture, see chapter 4).

2.6.3 Image processing

As mentioned above, the price to pay for the fast imaging is a relatively low signal-to-noise ratio, even on the doubly-integrated images. When we only want to know some general properties of the clouds, such as atom number or center-of-mass position, one may either integrate over all of the pixels or use an approximate fit function (see chapter 3). However, when one wants to study precisely the profiles of the cloud, more image processing is needed. One of the first sources of noise is the presence of fringes on the absorption image due to interferences with back reflections of the imaging beams. To reduce the influence of these fringes, the reference image is taken with a short

delay (11 ms) with respect to the absorption, but some fringes may remain. To get rid of them, we use an algorithm[16] the principle of which is the following: among a series of reference images, it finds the best combination to remove as many fringes as possible. To do that, we consider the absorption image with a mask at the position of the atoms, then find the linear combination of reference images which best looks like the remaining of the absorption image. This linear combination is then taken as the new reference image. The results of this treatment are shown in Figure 2.11. Even though the effect is no very visible on the 2D images (Figure 2.11a), it clearly reduces the fringes on the doubly integrated profiles (Figure 2.11b).

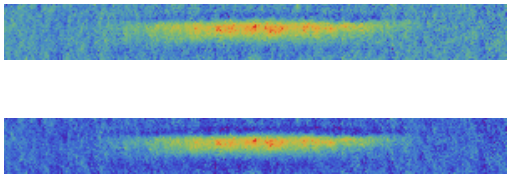

(a) Comparison of the 2D images. Top: raw image. Bottom: processed image.

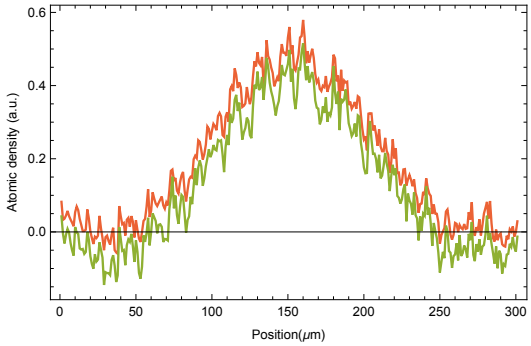

(b) Comparison of the doubly integrated profiles. In green: raw profile. In red: processed profile.

Figure 2.11: Effect of the fringe removal algorithm.

This algorithm is not necessary to analyze the data presented in chapter 3, but has proven to be very useful for the study of chapter 4.

2.7 Double Degeneracy

By means of the methods presented in the first sections of this chapter, we are able to obtain doubly degenerate Bose and Fermi gases. This sections aims at giving the tools that we use for basic data analysis.

2.7.1 Bosons

Typical optical density images of the bosonic cloud are given in Figure 2.12 for both radial and axial imaging. In the axial direction, we have access to the time-of-flight, singly integrated optical density, while the radial imaging gives access to the *in situ* doubly integrated optical density. In practical, even when we imaged in the axial direction, we only used the doubly integrated optical density. The doubly integrated optical density of Figure 2.12b is given in Figure 2.13. We model the *in situ* density

[16] developed by Shannon Whitlock

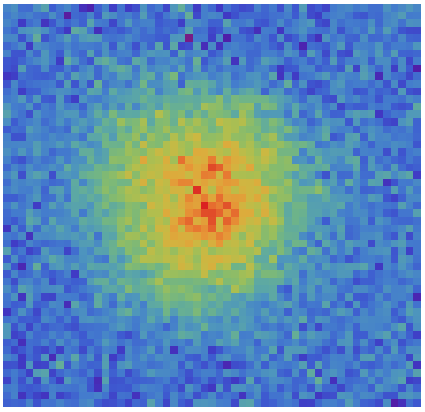

(a) Axial direction.
Time of flight 4 ms.

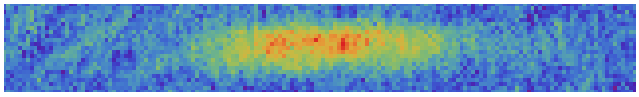

(b) Radial direction.
Time of flight 100 µs.

Figure 2.12: Singly integrated optical density images of bosonic clouds.

profile of a thermal cloud at temperature T by[17]

$$\bar{n}_{th}(z) = \bar{n}_{th}(0) \exp\left(-\frac{(z-z_0)^2}{z_{th}^2}\right), \tag{2.1}$$

where z_0 is the position of the center of the cloud, and z_{th} its thermal width, given by

$$k_{\mathrm{B}}T = \frac{1}{2} m_{\mathrm{b}} \omega_z^2 z_{th}^2.$$

The measurement of the width of the thermal cloud thus gives access to the temperature of the whole cloud.

In the Thomas-Fermi limit, the doubly-integrated profile of the condensate can be described by

$$\bar{n}_c(z) = \bar{n}_c(0) \max\left(\left(1 - \frac{(z-z_0)^2}{l_{TF,z}^2}\right)^2, 0\right), \tag{2.2}$$

where $l_{TF,z} = \sqrt{\frac{2\mu_{\mathrm{b}}}{m_{\mathrm{b}}\omega_z^2}}$ is the Thomas-Fermi radius of the cloud and has already been defined in subsection 1.3.2. Density profiles of partly condensed clouds can be fitted using a bimodal fit, taking into account the thermal cloud with equation (2.1) and the condensate with equation (2.2). This gives access to both the temperature, via the gaussian fit, and to the condensed fraction N_c/N_{b}. The relation between condensed fraction and temperature, $N_c/N_{\mathrm{b}} = 1 - (T/T_{c,\mathrm{b}})^3$, provides a consistency check of the temperature measurement.

Figure 2.13 shows the doubly integrated of a relatively hot cloud and its associated bimodal fit, corresponding to a temperature of 230 nK.

For our coldest clouds, no thermal fraction is visible (see Figure 2.14 for instance), and we assure that the condensed fraction is above 90 %. This implies that the temperature is below 80 nK.

[17] Even though a description by a polylog function would be more accurate, this one gives similar results and converges faster.

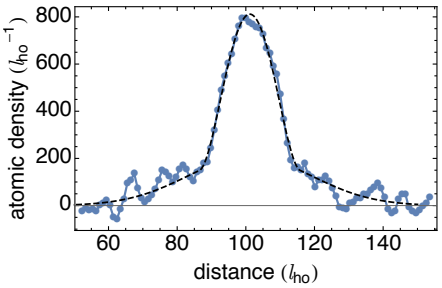

Figure 2.13: Doubly integrated density profile of a relatively hot bosonic cloud. Blue line: experimental profile. Dashed black line: bimodal fit of the density distribution. Here, the temperature extracted from the thermal cloud width is 233 nK, while the condensed fraction is $\sim 50\,\%$, corresponding to a temperature of 238 nK.

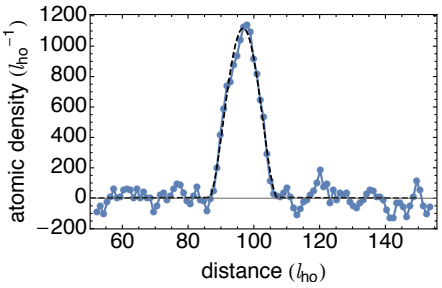

Figure 2.14: Doubly integrated density profile of a cold bosonic cloud. Blue line: experimental profile. Dashed black line: bimodal fit of the density distribution. No thermal fraction is visible, corresponding to a cloud at a temperature below 80 nK.

2.7.2 Fermions

The shape of the density profile of a two-component Fermi cloud depends on the interaction strength $k_F a_{ff}$: on the deep BEC side, the density profile will be the same as that of an atomic BEC, while at unitarity it will have the same shape as a non-interacting Fermi gas. There is no analytical expression in the general case. Moreover, there is no obvious modification of the profile when crossing the critical temperature for superfluidity, as it was the case for the bosons with the appearance of the BEC peak. However, in the regimes studied in this thesis, we stayed relatively close to unitarity ($|1/k_F a_{ff} < 1$), and the profile of the Fermi gas could be well described by the Thomas-Fermi profile of a unitary Fermi gas:

$$\bar{n}_f(z) = \bar{n}_f(0) \max\left(\left(1 - \frac{(z-z_0)^2}{l_{TF,z}^2}\right)^{5/2}, 0\right),$$

where here the Thomas-Fermi radius $l_{TF,z}$ is given by $l_{TF,z} = \xi^{1/4}\sqrt{\frac{2E_F}{m_f\omega_z^2}}$. An example of the fit of the fermions profile is given in Figure 2.15. The Fermi cloud profile does not give access to its temperature, but since it is in equilibrium with the bosonic cloud, they have the same temperature. The Bose gas thus acts as a thermometer for the Fermi gas. As a result, the temperature for cold Fermi gases is also below 80 nK, which

is below the critical temperature for superfluidity at unitarity $T_{c,\mathrm{f}} = 0.19\,T_\mathrm{F} = 170\,\mathrm{nK}$. The Fermi cloud is thus superfluid.

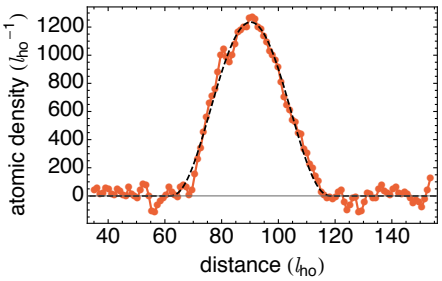

Figure 2.15: Doubly integrated density profile of a fermionic cloud. Red line: experimental profile. Dashed black line: Thomas-Fermi fit of the density distribution.

2.8 Conclusion

In this chapter we have presented the lithium experiment. Some visitor in the lab once said that "this experiment contain[ed] every textbook cooling stage" used in cold atoms. This is not such a big exaggeration. Learning how to run the machine is thus a tough task, but is a good way to learn how to cool and trap atoms. The major specificity of this experiment is the use of crossed-thermalization in two evaporative cooling stages, the first one where ^{7}Li cools ^{6}Li, and the second one where ^{6}Li cools ^{7}Li. This way, we could obtain a double Bose-Fermi superfluid mixture of ^{6}Li and ^{7}Li which was a long sought goal of the helium community. As will be described in chapter 3, we could for instance probe the effect of the Bose-Fermi interaction on the collective excitations of the mixture and use this interaction to explore the critical velocity of the superfluid mixture. However, some of the parts of this lithium experiment start to be very old, and it was time to build a new experiment that would be more versatile and reliable. I started this project during my PhD and it is describe in chapter 5.

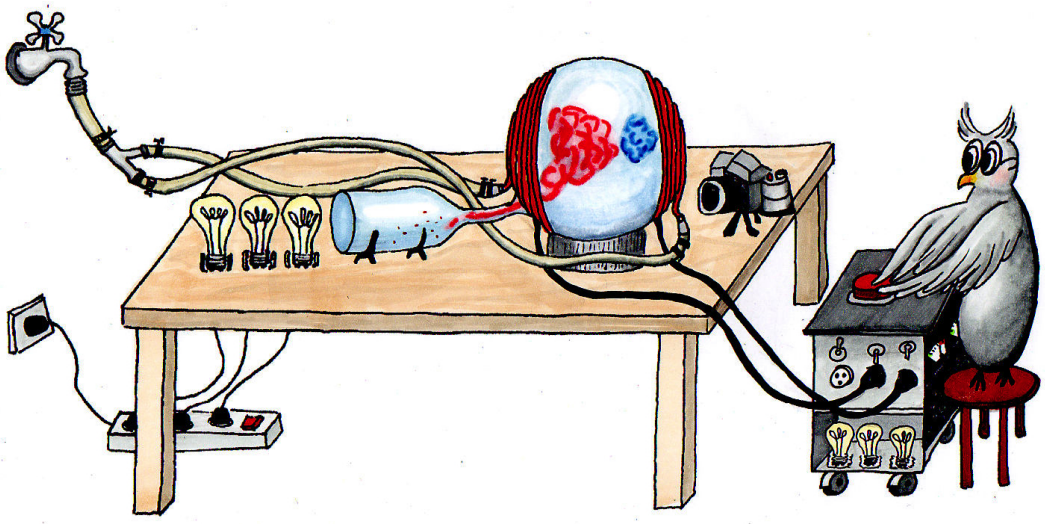

Chapter 3

Collective modes of the mixture

The first proof of superfluidity in liquid helium was given in 1938 by Allen and Misener [Allen and Misener, 1938], and by Kapitza [Kapitza, 1938], by measuring the viscosity of a flow in a capillary tube and finding that it did not obey Poiseuille law.

It was soon followed by other striking effects, such as the fountain effect [Allen and Jones, 1938], or the presence of vortices [Hall and Vinen, 1956b]. Similar phenomena were also observed for superfluid ^{3}He [Osheroff *et al.*, 1972b, Osheroff *et al.*, 1972a]. Years later, after the first realization of Bose-Einstein Condensates [Anderson *et al.*, 1995, Davis *et al.*, 1995a] in ultracold atoms, phase-coherence was observed [Andrews *et al.*, 1997b, Bloch *et al.*, 2000], and the presence of vortices in rotating clouds provided a proof of the superfluidity of these atomic ensembles [Madison *et al.*, 2000], as well as the existence of a critical velocity [Raman *et al.*, 1999]. When Fermi superfluids were realized [DeMarco and Jin, 1999], first evidences of their superfluidity were initially provided by the appearance of a molecular BEC after projection of the Fermi gas onto a molecular gas [Regal *et al.*, 2004b]. Later, the observation of vortices [Zwierlein *et al.*, 2005] and critical velocity [Miller *et al.*, 2007] were definitive proofs, and since then, other proofs of superfluidity for ultracold gases have been put forward, such as the existence of second sound [Sidorenkov *et al.*, 2013]. In this chapter, we will probe the superfluidity of the mixture with a counterflow.

In his original argument [Landau, 1957], Landau showed that an impurity moving in a superfluid cannot create any excitations below a certain critical velocity v_c (see subsection 3.3.2), such that:

$$v_c = \min_{\boldsymbol{p}} \left(\frac{\varepsilon(\boldsymbol{p})}{p} \right),$$

where $\varepsilon(\boldsymbol{p})$ is the dispersion relation of the superfluid. This prediction was successfully demonstrated in superfluid helium [Wilks and Betts, 1987]. Another way to probe superfluidity for cold atoms was thus to consider an impurity moving inside a Fermi superfluid or inside a BEC, and to observe the onset of dissipation for these systems. For bosons, critical velocity was measured both in 3D [Raman *et al.*, 1999] and in 2D [Desbuquois *et al.*, 2012] using a stirring laser as an impurity: a bosonic cloud is prepared at low temperature and stirred using a laser. Above a certain stirring velocity, an onset of heating is observed and this defines the critical velocity. Instead of a stirring laser beam, other experiments used moving atomic impurities in a static BEC [Chikkatur *et al.*, 2000] to probe the critical velocity. Experiments with two BECs flowing into each other have shown that the critical velocity between them was very small [Hall *et al.*, 1998], and that their motion was damped. In Fermi gases, the critical velocity has been probed as well, but the measured critical velocity proved to be $\approx 40\%$ below Landau's prediction [Miller *et al.*, 2007, Weimer *et al.*, 2015].

The first realization in our group of a Bose-Fermi superfluid mixture raised new questions regarding the behavior of a rotating Bose and Fermi superfluid mixture [Wen and Li, 2014], the effect of interactions between BEC's and Fermi superfluid's quasi-particle on their lifetime [Zheng and Zhai, 2014], the damping rate of the counter-flow [Shen and Zheng, 2015, Chevy, 2015], or the critical velocity of the mixture [Abad *et al.*, 2015, Castin *et al.*, 2015]. Experimentally, the mixture provided a new approach to measure the critical velocity, because the Bose superfluid, of relatively small size, serves as (quasi) local probe of the Fermi superfluid.

In this chapter we describe the measurement of the critical velocity of a Bose-Fermi superfluid mixture, through the study of its counterflow. We create a Bose-Fermi superfluid in a harmonic trap as explained in chapter 2, and we excite the dipole modes of the system, leading to oscillations of the BEC and of the Fermi superfluid.

The long-lived oscillations of the system are a first evidence for the double superfluidity and more proofs will be put forward in the following. In a first series of experiments, we show that the (weak) interactions between ^{6}Li and ^{7}Li do not prevent superfluidity, unlike in ^{3}He-^{4}He mixtures. The reported observation of long-lived oscillations allow for precise frequency measurement and provide insightful information on the local potential, which results in a new method to measure the equation of state. A second set of experiments is dedicated to the exploration of the limits of superfluidity. The relative critical velocity between the two clouds is investigated by studying the onset of dissipation in the BEC-BCS crossover. The measured critical velocity is compared to both theory [Landau, 1957, Castin *et al.*, 2015] and experiments [Miller *et al.*, 2007, Weimer *et al.*, 2015]. In a third set of experiments, the robustness of superfluidity as a function of temperature is probed. We use a more sophisticated frequency analysis to ensure model-free measurement of the frequencies. We observe an unexpected phase-locking of the oscillations and explain it by a Zeno-like model.

3.1 Dipole modes excitation

3.1.1 The mixture

At the end of evaporation, the system is composed of a mixture of ultracold bosons in $|2_\mathrm{b}\rangle$ state and fermions with equal number of atoms in $|1_\mathrm{f}\rangle$ and $|2_\mathrm{f}\rangle$ states. We typically have $N_\mathrm{f} = 60 - 100 \cdot 10^3$ and $N_\mathrm{b} = 10 - 29 \cdot 10^3$ at a temperature $\lesssim 80\,\mathrm{nK}$[1]. Both clouds are in the same hybrid magnetic-optical trap and feel the same trapping potentials[2]. Radial confinement is made by the optical trap (with a trapping frequency of $\nu_r = 470\,\mathrm{Hz}$), and axial confinement is made mainly by the magnetic trap (with a trapping frequency of about $\nu_z = 15\,\mathrm{Hz}$)[3]. The resulting trap is thus cylindrico-symmetric. Despite the high aspect-ratio of this cigar-shaped trap, the dynamics are still 3D, since $T \gg \hbar\omega_r/k_\mathrm{B} \approx 20\,\mathrm{nK}$ (where $\omega_r = 2\pi\nu_r$ and $\omega_z = 2\pi\nu_z$). An external magnetic field in the range of 700 to 900 G enables us to set the superfluid at the vicinity of the multiples Feshbach resonances (at 846 and 894 G for ^{7}Li and at 832 G for ^{6}Li). This way, the bias field and the magnetic field curvature responsible for axial trapping can be tuned independently. In the experiments reported here, the axial confinement is held constant, while the bias field was varied to tune the interaction strength $1/k_\mathrm{F}a_\mathrm{ff}$ between -0.4 and 0.8.

In such superfluid mixtures the Bose gas can serve as an excellent thermometer by taking advantage of the thermal fraction in the wings of the clouds. However, in the regime of parameters considered here the condensate fraction is typically above 90 %, such that the thermal component is barely detectable. In this case, we can still infer an upper bound on the temperature. Indeed, for an ideal[4] Bose gas in a harmonic trap the condensed fractionN_0/N is given by $N_0/N = 1 - (T/T_{c,\mathrm{b}})^3$. We can deduce

[1] It is possible to have hotter clouds with more atoms simply by stopping the optical evaporation at a higher optical power.

[2] But not the same trapping frequency as they have different masses.

[3] The magnetic trapping frequency is 15 Hz, the optical trapping frequency is about $1 - 2$ Hz. The trapping frequencies of the two species are within a ratio $\omega_\mathrm{f}/\omega_\mathrm{b} = \sqrt{m_\mathrm{b}/m_\mathrm{f}}$ because both isotopes are in the same potential.

[4] Here, the Bose-Bose scattering length is typically $\lesssim 100\,a_\mathrm{B}$ so the Bose gas is not ideal, but the

that $T \leq 0.5\,T_{c,\mathrm{b}}$, where $T_{c,\mathrm{b}} = 0.94\,\hbar\overline{\omega}_{\mathrm{b}} N_{\mathrm{b}}^{1/3}/k_{\mathrm{B}}$ is the critical temperature for Bose-Einstein condensation, and the upper bound for the temperature is $T \leq 80\,\mathrm{nK}$. The critical temperature for BEC (resp. Fermi superfluid at unitarity) is $T_{c,\mathrm{b}} = 200\,\mathrm{nK}$ (resp. $T_{c,\mathrm{f}} = 0.19\,T_{\mathrm{F}} = 170\,\mathrm{nK}$), so both clouds are clearly in the superfluid regime.

We mainly studied the center-of-mass oscillations of the Bose-Fermi mixture by exciting the oscillation mode (called the "dipole mode") in the harmonic trap. The position of the center-of-mass of both the bosonic and the fermionic cloud is recorded as a function of time. Those measurement were repeated for various sets of parameters, including:

- The bias magnetic field. This modifies both the fermion-fermion and the boson-boson interactions *via* Feshbach resonances. As we will see, this is mostly the modification of the fermion-fermion interaction that affects the oscillations.
- The amplitude of the oscillations. Since the oscillation frequency of the cloud is roughly constant, this changes the velocity of the clouds in the trap, and their relative velocity when they oscillate at different frequencies.
- The temperature of the clouds. Sine both clouds are at thermal equilibrium, they have the same temperature.

We performed three different kind of experiments, the corresponding parameters are shown in Table 3.1.

Description in	Magnetic field	oscillation amplitude	Temperature	Quantity measured
section 3.2	varied	small	low	frequency
section 3.3	varied	varied	low	damping
section 3.4	835 G	moderate	varied	frequency, (damping)

Table 3.1: Summary of the parameter space studied in the oscillation experiments.

3.1.2 Selective excitation of dipole modes

We excite the dipole modes of the system by displacing the centers of mass of both clouds. The centers of the magnetic and of the optical trap are different, so to excite the dipole modes of the system, we increase the optical trap power by typically a factor 3, and this displaces axially the minimum of the hybrid trap, and thus the cloud by a distance d. This is made with a timescale of 150 ms$\geq 1/\nu_z, 1/\nu_r$ in order to be adiabatic. The optical trap power is then reduced to its initial value, which brings back the center of the trap to its initial position, with a timescale of 20 ms, greater than the inverse of the radial frequency, not to excite the radial modes, but smaller than the inverse of the axial frequency, to excite the dipole modes. A scheme of the excitation process is shown on Figure 3.1.

corrections to $T_{c,\mathrm{b}}$ due to the interactions are negligible. Indeed, $\frac{\Delta T_{c,\mathrm{b}}}{T_{c,\mathrm{b}}} = 1.3 a_{\mathrm{bb}} n_{\mathrm{b}}^{1/3} \ll 1$ [Pitaevskii and Stringari, 2003].

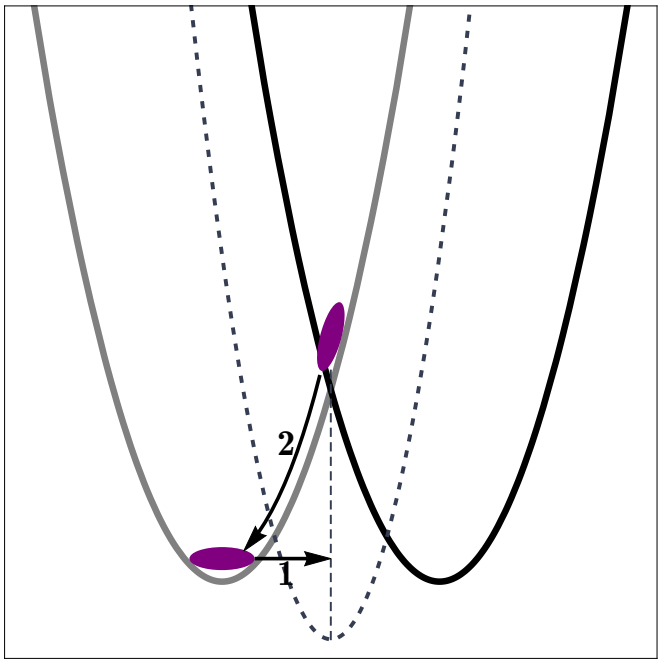

Figure 3.1: Scheme of the excitation process: first slowly displace the trap by a distance d, then release the cloud into the initial trap.

The clouds thus acquire some velocity and oscillate in the trap. We let them evolve during a variable time t before imaging them with double *in situ* imaging (see subsection 2.6.1) and measuring their position. With this process, the compression is very small, and the axial Thomas-Fermi radius of the clouds is modified by less than 10%. We neglect it in a first approximation. In section 3.6 we show that the modifications of the radii are periodic, which shows that quadrupole modes are slightly excited.

3.1.3 Kohn's theorem

It is very well known that the motion of a single particle in a harmonic trap is a sinusoid of radial frequency $\sqrt{k/m}$, where m is the mass of the particle and $-k\boldsymbol{r}$ the restoring force. For N identical non-interacting particles, the result is obviously the same, and all particles oscillate at the frequency $\sqrt{k/m}$. One may wonder how this result is affected by the interactions. When considering only the center-of-mass of the particle ensemble, we can write (with $\boldsymbol{r}_i$ the position of particle i and $\boldsymbol{F}(\boldsymbol{r}_i - \boldsymbol{r}_j)$ the interaction force between two particles at positions $\boldsymbol{r}_i$ and $\boldsymbol{r}_j$):

$$m\ddot{\boldsymbol{r}}_i = -k\boldsymbol{r}_i + \sum_j \boldsymbol{F}(\boldsymbol{r}_i - \boldsymbol{r}_j).$$

The center-of-mass position $\boldsymbol{r}_{CoM}$ thus obeys:

$$m\ddot{\boldsymbol{r}}_{CoM} = -k\boldsymbol{r}_{CoM} + \frac{1}{N}\sum_{i,j} \boldsymbol{F}(\boldsymbol{r}_i - \boldsymbol{r}_j).$$

Newton's third law implies that $\sum_{i,j} \boldsymbol{F}(\boldsymbol{r}_i - \boldsymbol{r}_j) = \boldsymbol{0}$, so the center-of-mass oscillation of identical particles in a harmonic trap is independent of the interactions. It was demonstrated here in the classical regime, but this result also holds in the quantum regime. Regarding the evolution of the shape of the ensemble, this problem was originally addressed by Kohn in [Kohn, 1961], who showed that for a gas of electrons in a uniform and constant magnetic field, the response to an uniform electric field $\vec{E} = \vec{E_0} \cos \omega t$ was independent of the interactions between the electrons. Its extension in [Brey *et al.*, 1989] generalized this result to the case of identical particles in a harmonic trap. Later, in [Dobson, 1994] the "harmonic potential theorem" demonstrates the rigid transport of of the many-body wavefunction.

In our system, we have interacting atoms and not electrons, but the same results hold. For an interacting, single species, atomic gas in a harmonic trap, the oscillations are undamped and at a constant frequency without modification of the shape of the cloud, whatever the interactions between atoms are. This is indeed what we observe in our experiments, with either bosons alone or fermions alone in the trap (see Figure 3.2 for instance for an example with bosons). The axial magnetic trap that we use is very harmonic, and there is (as also shown in Figure 3.2) no anharmonic terms that would lead to damping.

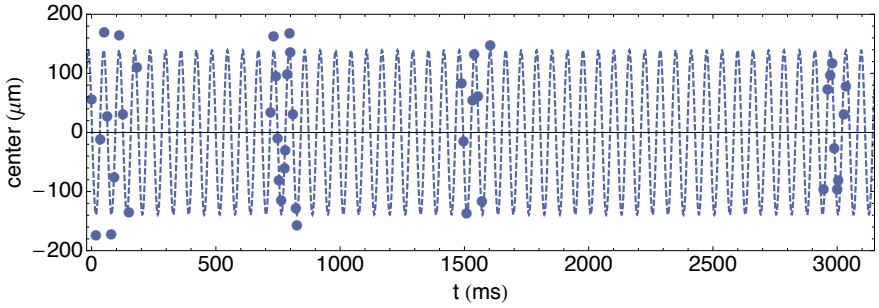

Figure 3.2: Axial center-of-mass oscillations of the BEC alone in the harmonic trap. We see long-lived oscillations with a frequency of 16.08(2) Hz for an initial oscillation amplitude of 140 μm.

3.2 Low temperature, low amplitude

3.2.1 Experiments

We first studied dipole modes of the clouds at low temperature, and for a small amplitude displacement. We typically displace the clouds by less than 100 μm. Imaging the cloud at constant time intervals during the oscillations allowed us to sketch a movie of the oscillations, which is shown on Figure 3.3, and displays long-lived undamped oscillations of the mixture.

In the following, we will note $\tilde{\omega}_\mathrm{b}$ (resp. $\tilde{\omega}_\mathrm{f}$) the oscillation frequency of the bosons (resp. fermions) in the mixture, and ω_b (resp. ω_f) the oscillation frequency of the bosons (resp. fermions) alone in the trap. Since there is no visible damping on a timescale of about 4 seconds, precision frequency measurements are possible.

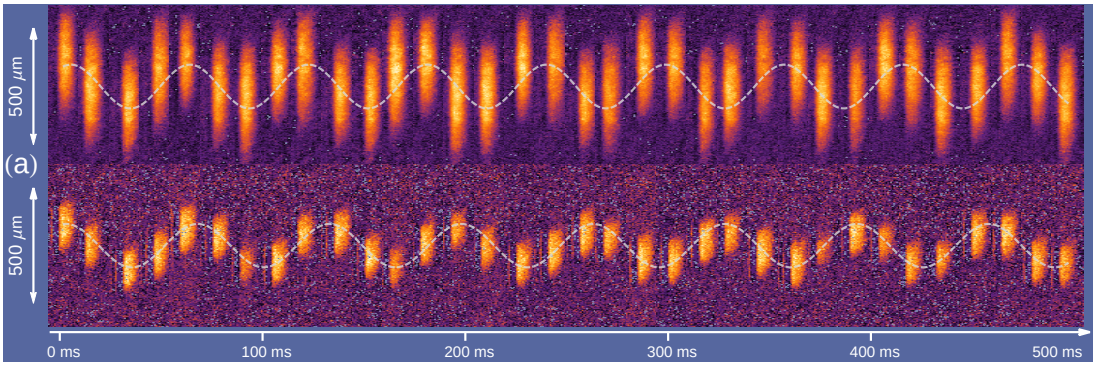

Figure 3.3: Center-of-mass oscillations of a Fermi superfluid (top) and of a Bose-Einstein Condensate (bottom) at a magnetic field of 835 G. The oscillation period of ^{6}Li (resp. ^{7}Li) is 59.7(1) ms (resp. 66.6(1) ms).

In our experiment, we measure at unitarity $\omega_\mathrm{b} = 2\pi \times 15.27(1)$ Hz and $\omega_\mathrm{f} = 2\pi \times 16.80(2)$ Hz. The ratio $\omega_\mathrm{f}/\omega_\mathrm{b} = 1.10$ is the expected value, slightly above the mass ratio $\sqrt{m_\mathrm{b}/m_\mathrm{f}} = \sqrt{7/6} = 1.08$ because of magnetic corrections[5]. However, when we excite the dipole modes of the superfluid mixture, what we observe is slightly different (see Figure 3.4).

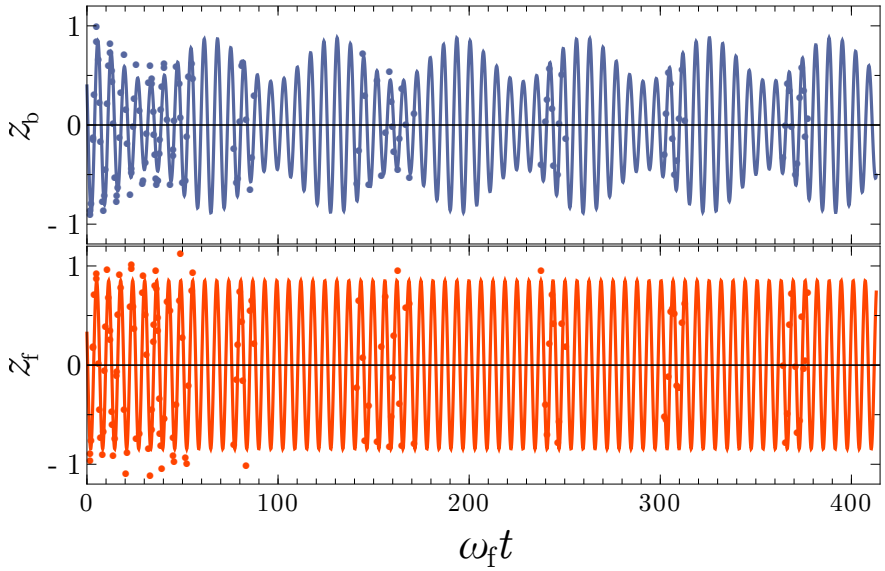

Figure 3.4: Evolution of the centers of mass of the mixture at low temperature ($\approx$ 100 nK), and for low-amplitude oscillations ($d \leq 50\,\mu$m). Solid lines are fits to the data using equations (3.8) and (3.9).

[5]The magnetic fields that we use in the experiment are all above 750 G so both clouds are in the deep Paschen-Back regime and their energy dependence with magnetic field is $\partial E/\partial B \approx \mu_\mathrm{B}$. The clouds are thus almost in the same trapping potential and $\omega_\mathrm{b}/\omega_\mathrm{f} = \sqrt{6/7}$. If we take into account the corrections to energy dependence with magnetic field, this ratio is slightly modified and we obtain $\omega_\mathrm{b}/\omega_\mathrm{f} \approx 1.10$ between 780 G and 880 G.

First, the oscillation frequency for the bosons is down-shifted to $\tilde{\omega}_\mathrm{b} = 2\pi \times 15.00(2)$ Hz while $\tilde{\omega}_\mathrm{f} \approx \omega_\mathrm{f}$. Second, we see a beat associated to an amplitude modulation of about 25% at a frequency $\tilde{\omega}_\mathrm{f} - \tilde{\omega}_\mathrm{b}$.

3.2.2 Bose-Fermi interaction

To understand the origin of the frequency shift of the bosons, let us first note that the number of bosons is much smaller than the number of fermions: $N_\mathrm{b} \ll N_\mathrm{f}$. We can thus treat the BEC as an impurity immersed in a Fermi superfluid. Similarly to what will be used in subsection 4.2.1 and to [Lobo *et al.*, 2006], we can say that the BEC feels now an effective potential

$$V_\mathrm{eff}(\boldsymbol{r}) = V(\boldsymbol{r}) + g_\mathrm{bf} n_\mathrm{f}(\boldsymbol{r}),$$

where the $g_\mathrm{bf} n_\mathrm{f}(\boldsymbol{r})$ takes into account the mean-field interaction between the bosons and the fermions. If we now make a first-order approximation and neglect the back-action of the bosons on the fermions[6], the fermionic density $n_\mathrm{f}(\boldsymbol{r})$ is given by the local density approximation, where $\mu_\mathrm{f}(\boldsymbol{r})$ is the local chemical potential of the fermions and μ_f^0 the global fermionic chemical potential

$$n_\mathrm{f}(\boldsymbol{r}) = n_\mathrm{f}^{(0)}(\mu_\mathrm{f}(\boldsymbol{r})) = n_\mathrm{f}^{(0)}(\mu_\mathrm{f}^0 - V(\boldsymbol{r})), \tag{3.1}$$

where $n_\mathrm{f}^{(0)}(\mu)$ is the equation of state of the Fermi superfluid, known at unitarity for $T \neq 0$ [Nascimbène *et al.*, 2010] and at $T = 0$ in the whole BEC-BCS crossover [Navon *et al.*, 2010]. If we now take into account the fact that the oscillation amplitude is small and that the BEC remains close to the center of the superfluid, we can make a Taylor-expansion of equation (3.1) and obtain:

$$n_\mathrm{f}(\boldsymbol{r}) = n_\mathrm{f}^{(0)}(\mu_\mathrm{f}(\boldsymbol{r})) = n_\mathrm{f}^{(0)}(\mu_\mathrm{f}^0) - \frac{\partial n_\mathrm{f}^{(0)}}{\partial \mu_\mathrm{f}} V(\boldsymbol{r}) = n_\mathrm{f}(\boldsymbol{r}=0) - \left.\frac{dn_\mathrm{f}^{(0)}}{d\mu_\mathrm{f}}\right|_{\mu_\mathrm{f}(\boldsymbol{r}=0)} V(\boldsymbol{r}).$$

The effective potential thus reads

$$V_\mathrm{eff}(\boldsymbol{r}) = g_\mathrm{bf} n_\mathrm{f}(\boldsymbol{r}=0) + V(\boldsymbol{r}) \left(1 - g_\mathrm{bf} \left.\frac{dn_\mathrm{f}^{(0)}}{d\mu_\mathrm{f}}\right|_{\mu_\mathrm{f}(\boldsymbol{r}=0)}\right) \tag{3.2}$$

From equation(3.2), we see that the potential remains harmonic, but its frequency is now given by:

$$\tilde{\omega}_\mathrm{b} = \omega_\mathrm{b} \left(1 - \frac{1}{2} g_\mathrm{bf} \left(\left.\frac{dn_\mathrm{f}^{(0)}}{d\mu_\mathrm{f}}\right|_{\mu_\mathrm{f}(\boldsymbol{r}=0)}\right)\right).$$

Since $g_\mathrm{bf} > 0$ and $\frac{dn_\mathrm{f}^{(0)}}{d\mu_\mathrm{f}} > 0$, we expect a downshift of the oscillation frequency, consistent with our observations. The value of this downshift can be calculated. Indeed,

[6] This is justified because of the small $N_\mathrm{b}/N_\mathrm{f}$ ratio. As it is shown in chapter 4, when the number of bosons is comparable to the number of fermions, it can strongly affect the Fermi cloud's profile.

the value of $\left.\frac{dn_{\mathrm{f}}^{(0)}}{d\mu}\right|_{\boldsymbol{r}=0}$ is known at unitarity from experiment and theory: the equation of state of a unitary Fermi gas is given by

$$\mu_{\mathrm{f}} = \xi \frac{\hbar^2}{2m_{\mathrm{f}}}(3\pi^2 n_{\mathrm{f}})^{2/3},$$

where $\xi = 0.38(1)$ is the Bertsch parameter. This leads to

$$n_{\mathrm{f}} = \frac{1}{3\pi^2}\left(\frac{2m_{\mathrm{f}}\mu_{\mathrm{f}}}{\xi\hbar^2}\right)^{3/2}.$$
$$\left.\frac{dn_{\mathrm{f}}^{(0)}}{d\mu}\right|_{\mu_{\mathrm{f}}(\boldsymbol{r}=0)} = \frac{m_{\mathrm{f}}}{\pi^2\hbar^2}\frac{k_{\mathrm{F}}}{\xi^{5/4}},$$

with k_{F} the Fermi wave-vector of the Fermi gas. It can also be calculated in the BEC-BCS crossover from the equation of state [Navon *et al.*, 2010, Astrakharchik *et al.*, 2004, Carlson *et al.*, 2003]. We now introduce the relative frequency shift $\frac{\delta\omega_{\mathrm{b}}}{\omega_{\mathrm{b}}} = \frac{\omega_{\mathrm{b}}-\tilde{\omega}_{\mathrm{b}}}{\omega_{\mathrm{b}}}$, and

$$\frac{\delta\omega_{\mathrm{b}}}{\omega_{\mathrm{b}}} = \frac{1}{2}g_{\mathrm{bf}}\left.\frac{dn_{\mathrm{f}}^{(0)}}{d\mu_{\mathrm{f}}}\right|_{\mu_{\mathrm{f}}(\boldsymbol{r}=0)}. \tag{3.3}$$

At unitarity, the predicted oscillation frequency is thus 14.97(2) Hz, very close to our measured frequency.

We can extend the study to the whole BEC-BCS crossover and measure the frequency shift for different magnetic fields between 860 G and 780 G (corresponding to $1/k_{\mathrm{F}}a_{\mathrm{ff}}$ between -0.4 and 0.8), we obtain the results shown on Figure 3.5 and compare them to equation (3.3). We can see very good agreement between theory and experiments, and this could be used as another method to measure the equation of state. Collective modes can provide precision measurements to probe the equilibrium properties of a many-body system, as was already done in [Tey *et al.*, 2013].

3.2.3 Sum-rule approach

3.2.3.1 Method

These results can also be found using a sum-rule approach [Stringari, 2004, Miyakawa *et al.*, 2000, Banerjee, 2007]. The dynamics of the system can be described using a Hamiltonian

$$\hat{H} = \sum_{i,j}\left(\frac{\hat{p}_{\mathrm{f},i}^2}{2m_{\mathrm{f}}} + \frac{\hat{p}_{\mathrm{b},j}^2}{2m_{\mathrm{b}}}\right) + U(\mathbf{r}_{\mathrm{f},i},\mathbf{r}_{\mathrm{b},j}), \tag{3.4}$$

where U is the total (trap+interaction) potential energy of the system. We note $|n\rangle$ and E_n the eigenstates and eigenvalues of the Hamiltonian. The ground state is $|0\rangle$ with energy E_0. We consider an excitation operator $\hat{F}_{\mathrm{f}}$ (resp. $\hat{F}_{\mathrm{b}}$) affecting the fermions (resp. the bosons) and define

$$\hat{F}(c_{\mathrm{f}},c_{\mathrm{b}}) = c_{\mathrm{f}}\hat{F}_{\mathrm{f}} + c_{\mathrm{b}}\hat{F}_{\mathrm{b}} \tag{3.5}$$

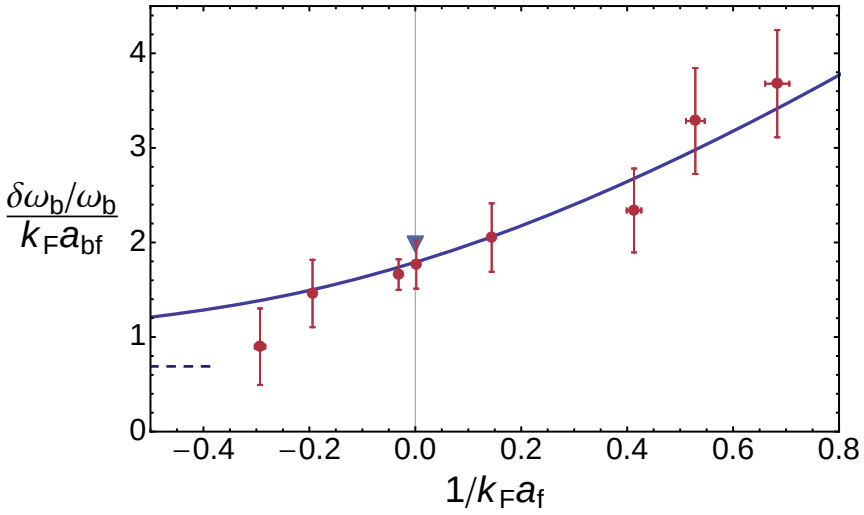

Figure 3.5: Evolution of the frequency shift of the dipole mode in the BEC-BCS crossover. Experiment (red dots) and theory (blue line) from the equation of state (equation (3.3) and [Navon *et al.*, 2010]), ideal Fermi gas (dashed line) and MIT prediction at unitarity [Ku *et al.*, 2012] (blue triangle).

the excitation operator for both species, depending on the mixing coefficients c_f and c_b. We can define the moments ('sum-rules') by

$$S_k = \sum_n (E_n - E_0)^k \left|\langle n|\hat{F}|0\rangle\right|^2.$$

In particular, S_1 and S_{-1} are defined as:

$$S_1 = \sum_n (E_n - E_0) \left|\langle n|\hat{F}|0\rangle\right|^2,$$
$$S_{-1} = \sum_n \frac{1}{E_n - E_0} \left|\langle n|\hat{F}|0\rangle\right|^2.$$

Assuming then that the system is mainly described by its ground state and two first excited states leads to

$$(E_1 - E_0)^2 \leq \frac{S_1}{S_{-1}} \leq (E_2 - E_0)^2,$$

$$\hbar^2\omega_1^2 \leq \frac{S_1}{S_{-1}} \leq \hbar^2\omega_2^2,$$

and the extrema of S_1/S_{-1} with respect to c_f and c_b give access to approximate values for excitation energies and frequencies of the system (or more precisely, to the upper bound for the lowest one and to the lower bound for the highest one).

3.2.3.2 Displacement of the cloud

To push the calculation further, it is necessary to calculate S_1 and S_{-1}. Using closure relation, S_1 can be re-written as

$$S_1 = \langle 0|\hat{F}\hat{H}\hat{F}|0\rangle = -\frac{1}{2}\langle 0|[[\hat{H},\hat{F}],\hat{F}]|0\rangle.$$

If $\hat{F}$ affects only the position degrees of freedom, as it is the case for the excitation described in subsection 3.1.2, and if $\hat{H}$ has the form $\hat{H} = \frac{\hat{p}^2}{2m} + V(\hat{r})$, then S_1 can be calculated exactly. The axial displacement of the system can be described by choosing

$$\hat{F}_\mathrm{f} = \sum_{i=1}^{N_\mathrm{f}} \hat{z}_{\mathrm{f},i}, \tag{3.6}$$

$$\hat{F}_\mathrm{b} = \sum_{j=1}^{N_\mathrm{b}} \hat{z}_{\mathrm{b},j}, \tag{3.7}$$

where $z_{\alpha=(\mathrm{f,b}),i}$ is the position along z of the i-th atom, and the Hamiltonian is given by equation (3.4). In this case, using the fact that $[[\hat{p}_z^2,z],z] = 2\hbar^2$, we have:

$$\begin{aligned}
S_1 &= -\frac{1}{2}\langle 0|[[\hat{H},\hat{F}],\hat{F}]|0\rangle \\
&= -\frac{1}{2}\left(c_\mathrm{f}^2\langle 0|[[\hat{H},\hat{F}_\mathrm{f}],\hat{F}_\mathrm{f}]|0\rangle + c_\mathrm{b}^2\langle 0|[[\hat{H},\hat{F}_\mathrm{b}],\hat{F}_\mathrm{b}]|0\rangle\right) \\
&= -\frac{1}{2}\left(N_\mathrm{f}\frac{2\hbar^2}{2m_\mathrm{f}} + N_\mathrm{b}\frac{2\hbar^2}{2m_\mathrm{b}}\right) \\
&= -\left(\frac{\hbar^2}{2m_\mathrm{f}}N_\mathrm{f}c_\mathrm{f}^2 + \frac{\hbar^2}{2m_\mathrm{b}}N_\mathrm{b}c_\mathrm{b}^2\right)
\end{aligned}$$

S_{-1} can be calculated using perturbation theory: consider a perturbed Hamiltonian $\hat{H}' = \hat{H} - k\,\hat{F}$, where k is the restoring force of the trap. The first-order perturbation theory gives access to the eigenstates $|n'\rangle$ of the perturbed system and

$$|0'\rangle = |0\rangle + \sum_n \frac{\langle n|\,\hat{F}\,|0\rangle}{E_n - E_0}\,|n\rangle\,,$$

which leads to:

$$\begin{aligned}
\langle 0'|\,\hat{F}\,|0'\rangle &= \langle 0|\,\hat{F}\,|0\rangle + 2k\sum_n \frac{|\,\langle 0|\,\hat{F}\,|n\rangle\,|^2}{E_n - E_0} \\
&= \langle 0|\,\hat{F}\,|0\rangle + 2kS_{-1}.
\end{aligned}$$

So $S_{-1} = \frac{1}{2k}(\langle 0'|\,\hat{F}\,|0'\rangle - \langle 0|\,\hat{F}\,|0\rangle)$, and $\hat{F}$ is given by equations (3.5), (3.6) and (3.7). Using Taylor expansion, $\langle 0'|\,\hat{z}_{\alpha,i}\,|0'\rangle$ can be expressed as:

$$\langle 0'|\,\hat{z}_{\alpha,i}\,|0'\rangle = \langle 0|\,\hat{z}_{\alpha,i}\,|0\rangle + \sum_{\beta=\mathrm{b,f}} \frac{\partial\,\langle 0|\,\hat{z}_{\alpha,i}\,|0\rangle}{\partial d_\beta}.$$

Noting $\langle z_\alpha \rangle = \langle 0 | \hat{z}_{\alpha,i} | 0 \rangle$ the center of mass of specie α =b,f, this leads to:

$$S_{-1} = \frac{1}{2k} \sum_{\alpha,\beta} N_\alpha c_\alpha c_\beta \frac{\partial \langle z_\alpha \rangle}{\partial d_\beta}.$$

To sum up, S_1 and S_{-1} are given by

$$\begin{aligned} S_1 &= -\left(\frac{\hbar^2}{2m_\mathrm{f}} N_\mathrm{f} c_\mathrm{f}^2 + \frac{\hbar^2}{2m_\mathrm{b}} N_\mathrm{b} c_\mathrm{b}^2 \right) \\ S_{-1} &= -\frac{1}{k} \left\{ c_\mathrm{f}^2 N_\mathrm{f} \frac{\partial \langle z_\mathrm{f} \rangle}{\partial d_\mathrm{f}} + c_\mathrm{b}^2 N_\mathrm{b} \frac{\partial \langle z_\mathrm{b} \rangle}{\partial d_\mathrm{b}} + c_\mathrm{f} c_\mathrm{b} \left(N_\mathrm{f} \frac{\partial \langle z_\mathrm{f} \rangle}{\partial d_\mathrm{b}} + N_\mathrm{b} \frac{\partial \langle z_\mathrm{b} \rangle}{\partial d_\mathrm{f}} \right) \right\}, \end{aligned}$$

where k is the restoring force of the axial magnetic trap, $\langle z_\alpha \rangle$ is the center of mass position of atoms of species α = b,f in the presence of a perturbing potential $-k \sum_\beta d_\beta \hat{F}_\alpha$ corresponding to a shift of the trapping potential of species β by a distance d_β. It yields:

$$\frac{S_1}{S_{-1}} = \hbar^2 k \frac{N_\mathrm{f} c_\mathrm{f}^2/m_\mathrm{f} + N_\mathrm{b} c_\mathrm{b}^2/m_\mathrm{b}}{c_\mathrm{f}^2 N_\mathrm{f} \frac{\partial \langle z_\mathrm{f} \rangle}{\partial d_\mathrm{f}} + c_\mathrm{b}^2 N_\mathrm{b} \frac{\partial \langle z_\mathrm{b} \rangle}{\partial d_\mathrm{b}} + c_\mathrm{f} c_\mathrm{b} \left(N_\mathrm{f} \frac{\partial \langle z_\mathrm{f} \rangle}{\partial d_\mathrm{b}} + N_\mathrm{b} \frac{\partial \langle z_\mathrm{b} \rangle}{\partial d_\mathrm{f}} \right)}$$

To study that function, we can introduce the change of variable $c'_\alpha = c_\alpha \sqrt{N_\alpha / m_\alpha}$ and $\psi = (a'_\mathrm{f}, a'_\mathrm{b})$. S_1/S_{-1} can be re-written in terms of ψ:

$$\frac{S_1}{S_{-1}} = \hbar^2 k \frac{\langle \psi | \psi \rangle}{\langle \psi | \mathcal{M} | \psi \rangle},$$

with $\mathcal{M}$, the effective mass operator, given by

$$\mathcal{M}_{\alpha\beta} = \sqrt{m_\alpha m_\beta} \sqrt{\frac{N_\alpha}{N_\beta}} \frac{\partial \langle z_\alpha \rangle}{\partial d_\beta},$$

and the scalar product defined by $\langle \psi | \psi' \rangle = \sum_\alpha \psi_\alpha \psi'_\alpha$. The frequencies ω_1 and ω_2 are then given by $\omega_i = \sqrt{k/\tilde{m}_i}$, where $\tilde{m}_i$ is an eigenvalue of $\mathcal{M}$. Since the matrix $\mathcal{M}$ is symmetric, usual perturbation theory gives access to its eigenvalues and eigenvectors, and

$$\begin{aligned} \tilde{m}_1 &= m_\mathrm{f} \left(1 - \frac{\partial \langle z_\mathrm{f} \rangle}{\partial d_\mathrm{b}} \right) \\ \tilde{m}_2 &= m_\mathrm{b} \left(1 - \frac{\partial \langle z_\mathrm{b} \rangle}{\partial d_\mathrm{f}} \right). \end{aligned}$$

Since we have experimentally $N_\mathrm{f} \gg N_\mathrm{b}$, this implies $\partial \langle z_\mathrm{b} \rangle / \partial d_\mathrm{f} \gg \partial \langle z_\mathrm{f} \rangle / \partial d_\mathrm{b}$, and we can identify the excitations frequencies $\{\omega_1, \omega_2\}$ to $\{\tilde{\omega}_\mathrm{b}, \tilde{\omega}_\mathrm{f}\}$ and obtain

$$\begin{aligned} \tilde{\omega}_\mathrm{f} &\simeq \omega_\mathrm{f} \\ \tilde{\omega_\mathrm{b}} &\simeq \omega_\mathrm{b} \left(1 + \frac{1}{2} \frac{\partial \langle z_\mathrm{b} \rangle}{\partial d_\mathrm{f}} \right). \end{aligned}$$

The crossed-susceptibility can be calculated using local density approximation, and we recover the previous results (equation (3.3) for instance) $\frac{\partial \langle z_\mathrm{b} \rangle}{\partial d_\mathrm{f}} = -g_\mathrm{bf} \left. \frac{dn_\mathrm{f}^{(0)}}{d\mu} \right|_{\mu_\mathrm{f}(\boldsymbol{r}=0)}$.

The eigenvectors give access to the dynamics of the system. If we note $\Psi'_{i=1,2} = (c'_\mathrm{f}, c'_\mathrm{b})$ the eigenvectors associated to eigenvalues ω_1 and ω_2, with perturbation theory we get

$$\Psi'_1 = \begin{pmatrix} 1 \\ \frac{\sqrt{m_\mathrm{f} m_\mathrm{b}}}{m_\mathrm{f}-m_\mathrm{b}} \sqrt{\frac{N_\mathrm{b}}{N_\mathrm{f}}} \frac{\partial \langle z_\mathrm{b} \rangle}{\partial d_\mathrm{f}} \end{pmatrix}$$
$$\Psi'_2 = \begin{pmatrix} \frac{\sqrt{m_\mathrm{f} m_\mathrm{b}}}{m_\mathrm{b}-m_\mathrm{f}} \sqrt{\frac{N_\mathrm{b}}{N_\mathrm{f}}} \frac{\partial \langle z_\mathrm{b} \rangle}{\partial d_\mathrm{f}} \\ 1 \end{pmatrix},$$

and the vectors $\Psi_{i=1,2} = (c_\mathrm{f}, c_\mathrm{b})$ corresponding to the excitation operator $\hat{F}$ are

$$\Psi_1 = \sqrt{\frac{m_\mathrm{f}}{N_\mathrm{f}}} \begin{pmatrix} 1 \\ \frac{m_\mathrm{b}}{m_\mathrm{f}-m_\mathrm{b}} \frac{\partial \langle z_\mathrm{b} \rangle}{\partial d_\mathrm{f}} \end{pmatrix}$$
$$\Psi_2 = \sqrt{\frac{m_\mathrm{b}}{N_\mathrm{b}}} \begin{pmatrix} \frac{m_\mathrm{f}}{m_\mathrm{b}-m_\mathrm{f}} \frac{N_\mathrm{b}}{N_\mathrm{f}} \frac{\partial \langle z_\mathrm{b} \rangle}{\partial d_\mathrm{f}} \\ 1 \end{pmatrix}.$$

It is now possible to express the initial condition $z_\mathrm{f}(t=0) = z_\mathrm{b}(t=0) = d$ on the (Ψ_1, Ψ_2) basis, and since the evolution of the eigenvector Ψ_i occurs at a frequency ω_i, in the experimentally relevant situation it is possible to obtain the time evolution of the system as

$$z_\mathrm{f}(t) = d[(1-\varepsilon\rho)\cos(\tilde{\omega}_\mathrm{f} t) + \rho\varepsilon \cos(\tilde{\omega}_\mathrm{b} t)], \tag{3.8}$$
$$z_\mathrm{b}(t) = d[-\varepsilon \cos(\tilde{\omega}_\mathrm{f} t) + (1+\varepsilon)\cos(\tilde{\omega}_\mathrm{b} t)]., \tag{3.9}$$

with $\rho = N_\mathrm{b}/N_\mathrm{f} \ll 1$ and

$$\varepsilon = \frac{m_\mathrm{b}}{m_\mathrm{b}-m_\mathrm{f}} \frac{\partial \langle z_\mathrm{b} \rangle}{\partial d_\mathrm{f}}.$$

The second factor in the expression of ε might be rather small, the first factor is actually quite large ($\frac{m_\mathrm{b}}{m_\mathrm{b}-m_\mathrm{f}} = 14$), and the value of ε is $\varepsilon = 0.25$. This actually makes the amplitude modulation very visible on the center-of-mass oscillations of the bosonic cloud. These functions (equations (3.8) and (3.9)) perfectly fit the data, as shown in Figure 3.4. More details on the calculations can be found in supplementary materials of [Ferrier-Barbut *et al.*, 2014]. This approach validates the description in terms of harmonic oscillators that will be used in the next paragraph.

3.2.4 Two coupled-oscillators model

To understand the amplitude modulation, it is necessary to take into account the back-action of the bosons on the fermions. A scheme of the system is given in Figure 3.6.

We now obtain the following system:

$$M_\mathrm{f} \ddot{z}_\mathrm{f} = -K_\mathrm{f} z_\mathrm{f} - K_\mathrm{bf}(z_\mathrm{f} - z_\mathrm{b}) \tag{3.10}$$
$$M_\mathrm{b} \ddot{z}_\mathrm{b} = -K_\mathrm{b} z_\mathrm{b} - K_\mathrm{bf}(z_\mathrm{b} - z_\mathrm{f}), \tag{3.11}$$

Figure 3.6: Schematic representation of the system. The fermions (on the right) and the bosons (on the left) are represented by two oscillators with spring constants K_f and K_b, and are coupled with a spring constant K_bf.

where $M_\mathrm{b} = N_\mathrm{b} m_\mathrm{b}$ (resp. $M_\mathrm{f} = N_\mathrm{f} m_\mathrm{f}$) is the total mass of the bosonic (resp. fermionic) cloud, $K_\mathrm{b} = M_\mathrm{b}\omega_\mathrm{b}^2$ (resp. $K_\mathrm{f} = M_\mathrm{f}\omega_\mathrm{f}^2$) is the spring constant of the axial magnetic confinement for the bosons (resp. fermions), and K_bf is a phenomenological weak coupling constant describing the mean-field interaction between the bosons and the fermions. To be consistent with the previous description, we take $K_\mathrm{bf} = -2K_\mathrm{b}\frac{\delta\omega_\mathrm{b}}{\omega_\mathrm{b}}$. We can now solve equations (3.10) and (3.11) with initial condition $z_\mathrm{f}(t=0) = z_\mathrm{b}(t=0) = d$. We note $\rho = N_\mathrm{b}/N_\mathrm{f} (\ll 1)$ and $\varepsilon = \frac{2m_\mathrm{b}}{m_\mathrm{b}-m_\mathrm{f}}\left(\frac{\tilde{\omega}_\mathrm{b}-\omega_\mathrm{b}}{\omega_\mathrm{b}}\right)$. We get, as before,

$$\begin{aligned}
\tilde{\omega}_\mathrm{f} &\approx \omega_\mathrm{f} \\
\tilde{\omega}_\mathrm{b} &= \omega_\mathrm{b}\left(1 - \frac{K_\mathrm{bf}}{2K_\mathrm{b}}\right) \\
z_\mathrm{f} &= d[(1-\varepsilon\rho)\cos(\tilde{\omega}_\mathrm{f} t) + \varepsilon\rho\cos(\tilde{\omega}_\mathrm{b} t)] \qquad (3.12)\\
z_\mathrm{b} &= d[-\varepsilon\cos(\tilde{\omega}_\mathrm{f} t) + (1+\varepsilon)\cos(\tilde{\omega}_\mathrm{b} t)]. \qquad (3.13)
\end{aligned}$$

Our system is analogous to a two-coupled-pendulum system which mass would be close. This almost exact tuning of the two oscillators leads to the observed strong modulation of the oscillations.

The adequacy of the $T = 0$ mean-field model, the absence of dissipation and the coherent energy exchange between the two gases provide another evidence for the superfluid character of the two clouds. Limits of superfluidity can be studied in more details by varying the amplitude of the oscillations, as shown below.

3.3 Low temperature, high amplitude

3.3.1 Experiments

As it was shown previously, the two clouds oscillate in the trap with different frequencies. They gradually get out of phase and acquire some relative velocity with respect to each other, the maximum value of which is given by $(\tilde{\omega}_\mathrm{b} + \tilde{\omega}_\mathrm{f})d$. By varying the value of d, we can thus tune the relative velocity between the two clouds and study the properties of the counterflow. One striking feature is that, though for low relative velocities we observe no damping (as discussed in section 3.2), above a certain critical velocity there is an onset of dissipation (see Figure 3.7). The relative motion is damped down to a value where their relative velocities are smaller than the critical velocity, and they then reach a steady-state regime similar to that of section 3.2.

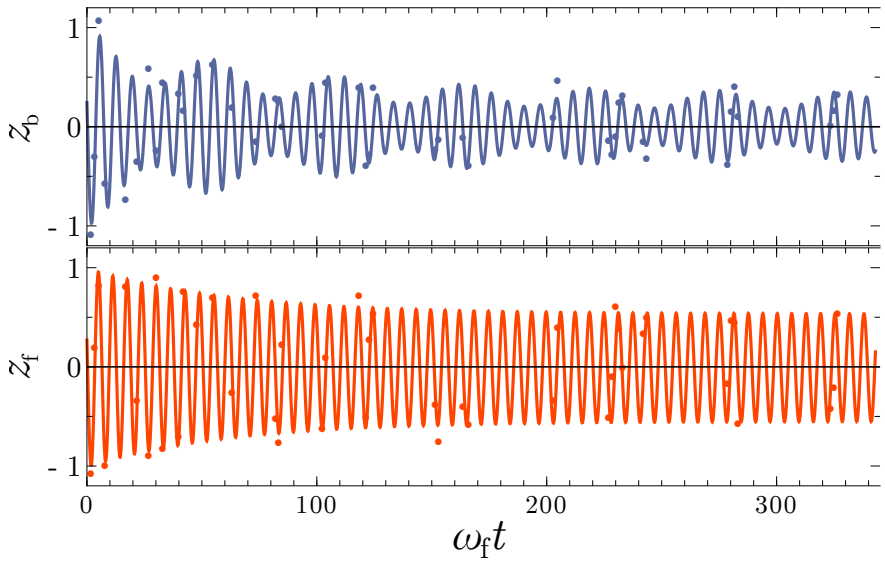

Figure 3.7: Center of mass oscillations at low temperature ($\approx$ 100 nK) for a high initial amplitude ($d \approx 150\mu$m). The oscillations are initially damped, until the relative velocity drops below the critical velocity. Then a steady-state regime is reached and lower amplitude oscillations are long-lived.

We can make a phenomenological fit of the data using the functions defined in equations (3.12) and (3.13) in the limit of $\rho \to 0$ and with ε fixed, but using a time-dependent amplitude:

$$d(t) = d_1 + d_2 e^{-\gamma_b t}$$

for the bosons and

$$d(t) = d_1 + d_2 e^{-\gamma_f t}$$

for the fermions. Due to the high number of parameters, the fit procedure is the following. We first fit te center-of-mass oscillation of the fermions with the function $(d_1 + d_2 e^{-\gamma_f t})\cos(\omega_f t)$. From this, we extract $\omega_f \approx \tilde{\omega}_f$, that we use to fit the center-of-mass oscillations of the bosons with $(d_1 + d_2 e^{-\gamma_b t})(-\varepsilon \cos(\tilde{\omega}_f t) + (1+\varepsilon)\cos(\tilde{\omega}_b t))$. The value of γ_b can be extracted for different relative velocities and plotted as a function of v_{max}/v_F, where v_{max} is the maximum relative velocity between the two clouds (see Figure 3.8). This shows clear evidence for a critical velocity, which can now be measured.

One may wonder what happens to coefficients d_1 and d_2 when damping is small. There actually may exist two time scales in the time evolution of the center-of-mass. The first one corresponds to damping due to friction between bosons and fermions, and this is the one we want to measure in this experiment. The other timescale corresponds to residual damping due to some small anharmonicities of the trap, with a timescale of 5 to 20 s. For high relative velocity between the two clouds, the first timescale is short, leading to high values of γ_b, on the order of a few s^{-1}. The residual damping is then neglected. However, for low relative velocity, both timescale have the same

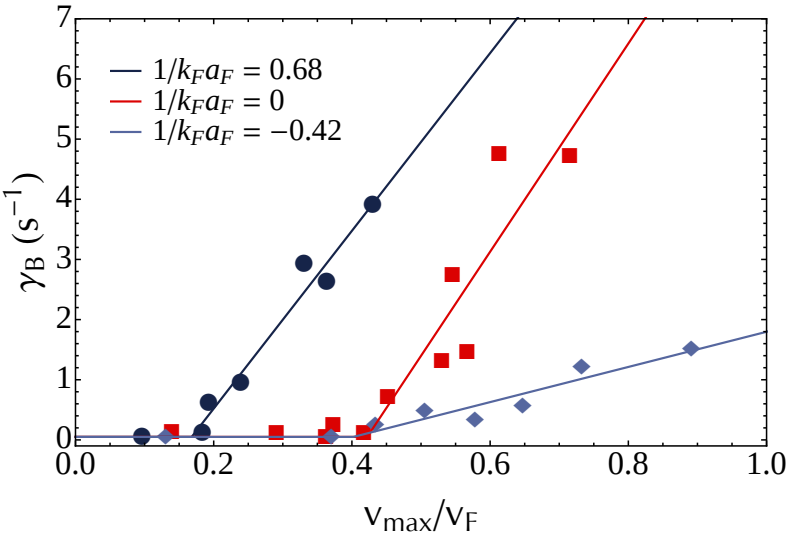

Figure 3.8: Damping rate of the bosons as a function of the relative velocity between the two clouds in the BEC-BCS crossover. Magnetic fields are 780 G ($1/k_F a_{ff} = 0.68$), 832 G ($1/k_F a_{ff} = 0$) and +880 G ($1/k_F a_{ff} = -0.42$).

magnitude, and the measured γ_b corresponds to some convolution between them. It is then over-evaluated. In any case, d_2 always has a finite value and γ_b can be measured.

Another way to obtain the critical velocity would have been to extract the amplitude d_1 of the long-lived oscillations: the oscillation amplitude goes from $d_1 + d_2$ for short evolution times down to d_1. Since after a few γ_b^{-1}, γ_f^{-1} there is no more damping of the oscillations, their relative velocity is necessarily below the critical velocity. Unfortunately, this procedure turned out to be hard to set up, because the value of d_1 is very sensitive to the fitted value of γ_b and γ_f, itself subject to noise. The final relative velocity of the two clouds was not constant for all dataset at a given magnetic field, even though it was always below the critical velocity. More studies are needed to go forward on this subject.

It was also tempting to use as well γ_f to study the critical velocity. However, the damping rate of the fermionic oscillations seems to be influenced by the ratio N_f/N_b, which is hard to keep constant, even within a dataset. No clear tendency on γ_f could be evidenced, but this could be the subject of future studies.

Another question that may be raised is where does the energy dissipated by friction goes. It turns out that it is dissipated by residual evaporation, leading to a loss of atoms. This also results into an evolution of the ratio N_f/N_b as a function of time, as already mentioned above.

3.3.2 Landau criterion for superfluidity

Here, we will first derive the historical Landau criterion for an impurity inside a superfluid, then its extension by Castin *et al.* [Castin *et al.*, 2015]. Let us consider an impurity of mass m moving with a velocity $\boldsymbol{v}$ inside a superfluid. It may dissipate energy by creating excitations of momentum $\boldsymbol{p}$ in the superfluid and reach a velocity

$\boldsymbol{v'}$. Let us note $\varepsilon(\boldsymbol{p})$ the dispersion relation of the excitations. Conservation laws lead to:

$$m\frac{\boldsymbol{v}^2}{2} = m\frac{\boldsymbol{v'}^2}{2} + \varepsilon(\mathbf{p})$$
$$m\boldsymbol{v} = m\boldsymbol{v'} + \mathbf{p}$$

Thus

$$\boldsymbol{v}\cdot\boldsymbol{p} = \frac{p^2}{2m} + \varepsilon(\boldsymbol{p})$$

and

$$v \geq \left(\frac{\frac{p^2}{2m} + \varepsilon(\boldsymbol{p})}{p}\right).$$

A necessary condition for excitation shedding is $v > v_c$, where

$$v_c = \min_{\boldsymbol{p}}\left(\frac{\frac{p^2}{2m} + \varepsilon(\boldsymbol{p})}{p}\right)$$

This sets a lower bound for the velocity needed to create excitations in a superfluid. For an impurity with a very large mass $m \to \infty$, this can be simplified as

$$v_c = \min_{\boldsymbol{p}}\left(\frac{\varepsilon(\boldsymbol{p})}{p}\right)$$

In the case where the superfluid is a homogeneous weakly-interacting BEC, the excitations are phonons. Since the phonon dispersion relation is linear, $\varepsilon_{\mathrm{b}}(\boldsymbol{p}) = c_{\mathrm{b}}^{\mathrm{s}}p$, the critical velocity is simply the sound velocity $c_{\mathrm{b}}^{\mathrm{s}}$:

$$v_c = c_{\mathrm{b}}^{\mathrm{s}} = \sqrt{gn/m}.$$

In the case where the superfluid is a strongly interacting Fermi gas, there exist two excitation branches. One of them is phonon-like with bosonic statistics[Minguzzi *et al.*, 2001], and at low momentum its dispersion relation $\varepsilon_{\mathrm{f}}^{b}(\mathbf{p})$ is given by

$$\varepsilon_{\mathrm{f}}^{b}(\boldsymbol{p}) \underset{p\to 0}{=} pc_{\mathrm{f}}^{\mathrm{s}},$$

where $c_{\mathrm{f}}^{\mathrm{s}}$ is the sound velocity in the Fermi cloud. The second branch is associated to pair-breaking and has fermionic statistics [Combescot *et al.*, 2006]. Its dispersion relation is given by

$$\varepsilon_{\mathrm{f}}^{f}(\boldsymbol{p}) = \sqrt{\left(\frac{p^2}{2m_{\mathrm{f}}} - \mu\right)^2 + \Delta^2}$$

At unitarity and on the BEC side of the resonance, the critical velocity is given by the sound velocity, whereas on the BCS side, the pair-breaking excitations dominate [Combescot *et al.*, 2006].

If we now consider a Fermi cloud and take as an impurity a BEC, the situation is quite similar. We note ε_{b} the dispersion relation of the BEC, M_{b} the mass of the BEC

and $\varepsilon_{\mathrm{f}}^{\sigma}$, with $\sigma = f$ (for pair-breaking excitations) or b (for phonon-like excitations) that of the fermions. The conservation laws lead to

$$\begin{aligned} M_{\mathrm{b}}\frac{\boldsymbol{v}^2}{2} &= M_{\mathrm{b}}\frac{\boldsymbol{v'}^2}{2} + \varepsilon_{\mathrm{b}}(\boldsymbol{p}) + \varepsilon_{\mathrm{f}}^{\sigma}(\boldsymbol{q}) + \boldsymbol{p}\cdot\boldsymbol{v} \\ M_{\mathrm{b}}\boldsymbol{v} &= M_{\mathrm{b}}\boldsymbol{v'} + \mathbf{p} + \mathbf{q}, \end{aligned}$$

where $\boldsymbol{p}$ (resp. $\boldsymbol{q}$) is the momentum of the excitation created in the BEC (resp. Fermi superfluid), and $\boldsymbol{p}\cdot\boldsymbol{v}$ is the Doppler shift of the excitation in the BEC. The lowest relative velocity allowing the creation of excitations corresponds to $\boldsymbol{v} = \boldsymbol{v'}$ and the critical velocity is then given by[7]

$$v_c = \min_{\substack{\sigma=f,b \\ \boldsymbol{p}}} \left(\frac{\varepsilon_{\mathrm{b}}(\boldsymbol{p}) + \varepsilon_{\mathrm{f}}^{\sigma}(\boldsymbol{p})}{p} \right),$$

and on the BEC side of the resonance, this can be further simplified in

$$v_c = c_{\mathrm{b}}^{\mathrm{s}} + c_{\mathrm{f}}^{\mathrm{s}},$$

the sum of the sound velocities for both superfluids. This formula, obtained in the case of homogeneous systems flowing into each other at a constant velocity, is all the more remarkable that it was unexpected. A naive answer would be that the critical velocity should be somehow the minimum of the two critical velocities, for instance. The results presented in subsection 3.3.3 and Figure 3.10 show that the adaptation of Landau's argument is indeed accurate.

3.3.3 Critical velocity

We measure γ_{b} as a function of $v_{\max}/v_{\mathrm{F}}$ for six different values of $1/k_{\mathrm{F}}a_{\mathrm{ff}}$ in the BEC-BCS crossover and we can extract the critical velocity using a phenomenological fit shown on Figure 3.8:

$$\gamma_{\mathrm{b}} = A\,\theta(v - v_{\mathrm{c}}) \left(\frac{v - v_{\mathrm{c}}}{v_{\mathrm{F}}} \right)^{\alpha}$$

where v_{F} is the Fermi velocity defined as $1/2m_{\mathrm{f}}v_{\mathrm{F}}^2 = E_{\mathrm{F}} = \hbar\overline{\omega}_{\mathrm{f}}(6N_{\mathrm{f}})^{1/3}$ and $\theta(x)$ is the Heaviside function defined as

$$\theta(x) = \begin{cases} 0 & \text{if } x < 0 \\ 1 & \text{if } x > 0. \end{cases}$$

Since there is currently no theoretical prediction for the behavior of γ_{b} as a function of $v_{\max}/v_{\mathrm{F}}$ for harmonically trapped gases, on Figure 3.8 we chose to fit with $\alpha = 1$ (as other previous studies [Miller *et al.*, 2007, Weimer *et al.*, 2015]) because it is consistent with a χ^2 test[8]. To avoid any loss of generality, the systematic influence of such a

[7] This is actually a rough estimate: for $\sigma = f$, corresponding to the pair-breaking excitations of the Fermi superfluid, it is only possible to create pairs of excitations that may have different momenta $\boldsymbol{q_1}$ and $\boldsymbol{q_2}$, not necessarily in the same direction.

[8] We measured the distance between the points and the fit function for different values of α between 0.5 and 2 and the minimum distance was always reached for values close to $\alpha = 1$.

choice is evaluated by letting α vary between 0.5 and 2 for all of our dataset (see Figure 3.9), this gives us lower and higher bounds for the measured critical velocity. We attract the reader's attention on the low damping rate on the BCS side, and on the small critical velocity on the BEC side.

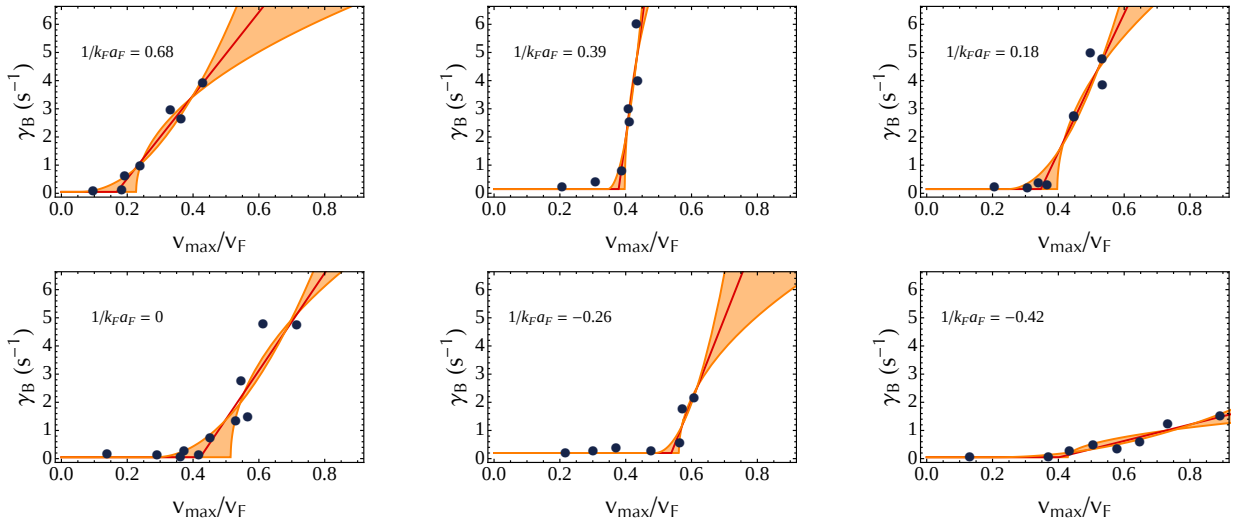

Figure 3.9: Damping rates of the center of mass oscillations versus maximal relative velocity in the BEC-BCS crossover in unit of the Fermi velocity v_F. Red line: fit with $\alpha = 1$. Orange zone: region spanned by the fitting function when varying α from 0.5 to 2. BEC limit corresponds to $1/k_F a_{ff} \gg 1$ and BCS limit to $1/k_F a_{ff} \ll -1$.

All of the parameters used to extract v_c in the BEC-BCS crossover are given in Table 3.2.

B (G)	780	800	816	832	860	880
$a_f(a_0)$	6.4×10^3	11.3×10^3	24.0×10^3	∞	-16.5×10^3	-10.3×10^3
$1/k_F a_{ff}$	0.68 ± 0.07	0.39 ± 0.01	0.18 ± 0.02	0 ± 0.002	-0.26 ± 0.05	-0.42 ± 0.03
$a_b(a_0)$	21.3	30.8	43.3	69.5	76.0	259
$c_b^s(10^{-2}v_F)$	9.6 ± 1.4	9.4 ± 0.14	11.0 ± 1.6	11.1 ± 1.7	11.4 ± 1.7	15.1 ± 2.2
v_c/v_F	$0.17^{+0.06}_{-0.10}$	$0.38^{+0.02}_{-0.04}$	$0.35^{+0.04}_{-0.11}$	$0.42^{+0.08}_{-0.14}$	$0.54^{+0.02}_{-0.06}$	$0.40^{+0.10}_{-0.20}$
$A(s^{-1})$	14.8 ± 1.4	85 ± 32	24.6 ± 4.3	17.3 ± 3.6	30 ± 11	2.9 ± 0.5
v_c/c_f^s	$0.53^{+0.19}_{-0.31}$	$1.11^{+0.06}_{-0.12}$	$0.99^{+0.11}_{-0.31}$	$1.17^{+0.22}_{-0.39}$	$1.46^{+0.05}_{-0.16}$	$1.05^{+0.26}_{-0.53}$

Table 3.2: Experimental parameters, sound velocity at the center of the Bose gas in an elongated geometry $c_b^s = \sqrt{\mu_b/2m_b}$, critical velocity v_c/v_F, damping rate $A(s^{-1})$, and v_c/c_f^s for $\alpha = 1$ in the BEC-BCS crossover. The typical number of bosons and fermions are constant in the crossover and are respectively $2.5 \pm 0.5 \times 10^4$ and $2.5 \pm 0.5 \times 10^5$.

The extracted critical velocity as a function of $1/k_F a_{ff} f$ is displayed on Figure 3.10, as well as the sound velocity for an elongated Fermi gas c_f^s calculated by integration over the transverse direction [Capuzzi *et al.*, 2006, Luo *et al.*, 2007, Astrakharchik,

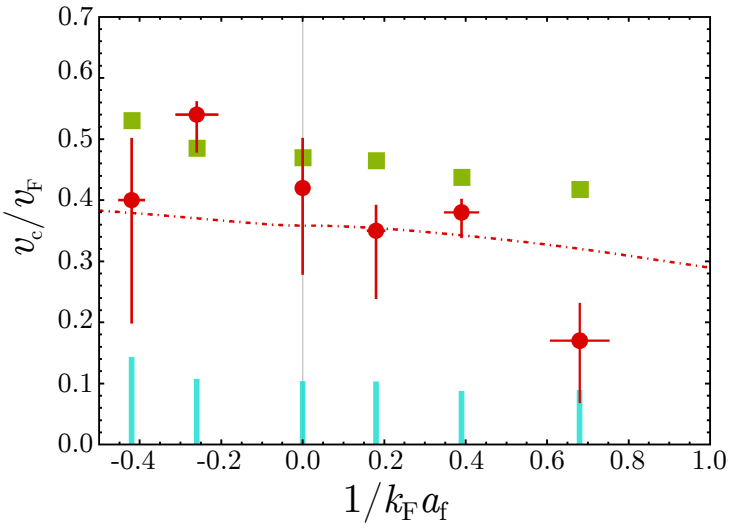

Figure 3.10: Critical velocity of the Bose-Fermi superfluid counterflow in the BEC-BCS crossover normalized to the Fermi velocity v_F. Red dots: measurements. Red dot-dashed line: sound velocity c_f^s of an elongated homogeneous Fermi superfluid deduced from its equation of state [Navon *et al.*, 2010, Astrakharchik, 2014] after integration of the density in the transverse plane, and measured in [Joseph *et al.*, 2007]. Blue bars: calculated sound velocity c_b^s of the elongated ^{7}Li BEC for each magnetic field, (880 G, 860 G, 832 G, 816 G, 800 G, 780 G). Green squares indicate the prediction $v_c = c_f^s + c_b^s$.

2014, Stringari, 1998, Navon *et al.*, 2010]. The sound velocity c_b^s for the Bose gas is shown for our experimental points[9]. It is averaged on the whole BEC [Stringari, 1998, Fedichev and Shlyapnikov, 2001]. As for c_f^s, it is averaged in the $x-y$ (radial) plane. However, since both c_f^s and v vary as a function of z, the axial position in the harmonic trap, one may wonder where the ratio v/c_f^s is maximal in the Fermi cloud frame. That position would be the relevant one when studying the critical velocity.

Polytropic equation of state

It is actually possible to show that this ratio is maximum at the center of the cloud. In the case of a gas with a polytropic equation of state, this can be derived analytically: in the frame of the Fermi cloud, we can describe the trajectory of the BEC by the simple harmonic oscillation

$$z_B(t) = Z_0 \cos(\omega_B t),$$

where we have omitted the slow beating of the amplitude Z_0 due to the oscillation-frequency difference between bosons and fermions. The velocity of the BEC is then

[9] Since $c_b^s = \sqrt{\mu_b/m_b} = \sqrt{g_{bb} n_b/m_b}$, it does vary for our dataset, especially since g_{bb} depends on the magnetic field and notably diverges for a magnetic field of 845.5 G. As it is not a function of $k_F a_{ff}$ it would be meaningless to plot it on Figure 3.10.

$v(z) = -Z_0\omega_\mathrm{B}\sin(\omega_\mathrm{B}t)$, hence

$$\left(\frac{v(z)}{v(z=0)}\right)^2 = \left(1 - \frac{z^2}{Z_0^2}\right),$$

For a polytropic equation of state, the local sound velocity in the Fermi cloud is given by [Capuzzi *et al.*, 2006]

$$\begin{aligned} c_\mathrm{s}^\mathrm{F}(z)^2 &= \frac{\gamma}{\gamma+1}\frac{\mu_\mathrm{F}(z)}{m_\mathrm{F}} \\ c_\mathrm{s}^\mathrm{F}(z)^2 &= \frac{\gamma}{\gamma+1}\frac{\mu_\mathrm{F}(0)}{m_\mathrm{F}}\left(1 - \frac{z^2}{z_\mathrm{TF}^2}\right), \end{aligned}$$

where z_TF is the Thomas-Fermi radius of the cloud, and the local chemical potential $\mu_\mathrm{F}(z)$ was obtained using the local density approximation. Combining equations 3.3.3 and 3.15, we then obtain

$$\frac{v_\mathrm{B}(z)^2}{c_\mathrm{s}^\mathrm{F}(z)^2} = \frac{v_\mathrm{B}(z=0)^2}{c_\mathrm{s}^\mathrm{F}(z=0)^2}\frac{1 - z^2/Z_0^2}{1 - z^2/z_\mathrm{TF}^2},$$

which is maximum for $z = 0$ when $Z_0 \leq z_\mathrm{TF}$. In the general case, numerical calculations can be performed using the equation of state. Example of such calculations at unitarity are shown in Figure 3.11 (where the gas is still polytropic) and are consistent with the above analytical results.

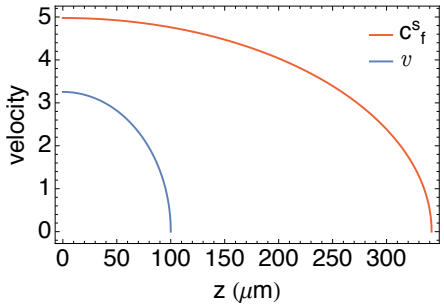

(a) $c_\mathrm{f}^\mathrm{s}(z)$ and $v(z)$ in the Fermi cloud frame

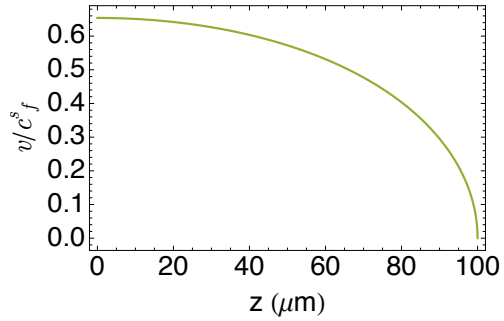

(b) Ratio $v(z)/c_\mathrm{f}^\mathrm{s}(z)$ in the Fermi cloud frame

Figure 3.11: Calculated $c_\mathrm{f}^\mathrm{s}(z)$, $v(z)$ (left) and ratio $v(z)/c_\mathrm{f}^\mathrm{s}(z)$ (right) using the equation of state, for a $Z_0 = 100\,\mu\mathrm{m}$ displacement of the BEC in a Fermi cloud with $N_\mathrm{f} = 300{\cdot}10^3$ atoms at unitarity. The curves obtained for different magnetic fields show similar evolution.

Our measured critical velocity is consistent with Castin *et al.* prediction [Castin *et al.*, 2015], but a χ^2 test on our results does not discriminate between a critical velocity equal to Castin *et al.* prediction and to the sound velocity of the fermions.

3.3.4 Discussion

One may wonder the origin of the anomalously small value for the critical velocity at 780 G. It turns out that inelastic losses increase on the BEC side of a fermionic

Feshbach resonance and heat up the system [Regal *et al.*, 2004a]. This is confirmed by the fact that we were unable to take data at 760 G due to a strong reduction of the lifetime of the mixture. This hypothesis is also supported by the presence of a clearly visible pedestal in the density profiles of the BEC taken at 780 G. At this value of the magnetic field, we measure a $\sim 60\%$ condensed fraction, corresponding to a temperature $T/T_{c,\mathrm{b}} \sim 0.5$. Even though the two clouds are still superfluids as demonstrated by the critical behavior around v_c, the increased temperature could be responsible for the decrease of v_c.

It is actually surprising how high the critical velocity is, especially when comparing to other experiments performed in this direction [Weimer *et al.*, 2015, Miller *et al.*, 2007]. The first point is that the BEC is completely contained in the Fermi superfluid and probes only its central (superfluid) part and not the outer (non-superfluid) wings, in strong opposition with the one of the other reported experiments [Weimer *et al.*, 2015] where the probe was a laser beam piercing the whole cloud, including its non-superfluid parts. In the other reported experiment [Miller *et al.*, 2007], the probe is a $\{20{,}60\}$ µm moving lattice in a cloud with Thomas Fermi radii of $\{63{,}91{,}82\}$ µm. The size of the lattice is thus smaller but comparable to the size of the cloud and it may probe as well its non-superfluid part. Second, the BEC is much smaller than the Fermi cloud (Thomas-Fermi radii of $\{73, 3, 3\}$µm to compare with $\{350, 13, 13\}$µm), so it enables us to probe locally the cloud. Third, the interaction between bosons and fermions is weak, so the presence of the BEC does not causes strong density modifications for the fermions and thus limits vortex shedding. The production of vortices is known to be one of the factors reducing the critical velocity in other experiments [Singh *et al.*, 2015].

3.4 High temperature, moderate amplitude

3.4.1 Experiments

We now study finite-temperature effects in the Bose-Fermi counterflow. To have hotter clouds, we stop the evaporation at a higher optical power[10]. We thus have more atoms, and the radial trap frequencies are different for each temperature, but since they scale as $\sqrt{U}$, where U is the optical power, they can be inferred from the low-power trap frequencies without us having to re-calibrate them. The temperature can be measured using the profile of the Bose gas: either by using the condensed fraction (scaling as $(T/T_{c,\mathrm{b}})^3$), for temperature below the transition temperature for Bose-Einstein condensation, or by fitting the thermal pedestal with a Gaussian function the width of which gives the temperature of the cloud, for temperatures above the transition temperature. A typical measurement for the high-temperature oscillations is shown on Figure 3.12.

We see two remarkable features here: first, the oscillation is damped down to zero amplitude for both clouds, while the fermions has not been visibly affected in the previous experiments. Second the two clouds are locked in phase to a high degree and

[10] We first tried to evaporate at low temperature and then re-compress the cloud, in order to keep the atom number constant, but this proved to cause strong shot-to-shot fluctuations and forced us to use another method.

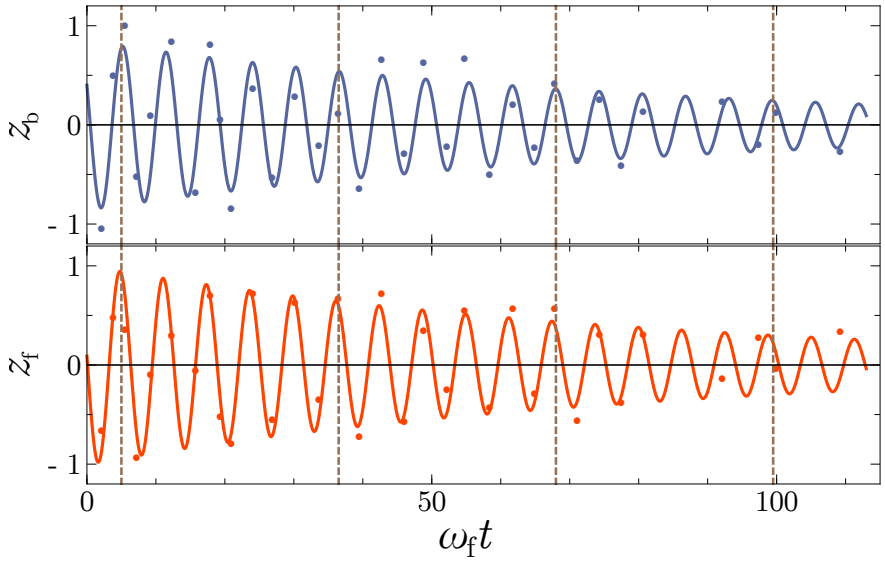

Figure 3.12: Center of mass oscillations at high temperature ($T/T_F = 0.4$) for a moderate initial displacement ($z_0 = 80\,\mu m$). Bosonic and fermionic motions are damped with the same damping constant, and phase-locking is observed. The dashed lines are guides to the eye.

oscillate at almost the same frequency, which turns out to be the frequency of the fermions.

3.4.2 Frequency analysis

Since the data points were taken at non-evenly spaced time positions[11], it is not possible to perform standard Fourier analysis, such as Fast Fourier Transform. Instead, we have used a Lomb-Scargle algorithm (or 'least-square analysis') which measures the periodogram, *ie* the weight of the projection of data points on sines and cosines of fixed frequency.

For N data points $\{h_i = h(t_i)\}_{i=1,\dots,N}$ taken at times $\{t_i\}$, the periodogram is defined as

$$P_N(\omega) = \frac{1}{2\sigma^2}\left\{\frac{[\sum_j (h_j - \bar{h})\cos\omega(t_j-\tau)]^2}{\sum_j \cos^2\omega(t_j-\tau)} + \frac{[\sum_j (h_j - \bar{h})\sin\omega(t_j-\tau)]^2}{\sum_j \sin^2\omega(t_j-\tau)}\right\}$$

[11] The best compromise between the duration of the experimental acquisition and the precision of the frequency measurement was reached by taking several series of points spaced by approximately one quarter of an oscillation period, typically series of 6 points spaced by $\sim 15\,ms$, each series being $\sim 500\,ms$ apart from each other. This way, a first approximation of the period is given by closely spaced points, and it is refined by the existence of points farther separated without having to span precisely the whole $\sim 5\,s$ range.

where τ is given by

$$\tan(2\omega\tau) = \frac{\sum_j \sin 2\omega t_j}{\sum_j \cos 2\omega t_j};$$

its role is to make the periodogram independent of the time origin.

$$\bar{h} = \frac{1}{N}\sum_{i=1}^{N} h_i$$

and

$$\sigma = \frac{1}{N-1}\sum_{i=1}^{N}(h_i - \bar{h})^2$$

are the mean and the variance of $\{h_i\}_i$. The periodogram, or power spectrum, gives access to the statistical significance (*ie* the probability of rejecting the null hypothesis when it is true) of each of the evaluated frequencies. In other words, the significance is the *risk* (between 0 and 1) that the measured frequency does not have a physical meaning but rather is some artifact resulting from the noise. For all of the data presented here, this 'risk' is below 1.5%. Noting

$$P_{\max} = \max_{\omega} P_N(\omega),$$

the significance is proportional to $e^{-P_{\max}}$, and here a value of 10 for the power represents typically a significance of 0.002.

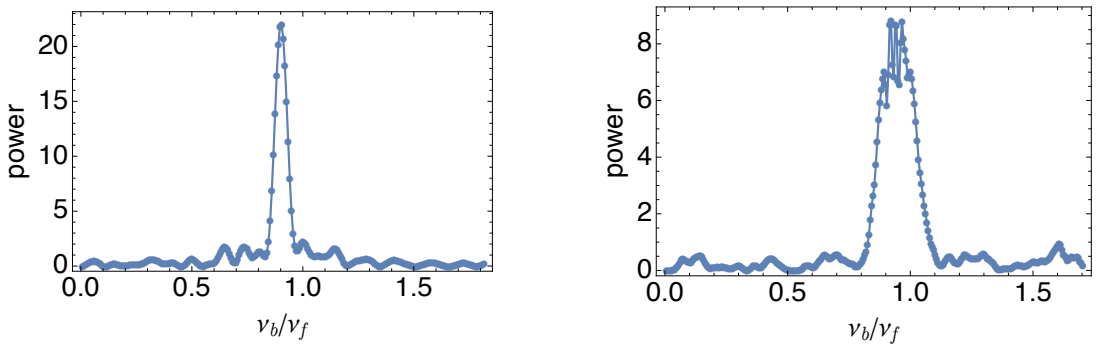

(a) $T/T_F = 0.03(2)$

(b) $T/T_F = 0.32(2)$

Figure 3.13: Lomb Scargle periodogram of the position of the bosons for both a cold (left) sample and a hotter (right) sample. A value of 10 for the powers represents typically a significance of 0.002 (see text).

This analysis applied to our data points is shown on Figure 3.13 for both a cold and a hot sample. It shows a clear peak for a value of $\omega_b/\omega_f \approx \sqrt{6/7}$ at low temperature, as expected, but the peak is shifted toward 1 at higher temperatures. We can gather all of the periodograms obtained at different temperatures, and the result is displayed on Figure 3.14. We can see that up to a temperature $T \approx 0.34\ T_F$, corresponding to $T \approx T_{c,b}$, the bosons oscillate at a frequency $\omega_b \approx \sqrt{6/7}\ \omega_f$ that one expects for such a mixture at low temperature, but that above that temperature, bosons are locked on

the fermions. It is remarkable that the shift in frequency happens close to the critical temperature for the bosons, while the superfluidity of the fermions was long gone.

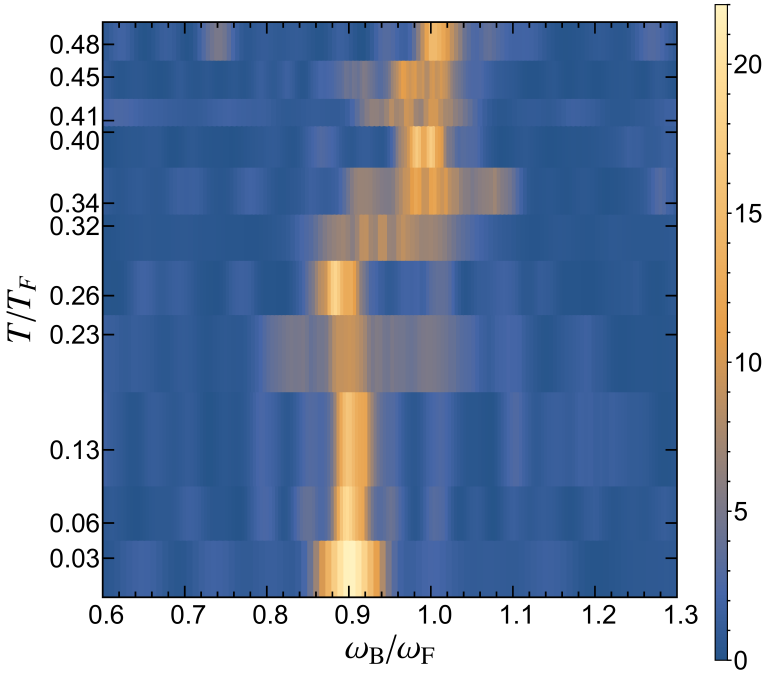

Figure 3.14: Power spectrum of the oscillations for different temperatures, obtained using the Lomb-Scargle algorithm of the center-of-mass displacement. Above $T \approx T_{c,B} \approx 0.34\,T_F > T_{c,F}$, oscillations of the Bose and Fermi clouds become locked together at ω_F.

It is possible to provide error bars for the determined frequencies, for instance by measuring the upper and the lower bounds for which the statistical significance is 10 times larger than that of the central frequency. This corresponds to a 10% uncertainty on ω_b. This is shown on Figure 3.15.

3.4.3 Damping

For each temperature, we can extract the damping rate γ_b. Using the functions defined in equations (3.13) and (3.12), with as before

$$d(t) = d_1 + d_2 e^{-\gamma_{b,f} t}, \tag{3.16}$$

for clouds at temperatures $T < 0.34\,T_F$, and

$$z_b(t) = d_0 e^{-\gamma_b t} \cos(\omega_f t)$$
$$z_f(t) = d_0 e^{-\gamma_f t} \cos(\omega_f t)$$

for clouds at temperatures $T > 0.34\,T_F$ because the oscillations are then damped to zero amplitude, and fixing the frequencies to those extracted from the Lomb-Scargle

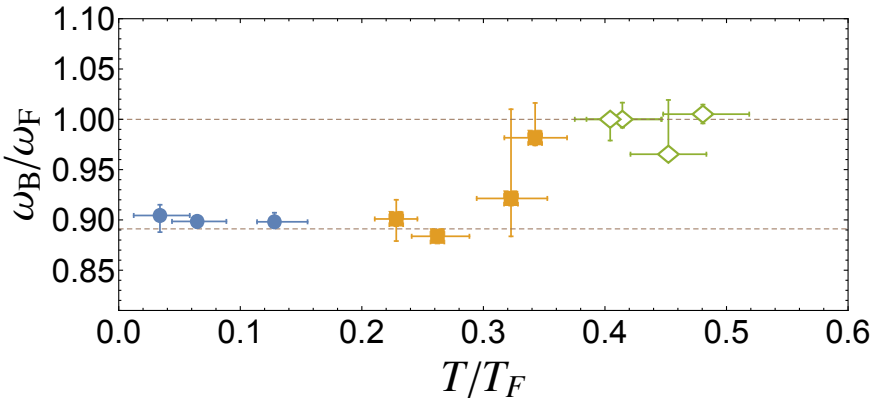

Figure 3.15: Ratio ω_b/ω_f as a function of T/T_F. The bottom dashed line indicates the prediction from the mean-field model of section 3.2. The top dashed line corresponds to $\omega_b/\omega_f = 1$. The blue dots correspond to situations where both the Fermi and the Bose clouds are superfluids, the yellow squares to a situation where the bosons are still superfluids but not the fermions, and for the green open diamonds, both clouds are in the normal phase.

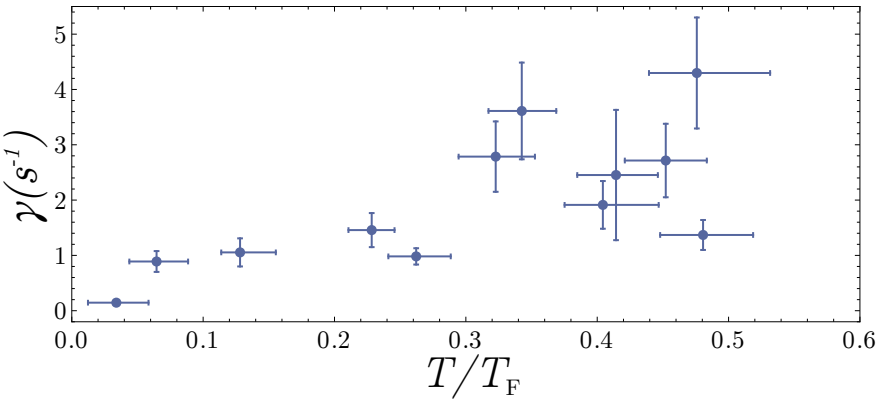

Figure 3.16: Damping rate of the oscillations of the bosons as a function of temperature in units of Fermi temperature. Horizontal error bars are mainly statistical and refer to uncertainties on temperature, and vertical error bars are fit uncertainties. This figure is preliminary because we have no evidence that γ is only a function of T_F and not of atom numbers or densities, that were not kept constant for this dataset.

algoritm (see subsection 3.4.2), we can obtain the evolution of the damping rate as a function of temperature, as shown on Figure 3.16.

The fact that the damping rate reaches a maximum at the temperature at which the phase-locking of the two clouds occurs is consistent with results from a two coupled oscillator model that will be discussed below.

From $T = 0$ to $0.34\,T_F$, damping increases as T/T_F increases: the fact that the clouds have a relative velocity and some friction leads to an increase of damping up to $T = 0.34\,T_F$. Above this temperature, friction is so high that both clouds oscillate at the same frequency and are (almost) perfectly in phase ($(\omega_f - \omega_b)/\omega_b \approx 0.2\%$). This

leads to a reduction of damping at higher temperatures.

3.4.4 Two coupled-oscillator model

We can re-use the model of coupled oscillators introduced in subsection 3.2.4 and extend it to the case where there is friction between the two clouds. We introduce a friction parameter Γ, and the motion equations now are

$$M_\mathrm{f}\ddot{z}_\mathrm{f} = -K_\mathrm{f} z_\mathrm{f} - K_\mathrm{bf}(z_\mathrm{f} - z_\mathrm{b}) - \Gamma(\dot{z}_\mathrm{f} - \dot{z}_\mathrm{b})$$
$$M_\mathrm{b}\ddot{z}_\mathrm{b} = -K_\mathrm{b} z_\mathrm{b} - K_\mathrm{bf}(z_\mathrm{b} - z_\mathrm{f}) - \Gamma(\dot{z}_\mathrm{b} - \dot{z}_\mathrm{f}).$$

These equations can be solved analytically. For different values of Γ, we fit the evolution of z_b using equations (3.13) with $d(t)$ as in equation (3.16), and extract the values of ω_b and γ_b. They are represented on figure Figure 3.17.

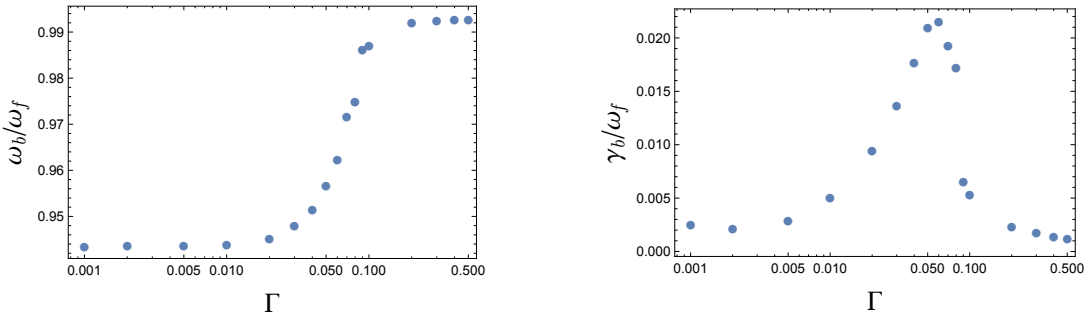

(a) (b)

Figure 3.17: Evolution of ω_b (a) and γ_b (b) as a function of Γ, the friction parameter, for a ratio $M_\mathrm{f}/M_\mathrm{b} = 10$. Phase locking accurs when $\Gamma \gtrsim \Gamma_0 = 0.06$, which corresponds to a maximum of dissipation between the clouds. Above Γ_0, the damping is reduced because the clouds stay in phase.

Assuming that friction is increased when increasing the temperature, the results from the damped coupled-oscillator model are in qualitative agreement with our data, where we had indeed noticed the presence of a maximum in damping. Note that since the number of atoms was not kept constant within the datasets, nor the ratio between bosons and fermions, this would require more data to be fully exploited. It is also very difficult to infer the value of Γ from the theory, and this prevents further comparison with the experiment.

3.4.5 Zeno-like model

The classical coupled oscillator model given above can be completed by a quantum phenomenological description using a Zeno-like model. Let us now consider that the bosons and the fermions are two coupled quantum harmonic oscillators. If we neglect the interspecies interaction and consider that all of the particles have the same mass m, the system is described by the Hamiltonian:

$$H = H_\mathrm{f} + H_\mathrm{b},$$

where $H_{\alpha=\mathrm{f,b}}$ is defined as:

$$H_\alpha = \frac{P_\alpha^2}{2M_\alpha} + \frac{M_\alpha \omega^2 Z_\alpha^2}{2} + H_{\alpha\mathrm{int}},$$

with P_α the total momentum of the cloud, Z_α the position of its center of mass and $M_\alpha = N_\alpha m$ its total mass. $H_{\alpha\mathrm{int}}$ affects only the internal variable and commutes with Z_α and P_α. The oscillations of the fermions and that of the bosons are then associated to two quantum numbers n_f and n_b, coupled to thermal baths described by ϕ_f and ϕ_b. We can thus describe the state of the system as $|n_\mathrm{f},n_\mathrm{b},\phi\rangle$, where $\phi = \{\phi_\mathrm{f},\phi_\mathrm{b}\}$.

Alternatively, we can make a change of variable, and use

$$\begin{aligned} P &= P_\mathrm{f} + P_\mathrm{b}, \\ Z &= (M_\mathrm{f} Z_\mathrm{f} + M_\mathrm{b} Z_\mathrm{b})/M, \\ p &= \mu(P_\mathrm{f}/M_\mathrm{f} - P_\mathrm{b}/M_\mathrm{b}), \\ z &= Z_\mathrm{f} - Z_\mathrm{b}, \\ M &= M_\mathrm{f} + M_\mathrm{b}, \\ M_r &= M_\mathrm{f} M_\mathrm{b}/M. \end{aligned}$$

With these new variables, the Hamiltonian of the system now reads

$$H = \frac{P^2}{2M} + \frac{M\omega^2 Z^2}{2} + \frac{p^2}{2M_r} + \frac{M_r \omega^2 z^2}{2} + H_\mathrm{f}^\mathrm{int} + H_\mathrm{b}^\mathrm{int},$$

and the motion can now be described by two new quantum numbers, N and n, where N represents the number of quanta of the *global* center of mass motion (bosons and fermions), and n the number of quanta of the relative motion. The state of the system is now described by $|N,n,\varphi\rangle$. The initial state, where both clouds are displaced and released together in the trap, corresponds to $|N_0,n=0,\varphi\rangle$. If both atomic species had the same mass, and without interactions, the clouds would remain in-phase, and stay in the $|N,n=0,\varphi\rangle$ state.

Let us now add the interspecies interactions. They are described by the Hamiltonian

$$H_\mathrm{b,f} = \sum_{i\leq N_\mathrm{f}, j\leq N_\mathrm{b}} U(z_{\mathrm{f},i} - z_{\mathrm{b},j}),$$

where $z_{\alpha,i}$ is the z-position of the i-th particle of species α. This Hamiltonian commutes with P and Z and therefore only couples to the relative variables z and p. It induces a coupling between the relative motion and the thermal bath.

Let us switch back off the interactions and consider the mass difference between the two species. If the species α has a mass $m_\alpha = m + \epsilon_\alpha \delta m/2$, with $\epsilon_\mathrm{f} = -1$ and $\epsilon_\mathrm{b} = +1$, its add to the Hamiltonian a kinetic energy term

$$\delta H_K = -\frac{\delta m}{2m} \sum_{i,\alpha} \epsilon_\alpha \frac{p_{i,\alpha}^2}{2m},$$

where the center-of-mass contribution can be isolated and that can be re-written as

$$\delta H_K = -\frac{\delta m}{2m}\left(\frac{P_\mathrm{b}^2}{2M_\mathrm{b}} - \frac{P_\mathrm{f}^2}{2M_\mathrm{b}}\right) + \delta H_K^\mathrm{int},$$

where δH_K^{int} commutes with P and Z. This term δH_K thus induces a coupling between the global degrees of freedom P and Z to the relative degrees of freedom p and z. In other words, it couples the initial state $|N_0,n=0,\varphi\rangle$ to $|N_0-1,1,\varphi\rangle$, then to $|N_0-i,i,\varphi\rangle$, where $0 \leq i \leq N_0$, and create relative center-of-mass displacement from the global center-of-mass displacement. Without interactions, there is no coupling to the bath, and the system may oscillate back and forth between the $|N_0,n=0,\varphi\rangle$ and the $|0,n=N_0,\varphi\rangle$ state 'forever'.

We can now re-write the full Hamiltonian of the system, including interactions and mass difference:

$$H = H_{\text{CoM}} + H_{\text{rel}} + H'_{\text{int}} + H_{\text{b,f}} + H_{\text{coh}},$$

with

$$\begin{aligned}
H_{\text{CoM}} &= \frac{P^2}{2M}\left(1-\rho\frac{\delta m}{m}\right) + \frac{M\omega^2}{2}Z^2,\\
H_{\text{rel}} &= \frac{p^2}{2M_r}\left(1+\rho\frac{\delta m}{m}\right) + \frac{M_r\omega^2}{2}z^2,\\
H'^{\text{int}} &= H_{\text{f}}^{\text{int}} + H_{\text{b}}^{\text{int}} + \delta H_K^{\text{int}},\\
H_{\text{coh}} &= \frac{\delta m}{m}\left(\frac{P\cdot p}{M}\right),
\end{aligned}$$

and $\rho = (M_{\text{b}} - M_{\text{f}})/M$. The H_{coh} term couples the global and the relative degrees of freedom, and $H_{\text{b,f}}$ couples the relative motion to the internal degrees of freedom of the two clouds, *i.e.* to the bath.

In summary, we know that Kohn's theorem forbids direct coupling between the (global) center of mass degrees of freedom and the thermal bath. But is does not prevent coupling between the relative motion and the bath, and though a $|N_0,0,\varphi\rangle$ state cannot be directly coupled to a $|N_0-1,0,\varphi'\rangle$ state, this transition is possible through a $|N_0-1,1,\varphi\rangle$ state. This description is summarized in Figure 3.18, where the degrees of freedom for the bath (described by φ) are omitted for simplicity. We note Ω the coupling between the global and the relative center of mass motion, and γ the coupling between the relative motion and the bath.

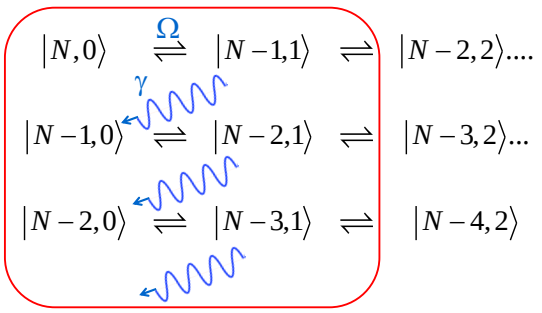

Figure 3.18: Radiative cascade of the center of mass motion. In $|N,n\rangle$, N (resp. n) refers to the center of mass (resp. relative) motion of the two clouds (see text).

If $\gamma \ll \Omega$, the system stays in the upper line of Figure 3.18 and there is only weak coupling to the bath. However, if $\gamma \gg \Omega$, as soon as the $|N_0-1,1,\varphi\rangle$ state is populated,

it decays into the $|N_0 - 1,0,\varphi'\rangle$ state, so that the relative motion is frozen ($n \equiv 0$) and the oscillations are damped ($N \to 0$). Here, $\Omega = \omega_\mathrm{f} - \omega_\mathrm{b}$, but γ may depend on temperature (but is hard to calculate in such a complex system), and this is then consistent with our observations. At high temperature, we can eliminate adiabatically the excited states of the relative motion, similarly to optical pumping in quantum optics, and the system evolves in the $|N,0,\varphi\rangle$ manifold.

This model provides a quantum interpretation of the origin of friction between the two clouds. It can be mapped on a Caldeira-Leggett [Caldeira and Leggett, 1983] used to study how dissipation arises for a quantum system interacting with a bath, except that for our system the bandwidth for the frequency distribution of the bath is narrow, while it is large and continuous for the Caldeira-Leggett model [Onofrio and Sundaram, 2015]. The phenomenon observed here are reminiscent to the synchronization of two spins immersed in a thermal bath predicted in [Orth *et al.*, 2010, Henriet and Hur, 2015] and may simulate decoherence in quantum networks [Chou *et al.*, 2008] or heat transport in crystals [Zürcher and Talkner, 1990].

3.4.6 At the origin of the frequency shift

A complementary analysis of the motion of the two clouds can be made by considering in the analysis that the BEC and its thermal fraction oscillate separately during of the oscillations. We can fit the data of the high temperature oscillations allowing two different values for the center-of-mass of the BEC z_BEC and for that of the thermal fraction z_thermal. Obviously, the determination of z_thermal at low temperature is challenging because the thermal pedestal is very small, while that of z_BEC is not defined above $T_{c,\mathrm{b}}$. For intermediate temperatures, however, we can perform the spectral analysis of z_BEC and z_thermal separately with the periodogram. They are displayed in Figure 3.19 for different temperatures. Results are striking: while the BEC oscillates at $\tilde{\omega}_\mathrm{b}$, the thermal fraction oscillates at ω_f. When the temperature is increased, the BEC reduces and the thermal fraction increases, and the weight of their respective frequencies on the global oscillation of the bosonic cloud varies accordingly. This explains the shift of bosonic oscillation frequency from $\tilde{\omega}_\mathrm{b}$ to ω_f when increasing the temperature. The observation of out of phase oscillations of the thermal cloud and the BEC can be compared to second sound experiments presented in [Andrews *et al.*, 1997a, Stamper-Kurn *et al.*, 1998], where a partly condensed cloud was oscillating in a harmonic trap. They set in motion only the thermal cloud, that dragged the oscillations of the condensate with damped out-of-phase oscillations at a frequency $\sim 5\%$ smaller than the trap frequency. Here, in the presence of fermions, the out-of-phase oscillation seems to be long-lived, at a frequency fixed by the trapping frequencies of the system.

However, what we do not understand so far is why the oscillation frequency of the bosonic thermal fraction is ω_f: for the fermions, the thermal cloud is a non-superfluid moving impurity and the critical velocity should be c_f^s. For the data presented here, the initial amplitude was 50 µm for an oscillation frequency of 18 Hz. The maximum relative velocity between the clouds is then $v_\mathrm{max} = 11\,\mathrm{mm.s^{-1}}$, while $c_\mathrm{f}^\mathrm{s} = 17\,\mathrm{mm.s^{-1}}$ in our experimental conditions. As a result, there should be no friction between the superfluid Fermi cloud and the thermal fraction and it is surprising that the thermal fraction oscillates at ω_f even below $T_{c,\mathrm{f}} = 0.2\,T_\mathrm{F}$ (as in Figure 3.19b). It also has to be

taken into account the fact that the superfluid fraction of the Fermi gas also shrinks towards the center of the trap, and that the thermal fraction of the Bose gas, spatially extended, is likely to explore the non-superfluid part of the Fermi gas. Further studies could be performed on this subject, for instance using the finite temperature equation-of-state of the Fermi gas from [Nascimbène *et al.*, 2010] to know the spatial location of the Fermi superfluid.

3.5 Advanced data analysis: PCA

It is also possible to use a more sophisticated analysis technique to analyze the data of the dipole modes. This provides a second analysis technique to confirm the previous study. It has the advantage of being fully model-independent. The analysis technique used here is based on Principal Component Analysis (PCA)[12] and has been used and described in a very pedagogical way in [Dubessy *et al.*, 2014]. PCA is a well-known image analysis technique used in various fields. It enables us to study correlations between a set of images and works in the following way:

- The studied system is a set of images (2D images as in [Dubessy *et al.*, 2014], or 1D profiles, as it will be the case here).
- The average image (AI) of the dataset is computed and subtracted from all of the images. We then obtain a new ensemble of images.
- Then the covariance matrix of this new ensemble is computed and diagonalized. The eigenstates represent the *directions* along which there is variation from the average image AI, and their associated eigenvalues the relative weight of these variations. These eigenstates, called Principal Components (PCs), represent typically variations in position, atom number, shape of the cloud, etc. Any kind of variation may show up in the PCs, provided that it concerns enough images and that its variation from the mean is noticeable.

In other words, the PCA consists in a change of basis for the description of the images. Instead of describing an image *via* its decomposition on the basis of the pixels $\{(1\,0\ldots0),(0\,1\,0\ldots0)\ldots(0\ldots0\,1)\}$, we look for another basis $\{AI, PC_1, PC_2, \ldots PC_{n-1}\}$ that would give an accurate description of all of the images of the dataset using a minimum number of vectors from the basis, and any image of the dataset ID can be projected on the principal components:

$$ID = c_0 AI + \sum_{i=1}^{n-1} c_i PC_i,$$

with $c_0 \geq c_1 \geq c_2 \geq c_3 \geq \cdots \geq c_{n-1}$. In practical, the first PCs are sufficient to describe each image quite accurately, with typically $\frac{|c_i|^2}{\sum_{i=0}^{n-1}|c_i|^2} < 1\%$ for $i \geq 5$. It is actually a very powerful way to increase the signal-to-noise ratio of a dataset: since most of the physical information is contained in only the first PCs, all of the following

[12] I would like to thank Romain Dubessy who took the time to come to the ENS to explain me the subtleties of the PCA.

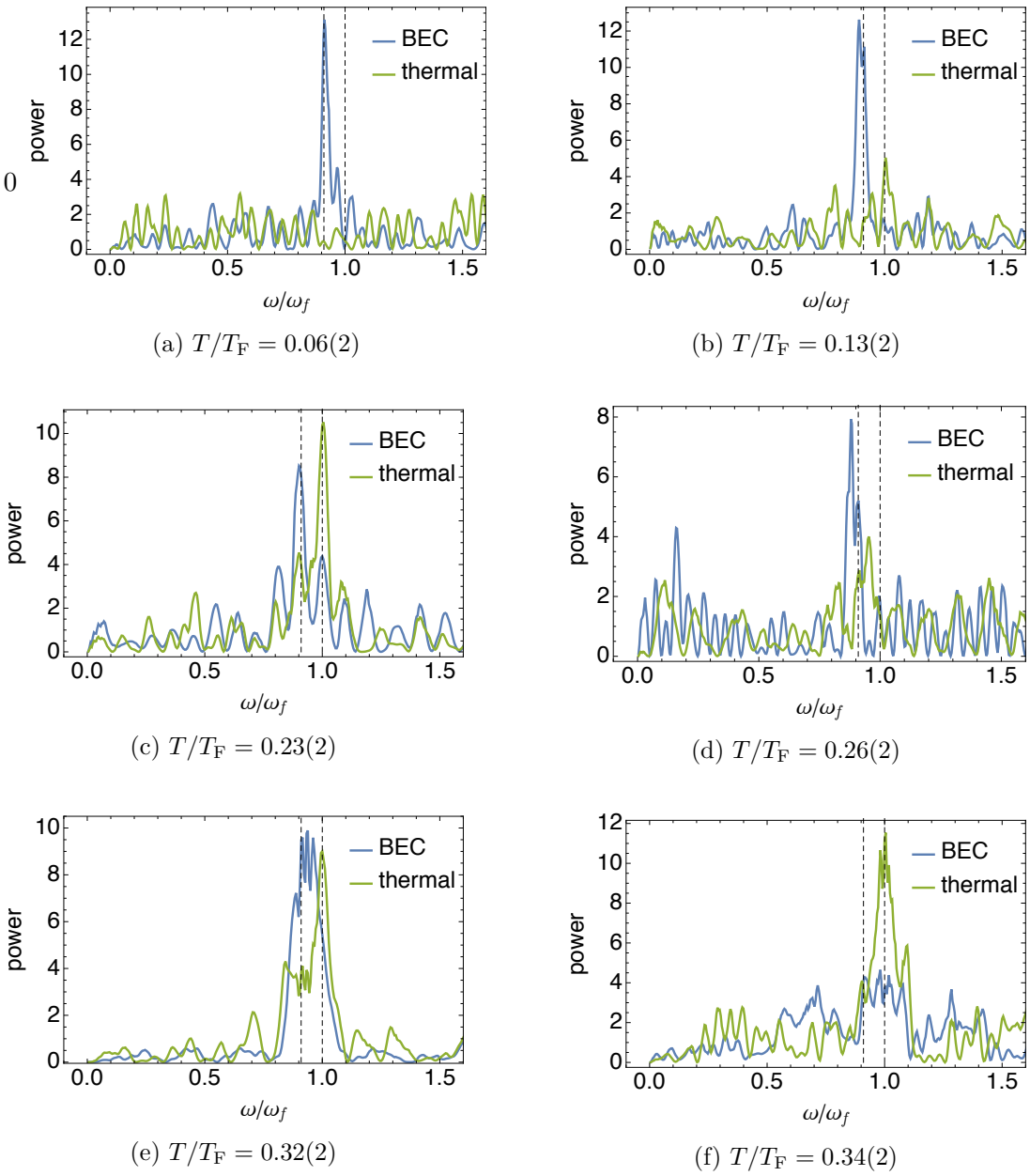

(a) $T/T_F = 0.06(2)$

(b) $T/T_F = 0.13(2)$

(c) $T/T_F = 0.23(2)$

(d) $T/T_F = 0.26(2)$

(e) $T/T_F = 0.32(2)$

(f) $T/T_F = 0.34(2)$

Figure 3.19: Spectral analysis of the oscillations of the BEC (blue) and of the thermal fraction (green) for different temperatures. Vertical dashed lines correspond to $\omega/\omega_f = \sqrt{6/7}$ and to $\omega/\omega_f = 1$. It is clear that the oscillation of the thermal fraction occurs at ω_f while that of the BEC occurs at ω_b. For low temperatures, the thermal fraction is very small and it is hard to determine accurately its position, while for high temperatures the BEC is almost gone and it is also hard to locate it accurately, which explains the low resolution of the frequency determination in those cases.

PCs represent mainly noise, and it is possible to reconstruct a less noisy image ID' by

projecting on the truncated basis [Desbuquois, 2013]:

$$ID' = c_0 AI + \sum_{i=1}^{5} c_i PC_i.$$

The first PCs given by the algorithm for an oscillating BEC in a harmonic trap are shown on Figure 3.20. The average image AI is shown on Figure 3.20a. As expected, we identify the first PC (Figure 3.20b) as describing the center-of-mass oscillation of the BEC. If the cloud were at rest, the second PC (Figure 3.20c) would represent compression and dilatation of the cloud. Here, however, it is a reminiscence of the center-of-mass oscillation: since the center-of-mass oscillation was strongly excited, its contribution to the second PC[13] is dominant over the compression and dilatation excitation, only weakly excited. The third PC (Figure 3.20d) represents atom number fluctuations: its shape is similar to the shape of the cloud. The fourth PC (Figure 3.20e) is another reminiscence of the center-of-mass oscillation.

Since the PCA algorithm is very fast, it can be used for an efficient analysis of the dipole mode. Once the Principal Component associated to the dipole-mode excitation is identified, each profile can be projected onto this component, and the scalar product between the PC and the profile tells '*how much the cloud is on the right or on the left*' for all times. We can then perform some spectral analysis (using for example the Lomb-Scargle algorithm) to obtain the oscillation frequency. For the dipole mode with the first PC, this method is very precise (see for instance Figure 3.21).

We can use this method to calculate again the shift of the bosonic frequency due to the presence of fermions as in section 3.2. The calculated shift is given in Figure 3.22, very similar to Figure 3.5. For this study, the bare oscillation frequency of the bosons was inferred from the oscillation frequency of the fermions in the mixture, $\omega_\mathrm{b} = \sqrt{6/7}\,\omega_\mathrm{f}$ instead of being obtained from interleaved measurements of bosons alone oscillations, as it was the case for data of Figure 3.5.

It is tempting to apply the same procedure to the second PC to study compression. However, as it can be demonstrated from numerical simulation, the second PC reflects both the compression of the cloud and the oscillations of the center-of-mass. Since here the most excited mode is the dipole mode, its contribution dominates the quadrupole-like Principal Component and, consistently, the spectral analysis of this component mainly shows contributions at $2\tilde{\omega}_\mathrm{f}$ and $2\tilde{\omega}_\mathrm{b}$.

[13] Indeed, since the density of the cloud is $n(x - a(t))$, when we do a Taylor expansion for a small center-of-mass oscillation this leads:

$$\begin{aligned} n(x - a(t)) = n(x) \\ - a(t)n'(x) \\ + \frac{a^2(t)}{2} n''(x) \\ - \dots . \end{aligned}$$

For a harmonic oscillation, $a(t) = a_0 \cos(\omega t)$, and the term $+\frac{a^2(t)}{2} n''(x)$ have indeed the second PC shape and oscillates at 2ω.

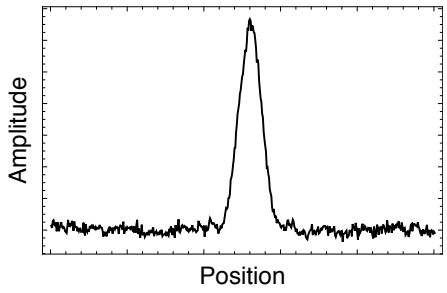

(a) Average Image (AI)

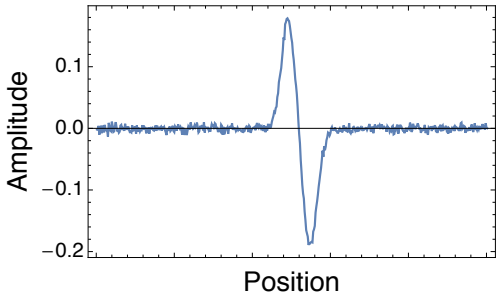

(b) First PC

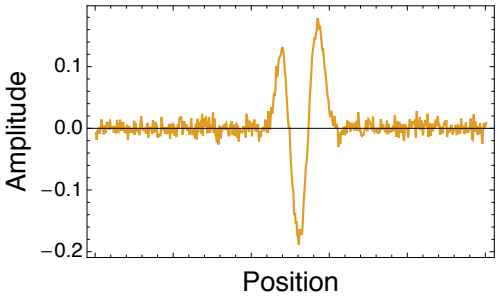

(c) Second PC

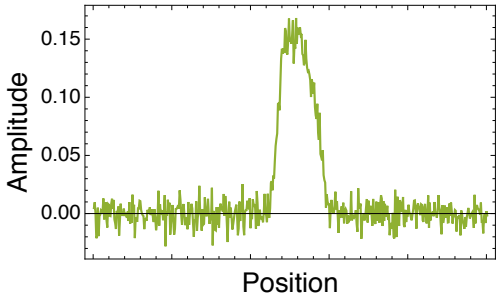

(d) Third PC

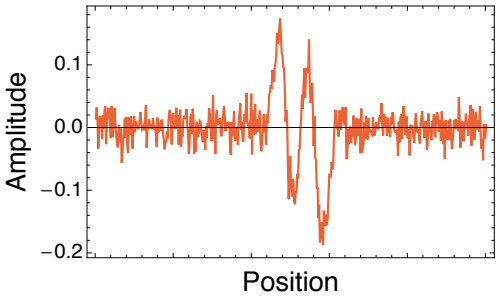

(e) Fourth PC

Figure 3.20: Average (a) and four first Principal Components (b)-(e) given by the Principal Component Analysis applied to a set of 85 images of an oscillating BEC. First PC corresponds to center-of-mass oscillation. Second PC is a combination between compression modes and the second-order signature of the center-of-mass oscillation. Third PC is related to atom number fluctuations and fourth PC is a third order signature of the center-of-mass oscillation.

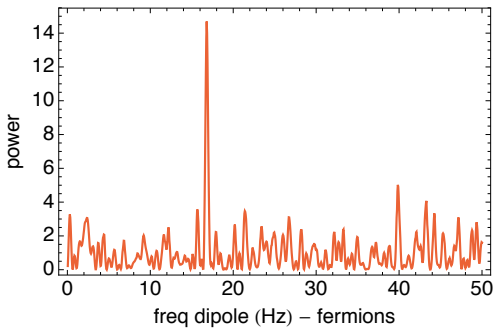

(a) Lomb Scargle periodogram for the fermions.

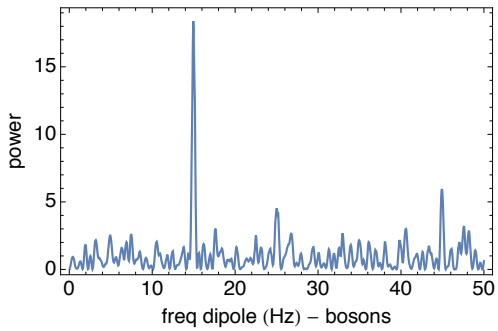

(b) Lomb Scargle periodogram for the bosons.

Figure 3.21: Lomb-Scargle periodogram of the projection of each profile on the Principal Component showing the dipole mode. Here, $\omega_{\mathrm{f}} = 2\pi \cdot 16.80(5)\mathrm{rad.s}^{-1}$ and $\omega_{\mathrm{b}} = 2\pi \cdot 14.95(5)\mathrm{rad.s}^{-1}$. Since this is a statistical analysis, the uncertainties are directly related to the total number of images in the dataset. Here, we had 35 images.

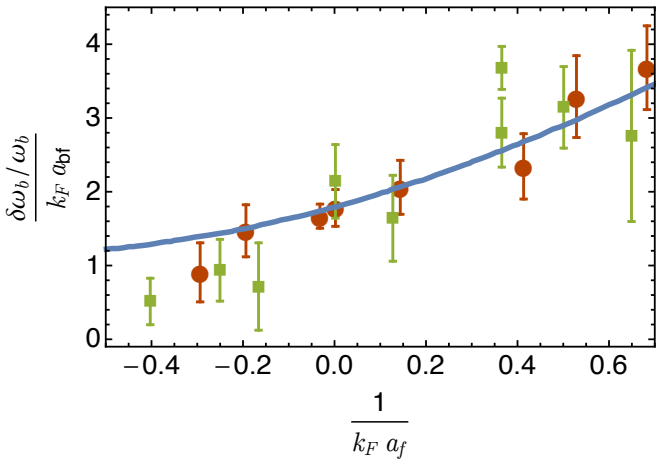

Figure 3.22: Green squares: shift of the bosonic frequency due to the presence of the fermions, calculated using the PCA and Lomb-Scargle algorithm. Red dots: data of Figure 3.5, extracted with the standard method. Blue line: theory, as in Figure 3.5.

3.6 Quadrupole modes

We wanted to see whether it was possible to extract information about the compression modes of the mixture using the dataset taken to study critical velocity. Even though it was not possible to use the PCA here for the reasons mentioned above, we could extract the Thomas-Fermi radius of each of the profiles, for different times, and perform a spectral analysis on them.

It was checked (see [Ferrier-Barbut, 2014]) that the Thomas-Fermi radius had less than 10% fluctuations and that they were mainly due to atom number fluctuations. However, it is possible to use the Lomb algorithm to get the spectral distribution of the time evolution of these radii. For the bosons, a frequency does not always ap-

pear in the spectrum and it seems that any periodic variation of the width of the cloud is smeared out by atom number fluctuations and it is not possible the compare breathing or higher-order modes to their expected behavior [Guéry-Odelin *et al.*, 1999, Guéry-Odelin and Stringari, 1999, Guéry-Odelin and Trizac, 2015]. However, for the fermions, there is a much clearer signal (see Figure 3.23a), and it is possible to extract the frequency of the axial quadrupole mode ω_f^Q and to draw the ratio ω_f^Q/ω_f as a function of $1/k_F a_{ff}$ in the BEC-BCS crossover, displayed in Figure 3.23b. They are compared to the hydrodynamic prediction in elongated harmonic traps: $\omega_f^Q = \sqrt{(3\gamma+2)/(\gamma+1)}\,\omega_f$ [Vichi and Stringari, 1999, Astrakharchik *et al.*, 2005, Combescot *et al.*, 2006, Amoruso *et al.*, 1999, Hu *et al.*, 2004], where γ is the polytropic exponent of the equation of state[14]. This leads to $\omega_f^Q/\omega_f = \sqrt{5/2} \approx 1.581$ on the BEC side and $\omega_f^Q/\omega_f = \sqrt{12/5} \approx 1.549$ at unitarity and on the BCS side. This has been measured in the BEC-BCS crossover [Bartenstein *et al.*, 2004a, Altmeyer *et al.*, 2007]. These values are indicated as dashed lines in Figure 3.23b.

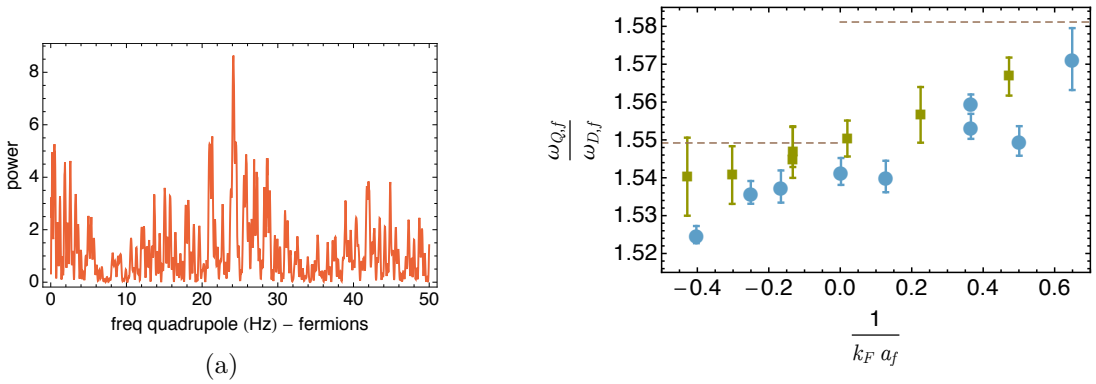

(a) (b)

Figure 3.23: (a) Lomb-Scargle periodogram of the time evolution of the Thomas-Fermi radius of the fermions. There is a clear peak at 24.11 Hz. (b) Evolution of the ratio ω_f^Q/ω_f as a function of $1/k_F a_{ff}$ in the BEC-BCS crossover. The dashed lines are the predictions for the molecular BEC ($1/k_F a_{ff} \gg 1$): $\omega_f^Q/\omega_f = \sqrt{5/2} \approx 1.581$ and at unitarity and on the BCS side ($1/k_F a_{ff} = 0$ and $1/k_F a_{ff} \ll -1$): $\omega_f^Q/\omega_f = \sqrt{12/5} \approx 1.549$. Green squares: measurements of quadrupole frequency for fermions alone, taken from [Bartenstein *et al.*, 2004a]. Blue circles: measurements of quadrupole frequency of the fermions in the presence of bosons, with the method explained above.

The values reported here are in good agreement with previous measurements from the Innsbruck group. They appear slightly downshifted but compatible with the combined error bars. This could be an effect of the presence of bosons in the trap but further studies would be needed on this subject.

[14] $\gamma = 1$ for the molecular BEC and $\gamma = 2/3$ in the unitary limit and on the BCS side [Stringari, 2007, Bartenstein *et al.*, 2004b].

3.7 Conclusion

We have studied the Bose-Fermi counterflow in various regimes of parameters, at low and high temperature and in the BEC-BCS crossover. The low temperature study below the critical velocity showed that one could measure precisely equilibrium quantities (the equation of state) using collective excitations. With respect to measuring the critical velocity, the use of the BEC as a local probe within the Fermi cloud allows for more sensitive measurements compared to earlier cases, which were subject to averaging effects over the trap inhomogeneities [Miller *et al.*, 2007, Weimer *et al.*, 2015]. Finally, the phase-locking of the oscillations at higher temperatures arises from the dissipation between the two clouds. What is remarkable here is that the phase locking does not result from high dissipation: the friction coefficient is still low compared to the individual oscillation frequencies, but is comparable to the frequency difference. Several questions remain open: so far, we have no full explanation for the high critical velocity that we measure, even though several reasons have been suggested. On another subject, it has been predicted that each component of the mixture conserves its inherent first sound while only a single second sound should exist, common to the whole superfluid mixture [Volovik *et al.*, 1975]. It would be very nice to perform experiments in this direction.

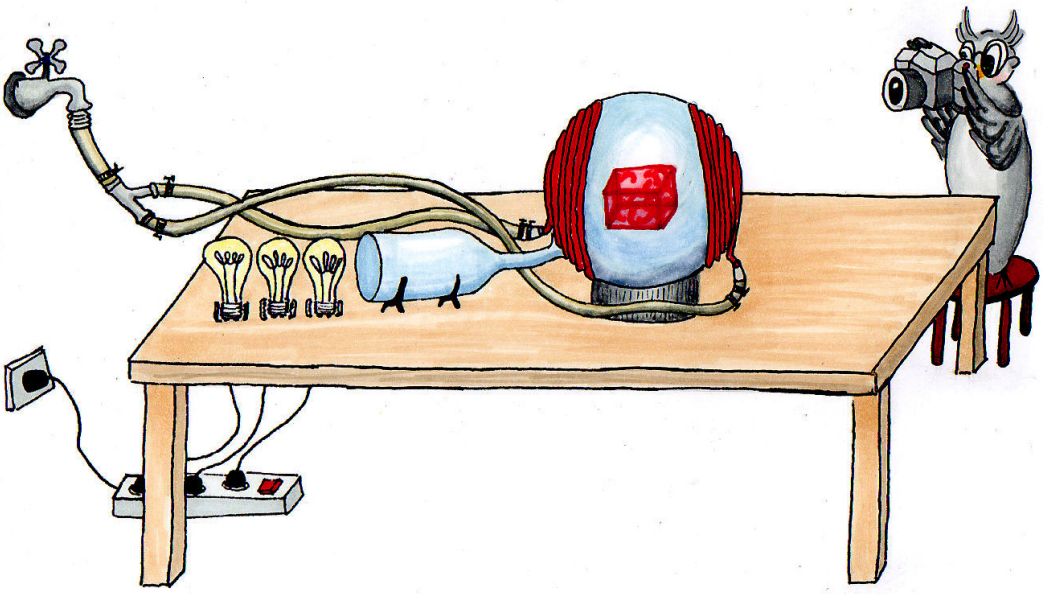

Chapter 4

Spin-imbalanced gases and flat bottom trap

In the previous chapter we studied the robustness of the Fermi superfluid against a counter propagating "obstacle". While in the latter investigation we challenged the Fermi superfluid by using the BEC as a dynamical perturbation, we now explore another pathway to compete with the fermionic superfluidity, in equilibrium. To this end we tune the relative spin population of the fermionic component, while the Bose

superfluid now serves as potential shaper. The effect of spin imbalance in Fermi gases has been long-studied both experimentally and theoretically. In fact, this topic is still a subject of debate and covers a scope which extends to solid state condensed-matter. In particular, this question is formally tightly connected to the one of superconductors in the presence of an external magnetic field. There, the practical difficulty rises from the fact that Meissner effect expels magnetic field from a superconductor (so for a type I superconductor, the value of the magnetic field is strictly zero within the material while for a type II superconductor, a magnetic field may exist, but it is then constrained into filaments which are in the normal state). Superconducting regions and regions with a non-zero magnetic field do not intersect, and there is no Cooper pairs in non-zero magnetic field regions. However, in ultracold atoms, it is sufficient to prepare a different number of atoms in two long-lived spin states, labeled $\uparrow$ and $\downarrow$. As the spin population $n_{\uparrow,\downarrow}$ is tied to a chemical potential $\mu_{\uparrow,\downarrow}$, the energy cost for adding or removing a fermion is different for a spin $\uparrow$ with respect to a spin $\downarrow$. The difference $\Delta\mu = \mu_\uparrow - \mu_\downarrow$, therefore obviously plays the role of magnetic field. The Fermi gas is then called *spin-imbalanced* and singlet pairing is frustrated since it requires equal numbers of up and down particles. The question now is: how robust is superfluidity with respect to this imbalance? It has been addressed theoretically very soon after the development of the BCS theory, by Clogston [Clogston, 1962] and Chandrasekhar [Chandrasekhar, 1962]. In the condensed matter context, the question regarded the maximum magnetic field that could be imposed on a superconductor without breaking superconductivity. Indeed, such a magnetic field imposes a population imbalance between the two spin states involved in BCS theory. It was demonstrated that the pairing that resulted in superconductivity was indeed stable against a finite population imbalance caused by the magnetic field, but the value of this critical imbalance was only known in the BCS limit and is exponentially small as the BCS gap. Aside from the BCS limit, both the value of this population imbalance and what happened to the gas above this imbalance was unknown. As a result, when ultracold superfluid Fermi gases were first realized in 2003 [Jochim *et al.*, 2003, Zwierlein *et al.*, 2003, Greiner *et al.*, 2003, Bourdel *et al.*, 2004], this issue was soon investigated, both at MIT [Zwierlein *et al.*, 2006a, Zwierlein *et al.*, 2006b, Shin *et al.*, 2006, Shin *et al.*, 2008, Shin, 2008] and at Rice University [Partridge *et al.*, 2006a, Partridge *et al.*, 2006b]. There were some discrepancies between these two experiments that could be solved afterwards, but they paved the way towards a better understanding of imbalanced Fermi gases. Another very important (and still unanswered) question is whether other types of pairing are conceivable. Several possibilities have been put forward, such as the long-sought Fulde–Ferrell–Larkin–Ovchinnikov (FFLO) phases, where there is pairing between particles with momenta of different amplitudes, resulting in a Cooper pair with non-zero momentum $\mathbf{q}$. This leads to a spatially modulated order parameter with wavevector $\mathbf{q}$. One of the main issues with the observation of FFLO phases is that they are predicted to appear only in a narrow range of parameter space, see Figure 0.1, and that ultracold Fermi gases are usually prepared in harmonic traps. This implies that the favorable conditions for FFLO could be reached only for a small fraction of the atoms and that any visible effect would be smeared out by neighboring regions of the cloud. Other possibilities, also predicted to appear in a narrow range of parameters, include gapless superfluid state [Liu and Wilczek, 2003] or a state with a

deformed Fermi surface [Müther and Sedrakian, 2002]. The use of a uniform trap (a 'box') would allow to zoom in for a small window of parameters.

During my PhD, we developed an idea to create a locally uniform trap for the Fermi gas using the repulsive interaction with the bosons. This chapter will be dedicated to the description of imbalanced gases and to the realization of the flat bottom trap. In a first section, I will give known results about superfluidity in imbalanced Fermi gases and explain how we used them to give another proof of the superfluidity of the ultracold Bose-Fermi mixture. Then, in a second section, I will detail a way to imprint a flat bottom trap (FBT) on the Fermi gas, and discuss its consequences in terms of critical polarization in a third section. Finally, in a fourth section, I will detail the realization of such a FBT in our experiment and give preliminary results.

4.1 Superfluidity in imbalanced Fermi gases

Firstly, let us restrict ourselves to the case of a two-component Fermi gas. The two components studied here are two of the Zeeman sub-levels of the same atom and have in particular the same mass. We will first describe the gas in a box, that is a gas which density is spatially uniform, and then expand the results to a gas in a harmonic trap which is more realistic experimentally.

4.1.1 Fermions in a box

In the case of an imbalanced Fermi gas in a box, the system will phase-separate into a fully paired superfluid phase, a normal phase and, possibly, in a very narrow range of parameters, in a FFLO phase, see Figure 0.1. They can be described by atomic densities n_s for the density of the superfluid, $n_\uparrow$ for that of the majority component in the normal phase, and $n_\downarrow$ for that of the minority component in the normal phase. The two phases have different densities and the ratio $n_\downarrow/n_\uparrow$ in the normal phase is fixed by equilibrium conditions.

Let us first consider the superfluid phase (labeled by s). In a superfluid fermions are paired into Cooper pairs (for weakly attractive systems) or molecules (in the strongly attractive regime). For all interaction strengths, the densities of both species in the superfluid phase are thus equal and will be noted n_s. On the BCS limit, the chemical potential of the gas is known: $\mu = \varepsilon_\mathrm{F}$, where ε_F is the Fermi energy of a uniform non-interacting Fermi gas: $\varepsilon_\mathrm{F} = \frac{\hbar^2}{2m_\mathrm{f}}(6\pi^2 n_\mathrm{s})^{2/3}$. On the BEC limit, it is known as well and is simply the mean-field interaction of the composite molecules shifted by the molecule binding energy: $\mu = -\frac{\hbar^2}{2m_\mathrm{f}a_\mathrm{ff}^2} + \frac{\pi\hbar^2 a_\mathrm{ff} n_\mathrm{s}}{m_\mathrm{f}}$. At unitarity, the scattering length diverges, so the only remaining energy scale in the system is the Fermi energy ε_F and the length scale is the inter-particle distance $n^{-1/3}$. As a result, the energy of a superfluid Fermi gas at unitarity has to be proportional to the energy of a noninteracting Fermi gas $\frac{3}{5}\varepsilon_\mathrm{F}$ [Heiselberg, 2001], with proportionality factor the Bertsch parameter $\xi = 0.38(1)$ [Ku *et al.*, 2012, Zürn *et al.*, 2013, Zwerger, 2012, Navon *et al.*, 2010]. The energy density e_s of the superfluid at unitarity can thus be written as:

$$e_\mathrm{s}[n_\mathrm{s}] \equiv \xi\frac{6}{5}\frac{\hbar^2}{2m_f}(6\pi^2 n_\mathrm{s})^{2/3} n_\mathrm{s} = \xi\frac{6}{5}\varepsilon_\mathrm{F} n_\mathrm{s}, \tag{4.1}$$

the factor 2 being due to the *two* components.

Regarding the normal phase, it is relevant to use the notion of fermionic polaron, introduced in [Chevy, 2006, Lobo *et al.*, 2006]. The polaron is a quasi-particle of effective mass m^* composed of a one atom of the minority component ($\downarrow$) accompanied by its interaction with the majority component ($\uparrow$). If only $\uparrow$ atoms were present, the energy density of the system would be the one of a noninteracting Fermi gas: $e_{\mathrm{n}}[n_\uparrow, n_\downarrow = 0] \equiv \frac{3}{5}\varepsilon_{\mathrm{F}\uparrow} n_\uparrow$, with $\varepsilon_{\mathrm{F}\uparrow} = \frac{\hbar^2}{2m_{\mathrm{f}}}(6\pi^2 n_\uparrow)^{2/3}$. Now, if we add some $\downarrow$ atoms, and note their binding energy E_{bind} with the Fermi gas of $\uparrow$ particles, we have $E_{\mathrm{bind}} = -3/5\varepsilon_{\mathrm{F}\uparrow}A$. Finally, with $\varepsilon^*_{\mathrm{F}\downarrow} = \frac{\hbar^2}{2m^*}(6\pi^2 n_\downarrow)^{2/3}$ the Fermi energy of the polaron of mass m^*, if several quasi-particles are present, they will have an energy density $\frac{3}{5}\varepsilon^*_{\mathrm{F}\downarrow} n_\downarrow = \frac{3}{5}\varepsilon_{\mathrm{F}\uparrow} n_\uparrow \frac{m_f}{m^*} x^{5/3}$. We can then write the energy density e_{n} of the normal phase as [Lobo *et al.*, 2006]:

$$e_{\mathrm{n}}[n_\uparrow, n_\downarrow] \equiv \frac{3}{5}\varepsilon_{\mathrm{F}\uparrow} n_\uparrow \left(1 - \frac{5}{3}Ax + \frac{m_f}{m^*}x^{5/3}\right), \tag{4.2}$$

where $x = n_\downarrow/n_\uparrow$ is the ratio between the densities of the minority and majority components. The description of the system in terms of majority atoms with non-interacting polarons is only valid for low $\downarrow$ densities with respect to $\uparrow$ densities. This implies $x \ll 1$. At higher x, the effect of interactions between quasi-particles also have to be taken into account [Pilati and Giorgini, 2008, Recati *et al.*, 2008], this is done by adding an extra term Fx^2 in the above equation ((4.2)):

$$\begin{aligned} e_{\mathrm{n}}[n_\uparrow, n_\downarrow] &\equiv \frac{3}{5}\varepsilon_{\mathrm{F}\uparrow} n_\uparrow \left(1 - \frac{5}{3}Ax + \frac{m_f}{m^*}x^{5/3} + Fx^2\right) \\ &\equiv \frac{3}{5}\varepsilon_{\mathrm{F}\uparrow} n_\uparrow \epsilon(x). \end{aligned} \tag{4.3}$$

The values of ξ, A, m_{f}/m^* and $F = (5/9)A^2$ have been measured [Navon *et al.*, 2010] and calculated [Prokof'ev and Svistunov, 2008, Combescot and Giraud, 2008, Mora and Chevy, 2010] at unitarity: $\xi = 0.38$, $A = 0.615$ and $m^*/m_{\mathrm{f}} = 1.20$. Though the above functions are strictly valid only at unitarity, we used them also around unitarity for specific values of $1/k_{\mathrm{F}}a_{\mathrm{ff}}$, using approximate values given in Table 4.1.

$1/k_{\mathrm{F}}a_{\mathrm{ff}}$	0	0.2	-0.25
B (G)	832.2	817	854
F	0.21	0.25	0.15
$\frac{5}{3}A$	1.025	1.118	0.866
ξ	0.37	0.22	0.54
m^*/m_{f}	1.20	1.30	1.12

Table 4.1: Summary of the values used to study the imbalanced mixture, extracted from [Navon *et al.*, 2010, Mora and Chevy, 2010]

Starting with a normal phase with $x = 0$, adding $\downarrow$ atoms will increase x and for $x = x_c$ there will be a first-order phase transition between a pure normal phase and a system with phase separated superfluid and normal states. At unitarity, matching

the pressures and the chemical potentials at the interface leads to $x_c = 0.4$ [Recati *et al.*, 2008, Lobo *et al.*, 2006]. This varies in the BEC-BCS crossover [Shin *et al.*, 2006, Navon *et al.*, 2010]: on the BEC side, pairing is very robust, and $x_c \to 1$, while it decreases on the BCS side. The limit above which superfluidity is destroyed by a too large imbalance between the two species is called the *Clogston Chandrasekhar limit*. In the condensed matter context where the imbalance was caused by a magnetic field, it was convenient to use, instead of the density ratio, the local polarization, defined as

$$p = \frac{n_\uparrow - n_\downarrow}{n_\uparrow + n_\downarrow},$$

which is also widely used in the cold atom community. The polarization p can be expressed as a function of the density ratio x, $p = \frac{1-x}{1+x}$, and the Clogston Chandrasekhar critical ratio $x_c = 0.4$ at unitarity corresponds to a critical local polarization $p_c = 43\%$.

4.1.2 Fermions in a harmonic trap

Uniform systems are easier to handle theoretically, but the ultracold Fermi gases realized experimentally are usually trapped by harmonic potentials, either optical or magnetic[1]. One can re-apply the results obtained above for a uniform system to the case of a harmonic trap using the local density approximation, or LDA. It is an approximation that states that a cloud trapped by a potential $V(\mathbf{r})$ can be seen as locally homogeneous at position $\mathbf{r}$ with a chemical potential $\mu - V(\mathbf{r})$. This approximation is valid only if the trapping potential varies slowly enough so that the cloud can follow its variations. Its violation in some experiments due to sharp boundaries [Partridge *et al.*, 2006a, Partridge *et al.*, 2006b, De Silva and Mueller, 2006b, Baur *et al.*, 2009] leads to the study of surface tension effects. In a harmonic trap, the local densities vary, hence the local polarization p and density ratio x vary as well. As a result, instead of the local quantities x and p, we rather use the total polarization P, that involves the total numbers of atoms of each species $N_\downarrow$ and $N_\uparrow$ in the trap:

$$P = \frac{N_\uparrow - N_\downarrow}{N_\uparrow + N_\downarrow}.$$

Applying the results of subsection 4.1.1 to a harmonic trap implies that the phase separation found in the homogeneous system translates into a layered structure in a trap. If the polarization is small, the cloud will separate in three concentric parts (see Figure 4.1a):

- A fully paired superfluid core: in the center of the cloud, there is a superfluid, that can be characterized by the presence of vortices [Zwierlein *et al.*, 2006a]. It implies the equality of the local atomic densities: $n_\uparrow = n_\downarrow$.
- A partially polarized non-superfluid phase, where $n_\uparrow > n_\downarrow$
- A fully polarized phase, where $n_\downarrow = 0$, and the $\uparrow$ atoms obey the ideal Fermi gas laws.

[1] Box potentials are becoming more and more popular [Gaunt *et al.*, 2013, Corman *et al.*, 2014].

When the polarization increases, the central superfluid part shrinks, and when it is too high (above 76% for a unitary Fermi gas [Nascimbène *et al.*, 2009, Zwierlein *et al.*, 2006a, Shin *et al.*, 2006]), there is no more superfluid part, the central part of the cloud is partially polarized and is surrounded by a fully polarized phase (see Figure 4.1b). Note the density jump in the minority density at the boundary of the superfluid, corresponding exactly to x_c from the homogeneous case. In this whole chapter, the calculations were made in the isotropic case and at unitarity for a gas with the same mean trapping frequency $\bar{\omega} = \omega_z^{1/3}\omega_r^{2/3}$. Adapting them to our cigar-shaped experiment thus requires a re-scaling of the length scales. For all the theory curves, results will be plotted in terms of the averaged oscillator length $\bar{l}_{\mathrm{ho}} = \sqrt{\hbar/m\bar{\omega}}$, while the experimental data that will be shown below will be given in units of axial harmonic oscillator length $l^z_{\mathrm{ho}} = \sqrt{\hbar/m\omega_z}$. For our experimental values of ω_z and ω_r, $\bar{l}_{\mathrm{ho}} = 3.6\,\mu\mathrm{m}$ and $l^z_{\mathrm{ho}} = 9.8\,\mu\mathrm{m}$.

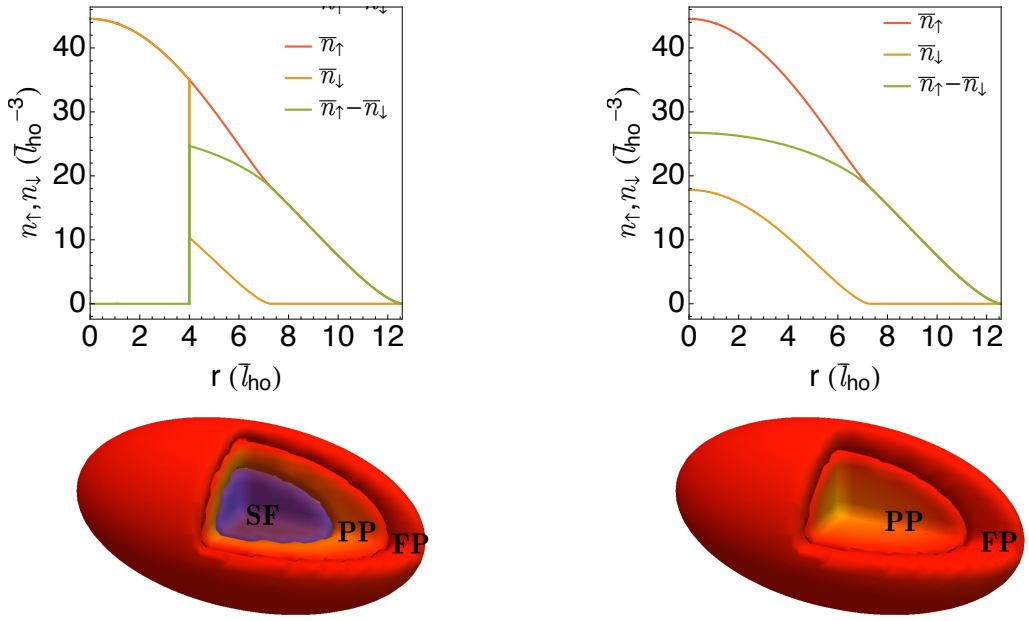

(a) Below the critical polarization, a superfluid lies in the center of the cloud.

(b) Above the critical polarization, there is no superfluid any more.

Figure 4.1: Calculated density profiles (top) and schematic representation (bottom) of an imbalanced Fermi gas in a spherical harmonic trap. Red (resp. yellow) curves represent the density of the majority $\uparrow$ (resp. minority $\downarrow$) component, and the green curve represents the density difference $n_\uparrow - n_\downarrow$. In purple is the superfluid (SF) phase where $n_\uparrow = n_\downarrow$, in faded yellow-to-red is the partially polarized (PP) phase with $n_\uparrow > n_\downarrow$, and in red is the fully polarized (FP) phase where $n_\downarrow = 0$.

4.1.3 Application: another evidence of superfluidity in the Bose-Fermi mixture

The superfluid is associated to pairing, which implies a local equality between ↑ and ↓ densities: $n_\uparrow = n_\downarrow$. Experimentally, we only have access to doubly integrated densities $\bar{n}(z)$, but it can be shown that $\frac{d\bar{n}(z)}{z\,dz} = -2\pi\frac{\omega_z^2}{\omega_\rho^2}n(z)$, provided the potential has ellipsoidal symmetry and verifies some weak local density approximation: it requires that iso-potential lines correspond to iso-density lines. This hypothesis resembles the LDA hypothesis but is weaker. The relation creates a direct link between $n(z)$ and $\bar{n}(z)$. The ellipsoidal symmetry implies that $n(x,y,z)$ is actually a function of $r = \frac{\sqrt{\omega_x^2x^2+\omega_y^2y^2+\omega_z^2z^2}}{\bar{\omega}}$, and, with ω_ρ defined as $\omega_\rho = \omega_x^{1/2}\omega_y^{1/2}$ and ρ as $\omega_\rho^2\rho^2 = \omega_x x^2 + \omega_y y^2$,

$$\bar{n}(z) = \int dx\,dy\,n\left(r = \frac{\sqrt{\omega_x^2x^2+\omega_y^2y^2+\omega_z^2z^2}}{\bar{\omega}}\right) \qquad (\bar{\omega} = \omega_x^{1/3}\omega_y^{1/3}\omega_z^{1/3})$$

$$\bar{n}(z) = \pi\frac{\bar{\omega}^2}{\omega_\rho^2}\int ds\,n(s) \qquad (s = \tfrac{\omega_\rho^2}{\bar{\omega}^2}\rho^2 + \tfrac{\omega_z^2}{\bar{\omega}^2}z^2,\ ds = 2\tfrac{\omega_\rho^2}{\bar{\omega}^2}\rho\,d\rho + 2\tfrac{\omega_z^2}{\bar{\omega}^2}z\,dz)$$

$$\frac{d\bar{n}(z)}{ds} = -\pi\frac{\bar{\omega}^2}{\omega_\rho^2}n(s)$$
$$\frac{d\bar{n}(z)}{z\,dz} = -2\pi\frac{\omega_z^2}{\omega_\rho^2}n(z),$$

where the $\frac{\omega_z^2}{\omega_\rho^2}$ term accounts for the fact that the potential is not spherical but ellipsoidal.

As a result, if we consider the density difference, $n_\uparrow - n_\downarrow = 0$ implies $\frac{d(\bar{n}_\uparrow-\bar{n}_\downarrow)}{dz}(z) = 0$, *i.e.* there is a plateau in the density difference, hereafter called the *superfluid plateau*. We use this result to provide another evidence of the superfluidity of the Bose-Fermi mixture. We prepared a BEC with an imbalanced Fermi superfluid at unitarity, and image both clouds with the simultaneous triple imaging technique explained in subsection 2.6.2. While the peak of the Bose-Einstein Condensation was clearly visible, the density difference of the two fermionic spin states showed a plateau, indicating superfluidity for both species (see Figure 4.2).

In this section, we have shown that an imbalanced Fermi gas phase separates into a superfluid and a normal phase. In a harmonic trap, this results in a cloud with concentric layers, the inner one being superfluid if the polarization is low enough. Although these results were obtained at unitarity, they can be extended in the BEC-BCS crossover, and we successfully used them to provide another evidence of the superfluidity of the Bose-Fermi mixture that we produced. Indeed, we observe a fully paired Fermi gas at the center of the trap. If this itself is not a definitive proof of superfluidity, it was shown with the observation of vortices in [Zwierlein *et al.*, 2006a] that fully paired regions in spin-imbalanced Fermi gases were superfluid.

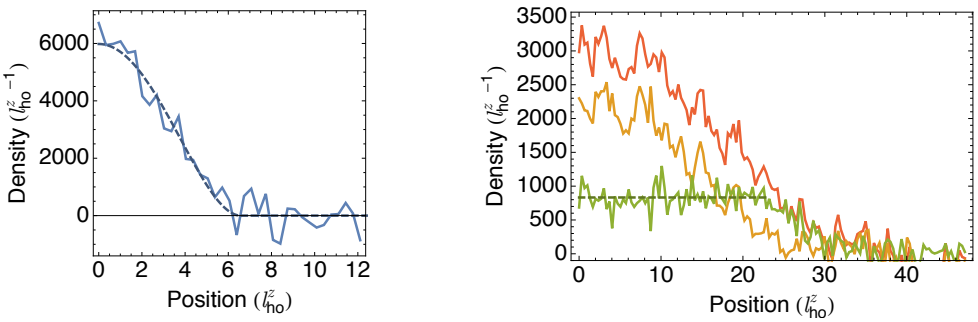

Figure 4.2: Doubly integrated density profiles of bosons and fermions resulting from triple simultaneous imaging described in subsection 2.6.2. In blue are the bosons, in red the majority ↑ component of the fermions, in yellow the minority ↓ component and in green their density difference. Bosons are imaged axially, fermions radially. Thomas-Fermi fit of the bosonic profile is shown in dashed blue line. The superfluid plateau in the density difference is indicated with a dark green dashed line. It implies the local equality $n_\uparrow = n_\downarrow$ and is associated to pairing and superfluidity. Here, $N_\mathrm{f} = 180 \cdot 10^3$, $N_\mathrm{b} = 38 \cdot 10^3$, and $P = 24\%$ at 817 G.

In the next sections, we will discuss how we can use the BEC to create an effective flat bottom trap (FBT) for the fermions, then discuss the effect of that specific trap on the Clogston-Chandrasekhar limits of the Fermi gas.

4.2 Realization of a flat bottom trap

In the limit of low atom number for bosons, we have shown in chapter 3 that there were no drastic change in the Fermi cloud's behavior due to the presence of bosons and that for instance the dipole mode frequency of the fermions was barely modified when $N_\mathrm{b} \ll N_\mathrm{f}$ and that the superfluidity of the Fermi cloud was not deeply affected by the presence of bosons. On the other hand, we have seen that even for high bosonic atom number, the Fermi cloud could still show concentric layers of phases with different polarization, see Figure 4.2. However, fermions and bosons do have a (weak) repulsive interaction that induces an energy shift of $g_\mathrm{bf} n_\mathrm{f}$ (for the bosons) and $g_\mathrm{bf} n_\mathrm{b}$ (for the fermions). Since the density of the Bose gas is much higher than that of the Fermi gas, we will focus of the effective trapping potential felt by the fermions (the effective trapping potential for the bosons is barely modified) [Mølmer, 1998, Amoruso *et al.*, 1998].

4.2.1 Prediction

Let us consider a mixture of a Bose-Einstein condensate and a two components (noted again ↑ and ↓) Fermi gas, in the vicinity of a Feshbach resonance for the Fermi gas. Here, both gases are confined by a harmonic trap with the same potential $V(r) =$

$1/2m_\alpha\omega_\alpha^2 r^2$, where α = b or f for bosons or fermions, respectively[2]. If we assume mean-field Bose-Bose and Bose-Fermi interactions, using the LDA, the local energy density $\mathcal{E}$ can be written as:

$$\mathcal{E} = \frac{g_{\mathrm{bb}}}{2} n_{\mathrm{b}}^2 + g_{\mathrm{bf}} n_{\mathrm{b}} (n_\uparrow + n_\downarrow) + e[n_\uparrow, n_\downarrow],$$

where $g_{\mathrm{bb}} = 4\pi\hbar^2 a_{\mathrm{bb}}/m_{\mathrm{b}}$ and $g_{\mathrm{bf}} = 2\pi\hbar^2 a_{\mathrm{bf}}(1/m_{\mathrm{b}} + 1/m_{\mathrm{f}})$ (within Born approximation [Zhang *et al.*, 2014]) are the coupling constants for Bose-Bose and Bose-Fermi interactions, respectively, and we assume that the Bose-Fermi scattering length is the same for both Fermi gas components. $e[n_\uparrow, n_\downarrow]$ refers to the Fermi-Fermi interaction. It is a complicated function in the general case, but is known at unitarity for a balanced ($n_\uparrow = n_\downarrow = n_{\mathrm{f}}/2$) superfluid Fermi gas, as defined in equation (4.1). For a spin-polarized Fermi gas at unitarity, the interaction energy is given by [Chevy, 2006, Lobo *et al.*, 2006] equation (4.3), and this can be extended in the BEC-BCS crossover from the equation of state with appropriate coefficients (given in Table 4.1).

It is now possible to obtain the chemical potentials as:

$$\mu_{\sigma=\uparrow,\downarrow} = w_\sigma[n_\uparrow, n_\downarrow] + g_{\mathrm{bf}} n_{\mathrm{b}} + V(r) \tag{4.4}$$

$$\mu_{\mathrm{b}} = g_{\mathrm{bb}} n_{\mathrm{b}} + g_{\mathrm{bf}}(n_\uparrow + n_\downarrow) + V(r), \tag{4.5}$$

where $w_\sigma[n_\uparrow, n_\downarrow] = \frac{\partial e[n_\uparrow, n_\downarrow]}{\partial n_\sigma}$ is the pressure equation of state of the fermions. At unitarity for a spin-balanced Fermi gas, $w_\sigma = \xi\varepsilon_{\mathrm{F}\sigma}$.

If we now replace n_{b} in equation (4.4) by its value from equation (4.5), we get:

$$\begin{aligned} \mu_\sigma &= w_\sigma[n_\uparrow, n_\downarrow] + \frac{g_{\mathrm{bf}}^2}{g_{\mathrm{bb}}}(n_\uparrow + n_\downarrow) + V(r)\left(1 - \frac{g_{\mathrm{bf}}}{g_{\mathrm{bb}}}\right) + \frac{g_{\mathrm{bf}}}{g_{\mathrm{bb}}}\mu_{\mathrm{b}} \\ \mu_{\mathrm{b}} &= g_{\mathrm{bb}} n_{\mathrm{b}} + g_{\mathrm{bf}}(n_\uparrow + n_\downarrow) + V(r). \end{aligned} \tag{4.6}$$

With equation (4.6), we see that for $g_{\mathrm{bf}} = g_{\mathrm{bb}}$, $n_\uparrow$ and $n_\downarrow$ do not depend on r any more: the repulsive interaction with the bosons compensates exactly the harmonic confining potential and the density of fermions is uniform anywhere where the bosons are present. The influence of $g_{\mathrm{bf}}/g_{\mathrm{bb}}$ is shown on Figure 4.3.

We see that at the condition $g_{\mathrm{bb}} = g_{\mathrm{bf}}$, the potential felt by the fermions is flat close to the center of the trap. This means that the 3D effective potential for the fermions is actually a flat bottom trap (FBT), composed of an ellipsoidal region where the potential is uniform, surrounded by a truncated harmonic potential. The center of the trap is an ellipsoidal 'box'.

4.2.2 Experimental conditions

The question now is how to realize the condition $g_{\mathrm{bf}} = g_{\mathrm{bb}}$. We want the BEC to be stable, which requires $a_{\mathrm{bb}} > 0$, and the possibility for the Fermi gas to be superfluid, which requires to be close to a Feshbach resonance for the Fermi cloud.

[2] In reality, the trap is not isotropic but is rather cigar-shaped with an aspect ratio of ~ 20. However, it does not matter here because in first approximation the two clouds feel the same potential, both radially and axially.

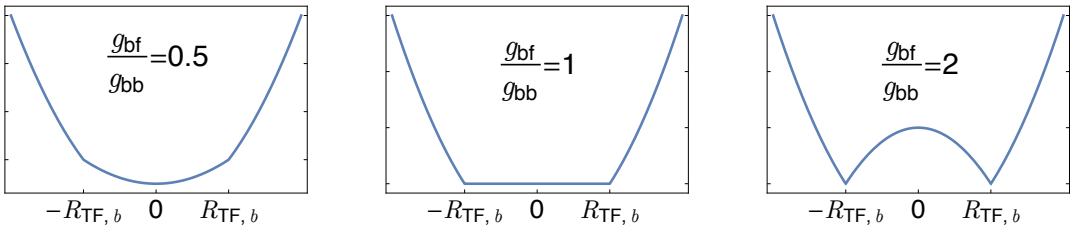

(a) $g_{\mathrm{bf}}/g_{\mathrm{bb}} = 0.5$, the fermions still feel some harmonic trapping potential, but its frequency is smaller than in the bare trap.

(b) $g_{\mathrm{bf}}/g_{\mathrm{bb}} = 1$, the fermions experience a flat potential in the whole volume occupied by the bosons and should be uniform.

(c) $g_{\mathrm{bf}}/g_{\mathrm{bb}} = 2$, the fermions are anti-trapped close to the center of the trap, we expect a peak fermion density close to $r = R_{\mathrm{TF,b}}$.

Figure 4.3: Shape of the potential felt by the fermions for different values of $g_{\mathrm{bf}}/g_{\mathrm{bb}}$.

4.2.2.1 Conditions for the magnetic field

In our system, the bosons are ^{7}Li, the fermions are ^{6}Li in two different spin states. The Bose-Fermi interaction is fixed with a scattering length of $a_{\mathrm{bf}} = 40.8\,a_0$, constant for a large range of magnetic fields, and equal for all Bose and Fermi spin-states combinations considered here. However, ^{7}Li has a number of Feshbach resonances (see Table 2.2), and both for $|1_{\mathrm{b}}\rangle$ and $|2_{\mathrm{b}}\rangle$ states it is possible to find a magnetic field where $a_{\mathrm{bb}} = 44.2\,a_0$, that is where $g_{\mathrm{bf}} = g_{\mathrm{bb}}$. However, to be close to a Feshbach resonance for ^{6}Li, it is favorable to use $|2_{\mathrm{b}}\rangle$ and a $|1_{\mathrm{f}}\rangle - |2_{\mathrm{f}}\rangle$ mixture. Then, one can choose between two different magnetic fields to achieve the condition $g_{\mathrm{bf}} = g_{\mathrm{bb}}$: $B = 816.8\,\mathrm{G}$ and $B = 854.2\,\mathrm{G}$, these two possibilities being around the broad Feshbach resonance for ^{6}Li (at $B = 832.2\,\mathrm{G}$). They are shown on Figure 4.4 as purple dots. Thus, it will then be possible to have either a BEC superfluid (with our experimental conditions, for a magnetic field of $B = 816.8\,\mathrm{G}$, this corresponds to $k_{\mathrm{F}}a_{\mathrm{ff}} = 5$ *i.e.* $1/k_{\mathrm{F}}a_{\mathrm{ff}} = 0.2$) or a BCS superfluid (for a magnetic field of $B = 854.2\,\mathrm{G}$, this corresponds to $k_{\mathrm{F}}a_{\mathrm{ff}} = -4$ *i.e.* $1/k_{\mathrm{F}}a_{\mathrm{ff}} = -0.25$) in a flat potential. This makes this combination an exciting playground to study the physics of Fermi superfluid in a flat trap.

4.2.2.2 Robustness of the flat trap

It is an important question to know the sensitivity of the flat bottom trap with respect to magnetic field variations: it is impossible experimentally to be exactly at the magnetic field where $g_{\mathrm{bf}} = g_{\mathrm{bb}}$. Typically in our experiment we may have $\lesssim 0.1\,\mathrm{G}$ day-to-day fluctuations. To quantify their effect, we compare the residual anti-trapping energy Δ defined on Figure 4.5 to the chemical potential of the fermions μ_{f} in the case of a balanced gas. The results are shown on Figure 4.6, for two different ranges of magnetic field. One can see that, on a $0.3\,\mathrm{G}$ interval around the target chemical potential, Δ/μ_{f} varies by less than 0.5%, to be compared for instance with gap energy at unitarity of $0.4\,\varepsilon_{\mathrm{F}}$, or with critical temperature for superfluidity of $0.2\,T_{\mathrm{F}}$. A residual trapping or anti-trapping energy on the order of $0.5\,\%$ of μ_{f} thus seems small enough to say that the flat potential conditions are verified.

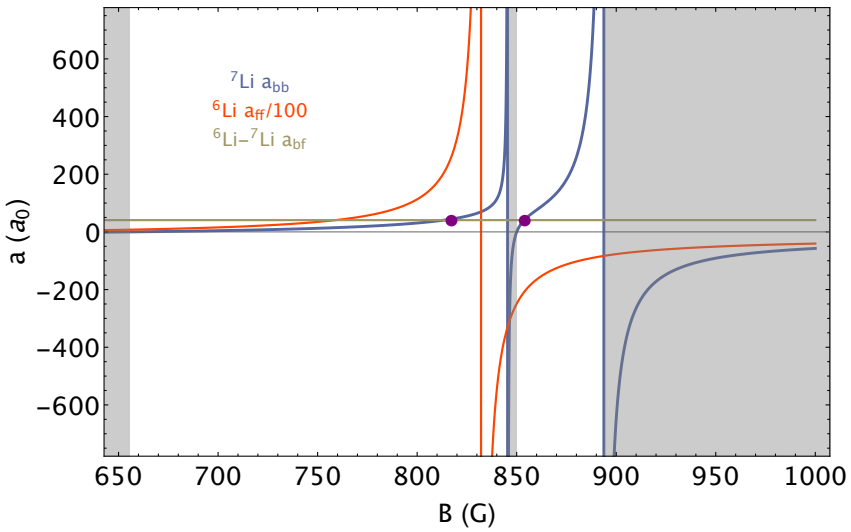

Figure 4.4: Evolution of the scattering lengths as a function of the magnetic field. In red, the $\uparrow$ / $\downarrow$ scattering length a_{ff} divided by 100, in blue, the Bose-Bose scattering length a_{bb}, in brown the Bose-Fermi scattering length a_{bf}. The shaded grey areas indicate the magnetic field values for which the BEC is unstable. The purple circles indicate the condition $g_{\mathrm{bf}} = g_{\mathrm{bb}}$.

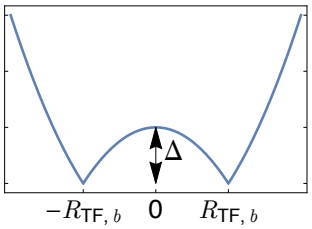

Figure 4.5: Definition of Δ, the residual anti-trapping energy

4.2.2.3 Stability of the mixture with respect to phase separation

Apart from the condition $a_{\mathrm{bb}} > 0$, required for the BEC to be stable, one may also wonder what are the conditions for the *mixture* to be stable: the compressibility matrix $[\partial\mu_\alpha/\partial n_\beta]_{\alpha,\beta=\mathrm{b,f}}$ must have positive eigenvalues [Viverit *et al.*, 2000]. This requires (in the case of a balanced Fermi gas):

$$\frac{\partial\mu_{\mathrm{b}}}{\partial n_{\mathrm{b}}}\cdot\frac{\partial\mu_{\mathrm{f}}}{\partial n_{\mathrm{f}}} \geq \frac{\partial\mu_{\mathrm{b}}}{\partial n_{\mathrm{f}}}\cdot\frac{\partial\mu_{\mathrm{f}}}{\partial n_{\mathrm{b}}}$$

This corresponds to:

$$\frac{\partial\mu_{\mathrm{f}}}{\partial n_{\mathrm{f}}} \geq \frac{g_{\mathrm{bf}}^2}{g_{\mathrm{bb}}},$$

that is:

$$\frac{\partial w(n_{\mathrm{f}})}{\partial n_{\mathrm{f}}} \geq \frac{g_{\mathrm{bf}}^2}{g_{\mathrm{bb}}},$$

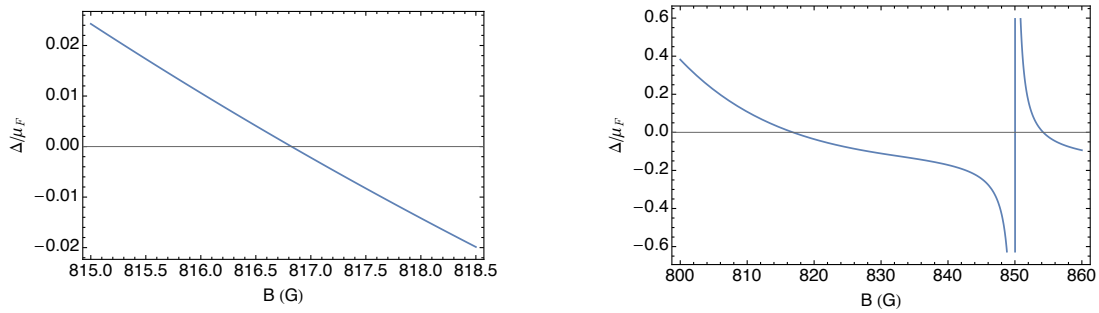

Figure 4.6: Variations of Δ/μ_f for different ranges of magnetic fields around the condition $g_b = g_{bf}$.

At unitarity, this leads to $n_f \leq 2.7 \cdot 10^{16}\,\mathrm{cm}^{-3}$, which is well verified with our experimental parameters ($n_f < 10^{14}\,\mathrm{cm}^{-3}$), and this will remain the case for $g_{bf} = g_{bb}$.

However, if we wanted to study phase-separation between the components of the mixture, it would be possible to go towards a magnetic field where a_{bb} goes to zero. For the $|2_b\rangle$ state that we are using, $a_{bb} = 0$ at $B = 850\,\mathrm{G}$ and at $B = 578\,\mathrm{G}$ [Shotan *et al.*, 2014]. The phase separation occurs when a_{bb} is still positive, *ie* before reaching the value $a_{bb} = 0$ that leads to the collapse of the condensate. Close to $B = 850\,\mathrm{G}$, the phase separation occurs about 50 mG away from $a_{bb} = 0$ and preliminary data that we took there show mainly the collapse of the BEC. However, towards $B = 578\,\mathrm{G}$, phase separation should occur below 730 G [Ferrier-Barbut, 2014], well before the collapse of the BEC, but this is then in the deep BEC regime for the fermions and their lifetime is reduced. We plan to do more experiments to investigate this possibility of phase separation to make a connection with what is happening in ^{4}He-^{3}He mixtures.

4.2.2.4 Deviations from Paschen-Back regime

In the range [800 G-900 G], ^{7}Li is not fully in the Paschen-Back regime. This results in a slightly different magnetic trapping for ^{7}Li and ^{6}Li: $V_{b,ax} = \beta V_{f,ax}$, with $\beta = 0.96 < 1$. The optical trapping stays the same for both isotopes[3]. This results in the axial trapping (mainly magnetic) being different for both isotopes while the radial trapping (mainly optical) is the same. Equation (4.6) can be re-written as:

$$\mu_\sigma = w_\sigma[n_\uparrow, n_\downarrow] + \frac{g_{bf}^2}{g_{bb}}(n_\uparrow + n_\downarrow) + V_f(r) - \frac{g_{bf}}{g_{bb}}V_b(r) + \frac{g_{bf}}{g_{bb}}\mu_b.$$

It is not possible any more to cancel harmonic trapping simultaneously in all three directions. For $g_{bb} = g_{bf}$ (at magnetic fields of 816.8 G and 854.2 G), this results in a residual axial trapping with a frequency $\omega'_f \approx \sqrt{1-\beta}\,\omega_f \approx 3\,\mathrm{Hz}$ for the fermions.

Alternatively, when $g_{bb} = \beta g_{bf}$ (for magnetic fields of 815.2 G and 854.0 G), axial trapping is canceled and the residual radial potential is anti-trapping, with anti-trapping frequencies of 74 Hz. The minima of potential would then follow the surface of a cylinder. To evaluate how important these deviations are from the true flat-bottom

[3] The isotopic shift is 10.5 GHz while the laser frequency is $3.0 \cdot 10^{14}$ Hz, leading to a relative difference between the two optical trapping potentials of $3 \cdot 10^{-5}$.

trap, one can evaluate the size of Δ, as it was defined in subsubsection 4.2.2.2, with respect to the fermions chemical potential μ_f. We have:

$$\begin{aligned}\frac{\Delta}{\mu_\mathrm{f}} &= \frac{\frac{1}{2}m_\mathrm{f}\omega_\mathrm{f}'^2 R_{\mathrm{TF,b}}^2}{\mu_\mathrm{f}} \\ &= \frac{\mu_\mathrm{b}}{\mu_\mathrm{f}}\frac{\omega_\mathrm{f}'^2}{\omega_\mathrm{b}^2}\frac{m_\mathrm{f}}{m_\mathrm{b}} \\ &= (1-\beta)\frac{\mu_\mathrm{b}}{\mu_\mathrm{f}} \\ &\lesssim 10^{-4}\end{aligned}$$

At 816.8 G, the trap is thus radially flat, and has a small residual trapping potential of 3 Hz. However, the above calculation shows that the corresponding change in energy is small compared to the chemical potential of the fermions, and it was neglected in both the theoretical calculations and the analysis.

At 854 G, the trap is axially flat, with some anti-trapping at a frequency of about 74 Hz. Still from the above calculations, the resulting energy change is also small with respect to μ_f and was also neglected.

In the following, we will always consider that the bottom of the trap is flat, and has ellipsoidal symmetry.

4.3 Critical polarizations in a flat bottom trap

4.3.1 Bosons and fermions in a box

If we turn back to the situation of a spin-polarized Fermi gas in a box described in subsection 4.1.1, in the presence of bosons, the situation is a bit modified [Ozawa *et al.*, 2014]. The Fermi gas is still separated into a normal and a superfluid phase, an we note n_bn (resp. n_bs) the densities of bosons in the normal (resp. superfluid) phase of the fermions. We can write the total energy densities $\mathcal{E}_\mathrm{s}$ and $\mathcal{E}_\mathrm{n}$ of the superfluid and normal phase:

$$\begin{aligned}\mathcal{E}_\mathrm{s} &= \frac{g_\mathrm{bb}}{2}n_{\mathrm{b}s}^2 + 2g_\mathrm{bf}n_{\mathrm{b}s}n_\mathrm{s} + e_\mathrm{s}[n_\mathrm{s}], \\ \mathcal{E}_\mathrm{n} &= \frac{g_\mathrm{bb}}{2}n_{\mathrm{b}n}^2 + g_\mathrm{bf}n_{\mathrm{b}n}(n_\uparrow + n_\downarrow) + e_\mathrm{n}[n_\uparrow, n_\downarrow]\end{aligned}$$

At unitarity, we recall equations (4.1) and (4.3) for the energy of fermions in the superfluid and the normal phases (with x defined as previously $x \equiv n_\downarrow/n_\uparrow$):

$$\begin{aligned}e_\mathrm{s}[n_\mathrm{s}] &\equiv \xi\frac{6}{5}\frac{\hbar^2}{2m_f}(6\pi^2 n_\mathrm{s})^{2/3}n_\mathrm{s} \\ e_\mathrm{n}[n_\uparrow, n_\downarrow] &\equiv \frac{3}{5}\varepsilon_{\mathrm{F}\uparrow}n_\uparrow\left(\underbrace{1 - \frac{5}{3}Ax + \frac{m_f}{m^*}x^{5/3} + Fx^2}_{\epsilon(x)}\right) \\ &\equiv \frac{3}{5}\varepsilon_{\mathrm{F}\uparrow}n_\uparrow\epsilon(x),\end{aligned}$$

and these results can be extended around unitarity using again Table 4.1.

Writing the equilibrium conditions between the superfluid and the normal phase leads to:

- Fermion chemical potential equality: $\mu_\uparrow + \mu_\downarrow = \mu_\mathrm{s}$. Since

$$\mu_\uparrow = \frac{\partial \mathcal{E}_\mathrm{n}}{\partial n_\uparrow} = g_\mathrm{bf} n_\mathrm{bn} + \varepsilon_{\mathrm{F}\uparrow}\epsilon(x) - \frac{3}{5}x\epsilon'(x)\varepsilon_{\mathrm{F}\uparrow},$$
$$\mu_\downarrow = \frac{\partial \mathcal{E}_\mathrm{n}}{\partial n_\downarrow} = g_\mathrm{bf} n_\mathrm{bn} + \varepsilon_{\mathrm{F}\uparrow}\epsilon(x) + \frac{3}{5}\epsilon'(x)\varepsilon_{\mathrm{F}\uparrow},$$
$$\mu_\mathrm{s} = \frac{\partial \mathcal{E}_\mathrm{s}}{\partial n_\mathrm{s}} = 2g_\mathrm{bf} n_\mathrm{bs} + 2\xi y^{2/3}\varepsilon_{\mathrm{F}\uparrow},$$

  leading to, with $y \equiv n_\mathrm{s}/n_\uparrow$,

$$\xi y^{2/3} - \frac{1}{2}\epsilon(x) - \frac{3}{10}\epsilon'(x)(1-x) = g_\mathrm{bf}\frac{(n_\mathrm{bn} - n_\mathrm{bs})}{\varepsilon_{\mathrm{F}\uparrow}}. \tag{4.7}$$

- Boson chemical potential equality: $\mu_\mathrm{bs} = \mu_\mathrm{bn}$. Since

$$\mu_\mathrm{bn} = \frac{\partial \mathcal{E}_\mathrm{n}}{\partial n_\mathrm{bn}} = g_\mathrm{bb} n_\mathrm{bn} + g_\mathrm{bf}(n_\uparrow + n_\downarrow),$$
$$\mu_\mathrm{bs} = \frac{\partial \mathcal{E}_\mathrm{s}}{\partial n_\mathrm{bs}} = g_\mathrm{bb} n_\mathrm{bs} + 2g_\mathrm{bf} n_\mathrm{s},$$

  leading to

$$g_\mathrm{bb}(n_\mathrm{bn} - n_\mathrm{bs}) = g_\mathrm{bf} n_\uparrow (2y - (1+x)). \tag{4.8}$$

  Combining equations (4.7) and (4.8) leads to:

$$\xi y^{2/3} - 2Gy - \frac{1}{2}\epsilon(x) - \frac{3}{10}\epsilon'(x)(1-x) + G(1+x) = 0, \tag{4.9}$$

  where G is defined as $G \equiv n_\uparrow g_\mathrm{bf}^2/(\varepsilon_{\mathrm{F}\uparrow} g_\mathrm{bb})$, corresponding to the ratio between the change in the energy of fermions caused by the induced interaction $-g_\mathrm{bf}^2/g_\mathrm{bb}$ in the static limit and the non-interacting Fermi energy.

- Equality of the pressure P_s of the superfluid phase and P_n of the normal phase at the boundary.

$$P_\mathrm{s} = 2g_\mathrm{bf} n_\uparrow y n_\mathrm{bs} + g_\mathrm{bb}\frac{n_\mathrm{bs}^2}{2} + \frac{4}{5}\varepsilon_{\mathrm{F}\uparrow} y^{5/3} n_\uparrow,$$
$$P_\mathrm{n} = g_\mathrm{bf} n_\uparrow (1+x) n_\mathrm{bn} + g_\mathrm{bb}\frac{n_\mathrm{bn}^2}{2} + \frac{2}{3}\varepsilon_{\mathrm{F}\uparrow} n_\uparrow \epsilon(x),$$

  leading to

$$2Gy^2 - \frac{4}{5}\xi y^{5/3} - G\frac{(1+x)^2}{2} + \frac{2}{5}\epsilon(x) = 0, \tag{4.10}$$

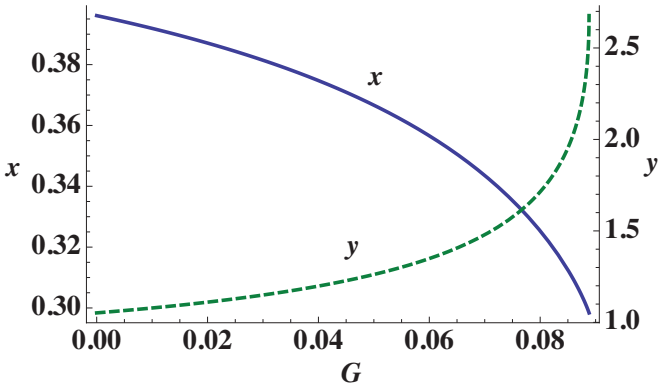

Figure 4.7: Solutions x and y to equations (4.9) and (4.10).

The solutions to the system composed of equations (4.9) and (4.10) are shown on Figure 4.7.

As long as $G < G_{\max} = 0.089$, we respect the stability conditions established in subsubsection 4.2.2.3 and there exist two solutions for x and y. When G goes to zero, we recover the $x = 0.4$ of the case without bosons (see subsection 4.1.1). When G increases, x decreases, which implies the superfluid phase is stabilized by the interactions with the bosons. The fact that y increases (with respect to its value without bosons $y = 1.05$) shows that the density jump at the interface becomes larger as G increases, as high as $2n_s/(n_\uparrow + n_\downarrow) \approx 4.1$ when $G = G_{\max}$, to be compared with the value 1.5 of the case without bosons. It is important to notice that these results do not depend on the bosonic density, and as long as some bosons are present, they should stabilize the superfluid Fermi gas, but the volume of Fermi gas that is stabilized will decrease with decreasing number of bosons.

4.3.2 Bosons and fermions in a harmonic trap

We now combine the results from section 4.2 and subsection 4.3.1, and study a mixture of a BEC and an imbalanced Fermi gas in a harmonic trap with $g_{bf} = g_{bb}$. This implies that the bottom of the trap is flat (as shown in Figure 4.3b). In the following, the region of the trap where the bosons are present, corresponding to where the potential is flat, will be called 'the core'. Using the method presented in subsection 4.3.1 enables us to obtain the density profiles of the clouds[4] within the local density approximation (see Figure 4.8a and Figure 4.8b top for instance). The fact that the flat-potential conditions do not occur exactly at unitarity but for $1/k_F a_{ff} = 0.2$ and $1/k_F a_{ff} = -0.25$ can also be taken into account using Table 4.1, but since the results do not differ significantly from the exact unitary case and to avoid any loss of generality, theoretical profiles are calculated at unitarity.

We can first identify two clear different regimes:

- If the polarization is small, the Fermi superfluid extends farther than the edge of the BEC (see Figure 4.8a).

[4]The source code was kindly provided by Tomoki Ozawa.

- If the polarization is large, the Fermi gas in the core will be all in the normal phase, thereby one expects a uniform partially polarized gas, surrounded by a non-uniform partially polarized phase, and then by a fully polarized phase (see Figure 4.8b).

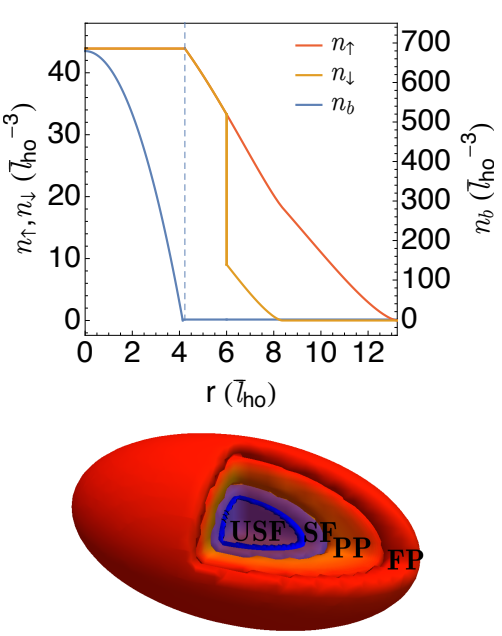

(a) For low polarization, a uniform superfluid (USF) lies in the core region.

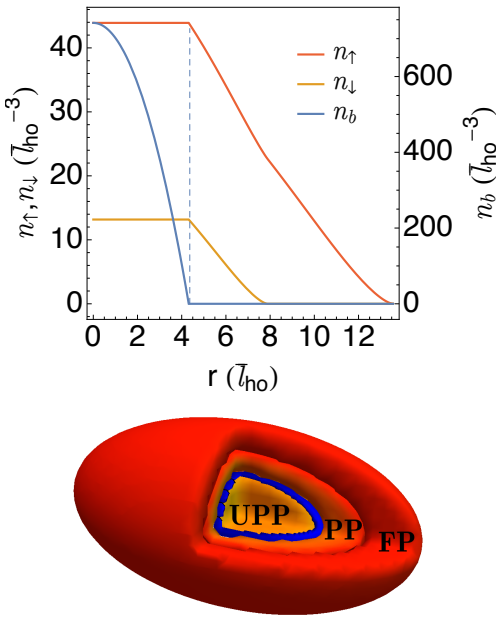

(b) For high polarization, the core region is occupied by a uniform partially polarized (UPP) phase.

Figure 4.8: Schematic representation of an imbalanced Fermi gas in a flat bottom trap. In purple is the superfluid (SF) phase, in faded yellow-to-red is the partially polarized (PP) phase, and in red is the fully polarized (FP) phase. The 'core' region, occupied by the bosons - hence the flat trap area - is circled in blue.

We can now define two critical situations:

(i) The superfluid occupies the whole core, but does not extend out of it.

(ii) The core is occupied by a partially polarized phase such that the ratio $n_\downarrow/n_\uparrow$ in the core is equal to the critical ratio for superfluidity (defined previously as x).

The radial density profiles corresponding to these situations are shown in Figure 4.9.

The critical polarization for each of these situations can be computed as a function of $N_\mathrm{f}/N_\mathrm{b}$ and depends only weakly on N_b. At unitarity, they are displayed on Figure 4.10a. They can also be computed for the two values of $k_\mathrm{F}a_\mathrm{ff}$ corresponding to our experimental realizations (namely $k_\mathrm{F}a_\mathrm{ff} = 5$ and $k_\mathrm{F}a_\mathrm{ff} = -4$), and the results are shown on Figure 4.10b and Figure 4.10c, respectively. We notice that, for

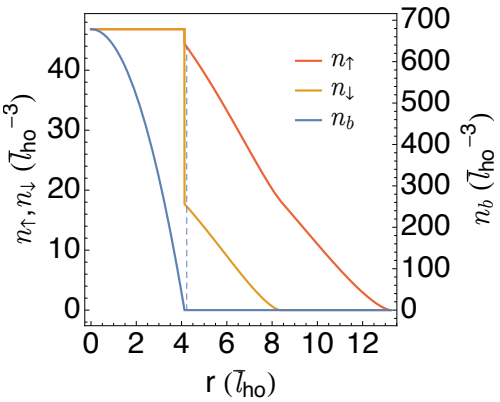

(a) Critical situation (i): the superfluid (with $n_\uparrow = n_\downarrow$) occupies the whole core and does not expand out of it.

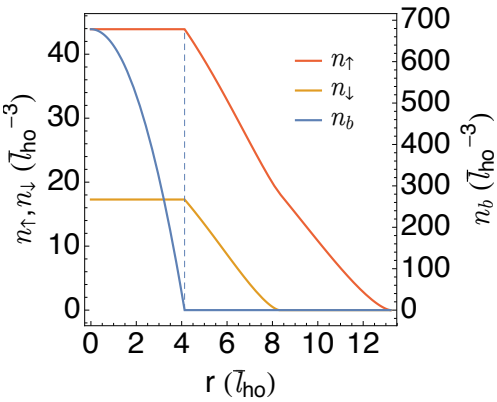

(b) Critical situation (ii): the partially polarized phase in the core is such as $n_\downarrow/n_\uparrow = 0.40$, the critical ratio for superfluidity.

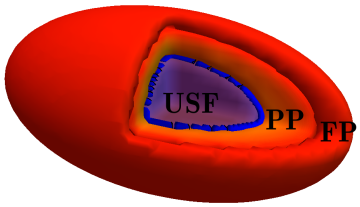

(c) Representation of critical situation (i).

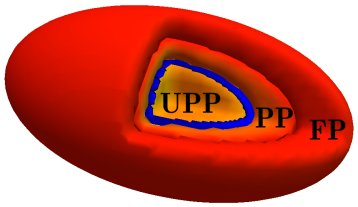

(d) Representation of critical situation (ii).

Figure 4.9: The two critical situations evoked in the text. The bosonic density is shown in blue, the spin-up density in red and the spin-down density in yellow. Calculations were made at unitarity, for $N_\mathrm{b} = 80 \cdot 10^3$, $N_\mathrm{f} = 150 \cdot 10^3$, and the corresponding polarizations are $P = 64\%$ (a) and $P = 75\%$ (b). Here $g_\mathrm{bb} = g_\mathrm{bf} = 10^{-3}\bar{l}_\mathrm{ho} m_\mathrm{b}/m_\mathrm{f}$. (c) and (d) are 3D representation of the situations described in (a) and (b) respectively.

$N_f/N_b \to \infty$, we retrieve the critical polarization for superfluidity in a harmonic trap. For all three cases, we notice that there is a non-zero range of polarization for which the core can neither be entirely superfluid nor entirely partially polarized. There is thus a phase-separation inside the core which is then 'non-homogeneous'.

4.3.3 Breakdown of flat bottom trap prediction

The obvious question now is: what happens in the dashed region of Figure 4.10? There exist two ways to get there: either starting from the critical situation of (i) and increasing the polarization, or starting from the critical situation of (ii) and decreasing the polarization. We then have coexistence of the superfluid and of the normal phase in the core region. Many scenarios are eligible, including exotic phases such as FFLO phases [Hu and Liu, 2006, Bulgac and Forbes, 2008, Parish *et al.*, 2007b, Radzihovsky and Sheehy, 2010].

If we restrict ourselves to simple scenarios which respect the ellipsoidal symmetry and have a limited number of Superfluid-Normal boundaries, we can suppose the core is separated into a normal phase and a superfluid phase, with either the superfluid phase at the center of the core, and the normal phase around it (Superfluid-Normal scenario, as in Figure 4.11a), or a central normal phase, and a superfluid around it in the core, and a non-homogeneous normal phase (Normal-Superfluid-Normal scenario, as in Figure 4.11b). The question is then whether the superfluid lies at the center of the cloud like a '**Kernel**' (Superfluid-Normal scenario), or whether it has the shape of a '**Shell**' around a normal phase (Normal-Superfluid-Normal scenario).

It is experimentally feasible to be both in the flat potential conditions and close to the unitary regime, and we can also vary the polarization. We only have access to the doubly-integrated profiles and not to the radial profiles, but the two scenarios explained previously have very different signatures in the doubly integrated profiles (see Figure 4.11c and Figure 4.11d). It should be possible to identify them experimentally.

(a) At unitarity

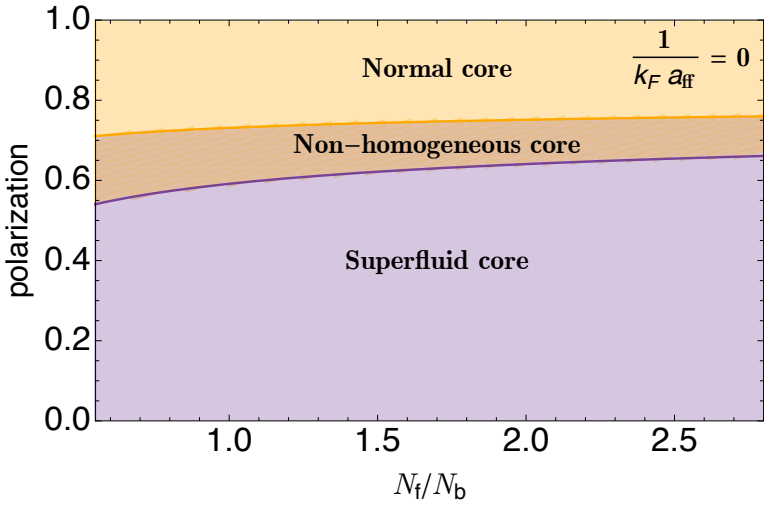

(b) BEC side

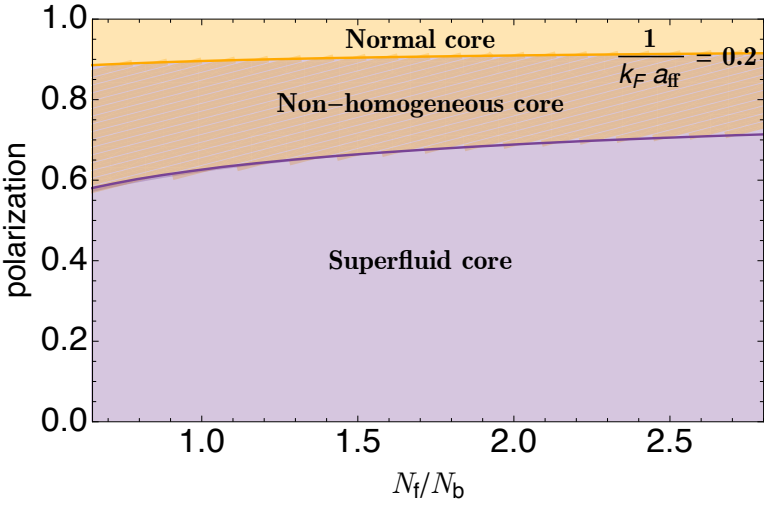

(c) BCS side

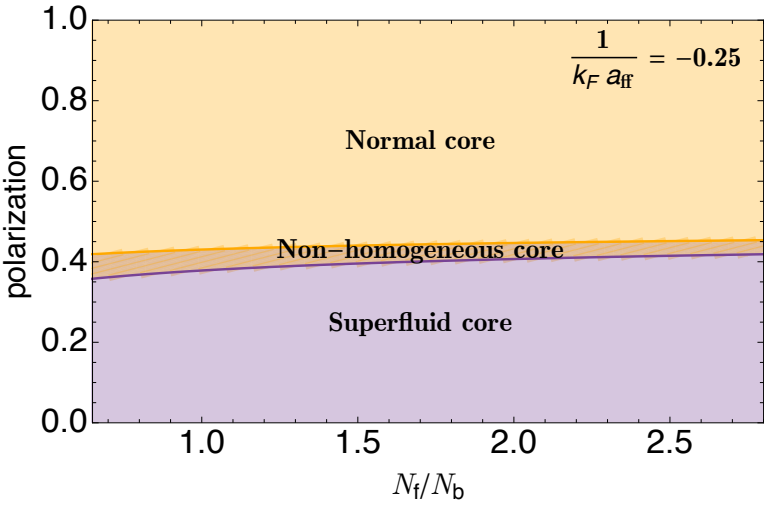

Figure 4.10: Critical polarizations for the core to be entirely normal (yellow area) or entirely superfluid (purple area), for different values of $\frac{1}{k_F a_{ff}}$ in the BEC-BCS crossover. The intermediate area of inhomogeneous core is in dashed purple-and-yellow.

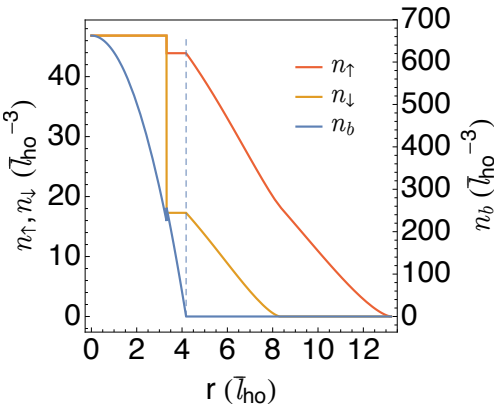

(a) Superfluid-Normal scenario, radial density profile.

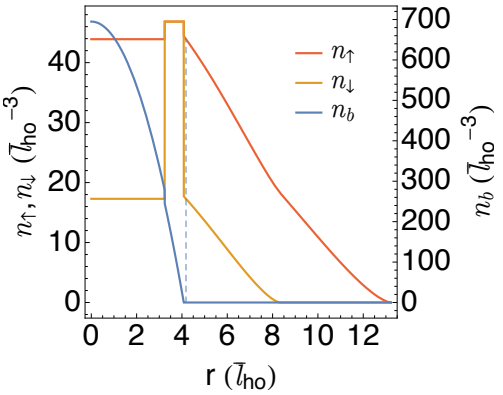

(b) Normal-Superfluid-Normal scenario, radial density profile.

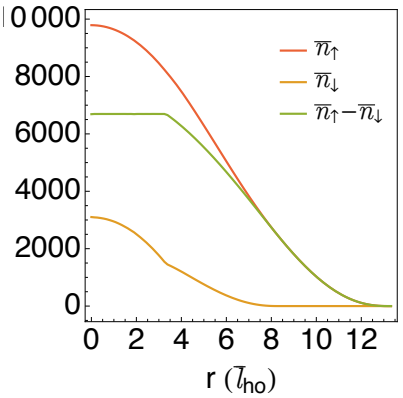

(c) Superfluid-Normal scenario, doubly-integrated density profile.

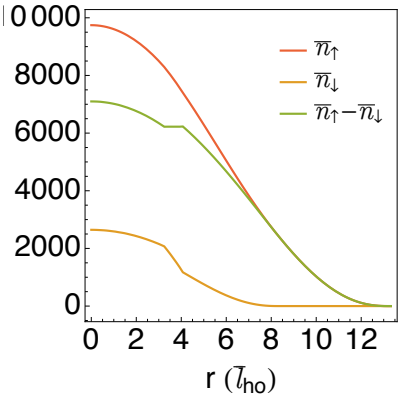

(d) Normal-Superfluid-Normal scenario, doubly-integrated density profile.

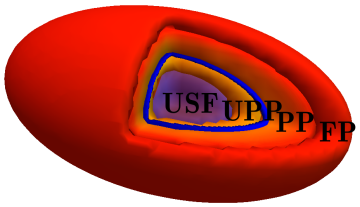

(e) 3D representation of Superfluid-Normal scenario.

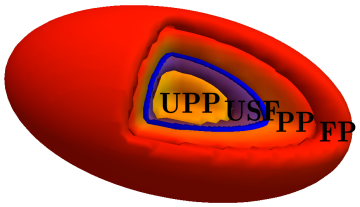

(f) 3D representation of Normal-Superfluid-Normal scenario.

Figure 4.11: Two possible scenarios involving a phase separation in the core. The calculations were made assuming an equal volume of superfluid and of normal phase in the core for these figures. The numbers of atoms are $N_\mathrm{f} = 144 \cdot 10^3$, $N_\mathrm{b} = 80 \cdot 10^3$ with $P = 0.69$. (a) and (b) figures show the radial density profiles, and (c) and (d) the corresponding doubly-integrated density profiles. Majority fermions ($\uparrow$) are shown in red, minority ($\downarrow$) in yellow, the difference ($n_\uparrow - n_\downarrow$) in green and bosons in blue. (e) and (f) are 3D representations of the two situations.

4.4 Experiments on imbalanced Fermi gases in a flat bottom trap

The rich variety of phenomena presented above led us to run the experiment at the magnetic fields for which a FBT was expected.

We took data for different total atom numbers and polarizations, using simultaneous triple imaging, with both fermionic spin states imaged transversally *in situ* and the bosons imaged axially after $t_{\mathrm{tof}} = 4\,\mathrm{ms}$ of time-of-flight. We have taken 1135 images at 817 G and 288 images at 854 G with Bose-Fermi mixture, and 405 images at 817 G with fermions alone, that we took for comparison purposes. In the Bose-Fermi mixture, the BEC density profile was found to be very close to a Thomas-Fermi distribution, despite the presence of fermions. On the other hand, as expected, the distribution of the Fermi component appears to be qualitatively affected by the presence of the BEC.

4.4.1 Bosonic Thomas-Fermi radius

Since the fermionic density is essentially uniform, the shape of the BEC remains a parabola[5]. The fermions are imaged *in situ* and rapidly blown away from the trap, so the BEC expands during time-of-flight as usual[6]. We can make a Thomas-Fermi fit of the bosonic profile and use it to extract the Thomas-Fermi radius after time of flight t_{tof}, $R_{\mathrm{TF,tof}}$. In the case of cigar-shaped traps, it is related to the *in situ* axial Thomas-Fermi radius $R_{\mathrm{TF,b}}$ by the relation [Castin and Dum, 1996]:

$$R_{\mathrm{TF,b}} = \frac{1}{\sqrt{1+\omega_r t_{\mathrm{tof}}}} \frac{\omega_r}{\omega_z} R_{\mathrm{TF,tof}}.$$

This expression is valid when any confinement is switched off at $t = 0$. In our case, we only switch off the optical dipole trap, that realizes mainly the radial confinement, and let the magnetic trap on. During the time of flight, the atoms feel some weakened trapping potential in the axial direction (with a new trapping frequency $\omega_{z,tof} \sim 2\pi \cdot 14\,\mathrm{Hz}$), and some anti-trapping potential in the radial direction (with a new frequency $\omega_{r,tof} \sim 2\pi \cdot 7\,\mathrm{Hz}$). The time evolution of the Thomas-Fermi radii is now given by:

$$\begin{aligned} R_{\mathrm{TF},z}(t = t_{\mathrm{tof}}) &= \lambda_z(t_{\mathrm{tof}}) R_{\mathrm{TF},z}(t = 0), \\ R_{\mathrm{TF},r}(t = t_{\mathrm{tof}}) &= \lambda_r(t_{\mathrm{tof}}) R_{\mathrm{TF},r}(t = 0), \end{aligned}$$

where the $\lambda_{j=r,z}$ obey [Castin and Dum, 1996]:

$$\begin{aligned} \ddot{\lambda}_r(t) &= \frac{\omega_r^2}{\lambda_z(t)\lambda_r^3(t)} - \omega_{r,tof}^2 \lambda_r(t), \\ \ddot{\lambda}_z(t) &= \frac{\omega_z^2}{\lambda_z^2(t)\lambda_r^2(t)} - \omega_{z,tof}^2 \lambda_z(t). \end{aligned}$$

[5] If there is a density jump in the fermionic density, the BEC is not strictly a parabola, but due to the high $n_{\mathrm{b}}/n_{\mathrm{f}}$ ratio (see section 4.2), this effect is barely visible on theoretical profiles (see blue curves in Figure 4.11a and Figure 4.11b), and below our signal-to-noise resolution.

[6] We checked the the bosonic cloud was not displaced during its time and flight, and thus not pushed by escaping fermions.

These equations can be solved numerically, and we find that for a time of flight of 4 ms, $\lambda_r(t_{\text{tof}}) = 11.9$ and $\lambda_z(t_{\text{tof}}) = 0.96$. These values can be compared with $\lambda_r = 11.9$ and $\lambda_z = 1.01$, obtained assuming true time of flight, with equations (1.1). The correction on λ_r is below our error bars. From the measured time of flight radius in the radial direction $R_{\text{TF},r}(t_{\text{tof}})$, we obtain the *in situ* radial Thomas-Fermi radius $R_{\text{TF},r}(t = 0) = R_{\text{TF},r}(t_{\text{tof}})/\lambda_r(t_{\text{tof}})$, then the *in situ* axial Thomas-Fermi radius $R_{\text{TF},z}(t = 0) = R_{\text{TF},r}(t = 0)\omega_r/\omega_z$. The Thomas-Fermi radius along the axial direction of the BEC can now be compared to the fermions characteristic lengths.

4.4.2 First observations

One first observation is that the peak density of the fermions is reduced by the presence of the bosons with respect to a cloud without bosons with the same number of fermions, as it can already be seen on Figure 4.12. This very simple effect shows that the bosons do impose some repulsive potential on the fermions, the density of which is reduced with respect to a cloud in a simple harmonic trap. However, that effect is not straightforward to quantify, due to the double integration in the two radial directions.

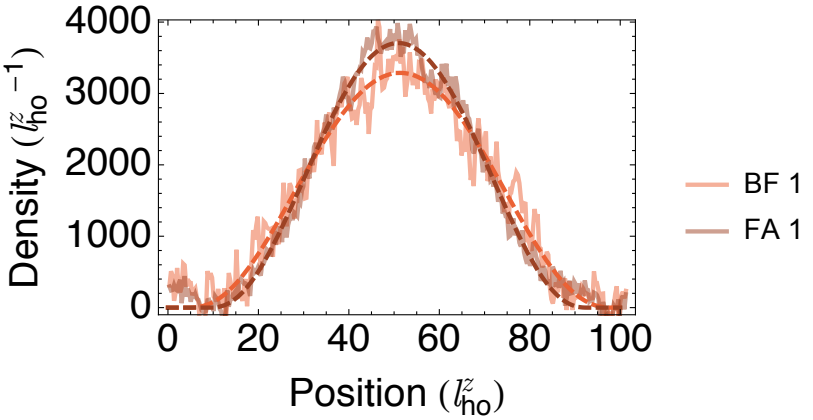

Figure 4.12: Comparison between the doubly integrated density profile of the majority component ($\bar{n}_\uparrow$) with bosons (light red curve) and without bosons (dark red curve), for the same polarization and number of fermions. Dashed lines are a guide to the eye.

We now focus on the influence of the bosons on the density profile difference $\bar{n}_\uparrow - \bar{n}_\downarrow$, where we expect to see signatures of the two scenarios described in subsection 4.3.3.

In Figure 4.13, we compare four distinct situations, yet with the same spin polarization of 60 %. The upper raw corresponds to two examples of the *fermions-alone* case (called FA 1 and FA 2), and serves as a reference for the samples of the lower raw (called BF 1 and BF 2) which are Bose-Fermi mixture in the FBT configuration with the same number of fermions.

The profiles of $\Delta\bar{n} = \bar{n}_\uparrow - \bar{n}_\downarrow$ (green line) show a clear difference depending on whether or not bosons are present. While the profiles obtained in the absence of bosons show a nice plateau, signaling the superfluid state, there appears to be differences in the mixture case. In Figure 4.13c (BF 1), we can see a central bump sitting on flat shoulders while in Figure 4.13d (BF 2) the superfluid plateau is smaller than in the

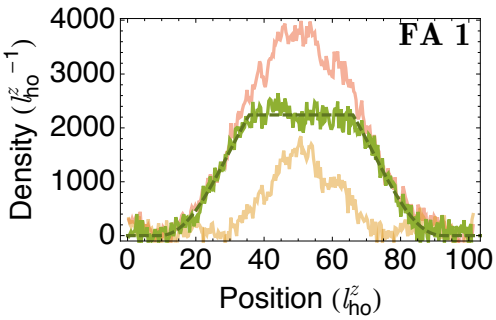

(a) $N_f = 180 \cdot 10^3$, no bosons.

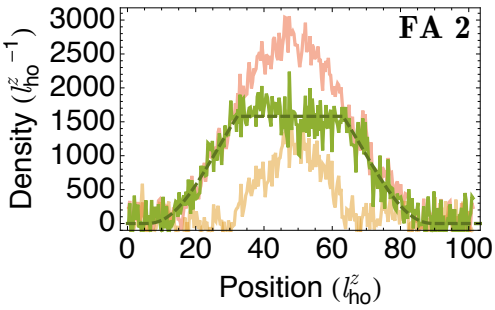

(b) $N_f = 125 \cdot 10^3$, no bosons.

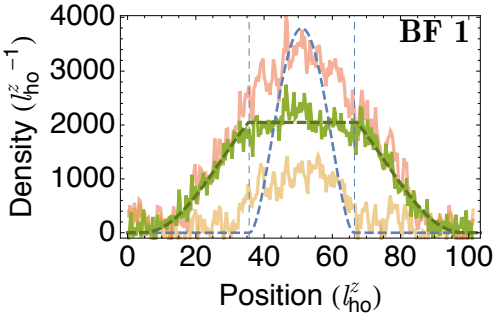

(c) $\mathbf{N_b = 63 \cdot 10^3}$, $N_f = 180 \cdot 10^3$.

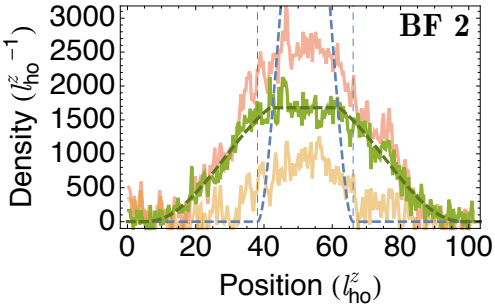

(d) $\mathbf{N_b = 88 \cdot 10^3}$, $N_f = 125 \cdot 10^3$.

Figure 4.13: Examples of doubly-integrated density profiles for a polarization of 60%. The top figures correspond to Fermi clouds prepared without bosons, while the bottom figures to Bose-Fermi mixtures. Red curve is the density of the majority component, yellow curve that of the minority component and the green curve to the density difference. The blue-dashed curve represents the reconstructed bosonic density from the time-of-flight image in another direction (when bosons are present). Units are in terms of harmonic oscillator length in the axial direction. These clouds were prepared at 817 G.

fermions-alone case (FA 2) and seems to be rounded. As we will see in the following, we will be able to match these two unusual structures with the Normal-Superfluid-Normal scenario (described in subsection 4.3.3, with a superfluid shell) on the one hand and with the Superfluid-Normal scenario on the other (with a superfluid kernel).

We now describe a refined analysis of the density profiles to get a deeper insight into these unusual structures.

4.4.3 Reconstruction Methods

Both methods described below rely on the isotropy of the atomic distribution, taken is a general sense: they apply to any ellipsoidal distribution. There is no hypothesis regarding the harmonicity of the potential and the LDA does not have to be fulfilled. It only assumes that iso-potential lines for the trapping potential correspond to iso-density lines for atomic density.

Double inverse Abel transform

The first method that we used is based on the Abel transform. It was used in [Bulgac and Forbes, 2007, Shin *et al.*, 2008, Shin, 2008, Horikoshi *et al.*, 2010, Van Houcke *et al.*, 2012] to extract the equation of state. It relies on a mathematical transform that physically corresponds to the integration of an axially symmetric image along one direction. Indeed, if we consider a function $f(\rho)$ in the $x-y$ plane with $\rho = \sqrt{x^2+y^2}$, then $F(y)$ is the integration of this function along x:

$$F(y) = \int_{-\infty}^{\infty} f\left(\sqrt{x^2+y^2}\right)\, dx \qquad\qquad dx = \frac{\rho\, d\rho}{\sqrt{\rho^2-y^2}}$$
$$F(y) = 2\int_{y}^{\infty} \frac{f(\rho)\rho\, d\rho}{\sqrt{\rho^2-y^2}}.$$

This can easily be extended to a cylindrico-symmetric function $f(\rho,z)$ in the $x-y-z$ space, with still $\rho = \sqrt{x^2+y^2}$:

$$F(y,z) = \int_{-\infty}^{\infty} f(\rho,z)\, dx = 2\int_{y}^{\infty} \frac{f(\rho,z)\rho\, d\rho}{\sqrt{\rho^2-y^2}}.$$

But now if f was spherically-symmetric with $f(\rho,z) = f(r = \sqrt{\rho^2+z^2}) = f(r = \sqrt{x^2+y^2+z^2})$, then the function $F(y,z) = F(\sqrt{y^2+z^2})$ has radial symmetry and can be integrated along y. We obtain:

$$\mathcal{F} = \int_{-\infty}^{\infty} F\left(\sqrt{y^2+z^2}\right)\, dy.$$

A representation of these two steps are given on Figure 4.14.

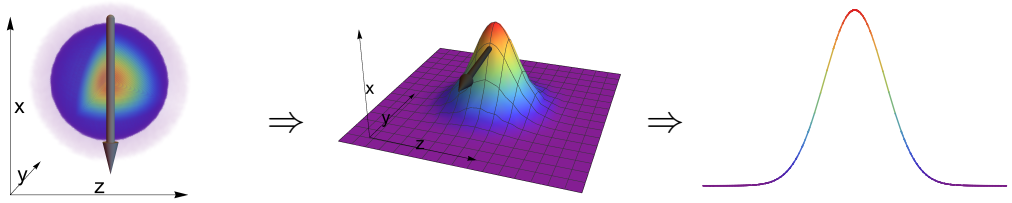

(a) Integration along x. (b) Integration along y. (c) Resulting 1D profile.

Figure 4.14: Schematic description of the two integration steps that lead to the double Abel transform. (a): integration of $f(r)$ along the x direction to obtain $F(y,z)$. (b): $F(R) = F(y,z)$ integrated along the y direction to obtain $\mathcal{F}(z)$. (c): $\mathcal{F}(z)$, doubly-integrated density profile.

The fact that here the potential is ellipsoidal but not spherical is not a problem because we just need to change the scaling of the z axis (for instance), with $z \leftarrow \frac{\omega_z}{\omega_r} z$. Here, the doubly-integrated density profiles would correspond to $\mathcal{F}(z)$, and singly-integrated density profiles and radial density profiles can be reconstructed iteratively

using the inverse Abel transform:

$$F(R=\sqrt{y^2+z^2}) = -\frac{1}{\pi}\int_R^\infty \frac{d\mathcal{F}(z)}{dz}\frac{dz}{\sqrt{z^2-R^2}}$$
$$f(\rho=\sqrt{x^2+y^2},z) = -\frac{1}{\pi}\int_\rho^\infty \frac{dF(y,z)}{dy}\frac{dy}{\sqrt{y^2-\rho^2}}$$

Although it is mathematically exact, this method implies to take second derivatives of the experimental profiles which is quite noisy. Moreover the division by $\sqrt{z^2-R^2}$ and $\sqrt{y^2-\rho^2}$ implies a division by zero close to the center of the cloud, and this amplifies the noise. It was thus impossible in our case to apply directly this method and we had to pre-process the data in order to use this analysis. Before discussing the pre-processing, I will give another mathematical relation between the radial profile and the doubly-integrated profile, based on a method proposed in [Fuchs *et al.*, 2003, De Silva and Mueller, 2006a, Cheng and Yip, 2007, Ho and Zhou, 2009] and used in our group [Nascimbène, 2010] to obtain the equation of state of the Fermi gas [Nascimbène *et al.*, 2010, Navon *et al.*, 2010]. It turns out to give the same results with much less amplification of the noise.

Weak LDA method

This method shares the same hypothesis with the previous one : ellipsoidal potential, non-necessarily harmonic. It was shown in subsection 4.1.3 that:

$$\frac{d\bar{n}(z)}{z\,dz} = -2\pi\frac{\omega_z^2}{\omega_\rho^2}n(z),$$

under some weak-LDA hypothesis, namely that the iso-potential lines correspond to the iso-density lines.

This relation only involves one derivative, and one division by z, such that the noise is strongly reduced with respect to the double-inverse Abel transform.

However, the experimental data is still too noisy to obtain a clear signal with the derivative. Several pre-processing methods can be used to smooth the profiles. To remain as model-free as possible, we chose to use high-order polynomials to fit the experimental profiles[7]. These polynomials can then be processed using either weak LDA method, or inverse-Abel transform. An example of the fit with 16^{th} order polynomials is shown in Figure 4.15. Discussions on the choice of the order polynomial are presented in Appendix A.

4.4.4 Evidence for a superfluid shell

The results of Abel Transform and weak LDA method are presented in Figure 4.16 from which we draw the following conclusions: as expected, the inverse Abel method is much noisier than the weak LDA method (this is amplified by the discretization of the

[7]It is clear that polynomials are C^∞ functions and will not represent the corner points of Figure 4.11c and Figure 4.11d. However, we considered that using piecewise functions as fit functions would not provide an objective criteria to discriminate between the Superfluid-Normal and Normal-Superfluid-Normal scenarios.

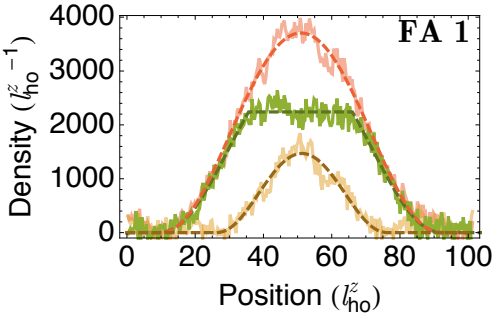

(a) $N_f = 180 \cdot 10^3$, no bosons.

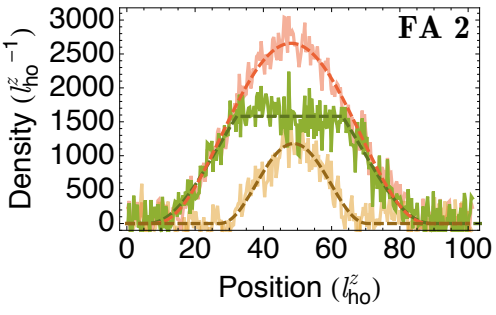

(b) $N_f = 125 \cdot 10^3$, no bosons.

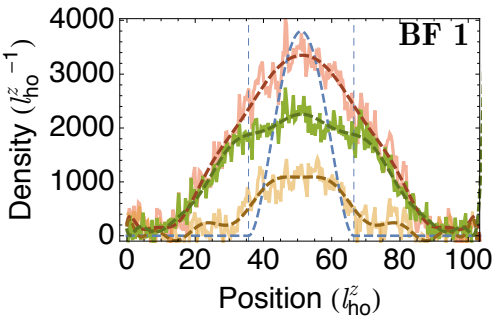

(c) $\mathbf{N_b = 63 \cdot 10^3}$, $N_f = 180 \cdot 10^3$.

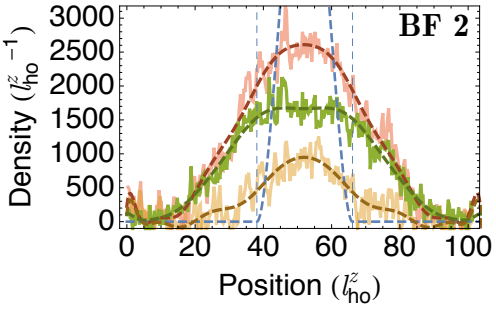

(d) $\mathbf{N_b = 88 \cdot 10^3}$, $N_f = 125 \cdot 10^3$.

Figure 4.15: Example of the polynomial fits on the doubly-integrated density profiles presented on Figure 4.13 The polarization is 60 % for all images. Top row: Thomas-Fermi fits applied to the *fermions-alone* (FA) cases. Bottom row: polynomial fit applied to the Bose-Fermi mixtures (BF). Red: $\bar{n}_\uparrow(z)$, yellow: $\bar{n}_\downarrow(z)$, green: $\bar{n}_\uparrow(z) - \bar{n}_\downarrow(z)$. Dashed thick lines: fits; thin solid lines: experimental data. Dashed blue line: reconstructed BEC profile. Vertical blue dashed lines indicate the Thomas-Fermi radius of the BEC when present.

polynomial, necessary for the Abel integrals to converge properly). In the following, we will thus restrict ourselves to the weak LDA method. The numerical computation is also much faster.

Regarding the shape of the profiles, we can make additional remarks:

- For the fermions alone (FA) (see Figure 4.16d and Figure 4.16b), the radial density of the difference $n_\uparrow(z) - n_\downarrow(z)$ always has a minimum near $z = 0$. The density jump at the boundary of the superfluid and normal phase (as on Figure 4.1a) that one would expect is not seen here because of the C^∞ polynomials used for the analysis.

- For the image with fermions and bosons (BF) (see Figure 4.16c and Figure 4.16a), the radial density of the difference $n_\uparrow(z) - n_\downarrow(z)$ shows a minimum at a distance $z \neq 0$, close to the Thomas-Fermi radius of the bosons, shown in dashed blue lines. This is not the case for all BF images, some show a minimum for the density difference near $z = 0$, as shown on Figure 4.17.

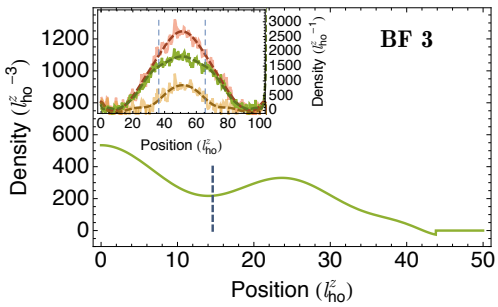

(a) $N_f = 126 \cdot 10^3$, $N_b = 63 \cdot 10^3$, $P = 64\%$, with weak LDA method.

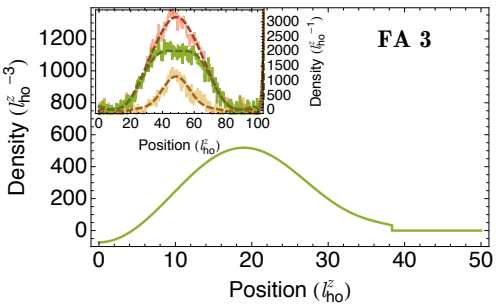

(b) $N_f = 126 \cdot 10^3$, $N_b = 0$, $P = 64\%$, with weak LDA method

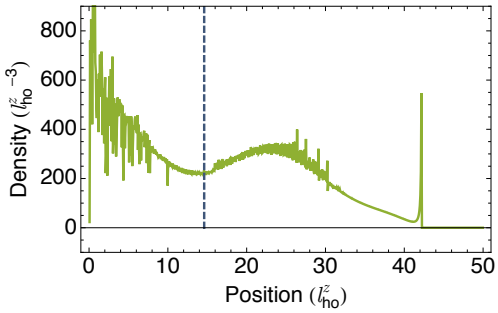

(c) $N_f = 126 \cdot 10^3$, $N_b = 63 \cdot 10^3$, $P = 64\%$, with inverse Abel transform.

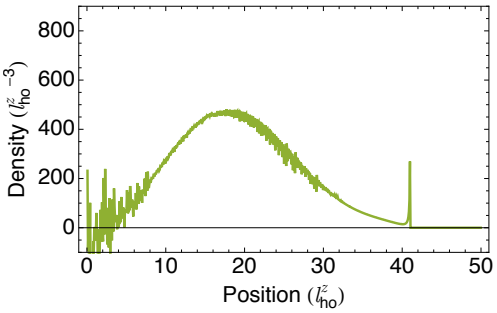

(d) $N_f = 126 \cdot 10^3$, $N_b = 0$, $P = 64\%$, with inverse Abel transform.

Figure 4.16: Comparison of typical radial profiles $n(z)$ obtained with weak LDA method (figures (a) and (b)) and inverse Abel transform (figures (c) and (d)), for fermionic clouds with (figures (a) and (c)) and without (figures (b) and (d)) bosons. Red: $n_\uparrow(z)$, yellow: $n_\downarrow(z)$, green: $n_\uparrow(z) - n_\downarrow(z)$. Insets: doubly-integrated density profiles with their polynomial fits. Vertical blue dashed lines indicate the Thomas-Fermi radius of the BEC.

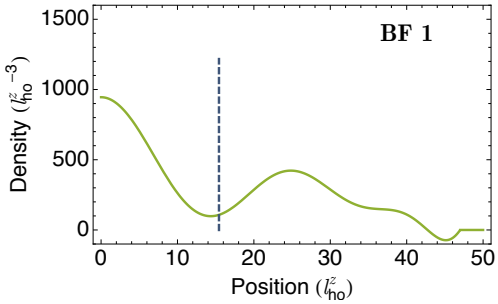

(a) $N_b = 63 \cdot 10^3$, $N_f = 180 \cdot 10^3$.

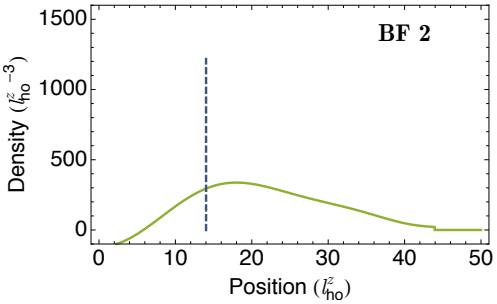

(b) $N_b = 88 \cdot 10^3$, $N_f = 125 \cdot 10^3$.

Figure 4.17: Reconstructed radial density profiles of two systems with similar atoms numbers and a polarization of 60 %, that show different behaviors for the radial density difference.

These two different behaviors are very reminiscent of the two proposals made in subsection 4.3.3 regarding what could happen between the two critical polarizations in the FBT. These images and others suggest that:

- When there are no bosons, there is no FBT and the superfluid always lies at the center of the cloud, as expected (see Figure 4.1a, and Figure 4.16b).
- For Figure 4.17a, there is a superfluid in the FBT that is forming as a shell around a partially polarized phase, like in the Normal-Superfluid-Normal scenario (see Figure 4.11b and Figure 4.11f).
- For Figure 4.17b, there is a superfluid at the center of the FBT, surrounded by a partially polarized phase, like in the Superfluid-Normal scenario (see Figure 4.11a and Figure 4.11e).

The fact that the minima in the radial density differences $n_\uparrow - n_\downarrow$ do not always go to zero is a numerical artifact resulting from the polynomial fit: having a radial density going precisely to zero requires a perfect cancellation the polynomial's derivative, which is not favored because the doubly integrated density profile is decreasing from the center. The radial density going precisely to zero thus requires the cancellation of both the first and second derivative (inflexion point). The same kind of arguments explains also why the minimum is local and does not extend on a broader area: the polynomial would have to be flat on a wide area, and this is not possible with a polynomial with order greater than one. Some numerical errors may also lead to a negative radial density difference for the SNN scenario as in Figure 4.17b. The influence of the order of the polynomial and a consistency check on theoretical profiles are given in Appendix A.

From the above analysis, we believe that a minimum in the reconstructed profile of the density difference indicates the presence of a superfluid located around the minimum. Three situations can be discriminated:

- Either there is a superfluid kernel, surrounded by an unpaired normal phase. In this case, the radial density difference has a minimum near $r = 0$.
- Either there is a superfluid shell, surrounding and surrounded by a normal phase. In this case, the radial density difference has a minimum close to $r = R_{TF,b}$.
- If the minimum is reached for $r = R_{TF,\uparrow}$, there is no superfluid and the cloud is entirely normal.

To evaluate the validity of these assumptions, we show the histogram of the repartition of $r_{\min}/R_{TF,\mathrm{b}}$ at 817 G (see Figure 4.18a). It is clearly bimodal, with a first group of data around $r_{\min}/R_{TF,\mathrm{b}} = 0$ (corresponding to a superfluid kernel), and another one around $r_{\min}/R_{TF,\mathrm{b}} \approx 0.8$ (corresponding to a superfluid shell). In addition, we plot $\frac{(n_\uparrow - n_\downarrow)(r=r_{\min})}{(n_\uparrow - n_\downarrow)(r=0)}$ as a function of $\frac{r_{\min}}{R_{TF,\mathrm{b}}}$ in Figure 4.18b. When $\frac{(n_\uparrow - n_\downarrow)(r=r_{\min})}{(n_\uparrow - n_\downarrow)(r=0)} = 1$, the minimum is located precisely at $r = 0$. Otherwise, this ratio indicates the depth of the minimum. We can see that the closer to $R_{TF,\mathrm{b}}$ the minimum is, the deeper it is. Similar results were obtained for images taken at 854 G. This result can be interpreted as a signature that the superfluid shell, when it is present, is located close to $R_{TF,\mathrm{b}}$.

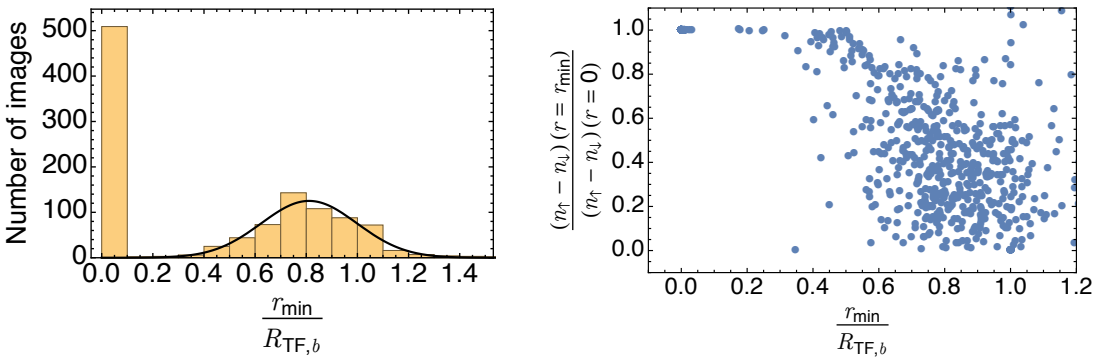

(a) (b)

Figure 4.18: (a) Histogram of the values of $r_{\min}/R_{TF,\mathrm{b}}$ at 817 G. The distribution is strongly bimodal. Black solid line is a Gaussian fit of the data centered around $r_{\min}/R_{TF,\mathrm{b}} = 0.8$. Central value is 0.8 and standard deviation 0.2. (b) Evolution of $(n_\uparrow - n_\downarrow)(r = r_{\min})/(n_\uparrow - n_\downarrow)(r = 0)$ as a function of $r_{\min}/R_{TF,\mathrm{b}}$ for images at 817 G. This shows two different behaviors: either the points are close to $(n_\uparrow - n_\downarrow)(r = r_{\min})/(n_\uparrow - n_\downarrow)(r = 0) = 1, r_{\min}/R_{TF,\mathrm{b}} = 0$ (509 points are superimposed here), or rather towards $(n_\uparrow - n_\downarrow)(r = r_{\min})/(n_\uparrow - n_\downarrow)(r = 0) \lesssim 0.8, r_{\min}/R_{TF,\mathrm{b}} \approx 0.6 \sim 1.1$ (423 points in this area, for a total of 1135 images).

The criteria used to attribute a superfluid kernel, a superfluid shell, or a non-superfluid character are thus the followings:

- If there is a minimum at $r = 0$, there is a superfluid kernel.
- If there is a minimum between $0.5\, R_{TF,\mathrm{b}}$ and $1.5\, R_{TF,\mathrm{b}}$ and the density difference ratio $\frac{(n_\uparrow - n_\downarrow)(r = r_{\min})}{(n_\uparrow - n_\downarrow)(r = 0)}$ is smaller than 0.6[8], there is a superfluid shell.
- Else, if no minimum is present, or if it is not deep enough, there is no superfluid.

4.4.5 Parameters influencing the superfluid shell on the BEC side

4.4.5.1 Presence of bosons

Once the criteria have been proposed, it is important to check whether they are pertinent and whether we can recover well-established results. We thus apply this method to images without bosons, hence without a flat bottom trap. We expect to see only superfluid kernels up to the Clogston-Chandrasekhar limit (76 % at unitarity, ~ 90 % at 817 G and ~ 57 % at 854 G).

At 817 G, we can check that all images with a polarization below 90 % show a superfluid kernel. The result of this analysis is shown in Figure 4.19.

The fact that nearly 100 % of the images without bosons show a superfluid kernel and no shell below the critical polarization validates the approach given above. The

[8] The value of 0.6 is chosen because the histogram as a function of $\frac{(n_\uparrow - n_\downarrow)(r = r_{\min})}{(n_\uparrow - n_\downarrow)(r = 0)}$ reveals a minimum at 0.7. Values above 0.8 correspond to superfluid kernels, and below 0.6 to superfluid shells.

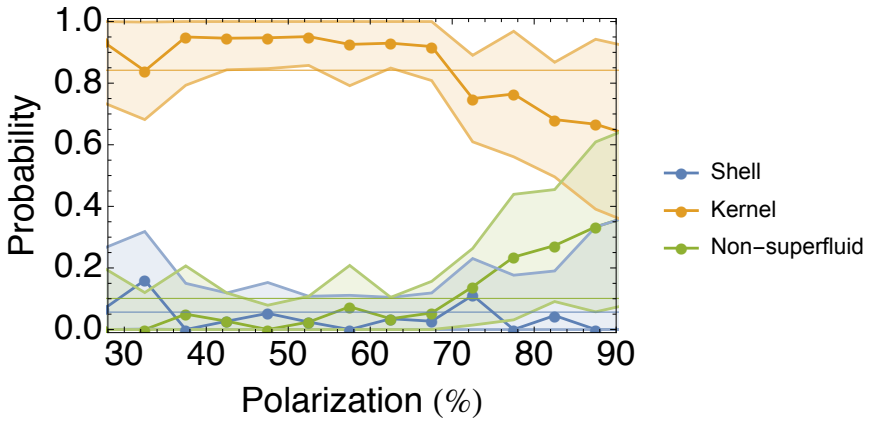

Figure 4.19: Probability of having a superfluid shell (blue), a superfluid kernel (yellow), or no superfluid (green), as a function of polarization. Data correspond to 405 images taken at 817 G ($1/k_{\mathrm{F}}a_{\mathrm{ff}} = 0.2$), without bosons. Shaded areas show 95 % confidence interval.

rise of the non superfluid curve around 85 % indicates the expected breakdown of superfluidity for large spin-imbalance.

4.4.5.2 Polarization

Effect on the existence of the superfluid shell

The same analysis as above can be applied to the data obtained at 817 G with bosons and fermions. Results are shown in Figure 4.20.

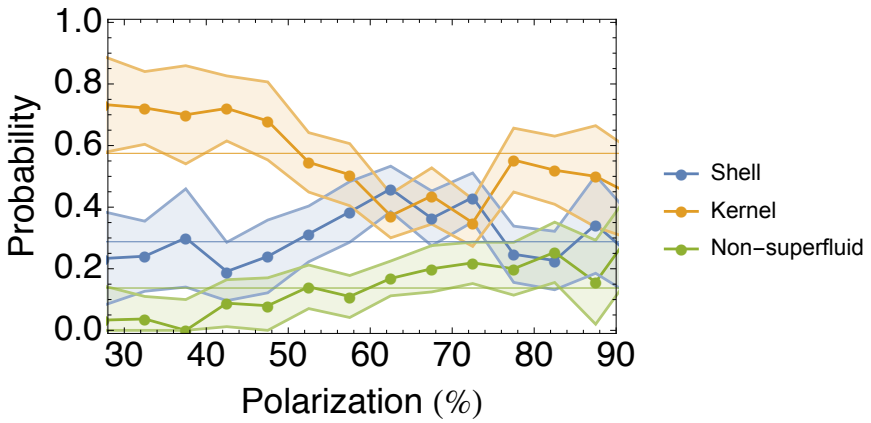

Figure 4.20: Probabilities at 817 G of having a superfluid shell (blue), a superfluid kernel (yellow), or no superfluid at all (green), as a function of spin-polarization, with their 95 % confidence intervals.

At 817 G (Figure 4.20), is seems that while the superfluid kernel is dominating up to a polarization of about 60 %, in the [60 %,75 %] polarization range, the probabilities of the superfluid kernel and superfluid shell are more or less equal. This equipartition

is in agreement with results from [Ozawa *et al.*, 2014] in which the Superfluid-Normal scenario (leading to a superfluid kernel) and the Normal-Superfluid-Normal scenario (leading to a superfluid shell) had similar energies. In this case, we indeed expect similar occupation probabilities for these two scenarios.

Effect on the size of the superfluid shell

Once the existence of the shell is established, it is possible to use a more adapted function to fit the data. Theoretical shell predictions of Figure 4.11b show that the radial density difference $n_\uparrow(r) - n_\downarrow(r)$ should be first non-zero and constant from $r = 0$ to $r = r_{S,\text{int}}$, corresponding to the inner normal phase, then equal to zero from $r = r_{S,\text{in}}$ to $r = r_{S,\text{out}} = R_{TF,\text{b}}$, then decreasing to zero from $r = R_{TF,\text{b}}$ to $r = R_{TF,\uparrow}$. Here $r_{S,\text{in}}$ and $r_{S,\text{out}}$ correspond the the inner and outer radii of the shell. If we recover the weak-LDA result from subsection 4.4.3 $\frac{d\bar{n}(z)}{z\,dz} = -2\pi\frac{\omega_z^2}{\omega_\rho^2}n(z)$, and apply it to the radial density difference described above, we obtain that the doubly integrated density is a continuous piecewise function that is a parabola from $z = 0$ to $z = r_{S,\text{in}}$, then a constant from $r_{S,\text{in}}$ to $r_{S,\text{out}}$, and finally decays from $r_{S,\text{out}}$ to $R_{TF,\uparrow}$. Graphical definitions of r_{min}, $r_{S,\text{in}}$ and $r_{S,\text{out}}$ are given in Figure 4.21.

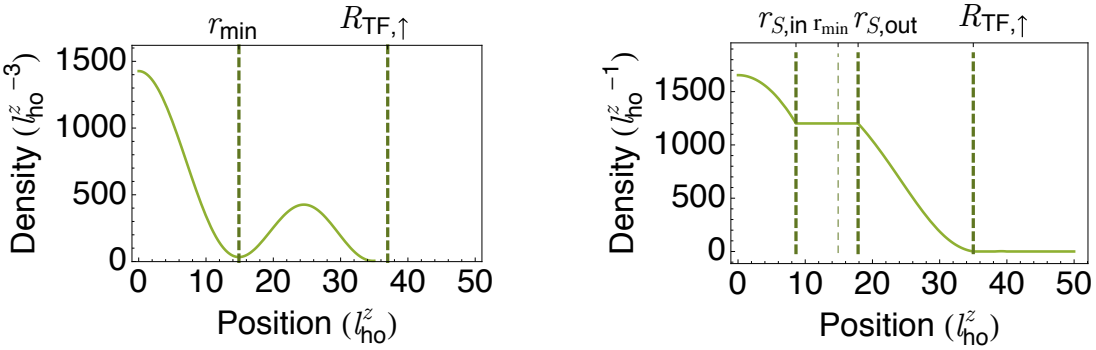

(a) (b)

Figure 4.21: (a) Definition of r_{min}, the minimum position of the reconstructed radial density difference. (b) Typical fit function used on a doubly-integrated density profile when a shell has been identified, and definition of $r_{S,\text{in}}$ and $r_{S,\text{out}}$. Definition of $R_{\text{TF},\uparrow}$ is recalled.

To obtain information about the shell, we thus use this model as a fit function, with $r_{S,\text{in}}$ and $r_{S,\text{out}}$ as free parameters. Typical shell fitted profiles are shown in Figure 4.22.

In Figure 4.23a is shown the evolution of $r_{S,\text{in}} - r_{\text{min}}$ and $r_{S,\text{out}} - r_{\text{min}}$, as well as $r_{\text{TF,b}} - r_{\text{min}}$, as a function of polarization. We see that r_{min}, the local minimum of the reconstructed radial density profile, is as expected roughly in the middle of the shell. The evolution of the shell thickness $r_{S,\text{out}} - r_{S,\text{in}}$ as a function of polarization is also shown in Figure 4.23b. In the [60 %,75 %] polarization range corresponding to the frequent observation of the superfluid shell, it seems that the thickness of the shell does not strongly depend on the polarization.

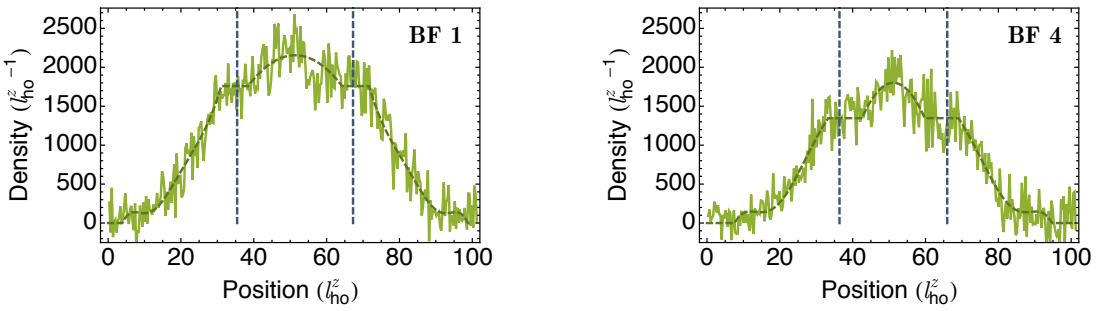

(a) $N_b = 63 \cdot 10^3$, $N_f = 180 \cdot 10^3$, $P = 60\%$. (b) $N_b = 30 \cdot 10^3$, $N_f = 60 \cdot 10^3$, $P = 64\%$

Figure 4.22: (a) Shell fit of BF 1. (b) Shell fit on another typical profile.

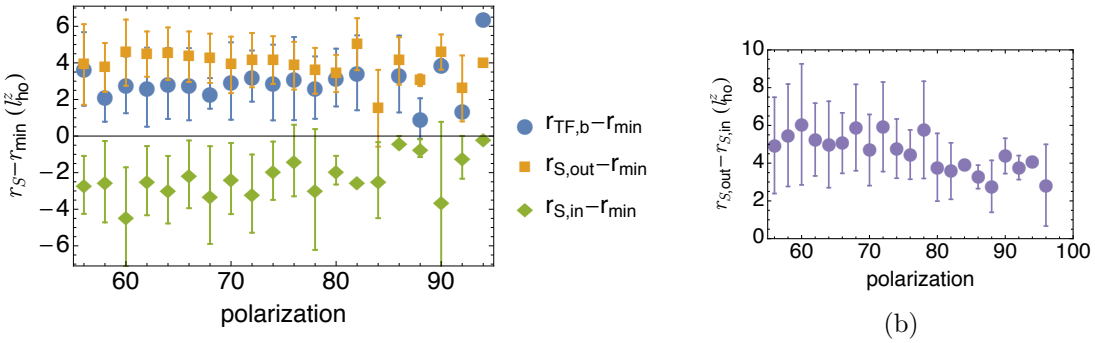

(a) (b)

Figure 4.23: (a) Evolution of $r_{S,\text{in}} - r_{\min}$ (green diamonds), $r_{S,\text{out}} - r_{\min}$ (yellow squares) and $r_{\text{TF,b}} - r_{\min}$ (blue dots) as a function of polarization. $r_{\min}$ is the local minimum of the reconstructed radial density profile, $r_{S,\text{in}}$ is the inner radius of the shell, and $r_{S,\text{out}}$ its outer radius. (b) Evolution of the shell thickness $r_{S,\text{out}} - r_{S,\text{in}}$ as a function of polarization. Error bars correspond to one standard deviation. $l_{\text{ho}}^z = 9.8\,\mu\text{m}$ is the harmonic oscillator length in the axial direction.

4.4.5.3 Influence of atom number

We now turn to the analysis of the effect of atom number on the shell thickness. We restrict the analysis to images the polarization of which is within the range [60 %,75 %] where the shell is relevant. Influence of bosonic N_b and fermionic N_f on the shell thickness is given in Figure 4.24. It seems that shell thickness decreases with increasing N_b, and increases with N_f but the large error bars do not allow us to conclude.

4.4.6 Parameters influencing the superfluid shell on the BCS side

The same analysis can be performed at 854 G, on the BCS side. This magnetic field is of particular interest because the interaction parameter $1/k_F a_{ff} \approx -0.25$ is close to the predicted FFLO conditions (see Figure 0.1). Similar behavior as for 817 G can be observed, with hints both for shells and for kernels (see for instance Figure 4.25a for a shell and Figure 4.25b for a kernel).

The same reconstruction procedure leads to reconstructed radial density profiles

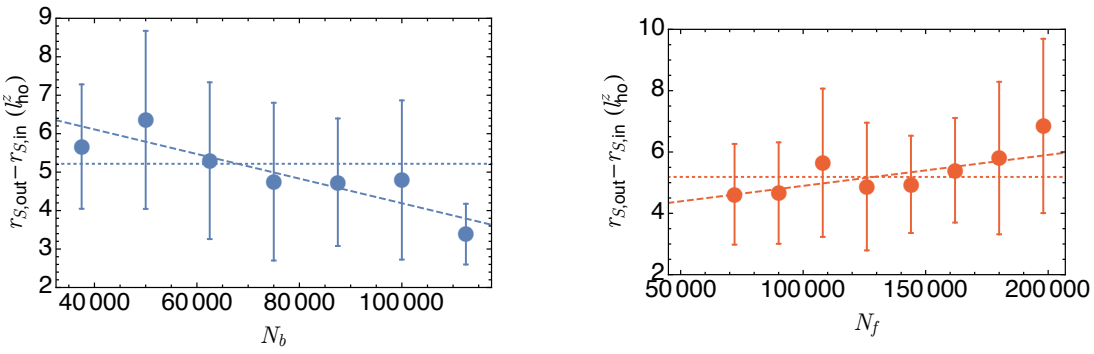

(a) (b)

Figure 4.24: (a) Evolution of $r_{S,\mathrm{out}} - r_{S,\mathrm{in}}$ as a function of bosonic atom number N_b, restricted to the [60 %,75 %] polarization range. (b) Evolution of $r_{S,\mathrm{out}} - r_{S,\mathrm{in}}$ as a function of fermionic atom number N_f, restricted to the [60 %,75 %] polarization range. Dashed lines: linear fits. Dotted lines: mean values. Error bars correspond to one standard deviation.

shown in Figure 4.25c and Figure 4.25d. As before, depending of the existence of a minimum close to $r = 0$ (as in Figure 4.25d), or for a finite r close to $R_{TF,\mathrm{b}}$ (as in Figure 4.25c), we use an adapted piecewise function to know the position and extension of the superfluid plateau. Fits using such piecewise functions on the profiles are shown in Figure 4.25e (for a shell) and Figure 4.25f (for a kernel).

Here again, the contrast of the minimum of the density difference (see green curves in Figure 4.25c and Figure 4.25d) can be plotted as a function of its position, and as before we find that the minimum is either located close to $r = 0$ or close to $r = R_{TF,\mathrm{b}}$, see Figure 4.26b, and the same criteria are used to discriminate between a superfluid kernel, a superfluid shell, or no superfluid at all.

However, at 854 G the statistical analysis is not conclusive, see Figure 4.27. This can be due to a lower number of images (288 instead of 1135). Another explanation would rely on the relative sharpness of the FBT condition (see subsubsection 4.2.2.2). Indeed, the dataset gathers images taken on different days, and since the FBT condition is sharper at 854 G than it is at 817 G, it is also possible that day-to-day magnetic field fluctuations drove the system back and forth across the $g_{\mathrm{bb}} = g_{\mathrm{bf}}$ condition, or simply that we made a small mistake in the magnetic field calibration that drove us away from the FBT condition and into the anti-trapping regime (see Figure 4.3c). This would explain the apparent prevalence of the superfluid shell in Figure 4.27. We plan to investigate this situation in much greater detail.

The dependence of the shell parameters at 854 G with the polarization and atom numbers are shown in Figure 4.28. They do not differ significantly from the ones at 817 G.

4.4.7 Portrait of the superfluid shell

With the information gathered above, we can draw a portrait of the superfluid shell. It is presented in Table 4.2.

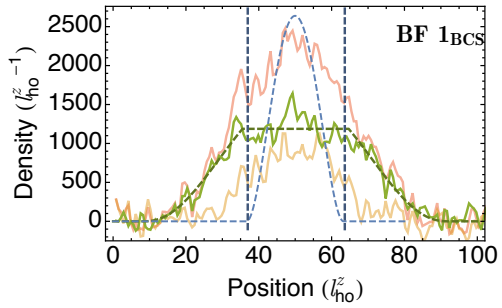

(a)

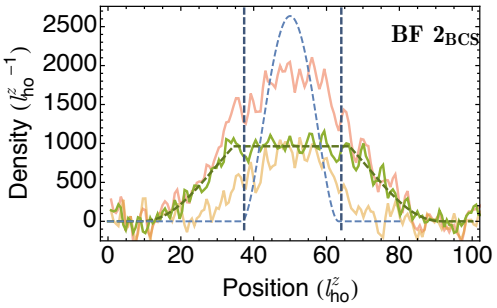

(b)

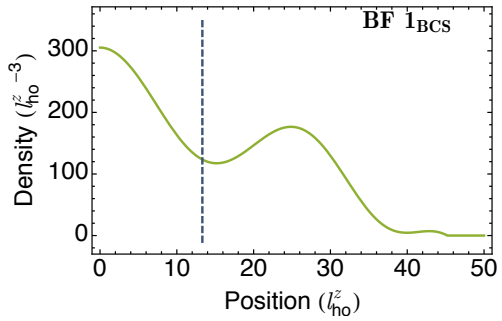

(c)

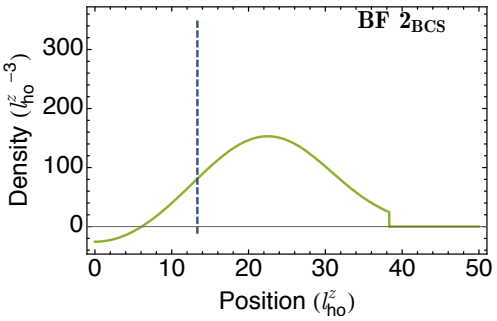

(d)

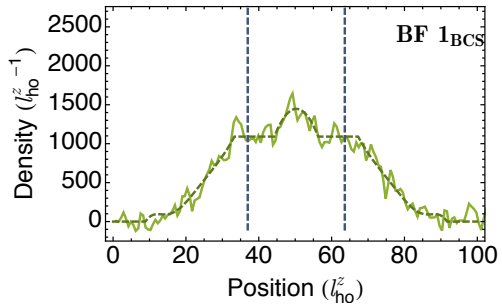

(e)
Shell example at 854 G

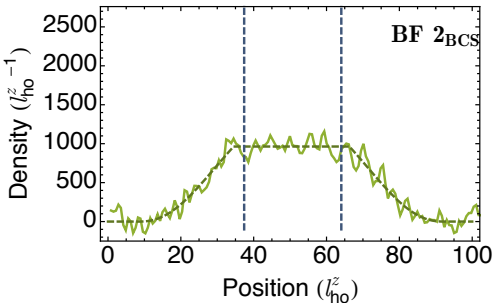

(f)
Kernel example at 854 G

Figure 4.25: (a) Typical density difference showing the existence of a superfluid shell at 854 G. Here $N_f = 110 \cdot 10^3$, $N_b = 38 \cdot 10^3$ and $P = 52\,\%$. (b) Typical density difference showing the existence of a superfluid kernel at 854 G. Here $N_f = 90 \cdot 10^3$, $N_b = 38 \cdot 10^3$ and $P = 48\,\%$. (c) and (d) Corresponding reconstructed radial density profiles with weak LDA method. (e) and (f) Green dashed curves: piecewise functions used to extract the position and thickness of the superfluid shell (e) or the extension of the plateau (f). Red and yellow dashed curves are guides to the eye for the doubly-integrated density of the majority (red curve) and minority (yellow curve) components. Vertical dashed blue lines indicate the Thomas-Fermi radius of the condensate.

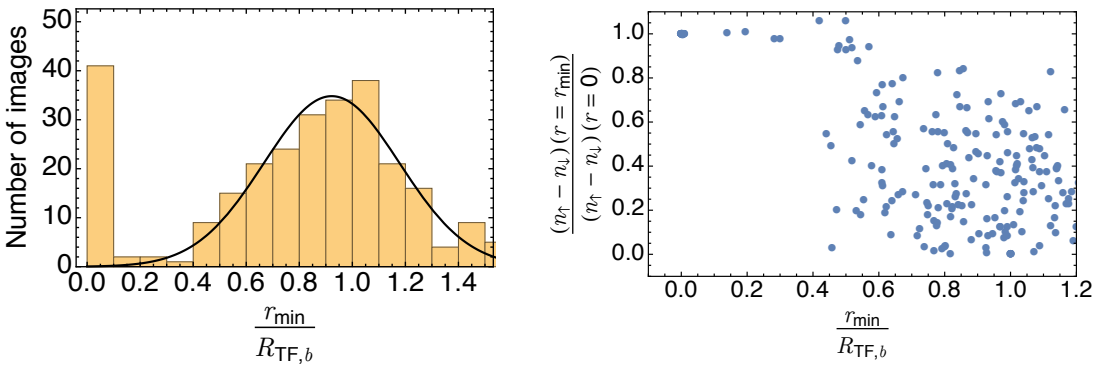

(a) (b)

Figure 4.26: (a) Histogram of the values of $r_{\min}/R_{TF,\mathrm{b}}$. The distribution is strongly bimodal. Black solid line is a Gaussian fit of the data centered around $r_{\min}/R_{TF,\mathrm{b}} = 0.9$. Central value is 0.9 and standard deviation 0.25. (b) Evolution of $(n_\uparrow - n_\downarrow)(r = r_{\min})/(n_\uparrow - n_\downarrow)(r = 0)$ as a function of $r_{\min}/R_{TF,\mathrm{b}}$ for images at 854 G. This shows two different behaviors: either the points are close to $(n_\uparrow - n_\downarrow)(r = r_{\min})/(n_\uparrow - n_\downarrow)(r = 0) = 1, r_{\min}/R_{TF,\mathrm{b}} = 0$ (41 points are superimposed here), or rather towards $(n_\uparrow - n_\downarrow)(r = r_{\min})/(n_\uparrow - n_\downarrow)(r = 0) \lesssim 0.8, r_{\min}/R_{TF,\mathrm{b}} \approx 0.6 \sim 1.1$ (165 points in this area, for a total of 288 images).

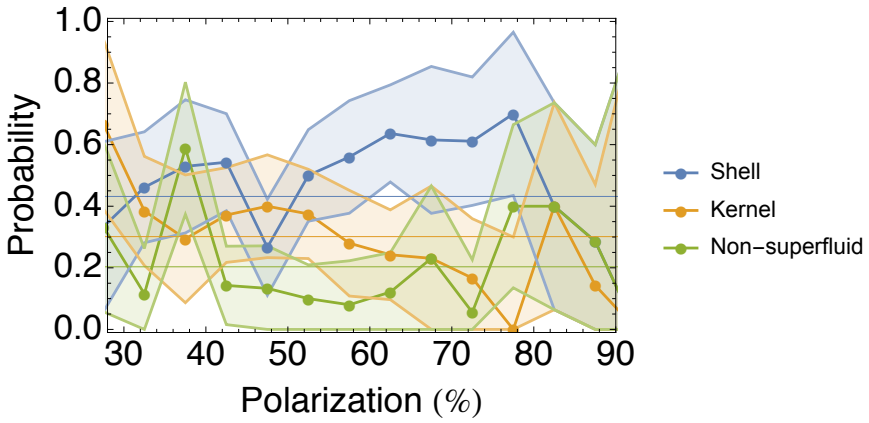

Figure 4.27: Probabilities at 854 G of having a superfluid shell (blue), a superfluid kernel (yellow), or no superfluid at all (green), as a function of spin-polarization, with their 95 % confidence intervals.

The parameter range that can be explored in the shell in represented by orange areas in Figure 4.29. It shows that the mean-field FFLO conditions are probably within a range accessible in the experiment.

4.5 Conclusion

In this chapter we have introduced a new way to realize an effective flat bottom trap for fermions. It relies on the idea that a BEC in a harmonic trap has a parabolic profile.

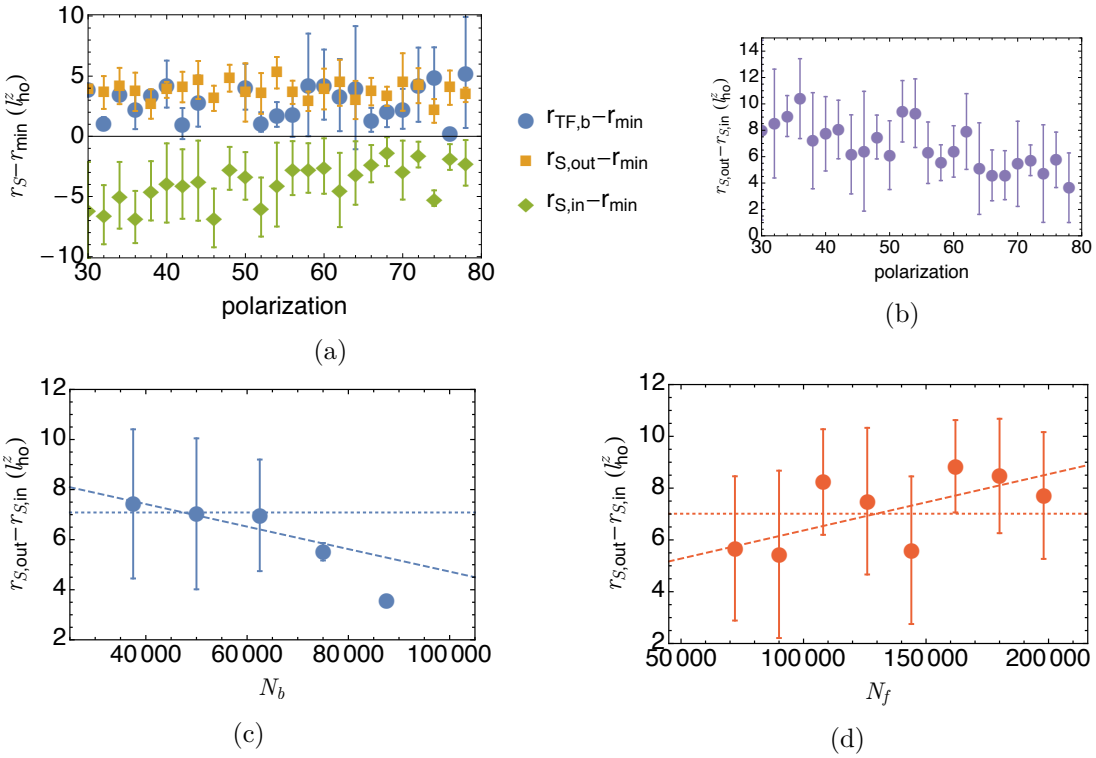

Figure 4.28: (a) Evolution at 854 G of $r_{S,\mathrm{in}} - r_{\mathrm{min}}$ (green diamonds), $r_{S,\mathrm{out}} - r_{\mathrm{min}}$ (yellow squares) and $r_{S,\mathrm{TF,b}} - r_{\mathrm{min}}$ (blue dots) as a function of polarization. r_{min} is the local minimum of the reconstructed radial density profile, $r_{S,\mathrm{in}}$ is the inner radius of the shell, and $r_{S,\mathrm{out}}$ its outer radius. (b) Evolution of the shell thickness $r_{S,\mathrm{out}} - r_{S,\mathrm{in}}$ as a function of polarization. (c) (resp. (d)) Evolution of $r_{S,\mathrm{out}} - r_{S,\mathrm{in}}$ as a function of boson number N_{b} (resp. fermion number N_{f}), restricted to the [40 %,60 %] polarization range. Dashed line is a linear fit, dotted line is the mean value of the shell thickness. Error bars correspond to one standard deviation. $l_{\mathrm{ho}}^z = 9.8\,\mu\mathrm{m}$ is the harmonic oscillator length in the axial direction.

Tunable mean-field interactions between the BEC and another species (here fermionic ^{6}Li) offers the possibility to cancel the trap curvature in the vicinity of the BEC volume. This method has some universal character, in the sense that it does not depend on the situation of the other species and could be applied, for instance, to both a single-component Fermi gas or to a two-component Fermi gas (spin-imbalanced or not). Since the Bose-Fermi scattering length of $\sim 41 a_0$ is mainly identical for all spin-states and independent of the magnetic field in a broad range ($\sim 700 - 900$ G) while the boson-boson scattering length encounters several Feshbach resonances, several combinations of states can be chosen, leading to different values for the interaction parameter $1/k_{\mathrm{F}}a_{\mathrm{ff}}$. In collaboration with the Trento group, we predicted that for a spin-imbalanced Fermi gas at unitarity in such a flat bottom trap, the Clogston-Chandrasekhar limit would be modified and that some new topological superfluid phases, such as a shell-shaped superfluid, could arise. The experimental implementation of the flat bottom trap, for two magnetic fields (817 G, on the BEC side and 854 G, on the BCS side) close

	BEC side	BCS side
Magnetic field (G)	817	854
Averaged $1/k_{\mathrm{F}}a_{\mathrm{ff}}$	0.2	-0.25
Polarization range for existence of shells	$[60\,\% - 75\,\%]$	$\sim [40\,\% - 60\,\%]$ ($\pm 10\,\%$)
Probability of shells in existence range	50(10) %	60(20) %
$1/k_{\mathrm{F}}a_{\mathrm{ff}}$ in shell	0.30(7)	-0.37(10)
Shell thickness	50(5) µm	70(5) µm
n_s in shell (cm^{-3})	$\sim 10^{12} - 5 \cdot 10^{13}$	$\sim 10^{12} - 5 \cdot 10^{13}$
% atoms in shell		
fermions	10-20 %	10-20 %
↑-atoms	10 %	10 %
↓-atoms	30-50 %	30-50 %

Table 4.2: Preliminary portrait of the shell

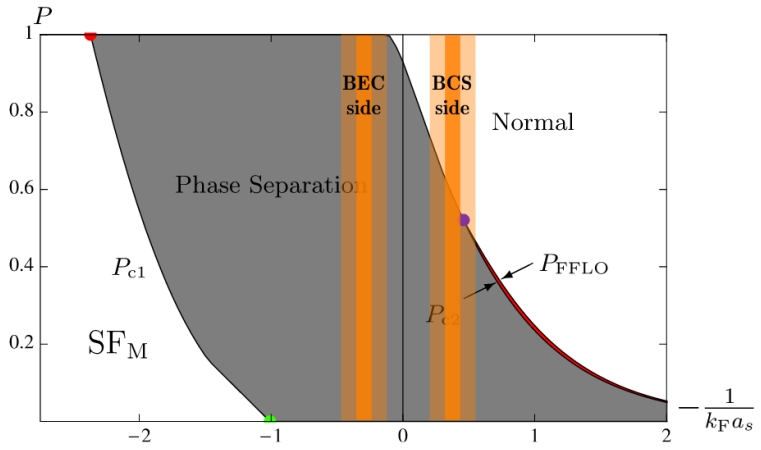

Figure 4.29: Mean-field phase diagram for FFLO phases. The areas indicated in bright orange correspond to the areas explored with the experiments presented here. The faint orange areas correspond to a range of interaction parameters accessible within the homogeneous area. Adaptation of Figure 0.1 from [Radzihovsky and Sheehy, 2010]. The gray area correspond to phase separation between a fully-paired superfluid and a polarized normal phase.

to unitarity $|1/k_{\mathrm{F}}a_{\mathrm{ff}}| \lesssim 0.25$ and the numerical reconstruction of the radial profiles from one-dimensional absorption images were realized. At 817 G, in the $[60\% - 75\%]$ polarization range, the repeated presence of a minimum in the reconstructed radial density difference was interpreted as an evidence for a superfluid shell. This superfluid shell could be seen only in images with a BEC, and is clearly made possible only by the presence of the bosons. This novel phase is consistent with mean-field theoretical predictions. It does not provide direct proof of the flat bottom trap, for instance it could be enhanced by a small anti-trapping potential in the BEC volume. This would

increase the fermionic density close to the bosonic Thomas-Fermi radius and favor the shell. The currently ongoing detailed study of the role of $g_{\mathrm{bb}}/g_{\mathrm{bf}}$ will clarify this situation and bring better knowledge of the flat bottom trap. Also the 854 G condition on the BCS side of the resonance deserves much more detailed studies.

Another point is that so far we always prepared the clouds at a magnetic field where $g_{\mathrm{bb}} > g_{\mathrm{bf}}$ before ramping it to the flat bottom trap condition. Dynamical aspects of shell formation would be original observations.

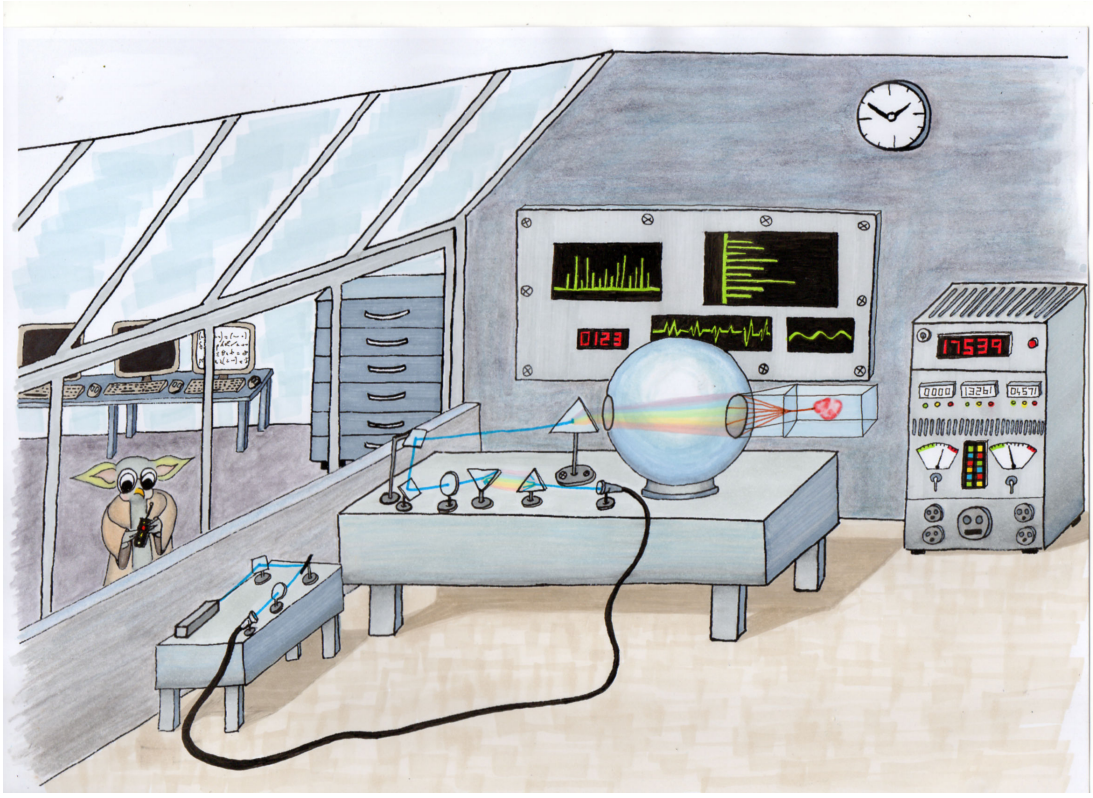
0123
17539
0000
13261
0457

Chapter 5

New Lithium Machine

During the first half of my PhD, I had been doing several side projects to improve the old lithium machine: adapting Cicero (a control software for cold atoms experiments) to the specificities of our experiment[1] in order to replace the MS DOS control computer, building a whole new laser system that would not rely on slave laser diodes, to increase laser power and run-to-run stability, preparing some beams for transverse cooling of the atoms flux before the Zeeman slower, etc. Finally, since some of the

[1]The historical experiment built by Florian Schreck was using Digital-to-Analog Converters (DAC) to generate analog signals.

parts of the historical lithium experiment started to be very old, and even though the two water leaks could be fixed and the broken coil replaced, it seemed that it was time to, instead of upgrading the experiment, build a complete new experiment that would be more versatile, more reliable, and would take advantage of a new technique unveiled in our group: sub-Doppler D_1 cooling. Using it, it is possible to skip all of the magnetic trapping stages of the previous experiment and have (hopefully) a much simpler and shorter experimental sequence. When it became unavoidable that our lab closed for a few months due to major construction work taking place at the ENS, we decided to use this period to start building the new experiment.

The goals are still to be able to produce a superfluid mixture of ^{7}Li and ^{6}Li, but with a faster experimental sequence, more reliable, with less day-to-day realignment, and a better optical access. This will enable us further push superfluidity studies in tailored optical potentials and to search for the famous FFLO phase in spin imbalanced systems.

This chapter is organized as follow: first, I will give the ideas at the origin of the new experiment, then describe its mechanical organization, its laser system, and finally write a few words about computer control and security circuit. The building is on its way but not over, so this document does not intend to give all of the details of the new experiment.

5.1 Overview

5.1.1 "Cahier des charges"

The design of the new experiment has to obey several requirements, and to provide improvements with respect to the old one. Requirements are listed below, with a proposal for their realization.

- Ultracold mixtures of ^{6}Li and ^{7}Li. This is the main specificity of our experiment, which led to the first realization of a double Bose-Fermi superfluid mixture, and there is a lot of experimental competences in the group regarding this point. We will use a 50/50 mixture of ^{6}Li and ^{7}Li in the oven.

- Fast sequence. This used to be a limitation of the old experiment, with $\geq 30\,$s of MOT loading and $\geq 20\,$s of RF evaporation. The repetition rate was at most one sequence per minute, usually more like one sequence every two minutes. The plan is to have a $20\,$s sequence, with a fast MOT loading and no RF evaporation (that will be replaced by D_1 cooling).

- High optical access for better imaging resolution. For this we need two chambers. One for the MOT and other pre-cooling stages ("MOT chamber"), and one for the actual physics experiments ("science chamber"). We already had a similar situation with the previous experiment, with the appendage acting as the science chamber, but optical access was strongly reduced by the presence of the Ioffe bars.

- Mechanical stability. On the old lithium experiment, all of the optics were mounted on high posts, and the MOT mirrors were held on high pillars. Here,

we plan to use low posts for the optical tables, and to mount the MOT and D_1 cooling optics very close to the atoms, directly on the MOT chamber.

- Laser stability. With 10 slave diodes, this was always a big problem as well. To circumvent it, we plan to use no diode except for two of the three master lasers, and amplify the optical power with Tapered Amplifiers (TAs)[2].

- Day-to-day stability. Within the new lab, it will be possible to have the experiment in one room, and to have the computer control on the other side of the wall. This way, perturbations of the experiment are minimized, with less dust, vibrations, etc.

- Relatively simple. With a limited number of traps, and using always ^{6}Li to cool down ^{7}Li, the experiment should be easier to handle.

- Versatile. We want to be able to study different aspects of the physics of ultracold gases, be able to install lattices, low-dimensions traps, or an imaging system with a very good resolution, etc. For this, the space around the science cell is so far completely empty. We also plan to do the computer control of the experiment with Cicero, a very convenient and practical software for cold atoms experiments designed by Aviv Kesheet at MIT. It will be much easier to make changes in the experimental sequence than with the historical software working with MS-DOS computers...

With such improvements we are very confident it the fact that we will be able to observe new original effects in Bose-Fermi mixtures. Most of these improvements rely on a specific cooling technique, called gray molasses D_1 cooling. Let us now detail a bit more about it before moving to the provisional experimental sequence.

5.1.2 D_1 cooling

In the old experiment, the temperature at the end of the CMOT stage is about 600 µK. Even though it has been made successfully by other groups [Fuchs *et al.*, 2007], it is not straightforward to load directly a MOT of lithium atoms into an optical dipole trap. Indeed, for the case of lithium (and conversely potassium), the temperature obtained at the end of the MOT stage are much higher than for other alcali atoms such as sodium, cesium or rubidium. The naive temperature limit for a two-level atom in an optical molasses is the Doppler temperature $T_D = \hbar\Gamma/2K_B$, where Γ is the width of the excited state. However, the first realization of optical molasses and magneto-optical traps [Chu *et al.*, 1985, Chu *et al.*, 1986, Lett *et al.*, 1988] showed that the temperatures reached were well below T_D. This could be explained later by taking into account a three-level structure for the atoms and polarization gradients for the lasers [Dalibard and Cohen-Tannoudji, 1989, Ungar *et al.*, 1989], and this effect is now known as Sisyphus cooling. It is widely used in different gray molasses schemes [Chu,

[2] TAs are optical amplifiers composed of a tapered-shaped gain medium. When they are seeded with properly aligned single mode frequency laser, the re-emit amplified light at the same frequency, at the price of a relatively poor spatial mode (max. 50 % coupling efficiency) and a background pedestal over a few nanometers in the frequency spectrum.

1991, Weidemüller *et al.*, 1994, Boiron *et al.*, 1998, Aspect *et al.*, 1988, Grynberg and Courtois, 1994, Boiron *et al.*, 1995]. On the contrary, the efficiency of Sisyphus cooling is strongly reduced for D_2 lines of lithium because excited states are not resolved: the total hyperfine splittings of 4.5 MHz for ^{7}Li and 18.0 MHz for ^{6}Li are comparable with their natural linewidth of $\Gamma = 5.9$ MHz.

Gray molasses were designed based on Sisyphus cooling more than 20 years ago, but it was rediscovered only recently by Fermix, the other team of the Ultracold Fermi group at LKB [Fernandes *et al.*, 2012]. Its principle is the following: consider a near-resonant laser beam (with detuning Δ) applied to a Λ-like three-level atom with two degenerate ground states and one excited state, and assume that one of the ground state is dark while the other one is bright. Which state is dark or bright depends on the atomic transition and of the light polarization, this may even vary in space (if the polarization varies). The dark state is transparent for the laser and is not coupled to the excited state, but may be coupled to the bright state via motional coupling. The bright state however is coupled to the excited state by the laser and will undergo a light shift proportional to the laser's intensity. If the light comes from counter-propagating beams, the resulting light intensity will be a standing wave and the light shift will be periodic: $\delta E = \frac{\hbar\Omega(r)^2}{4\Delta}$, with $\Omega(r)$ the Rabi frequency associated to the standing wave, proportional to the square root of the light's intensity. In the dressed atom picture that we will use in the following, since the excited to which the bright state is coupled have a finite linewidth Γ, the bright state also have some effective width $\Gamma' = \Gamma\frac{\Omega(r)^2}{\Delta^2}$. This is summed up in Figure 5.1.

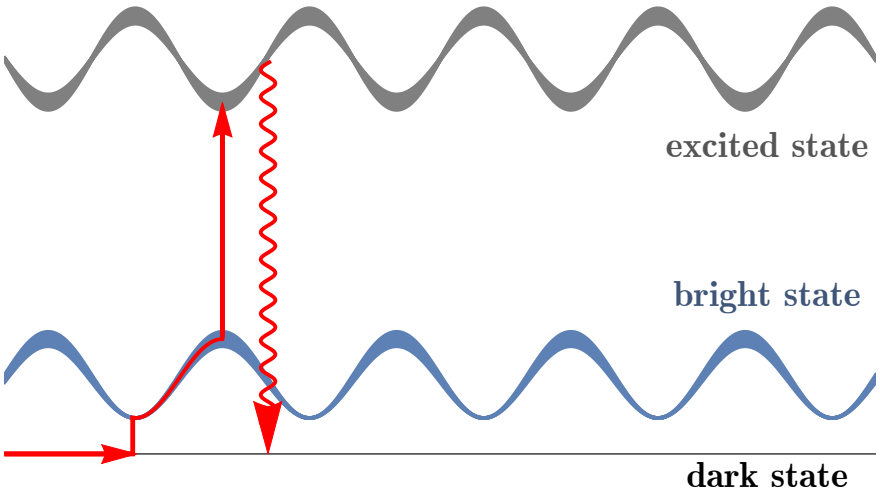

Figure 5.1: Scheme of the Sisyphus cooling for $\Delta > 0$ in the dressed atom picture. The dark state is shown in black, the bright state in blue, with its light shift and effective linewidth, and the excited state in gray.

The cooling process is now described for the case of a blue-detuned laser beam: $\Delta > 0$ (here a red-detuned laser beam, with $\Delta < 0$ would lead to heating). An atom in a dark state may be transferred to the bright state due to motional coupling.

This happens when the energy difference between the dark and the bright state is the smallest, that is in the valleys of the bright state's potential. The atom then climbs the valley, and its probability to be pumped into the excited state increases as the linewidth of the bright state increases, and is maximal at the top of the hills. Once it is pumped into the excited state, it may decay via spontaneous emission to the dark state, with a net loss of energy, so that the cloud is cooled down. Another circle may start again.

This method can be applied to any system with a dark state in the ground states manifold (this is the case for any transition $F \to F' \leq F$), provided that the excited state can be resolved. We thus have to use the D_1 line. We have successfully implemented this technique on the $F = 2 \to F' = 2$ transition of the D_1 line of ^{7}Li and obtained temperatures of 50 µK, more than ten time smaller than in the standard cooling sequence and with the same atomic density[Grier *et al.*, 2013]. The crucial point is that, now direct loading of an optical dipole trap can be achieved with a reasonable dipole trap power of $\sim$20 Watts focused over 40 µm [Burchianti *et al.*, 2014]. Our colleagues from Fermix experiment applied it simultaneously to ^{6}Li and ^{40}K [Sievers *et al.*, 2015]. It is now used in many other groups, such as Mumbai group [Nath *et al.*, 2013], Institut d'Optique group [Salomon *et al.*, 2013], LENS group [Burchianti *et al.*, 2014], Ketterle group at MIT (private communication), and others.

5.1.3 Experimental sequence

The organization for the new experimental sequence is the following. We plan to keep on having ^{6}Li and ^{7}Li mixtures. Both species exit the same oven, are slowed down by an inverted Zeeman slower, and then trapped into a MOT. The MOT should have more ^{6}Li than ^{7}Li atoms with a loading rate on the order of 10 seconds. After this, we run a compressed MOT (CMOT) to increase phase-space density. A gray molasses should then be imposed to the cloud. Here, some uncertainties remain: a D_1 blue-detuned molasses will cool down ^{6}Li atoms, but we haven't decided yet how we will cool down ^{7}Li atoms. So far, we have three options:

- If the thermalization with ^{6}Li is sufficiently efficient and no further cooling will be needed.
- If not, we can try to implement a blue-detuned D_1 molasses on ^{7}Li. However, due to a coincidence between ^{7}Li D_1 line and ^{6}Li D_2 line, this may heat up ^{6}Li.
- The efficiency of far red detuned lithium cooling has also been demonstrated in [Hamilton *et al.*, 2014]. This can also be implemented in the new experiment.
- In the last case, we can implement a UV-MOT cooling stage, as was shown in [Duarte *et al.*, 2011]. This technique is the least-favored one, because it requires special optics and a coherent source at 323 nm, a wavelength range where power is still limited.

After this D_1 cooling stage, the phase-space density will be high enough to allow direct loading into a far-detuned 200 W optical dipole trap for both species to perform optical transport into the science cell. We plan to do optical transport with focus-tunable

lenses, as was demonstrated in [Léonard *et al.*, 2014]. This tunable lens is sensitive to temperature variations and might be subject to thermal lensing. To overcome this, we plan to do a pre-evaporation stage with the two lowest spin states of ^{6}Li before transport[3], in a dipole trap different from the one that we will use for optical transport. Since at low magnetic fields, the scattering length between ^{6}Li Zeeman sub-levels is very small (see Figure 5.2), we need to go at a magnetic field of 300 G. There, the scattering length between the spin states is around $-300\,a_B$, which allows efficient evaporation. The ^{7}Li is sympathetically cooled by ^{6}Li, with interspecies scattering length of $\sim 40\,a_B$. Some optical pumping on ^{7}Li might be realized at this stage to ensure state purity of ^{7}Li. In the science cell, we ramp up the magnetic field up to ≈ 800 G and resume the evaporation of ^{6}Li down to quantum degeneracy. We then have several projects in mind, for instance using the high optical access and spatial resolution of the science cell to load the atoms in a flat potential, as was demonstrated in [Gaunt *et al.*, 2013, Corman *et al.*, 2014], and investigate the phase diagram of strongly correlated fermions with and without spin polarization.

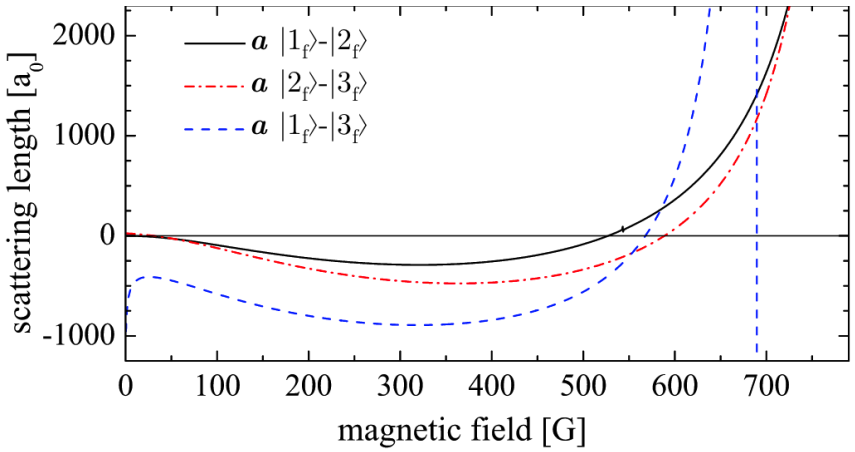

Figure 5.2: Evolution of the ^{6}Li scattering lengths as a function of magnetic field for different Zeeman sub-levels combinations from [Ottenstein *et al.*, 2008]. The labeling of the levels refer to Figure 2.3.

5.2 Mechanical setup

The mechanical design of the new experiment is represented in Figure 5.3. It will be detailed in the following sections.

5.2.1 Oven

The oven is composed of a T-like tube[4], the same as the one on Figure 2.6. Lithium will be inserted from the top and heated up at 510°C in order to get a high vapor

[3] After the D_1 cooling stage, ^{6}Li atoms will be naturally in the two-lowest-spin states of the system: $|F = 1/2, m_F = \pm 1/2\rangle$.

[4] custom-made from MDC-Vacuum

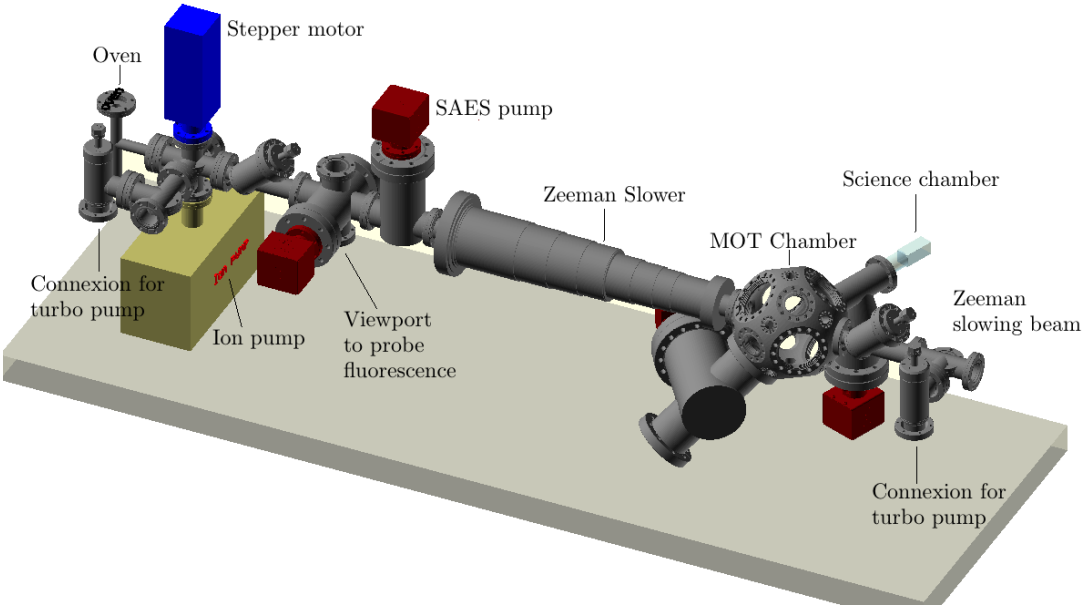

Figure 5.3: Scheme of the new Li experiment. The oven is at the extreme left, SAES pumps are in red, in blue is the atomic beam block rotating mount and motor. The main cell is the MOT chamber and the science cell is in light blue at the back of the MOT cell.

pressure. There will be a 50/50 mixture of ^{6}Li and ^{7}Li in the oven. In the previous experiment, the horizontal part of the tube tended to clog with lithium, leading to low atomic flux and low atom number in the MOT. The tube can be unblocked by heating it up for a while, but the major problem consisted in the fact that we never knew whether the tube was blocked or the experiment just not working so well. To prevent this in the new experiment, viewports to monitor the atom flux have been planned. A rotatable stepper motor[5] (in blue on Figure 5.3) will be used to block the atomic jet when the experiment is not running or after the loading stage of an experimental sequence.

5.2.2 Vacuum system

To ensure a good vacuum in the experiment, we have chosen the following scheme :

- Two turbo pumps can be placed at each end of the experimental apparatus, which will allow the opening of the part containing the oven (to reload or change it) and the part containing the last window of the Zeeman slower (to clean it) without breaking the vacuum of the two main cells. They will not be present during the day-to-day run of the experiment and are not indicated in Figure 5.3, only their connexions are shown.
- One 40 L.s^{-1} ion pump[6] will be placed close to the oven.

[5] Brimrose BRM-275 670002-03
[6] Agilent Technologies StarCell Vaclon Plus 40

- Two 200 L.s^{-1} SAES pumps[7] will be placed afterwards to ensure differential pumping stages.
- One 500 L.s^{-1} SAES pump[8] will pump directly on the MOT chamber
- A last 200 L.s^{-1} SAES pump[9] will ensure a differential pumping stage between the MOT chamber and the science chamber.

To improve the pumping efficiency of the SAES pumps, we chose to connect them to larger tubes: the flanges of NEXTORR D200-5 is CF40 and that of NEXTORR D500-5 is CF63. We will use zero-length reducers[10] to connect them to custom-made tees and crosses[11] so that they can pumps into CF63 and CF100 tubes respectively.

5.2.3 Cells and optical transport

We have decided to use a two-cell setup for the new experiment, with some optical transport between them. This solution has several advantages: a better vacuum in the science cell, and a better optical access to ensure a high versatility to the new experiment. The MOT cell[12] has numerous viewports and we plan to dedicate each of them to a specific function (MOT beams, D_1 cooling, Zeeman slower, imaging, fluorescence, optical transport, ...). The use of each viewport will be detailed in subsection 5.3.3. The science cell[13] is the place where we will produce and study quantum degenerate gases. The plan is to have two facing microscopes to have a high spatial resolution and to be able to imprint custom-made potential on the atoms. The thin 3 mm walls allow the use of some semi-custom commercial microscope.

There will be a $\sim$ 20 cm optical transport between those two cells. Optical transport is usually performed using a corner mirror on an extremely stable translation stage. However, a new option have been developed recently in Tilman Esslinger's group [Léonard *et al.*, 2014] using focus-tunable lenses[14]. These lenses are composed of some optical fluid inside a sealed deformable polymer membrane that has a disk shape. A flat ring applied on the outer part of the lens with more or less pressure pushes more or less the fluid towards the center, making use of the membrane elasticity. This changes the curvature radius of the lens and, as a result, its focal length. A schematic representation is given on Figure 5.4. To ensure best working conditions, it is only needed to hold the lens horizontally (so that gravity deforms the membrane homogeneously), and to use a highly stable current controller. The whole system is extremely cost-efficient.

[7] NEXTORR D200-5. These pumps are hybrid between ion pumps and getters and have a very high pumping efficiency for H_2.
[8] NEXTORR D500-5.
[9] NEXTORR D200-5.
[10] Lesker RF600x450 and RF450x275M
[11] MDC Vacuum ZCRT40-63, ZCRT63-100, ZCRT40-63-Conical, ZCRX6-2-63-4-40
[12] Kimball Physics MCF450-SphCube-E6C8A12
[13] custom-made from ColdQuanta. It is a 25x25x60 mm glass-cell with 3 mm thick walls, AR coatings inside and outside, and a 2° wedge at the end to avoid standing waves during optical transport.
[14] Optotune

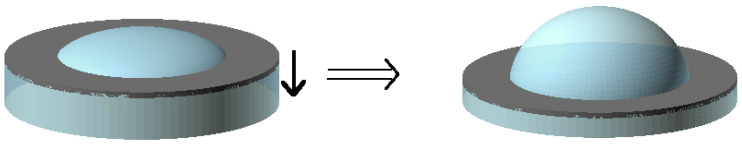

Figure 5.4: Scheme of the process used to change the focal length of the lens. The gray outer rim is pushed downwards and the liquid is pushed inwards. Making use of the membrane's elasticity, the curvature radius is changed, which modifies the focal length. On the left, the tunable lens is tuned to a large focal length, on the right to a small one.

The lens is actually being tested[15], and even though we have not fully decided the optical scheme yet, it is likely that we will load the atoms in a first very powerful dipole trap[16] to make a pre-evaporation, then load them into a second weaker dipole trap that will go through to tunable lens system to transport them. We will probably use a combination of two focus-tunable lenses in order to be able to move the focal point of the beam without changing its waist nor moving the lens.

5.3 Laser setup

To cool the Li gases to degeneracy, we will use both the D_1 and D_2 lines of each isotope. Since there is a coincidence between the D_1 of ^{7}Li and the D_2 of ^{6}Li (which are distant only by 20 MHz), and since the hyperfine splitting for the ground state is at most 800 MHz (for ^{7}Li), we only need three master laser to generate all of the frequencies used in the experiment, the other frequencies are derived from that of the master's lasers using Acouto-Optic-Modulators (AOMs) and Electro-Optic-Modulators (EOMs). We already have one solid-state laser at 670 nm providing a laser power of 800 mW and two Toptica[17] lasers producing a laser power of 500 mW each. The plan in the new experiment is to have a vast majority of ^{6}Li atoms in the MOT and to use ^{6}Li to evaporatively cool ^{7}Li, so most of the optical power will be dedicated to ^{6}Li.

5.3.1 Laser Scheme

The frequencies needed for the new experiment are given in Table 5.1. Proposed laser schemes are shown in Figure 5.6, Figure 5.5 and Figure 5.7. The ideas that led to this design are the following: laser power has always been a problem, so we want to reuse as much of the optical power as possible. As a result, light for applications that happen at different times in the experiment can be derived from the same sources (*e.g.* MOT beams and imaging beams can be derived from the same sources because when we image the clouds the MOT is switched off). Some very precise calculations of the transition frequencies for lithium were realized in [Sansonetti *et al.*, 2011], and the frequencies listed in Table 5.1 are given with respect to center-of-gravity (cog) of

[15] Thanks to Thomas Reimann, who takes care of the realization of the optical transport part.
[16] Made by a 300 W laser from IPG photonics, YURT-300-LP-WC
[17] TA Pro at 670 nm

the D_1 and D_2 lines. These centers-of-gravity are within a few megahertz from the crossovers which serve as experimental reference points.

Function	Reference	Detuning (MHz) (with respect to cog)
^{7}Li P ZS	D_2 ^{7}Li	−753.3
^{7}Li R ZS	D_2 ^{7}Li	+53.5
^{7}Li P MOT	D_2 ^{7}Li	−443.5
^{7}Li R MOT	D_2 ^{7}Li	+363.5
LFI ^{7}Li	D_2 ^{7}Li	−403.5
HFI1 ^{7}Li	D_2 ^{7}Li	−623.5
HFI2 ^{7}Li	D_2 ^{7}Li	−803.5
OP ^{7}Li	D_2 ^{7}Li	+403.5
^{7}Li P D_1	D_1 ^{7}Li	−355.9
	D_2 ^{6}Li	+125
^{7}Li R D_1	D_1 ^{7}Li	+447.7
	D_2 ^{6}Li	+928.6
^{6}Li P ZS	D_2 ^{6}Li	−464.1
^{6}Li P MOT	D_2 ^{6}Li	−154.1
LFI ^{6}Li	D_2 ^{6}Li	−114.1
HFI1 ^{6}Li	D_2 ^{6}Li	−1314.1
HFI2 ^{6}Li	D_2 ^{6}Li	−1394.1
OP ^{6}Li	D_2 ^{6}Li	+104.1
^{6}Li R ZS	D_1 ^{6}Li	−222.9
^{6}Li R MOT	D_1 ^{6}Li	+87.1
^{6}Li P D_1	D_1 ^{6}Li	−101.1
^{6}Li R D_1	D_1 ^{6}Li	+127.1

Table 5.1: Light frequencies needed for the new experiment. Here the letter 'P' stands for Principal, 'R' for Repumper. Frequencies are given with respect to the centers of gravity (cog) of the Li D lines.

5.3.2 Optical realization

We need three master lasers: one for the D_2 line of each isotope and one for the D_1 line of ^{6}Li. The two master lasers for the D_2 line of each isotope will be produced from Toptica BoosTA system. It is composed of one master diode, producing a power of about 10 mW, that can be locked onto an atomic frequency and whose power is amplified by a Tapered Amplifier (TA) up to 500 mW. However, the TA output mode is not a Gaussian TEM_{00} mode, and injecting it properly into a fiber requires some appropriate beam shaping and may be challenging. In practice, about half of the power is lost by fiber injection. For the D_1 line of ^{6}Li, we plan to use a solid-state laser built by our group [Eismann *et al.*, 2012]. This laser has a total output power of 800 mW in a Gaussian TEM_{00} mode and was already used in our group for D_1 cooling of ^{7}Li [Grier *et al.*, 2013]. Another version [Eismann *et al.*, 2013, Kretschmar *et al.*,

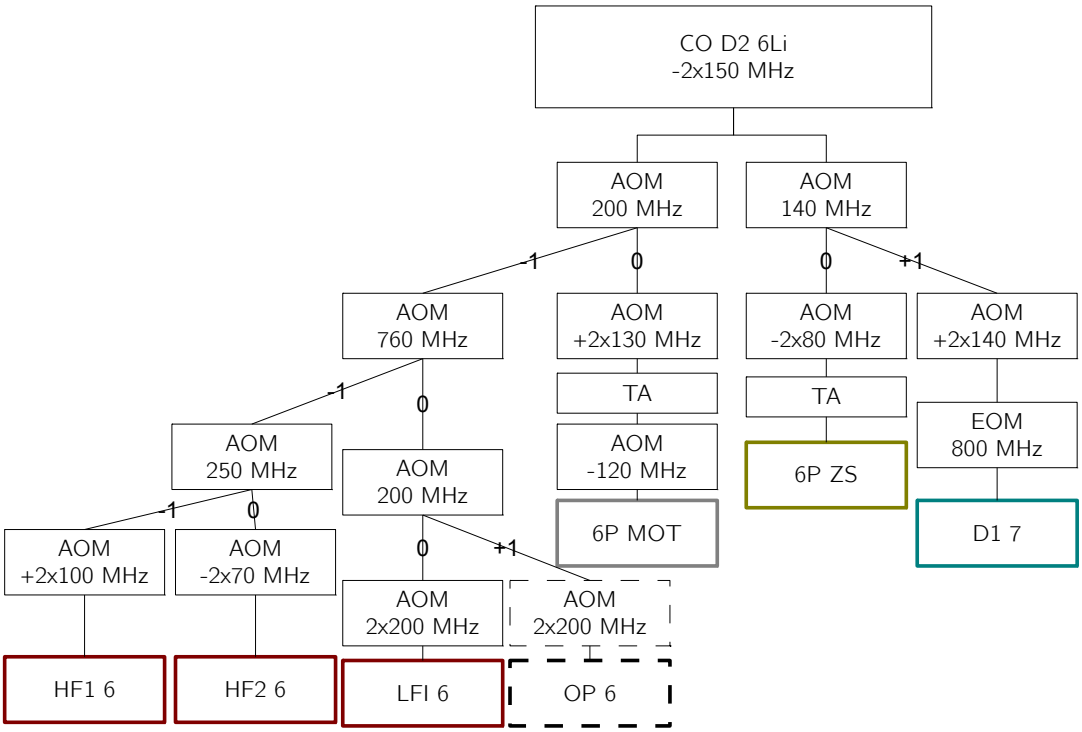

Figure 5.5: Proposed laser scheme for the D_2 lines of ^{6}Li for the new experiment. Golden boxes correspond to Zeeman slowing light, silver boxes to MOT light, blue cases to D_1 cooling light, red cases to imaging light and dashed cases to (so far) optional beams.

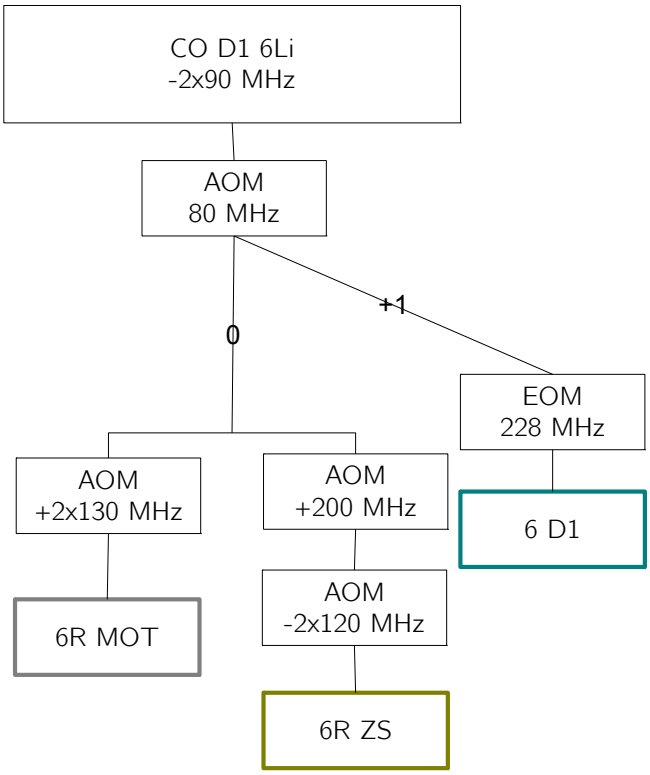

Figure 5.6: Proposed laser scheme for the D_1 lines of ^{6}Li for the new experiment. Same color code as for Figure 5.5.

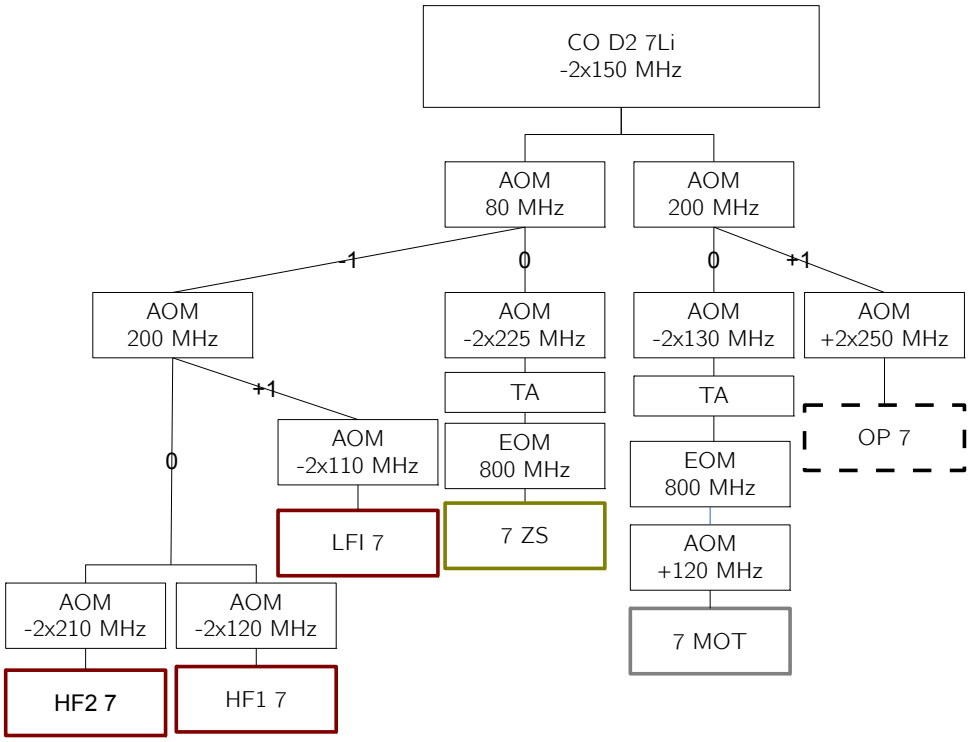

Figure 5.7: Proposed laser scheme for the D_2 lines of ^{7}Li for the new experiment. Same color code as for Figure 5.5.

2016] has a total output power of more than 2 W. Since D_1 cooling requires a lot of optical power[18], this repartition seems to be the best choice, even though it would have been nice to have some narrow-linewidth light on the D_2 lines for imaging[19] to improve imaging resolution.

The light emitted by the three master lasers is then split and sent through AOMs and EOMs to reach the right frequency, and the lights for the MOT and the Zeeman slowing beam are finally re-amplified by TAs before being combined and sent onto the atoms.

5.3.3 Mechanical installation

The laser setup around the MOT cell is given on Figure 5.8.

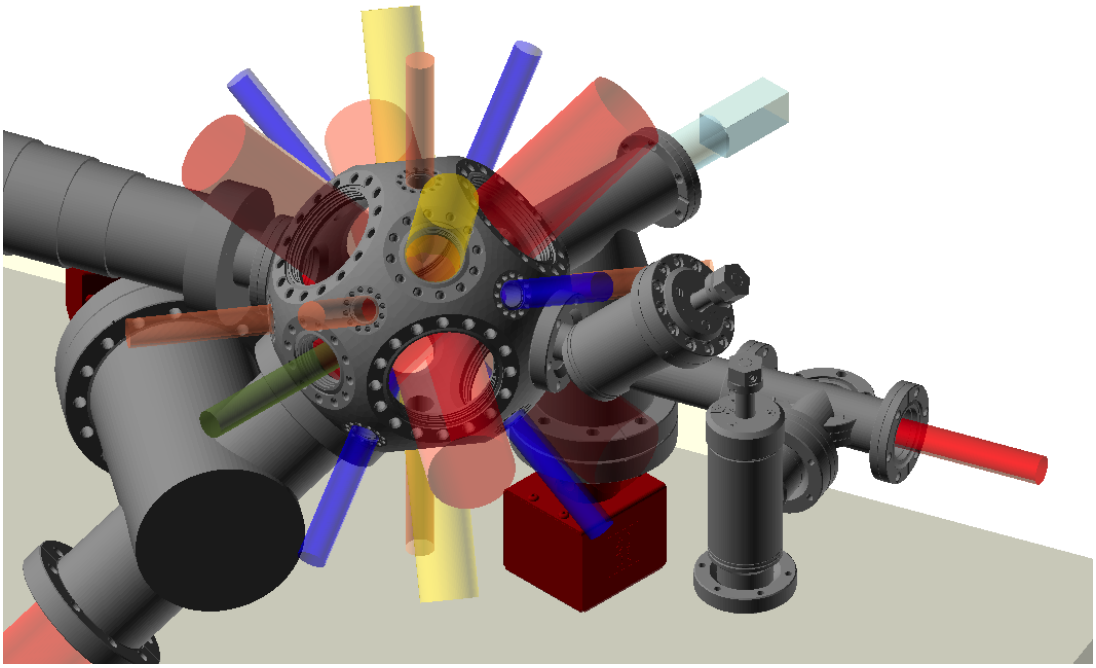

Figure 5.8: Laser arrangement around the MOT cell. The horizontal red beam is the Zeeman beam. The faint red beams are the MOT beams. The orange beams will be used for D_1 cooling. The yellow beams will be used for absorption and fluorescence imaging. The green beam will be used for optical transport into the science cell. The blue beams are for an optional blue MOT. One of the yellow or blue beams will also be used (with dichroic optics) for the high-power dipole trap and pre-evaporation in order to use low-power optics on the optical transport path (the tunable lens can only handle a few watts of optical power, not the few tens of watts needed for an efficient loading in the optical dipole trap).

[18] We want to be able to illuminate the clouds with an intensity of several tens of $I_{\text{sat}} = 2.54\,\text{mW/cm}^{-2}$ (typically $I \approx 50 I_{\text{sat}}$) on the whole volume of the Compressed MOT.

[19] The solid-state lasers can easily be stabilized to sub-100 kHz linewidth while that of diode lasers or TAs is usually of several 100 kHz.

We have also developed a compact design[20] to install MOT beams and D_1 cooling beams directly on the MOT chamber: the MOT CF63 windows and the D_1 CF16 windows are fixed on the cell using four long setscrews, on which we plan to use extra nuts to fix some adaptation plates to support a beam-guide system [21]. A photo of the partially-mounted MOT chamber with the setscrews apparent is shown on Figure 5.9.

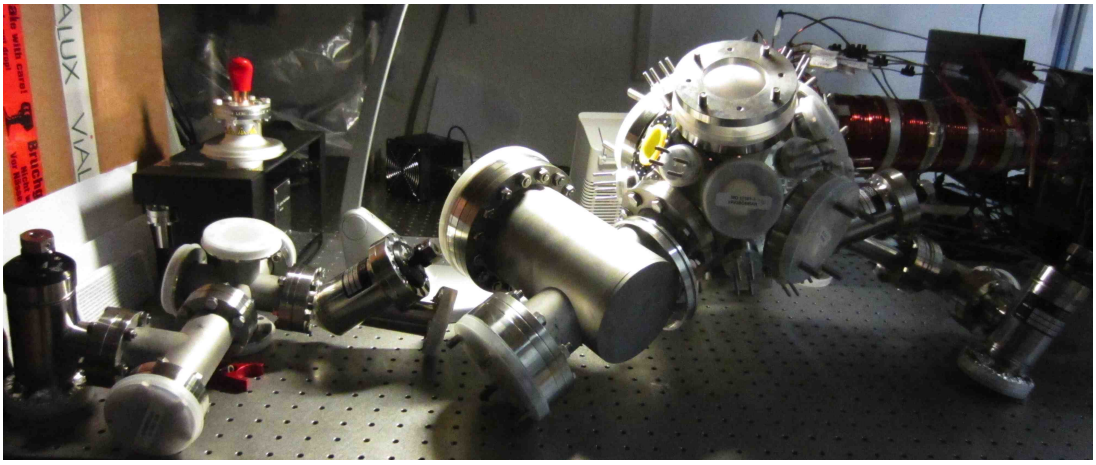

Figure 5.9: Photo of the partially-mounted MOT chamber. The white plastic covers are only to protect flanges and viewports from dust and chocks until construction is achieved. The long setscrews are very visible both on CF63 (MOT beams) and CF16 (D_1 cooling beams) flanges. One adapter plate is installed on the top CF63 viewport. The yellow plug is where the Zeeman slower will be installed.

A scheme of the designed beam guides is shown on Figure 5.10.

We expect this cage mount to be simple to align, very stable, with a compact design.

[20] with the help of Cedric Enesa.

[21] Beam Guide system, with mixed elements from Radiant Dyes (RD) and from Thorlabs(Th).

- For the MOT input: RD fiber plate / RD plate with $f' = 8\,\text{mm}$ aspheric lens to collimate fiber output / RD support with polarizing beam splitter (PBS) cube to clean the polarization / RD plate with $f' = 8\,\text{mm}$ aspheric lens - first lens of telescope / RD plate with $\lambda/4$ wave plate / RD to Th adapters / Th plate with $f' = 100\,\text{mm}$ lens - last lens of telescope / Th to Kimball cell adapter.

- And MOT retro-reflexion: Th to Kimball cell adapter / Th plate with $\lambda/4$ wave plate / Th plate with mirror.

- For D_1 input: RD fiber plate / RD plate with $f' = 8\,\text{mm}$ aspheric lens to collimate fiber output / RD support with polarizing beam splitter (PBS) cube to clean the polarization / RD plate with $\lambda/4$ wave plate / RD to Kimball cell adapter.

- And D_1 retro-reflexion: RD to Kimball cell adapter / RD plate with $\lambda/4$ wave plate / RD plate with mirror.

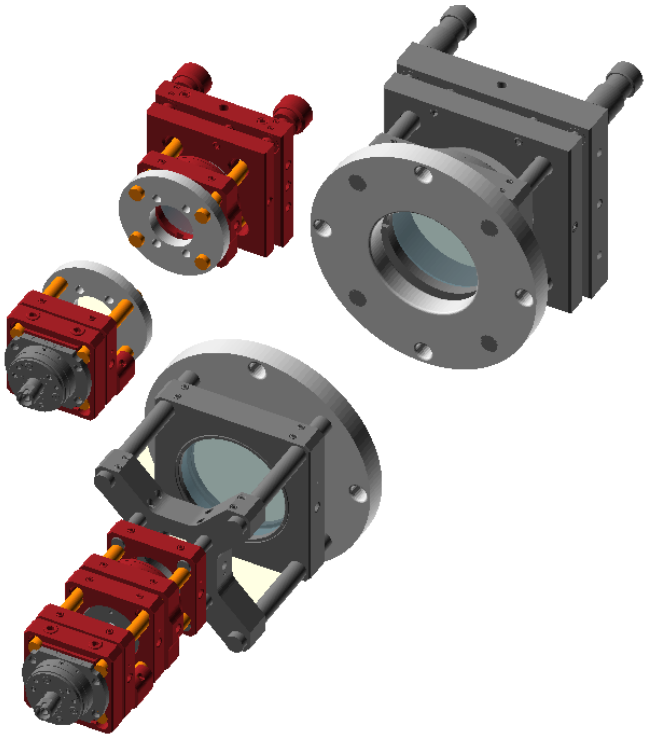

Figure 5.10: Scheme of the cage mounts for D_1 (top) and MOT (bottom) beams. In red are the Radiant Dyes elements, in dark gray the Thorlabs elements, and in light gray the home-made elements.

5.4 Magnetic fields

A number of different magnetic fields have to be imposed on the atoms to slow and cool them. The first one, the Zeeman slower field, has already been evoked in the previous sections. It is described in more details here, as well as the coils designed to compensate for stray magnetic fields. The main ideas for the MOT coils will also be discussed, before writing a few words about the prospective magnetic fields of the science cell region.

5.4.1 Zeeman slower

The Zeeman slower[22] aims at slowing the atoms exiting the oven with an average velocity of 1400 m/s down to a velocity of about 50 m/s, at which they can be captured by a Magneto-Optical Trap. We chose to implement a Zeeman Slower in a spin-flip configuration, *i. e.* the magnetic field produced by the Zeeman slower crosses zero before the end of the tube (see Figure 5.13). This has several advantages: a smaller absolute magnetic field value leading to a smaller power consumption, and it also prevents the slowing beam to be resonant either for atoms in the MOT or for atoms in the oven. Inspired by Fermix experiment's design, we chose to implement the varying

[22] designed by Shuwei Jin

magnetic field by solenoids of different lengths, crossed by the same current of about 20 A.

The Zeeman slower tube, composed of a 60 cm long tube and two CF40 flanges (one rotatable, towards the cell, and one non-rotatable, towards the oven), was first outgased at a temperature of about 350 °C for about two weeks, while pumping with a turbo pump[23]. The outgasing is performed in order to desorb as much of the H_2 absorbed in the wall of the tube as possible. The final pressures reached at the end of the outgasing were: $P_{N_2} = 7{,}0 \cdot 10^{-10}$ mbars, $P_{H_2} = 2{,}3 \cdot 10^{-8}$ mbars and $P_{H_2O} = 7{,}7 \cdot 10^{-10}$ mbars at 350°C. By decreasing slowly the temperature, we could interpolate a pressure of $P_{H_2} \approx 6{,}7 \cdot 10^{-10}$ mbars at ambient temperature (with only turbo pumping). This first outgasing was necessary because once the Zeeman slower is wired up, outgasing temperatures cannot exceed 200°C without a risk of damaging the coils.

To wire up a Zeeman slower, it is better to use a lathe (turning machine), both for rapidity and precision. We used U-shaped supports both as a support for the coils and to adjust the length of the Zeeman slower. The first layer is made of heating cable[24]. It will be used for a second outgasing of the Zeeman slower, up to 200°C. Temperature will be monitored thanks to three thermocouples (one in the center, two on the sides) that go up to 400°C. This first layer is then covered with Kapton tape to avoid heating of the coils during the outgasing phase. Then follow two layers of annealed hollow copper tube for cooling[25]. We then wrapped the whole tube in aluminum foil in order to even the tube surface for wiring of the electric layers. The wire for the coils[26] has a rectangular shape for easy wiring. A scheme of the Zeeman slower is displayed in Figure 5.11. We first wired up the inverted Zeeman slower (8 layers of 9 turns) and wired up a spare 9^{th} layer for security. A picture of the Zeeman slower is shown on Figure 5.12. We could test the magnetic field produced by the Zeeman slower using a gauss-meter, and the results are displayed on Figure 5.13 for a current of $I = 20$ A. The agreement between expected and measured variation is very satisfactory.

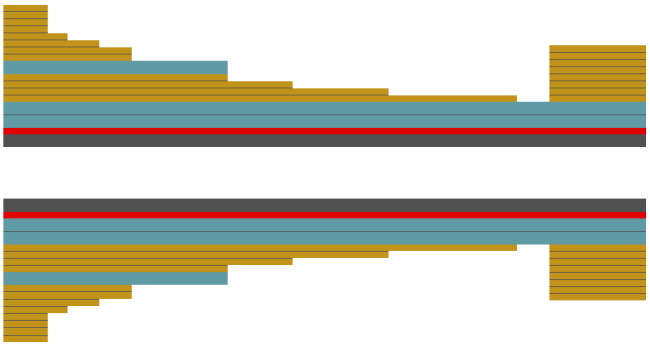

Figure 5.11: Schematic cut of the Zeeman Slower. The CF40 tube walls are indicated in gray. The heating layer for the second outgasing is shown in red, the cooling layers in blue, and the coils in gold.

[23] Pfeiffer Vacuum

[24] Garnisch GmbH, Heating Cable Wigaflex T2-06 1.00 Ω/m

[25] Euralliage, outer diameter 6 mm, inner diameter 4 mm.

[26] APX, CL H 1.60x2.50 GR2 DIN 355, width: 2.5 mm (+2 × 0.17 mm insulation), thickness: 1.6 mm (+2 × 0.12 mm insulation)

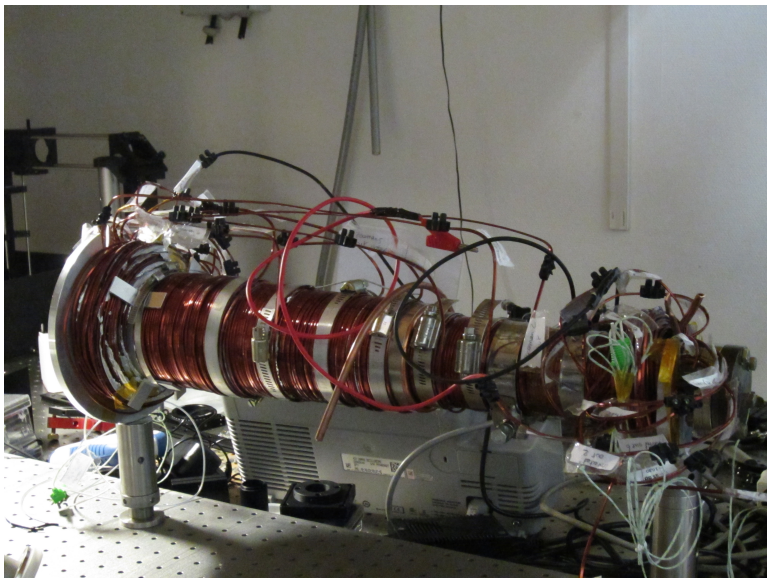

Figure 5.12: Picture of the Zeeman Slower

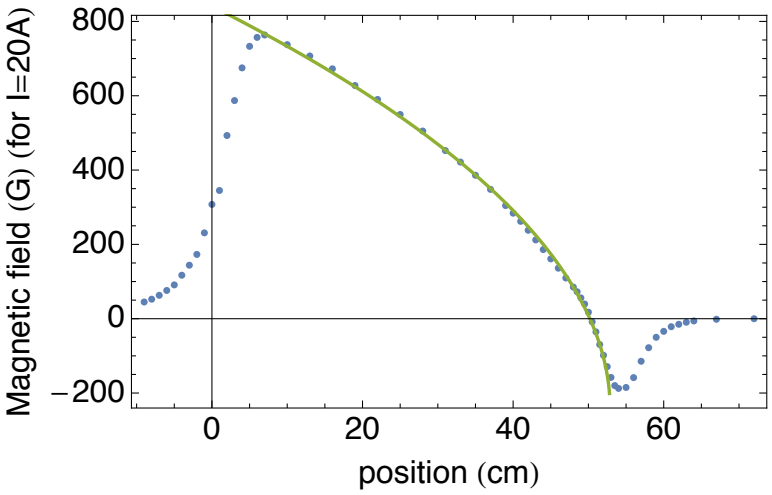

Figure 5.13: Measured magnetic field in the Zeeman Slower (blue dots) and expected variation of the magnetic field (green curve). Dimensions are not respected.

5.4.2 Compensation coils

5.4.2.1 For the Zeeman slower

The end of the Zeeman slower results in a non-zero magnetic field ($B \approx 4\,\mathrm{G}$) in the middle of the MOT chamber, which is a problem for the MOT. To compensate for this, a compensation coil will be winded up on the other side of the cell and its current adjusted to ensure a zero magnetic field at the center of the chamber. The support for the coil will be fixed directly around the CF40 flange opposite of the Zeeman slower.

5.4.2.2 In 3 directions

Around the 6 CF63 windows for the MOT beams, we plan to have six small coils in order to compensate for any residual stray magnetic field. They should be able to generate a magnetic field of about 2 G in any direction. Their support will also be fixed directly around the CF63 view-ports. Their current will be adjustable separately and optimized directly on the MOT position and fluorescence.

5.4.3 MOT-Feshbach coils

Now that we have the possibility of zeroing the bias magnetic field in the MOT chamber, we can turn to the realization of the magnetic gradient for the MOT. Due to the high volume of the MOT chamber it is not possible to put the coils very close to it, so we use high current and water cooled wires.

5.4.3.1 MOT

A pair of coils with currents in opposite directions will be used to create the magnetic field gradient necessary for the MOT. It will be approximately 25 G.cm^{-1}, for a current of about 100 A. Because of spatial cluttering, it will not be possible to put the coils in a real anti-Helmholtz configuration (with the distance between the coils equal to their radius), but the calculated magnetic field is reasonably linear on a few centimeters, which is much larger than the diameter of the MOT beams and thus won't be a problem. The initial MOT stage will be followed by a compressed MOT stage, where the current in the coils is increased (to about 200 A) in order to increase atomic density. It is then necessary to switch off rapidly the MOT coils to perform sub-Doppler D_1 cooling and then load into a powerful dipole trap. Some square hollow core copper tube[27] was bought for these coils. To ensure a good optical access, some conical coils are currently being designed.

5.4.3.2 Feshbach fields

Once the atoms are loaded into the dipole trap, we want to transport them. However, the optical power needed to transport them at a temperature of 50 µK is about 150 W and may lead to thermal lensing effects. To transport the atoms with a smaller optical power, it is necessary to pre-cool them, using evaporative cooling in a dipole trap. At zero magnetic field, the collisional scattering cross-section of ^{6}Li between two of its Zeeman sub-levels is very small (see Figure 5.2), and to ensure efficient evaporation we plan to increase the field to about 300 G, where $a \approx -300\,a_0$ for the $|1_\mathrm{f}\rangle - |2_\mathrm{f}\rangle$ mixture and $a \approx -800\,a_0$ for the $|1_\mathrm{f}\rangle - |3_\mathrm{f}\rangle$ mixture. This will be done using the MOT coils with a current of about 200 A in parallel directions. Since the current in the MOT coils is fixed at zero during the D_1 cooling stage that lasts typically 5 ms, this leaves enough time to switch from anti-parallel to parallel current configuration.

[27] APX, outer side 4 mm, inner side 2 mm

5.4.4 Science cell magnetic fields

The objective for the science cell magnetic fields is to be able to generate magnetic field of up to 1000 G in order to exploit the Feshbach resonances of both ^{6}Li and ^{7}Li, and to be able to generate a variable curvature to use a hybrid magnetic-optical trap. For the Feshbach field we need a pair of coils in Helmholtz configuration, and for the curvature we only have to be in a non-Helmholtz configuration. The plan is thus to have a pair of coils in Helmholtz configuration quite close to the cell, maybe conical, with an inner diameter large enough to have the microscopes going through. Here also, the conical design would reduce spatial cluttering and leave a better optical access. Another independent pair of coils, probably farther away from the cell, will be designed for the curvature field. In the previous lithium experiment, a clever design of the coils was made so that the bias field of the Feshbach coils (in G.A^{-1}) was the opposite of that of the curvature coils [Tarruell, 2008]. This resulted in the axial confinement being very easy to tune. We are currently designing a similar solution for the new experiment.

5.5 Security and computer control

A security box[28] will be used to monitor the temperatures of the critical elements of the experiment: Zeeman slower, oven, coils, etc. and to overlook the water flux that is supposed to cool them. In case the temperature gets too high or the flux too low, the currents will be shut down. The computer control will be made by Cicero, a software developed at MIT. It is composed of two sub-softwares, Atticus, which deals with communication between the computer and the experiment through National Instrument cards, and Cicero itself, to design the experimental sequence. During my PhD, I modified Cicero so that it can address Digital to Analog Converters (DACs); the corresponding user's manual is given in Appendix B. It is a very powerful and convenient software, with the a good ability to deal with the different time scales of an ultracold atom experiment.

5.6 Conclusion

The historical lithium experiment has proven its capability to give and produce great results with however a heavy day-to-day maintainability. The project of building a complete new one instead of renewing it allowed the construction to be made in parallel with the running of the old experiment. We could make use of the full man power of the Ultracold Fermi gases group (including Fermix team) during the shut down due to construction work, and they were really a great help for the project. From my personal point of view, it was very exciting and rich to start building a new experiment once I mastered the old one. The possibilities opened by the new experiment are numerous and I hope that the future PhD students will take advantage of them.

[28] Designed by Mihail Rabinovic.

Conclusion

Summary

The realization during my PhD of the first superfluid Bose-Fermi mixture opened a vast field of investigation regarding the physics of the mixture. Due to the weak interaction between the Bose and the Fermi cloud, the BEC acts both as a sensitive probe and as a precision tool on the Fermi cloud.

Firstly, we investigated the properties of the Bose-Fermi counterflow. In the superfluid regime, the mean-field effect of the Fermi gas on the BEC is evaluated with precision spectroscopy measurements, in very good agreement with calculations. For a high-velocity counterflow, the Bose gas acts as a local probe to measure the critical velocity of the mixture. Our results are in agreement with Landau's criterion [Castin *et al.*, 2015] for superfluidity, in contrast with previous experiments [Miller *et al.*, 2007, Weimer *et al.*, 2015]. At high temperature, we observe an unexpected synchronization of the two thermal clouds, associated to a reduction of dissipation. Further experiments will make use of the out-of-phase motion of the BEC and its thermal fraction to explore the second sound of the mixture, predicted to be common to both components.

Second, we explored the opportunity to use the BEC as a precision tool to engineer a flat-bottom trapping potential for the fermions and investigated the effect of such a trap on Clogston-Chandrasekhar limit. We predicted the existence of a finite range of polarization for which a shell-shaped superfluid was energetically possible, and we provided first experimental evidences of the observation of such a shell. It topologically differs both from the habitual bulk superfluids and from toroidal superfluids reported in Bose systems [Ramanathan *et al.*, 2011, Wright *et al.*, 2013b, Wright *et al.*, 2013a, Mathey *et al.*, 2014, Yakimenko *et al.*, 2015, Beattie *et al.*, 2013]. This flat bottom trap can also be used to prepare uniform spin-imbalanced Fermi gases and search for the FFLO phase, which parameters seem to be within the reach of our experimental realizations.

Perspectives

Regarding the superfluid shell in the Bose-Fermi mixture, a remaining open question concerns the dynamics of the shell formation, and the response of the system to a quench of the potential shape. This can be investigated using rapid magnetic field ramps.

The existence of Feshbach resonances between ^{6}Li and ^{7}Li makes possible the realization of a superfluid Bose-Fermi mixture with one of the Fermi gas components strongly interacting with the Bose gas[29]. This may have an influence on superfluidity and on Clogston-Chandrasekhar limit, making it an intriguing system to explore.

Lastly, the ongoing construction of a new experiment opens the way to studies of other properties of the mixture. The implementation of a box potential will enable us to obtain fully homogeneous Bose-Fermi mixtures, in which we plan to study for instance vortex formation and organization. Indeed, for such a Bose-Fermi mixture, the vortices are expected to arrange in a square lattices, as it is the case for some Bose-Bose mixtures [Ho and Shenoy, 1996, Liu *et al.*, 2014, Kuopanportti *et al.*, 2012, Jezek *et al.*, 2004] and in contrast with hexagonal Abrikosov lattices encountered for single Bose or Fermi superfluids. We also plan to take advantage of the box potential to measure the critical velocity of a uniform Fermi gas and compare it with Landau's criterion. Up to date, there are only few box potentials for fermions[30], and the playground is vast.

[29] With $|1_\mathrm{f}\rangle$, $|2_\mathrm{f}\rangle$ and $|4_\mathrm{b}\rangle$ at 800 G for instance, see Table 2.2.
[30] Martin Zwierlein at MIT is currently implementing one.

Appendices

Appendix A

Consistency check of FBT analysis

When doing the polynomial fit to the data, we evaluated the influence of using a non-adequate function to fit the density profiles and the influence of the order of the polynomial. We used simulated profiles from Normal-Superfluid-Normal and Superfluid-Normal scenarios that we fitted using polynomials of various order. Results are shown on Figure A.1.

A compromise has to be found between a too small order leading to an imprecise description, and a too high order where the polynomial starts to fit the noise leading to oscillations. We chose to use polynomials of order $n = 16$. The fact that the minimum in the density difference does not go to zero for the NSN scenario is very visible on the analysis of the theoretical profile, as well as the fact that for the SNN scenario the density difference may be negative close to $z = 0$.

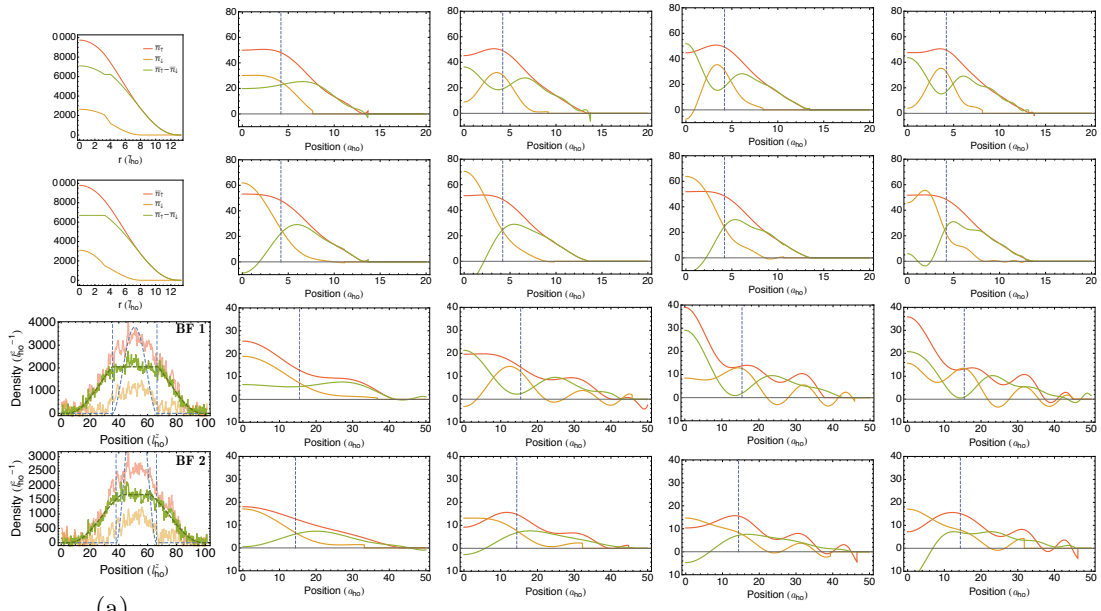

(a) (b) $n = 12$. (c) $n = 16$. (d) $n = 20$. (e) $n = 24$.

Figure A.1: Influence of the order n of the polynomials used to fit the data. The left column are the doubly integrated density profiles. First raw: theoretical profiles for NSN scenario. Second raw: theoretical profiles for SNN scenario. Third raw: $N_\mathrm{f} = 180 \cdot 10^3$, $N_\mathrm{b} = 63 \cdot 10^3$, $P = 60\%$. Fourth raw: $N_\mathrm{f} = 125 \cdot 10^3$, $N_\mathrm{b} = 88 \cdot 10^3$, $P = 60\%$. The $\uparrow$ density is represented in red, the $\downarrow$ in yellow, the density difference in green, and the blue vertical dashed lines indicate the Thomas-Fermi radius of the BEC. Here the densities are given in terms of the averaged harmonic oscillator length $\sqrt{\frac{\hbar}{m\bar{\omega}}}$.

Appendix B

Cicero for Lithium User's Manuel

B.1 Introduction - Caution

Introduction

This is meant to be a manual explaining the main changes done to the software Cicero in order to have it running on the Lithium Experiment that uses Digital to Analog Converter boxes.

Caution

- Do not name a device using capital letters. The only capital letter should be the 'D' of 'Devbanane'.
- Do not try to run Cicero for Lithium without a FPGA variable timebase. This will not work.
- The function 'Output Now' that could be used to check whether Digital or Analog channels were working is not fully implemented with DAC channels. ('Output now' is a static method, and since we can't address several DACs simultaneously, it cannot be adapted easily).

B.2 Configuration of Atticus

I give here the step-by-step procedure to install Cicero with at least on digital card dedicated to DAC outputs.

Start by configuring Atticus as explained in Aviv Kesheet's manual. For the FPGA :

- Install FPGA XEM3001 drivers, and run software FrontPanel.
- Click on 'Configure PLL button' and set the frequency of CLK1 to the desired frequency as master clock. A suitable choice is 10MHz

- Click on EEPROM Write and Apply buttons to store these settings.
- Wire the variable frequency clock (bus JP2 pin 17) and its ground (bus JP2 pin 19) to the PFI4 of ONE of the NI cards

For the server :

- set UseOpalKellyFPGA to True
- In the connections menu, set a connection between PFI4 (source) and PXI _Trig7 (destination) - this is because the Trig terminals are shared between the cards-, and between PFI4 (source) and PFI0(destination) - this part is to isolate the strobe for DAC devices.

In the FPGA menu :

- set UsingVariableTimebase to True
- set MySampleClockSource to DerivedFromMaster
- set the SampleClockRate to the frequency of the master clock (ex : 10000000 for 10MHz)

For all of the NI devices,

- set MySampleClockSource to External
- set SampleClockExternalSource to PXI _Trig7 (or as defined in the devices configuration, so that it is linkable to the clock)
- set SampleClockRate to the FPGA sample clock rate
- set UsingVariableTimebase to True
- set SoftTriggerLast to False
- set StartTriggerType to SoftwareTrigger

Now you have to dedicate one of the digital cards to be DAC card. The DAC card will not be able to output digital signals any more. For this card:

- set DACChannelsEnabled to True, AnalogChannelsEnabled to False and DigitalChannelsEnabled to False.
- The digforDAC Channels should appear in the list of Hardware channels. These are digital channels that will be used to output the DAC commands Use the button 'Exclude Channels' to get rid of the DigforDAC channels that won't be used for DAC Address nor DAC Value.
- In the ServerSettings, edit the ChannelsforAddress and ChannelsforValue lists with the desired digforDAC channels.
- Be careful, you need exactly 8 channels for address and 16 channels for value. The order is important.

- Be careful, the bits are rather mixed up in the DAC boxes. The first 8 bits of the bus are for Address, then the next 3 bits are lost, then the next 8 bits are for Value, another 3 bits are lost, the next 8 ones are also for Value, and the last 2 are lost again.

- Now you can see 2^8 DAC channels appear in the channels list. Exclude the unused ones. The binary address of DAC boxes is either 110xxxxx or 10xxxxxx, depending on the generation, which means that you may use channels from 128 (10000000) to 223 (11011111) (the values given here refer to the old lithium experiment).

- The DAC channels will now appear in Cicero Word Generator. You can bound them to logical channels in the Add Logical Channel menu, give them a conversion equation, and all of the features available for Analog Channels in Cicero.

B.3 Changes made to the software

To deal with DAC channels, one need to start with Atticus, and tell it DAC channels exist, and how to create and configure them. Then I had to add in Cicero some code so that DAC channels can be programmed and dealt with. After that, i had to explain Atticus how to output the DAC values.

Atticus 1

First of all, i added two channel types to the preset types (that were digital, analog, series, gpib) : digforDAC and DAC. The digforDAC is for a real physical channel (ex:port1, line0), while the DAC channel is somehow a virtual channel, made by the combination of digforDAC channels with the right value. Then, i allowed some of the digital card to be specified as being 'digforDAC'. Usually, when a card is programmed, its channels appear in the physical channels list. When a card has its 'digforDACchannelsEnabled', its channels also appear in the channels list. You can allow some of them to be channels for DAC address, and some to be Channels for DAC value. At the end of the sequence, the computer will parse through the channels and tell each of the ChannelsforAddress which value it has to output. Well, once you've got some Channels for Address (say, x), the corresponding number of DAC channels (2^x) will appear in the list of available channels. This is the list that will be read by Cicero Word Generator, so i strongly recommend that you remove all of the unused DAC channels from this list in order to avoid mistakes.

Cicero

The DAC channels are now created, and Cicero will see them. Not much change has been made in Cicero itself, I just looked for the occurrences of 'analog' and copied them into 'DAC'. The data concerning the sequence is produced the same way as before. However, on producing the buffers, i had to change a few things, but this was made in DataStructures.

DataStructures

How it is done : basically, all of the timesteps of the sequence are saved with

- Which analog channel is on during this timestep ? What are the associated waveforms ? What is the precision required ?
- Which DAC channel is on during this timestep ? What are the associated waveforms ? What is the precision required ?
- Which digital channel is on or off ? Is there pulses ?

Before, the computer had this precision required that more or less set the main period of this step and just had to check if a channel had to be switch on or off in the middle of a period. This was used to generate the VariableTimebase data, which consists in a dictionary of timesteps, to which are linked a list of 'segments', each segment being characterized by a number of counts (= its length divided by the master sampleclock period). Then this dictionary is given to a function which calculates the values the channels have to take for each segment, and this is the buffer generation. Each segment corresponds to one line of the buffer, it's one 'clic' of the clock.

Now, it is divided in several steps.

1. The first step is still the same, working together with the DAC and analog channels, and taking the precision as the minimum of the two required precisions, the computer generates a 'primary' variable timebase.
2. Then, it generates the DAC buffer the same way the analog buffer was generated previously. The trouble is, during a ramp for example, several DAC channels (let's say 2) may have to change their value at the same time, and this can't be done because we need all of the channels of the digforDAC card to address one DAC channel. So the computer has to talk to a channel, then quickly talk to the other one.
3. So the next step is to look into the DAC buffer, to find for which segments at least two DAC channels have to change, which are the DAC channels involved, and then split the segment into the necessary number of new segments so that the computer talks to all of the channels without delaying the rest of the sequence. This outputs a dictionary that links the 'bad' segments to the DAC channels that change in it. A way of skipping this step would be to force the computer to address all of the 40 DACs at each segment, but we decided this would increase the buffer size too much.
4. Then, i have to generate this new timebase splitting the segments of the first one when needed. We have to define how fast the computer switches between the DAC channels, and this can't be arbitrary low (see below, about strobe). This time is called 'Time needed to update Bus' or 'TimeBusUpdate' in the code.
5. To produce the new DAC buffer, we can't use the same function as before with the new timebase segments dictionary because we would meet the same problem as before with several DACs changing their value at the same time. We have to

produce a 'primary' DAC buffer, with the old variable timebase dictionary, and then copy 'manually' the values into a bigger buffer.

Old Buffer		New Buffer	
DAC 1	DAC 2	DAC 1	DAC 2
0	0	0	0
1	2	1	0
		1	2
0	2.2	0	2
		0	2.2
0	0	0	0

6. For the analog and the real digital buffer, it's fine, we can use the same function as before (and we have to do it in order to get the right buffer size). It should also deal appropriately with the pulses.

At the end of this stage, both the variable timebase and the buffers are generated.

Atticus 2

This is now the last part, which consists in outputting correctly the signals. In *DaQmxTaskGenerator*, it takes a sequenceData, that includes mostly the buffers and the timebase, and creates a task that is loaded on the NI cards. Now, it looks at the buffer, for each line, finds which DAC signal is concerned, then translates its value and address into binary, then into bytes, and finally loads all of them on the card. Nothing changed for the digital or analog cards, we just have to make sure the length of each buffer is a multiple of 4.

It also goes into the writer for FPGA tasks to make sure the FPGA outputs a number of signals that is a multiple of 4 (otherwise the NI cards don't work properly).

Appendix C

Publications and preprints

- "Λ-enhanced sub-Doppler cooling of lithium atoms in D_1 gray molasses",
  Andrew T. Grier, Igor Ferrier-Barbut, Benno S. Rem, Marion Delehaye, Lev Khaykovich, Frédéric Chevy, and Christophe Salomon
  Physical Review A **87**, 063411 (2013)

- "A mixture of Bose and Fermi superfluids",
  Igor Ferrier-Barbut, Marion Delehaye, Sébastien Laurent, Andrew T. Grier, Matthieu Pierce, Benno S. Rem, Frédéric Chevy, and Christophe Salomon
  Science **345**, 1035-1038 (2014)

- "Chandrasekhar-Clogston limit and critical polarization in a Fermi-Bose superfluid mixture",
  Tomoki Ozawa, Alessio Recati, Marion Delehaye, Frédéric Chevy, and Sandro Stringari
  Physical Review A **90**, 043608 (2014)

- "Critical velocity and dissipation of an ultracold Bose-Fermi counterflow",
  Marion Delehaye, Sébastien Laurent, Igor Ferrier-Barbut, Shuwei Jin, Frédéric Chevy, and Christophe Salomon
  Physical Review Letters **115**, 265303 (2015)

- "Universal loss dynamics in a unitary Bose gas",
  Ulrich Eismann, Lev Khaykovich, Sébastien Laurent, Igor Ferrier-Barbut, Benno S. Rem, Andrew T. Grier, Marion Delehaye, Frédéric Chevy, Christophe Salomon, Li-Chung Ha, and Cheng Chin
  Submitted to Physical Review X

C.1 Λ-enhanced sub-Doppler cooling of lithium atoms in D_1 gray molasses

Andrew T. Grier, Igor Ferrier-Barbut, Benno S. Rem, Marion Delehaye, Lev Khaykovich, Frédéric Chevy, and Christophe Salomon

Physical Review A **87**, 063411 (2013)

PHYSICAL REVIEW A **87**, 063411 (2013)

Λ-enhanced sub-Doppler cooling of lithium atoms in D_1 gray molasses

Andrew T. Grier,[1,*] Igor Ferrier-Barbut,[1] Benno S. Rem,[1] Marion Delehaye,[1] Lev Khaykovich,[2] Frédéric Chevy,[1] and Christophe Salomon[1]

[1]*Laboratoire Kastler-Brossel, École Normale Supérieure, CNRS and UPMC, 24 rue Lhomond, 75005 Paris, France*

[2]*Department of Physics, Bar-Ilan University, Ramat-Gan 52900, Israel*

(Received 26 April 2013; published 12 June 2013)

Following the bichromatic sub-Doppler cooling scheme on the D_1 line of ^{40}K recently demonstrated in Fernandes *et al.* [Europhys. Lett. **100**, 63001 (2012)], we introduce a similar technique for ^{7}Li atoms and obtain temperatures of 60 μK while capturing all of the 5×10^8 atoms present from the previous stage. We investigate the influence of the detuning between the the two cooling frequencies and observe a threefold decrease of the temperature when the Raman condition is fulfilled. We interpret this effect as arising from extra cooling due to long-lived coherences between hyperfine states. Solving the optical Bloch equations for a simplified Λ-type three-level system we identify the presence of an efficient cooling force near the Raman condition. After transfer into a quadrupole magnetic trap, we measure a phase space density of $\sim 10^{-5}$. This laser cooling offers a promising route for fast evaporation of lithium atoms to quantum degeneracy in optical or magnetic traps.

DOI: 10.1103/PhysRevA.87.063411 PACS number(s): 37.10.De, 32.80.Wr, 67.85.−d

I. INTRODUCTION

Lithium is enjoying widespread popularity in the cold-atom trapping community thanks to the tunability of its two-body interactions and its lightness. Both the fermionic and the bosonic isotopes of lithium feature broad, magnetically tunable Feshbach resonances in a number of hyperfine states [1]. The presence of these broad resonances makes lithium an attractive candidate for studies of both the Fermi- and Bose-Hubbard models [2] and the strongly correlated regime for bulk dilute gases of Fermi [3] or Bose [4–6] character. Its small mass and correspondingly large photon-recoil energy are favorable factors for large area atom interferometers [7] and precision frequency measurements of the recoil energy and fine structure constant [8]. Under the tight-binding lattice model, lithium's large photon-recoil energy leads to a larger tunneling rate and faster time scale for superexchange processes, allowing for easier access to spin-dominated regimes [9]. Finally, lithium's small mass reduces the heating due to nonadiabatic parts of the collision between ultracold atoms and Paul-trapped ions. This feature, together with Pauli suppression of atom-ion three-body recombination events involving ^{6}Li [10], potentially allows one to reach the s-wave regime of ion-atom collisions [11].

However, lithium, like potassium, is harder to cool using optical transitions than the other alkali-metal atoms. The excited-state structure of the D_2 transition in lithium lacks the separation between hyperfine states for standard sub-Doppler cooling techniques such as polarization gradient cooling [12–14] to work efficiently. Recently, it has been shown by the Rice group that cooling on the narrow $2S_{1/2} \rightarrow 3P_{3/2}$ transition produces lithium clouds near 60 μK, about half the D_2-line Doppler cooling limit [15], and can be used for fast all-optical production of a ^{6}Li quantum degenerate Fermi gas. However, this approach requires special optics and a coherent source at 323 nm, a wavelength range where power is still limited. Another route is to use the three-level structure of the atom as implemented previously in neutral atoms and trapped ions [16–22]. The three-level structure offers the possibility of using dark states to achieve temperatures below the standard Doppler limit, as evidenced by the use of velocity-selective coherent population trapping (VSCPT) to produce atomic clouds with subrecoil temperatures [23]. In another application, electromagnetically induced transparency has been used to demonstrate robust cooling of a single ion to its motional ground state [19,24].

In this paper, we implement three-dimensional bichromatic sub-Doppler laser cooling of ^{7}Li atoms on the D_1 transition. Figure 1 presents the ^{7}Li level scheme and the detunings of the two cooling lasers that are applied to the atoms after the magneto-optical trapping phase. Our method combines a gray molasses cooling scheme on the $|F = 2\rangle \rightarrow |F' = 2\rangle$ transition [25,26] with phase-coherent addressing of the $|F = 1\rangle \rightarrow |F' = 2\rangle$ transition, creating VSCPT-like dark states at the two-photon resonance. Instead of UV laser sources, the method uses laser light that is conveniently produced at 671 nm by semiconductor laser sources or solid-state lasers [27,28] with sufficient power. This enables us to capture all of the $\simeq 5 \times 10^8$ atoms from a MOT and cool them to 60 μK in a duration of 2 ms.

We investigate the influence of the relative detuning between the two cooling lasers and observe a threefold decrease of the temperature in a narrow frequency range around the exact Raman condition. We show that extra cooling arises due to long-lived coherences between hyperfine states. We develop a simple theoretical model for a sub-Doppler cooling mechanism which occurs in atoms with a Λ-type three-level structure, in this case, the $F = 1$, $F = 2$, and $F' = 2$ manifolds of the D_1 transition in ^{7}Li. The main physical cooling mechanism is contained in a 1D bichromatic lattice model. We first give a perturbative solution to the model and then verify the validity of this approach with a continued fraction solution to the optical Bloch equations (OBEs).

II. EXPERIMENT

The stage preceding D_1 sub-Doppler cooling is a compressed magneto-optical trap (CMOT) in which, starting from a standard MOT optimized for total atom number, the

*Corresponding author: agrier@lkb.ens.fr

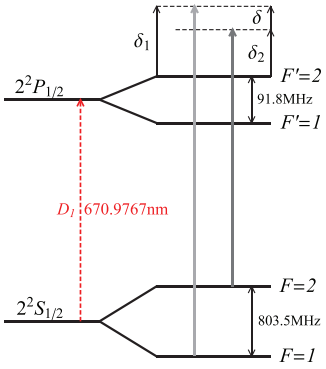

FIG. 1. (Color online) The D_1 line for ^{7}Li. The cooling scheme has a strong coupling laser (principal beam, black solid arrow) δ_2 blue detuned from the $|F=2\rangle \rightarrow |F'=2\rangle$ transition and a weak coupling laser (repumper, gray solid arrow) δ_1 blue detuned from the $|F=1\rangle \rightarrow |F'=2\rangle$ transition. The repumper is generated from the principal beam by an electro-optical modulator operating at a frequency $803.5+\delta/2\pi$ MHz, where $\delta=\delta_1-\delta_2$.

frequency of the cooling laser is quickly brought close to resonance while the repumping laser intensity is diminished in order to increase the sample's phase space density [29]. The CMOT delivers 5×10^8 ^{7}Li atoms at a temperature of 600 μK. The atoms are distributed throughout the $F=1$ manifold in a spatial volume of 800 μm $1/e$ width. Before starting our D_1 molasses cooling, we wait 200 μs to allow any transient magnetic fields to decay to below 0.1 G. The light used for D_1 cooling is generated by a solid-state laser presented in [27]. The laser is locked at frequency ω_2, detuned from the $|F=2\rangle \rightarrow |F'=2\rangle$ D_1 transition in ^{7}Li by δ_2. It is then sent through a resonant electro-optical modulator (EOM) operating at a frequency near the hyperfine splitting in ^{7}Li, $\nu_{\mathrm{EOM}}=803.5\ \mathrm{MHz}+\delta/2\pi$. This generates a small-amplitude sideband, typically a few percent of the carrier, at frequency ω_1. We define the detuning of this frequency from the $|F=1\rangle \rightarrow |F'=2\rangle$ transition as δ_1 (such that $\delta=\delta_1-\delta_2$), as shown in Fig. 1. Using about 150 mW of 671-nm light we perform a three-dimensional D_1 molasses as in [25], with three pairs of $\sigma^+-\sigma^-$ counterpropagating beams. The beams are of 3.4-mm waist and the intensity (I) of each beam is $I\gtrsim 45I_{\mathrm{sat}}$, where $I_{\mathrm{sat}}=2.54\ \mathrm{mW/cm^2}$ is the saturation intensity of the D_2 cycling transition in lithium.

We capture all of the atoms present after the CMOT stage into the D_1 gray molasses. The $1/e$ lifetime of atoms in the molasses is $\geqslant$50 ms. After being cooled for 1.5–2.0 ms, the temperature is as low as 40 μK without optical pumping or 60 μK after optical pumping into the $|F=2,m_F=2\rangle$ state for imaging and subsequent magnetic trapping. In contrast with [25], we find no further reduction in the steady-state temperature by slowly lowering the light intensities after the initial 2.0 ms.

During the molasses phase, we find a very weak dependence on the principal laser detuning for $3\Gamma\leqslant\delta_2\leqslant6\Gamma$. For the remainder of this article, we use a principal laser detuning of $\delta_2=4.5\Gamma=2\pi\times26.4$ MHz. In Fig. 2(a), the temperature dependence upon the repumper detuning is displayed for

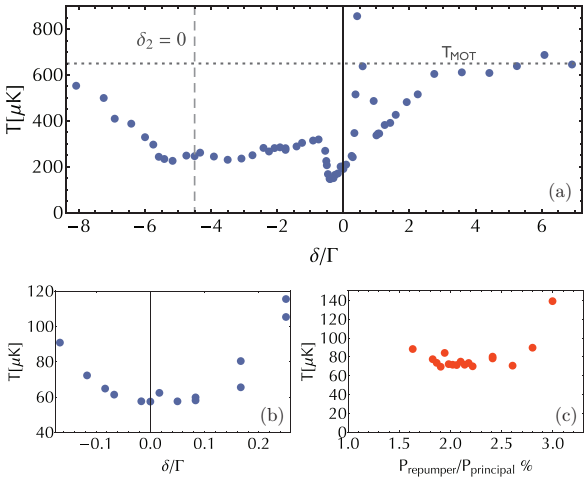

FIG. 2. (Color online) (a) Typical temperature of the cloud as a function of the repumper detuning for a fixed principal beam detuned at $\delta_1=4.5\Gamma=2\pi\times26.4$ MHz. The dashed vertical line indicates the position of the resonance with transition $|F=2\rangle\rightarrow|F'=2\rangle$, the dotted horizontal line shows the typical temperature of a MOT. (b) Magnification of the region near the Raman condition with well-aligned cooling beams and zeroed magnetic offset fields. (c) Minimum cloud temperature as a function of repumper power.

typical conditions. For $-9\leqslant\delta/\Gamma\leqslant-6$, the temperature drops from 600 μK (the CMOT temperature) to 200 μK as gray molasses cooling gains in efficiency when the weak repumper comes closer to resonance. For $-6\leqslant\delta/\Gamma\leqslant-1$, the cloud temperature stays essentially constant but, in a narrow range near the position of the exact Raman condition ($\delta=0$), one notices a sharp drop of the temperature. For δ slightly blue of the Raman condition, a strong heating of the cloud occurs, accompanied by a sharp decrease in the number of cooled atoms. Finally for $\delta\geqslant\Gamma$, the temperature drops again to a level much below the initial MOT temperature until the repumper detuning becomes too large to produce significant cooling below the CMOT temperature.

Figures 2(b) and 2(c) show the sensitivity of the temperature minimum to repumper deviation from the Raman condition and repumper power, respectively. The temperature reaches 60 μK in a $\pm$500-kHz interval around the Raman resonance condition. After taking the data for Fig. 2(a), the magnetic field zeroing and beam alignment were improved, which accounts for the frequency offset and higher temperature shown in Fig. 2(a) relative to Figs. 2(b) and 2(c). The strong influence of the repumper around the Raman condition with a sudden change from cooling to heating for small and positive Raman detunings motivated the study of the bichromatic-lattice effects induced by the Λ-type level configuration which is presented in the next section.

III. MODEL FOR HYPERFINE RAMAN COHERENCE EFFECTS ON THE COOLING EFFICIENCY

In order to understand how the addition of the second manifold of ground states modifies the gray molasses scheme,

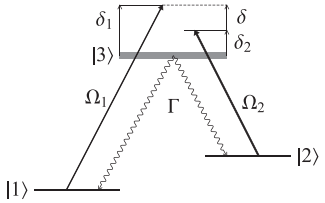

FIG. 3. The Λ level scheme. An intense standing wave with Rabi frequency Ω_2 and a weaker standing wave with Rabi frequency Ω_1, detuning δ_1, illuminate an atom with three levels in a Λ configuration.

we analyze a one-dimensional model based on a Λ-type three-level system schematically represented in Fig. 3.

A. The model

This model includes only the $F = 1,2$ hyperfine ground states and the $F' = 2$ excited state ignoring the Zeeman degeneracy; hence, standard gray molasses cooling [26] does not appear in this model. The states are addressed by two standing waves with nearly the same frequency $\omega_1 \simeq \omega_2 \simeq \omega = kc$ but spatially shifted by a phase ϕ. The principal cooling transition $F = 2 \to F' = 2$ is labeled here and below as transition 2, between states $|2\rangle$ and $|3\rangle$ with a Rabi frequency $\Omega_2 = \Gamma\sqrt{I/2I_{\rm sat}}$, where I is the laser light intensity and $I_{\rm sat}$ the saturation intensity on this transition. The repumper transition is labeled 1, between states $|1\rangle$ and $|3\rangle$ with Rabi frequency Ω_1 much smaller than Ω_2.

The corresponding Hamiltonian for the light-atom interaction in the rotating wave approximation (at ω) is

$$\begin{aligned}\hat{\mathcal{H}}_{\rm a.l.} &= \hbar\Omega_2\cos(kz)\,(|2\rangle\langle 3| + \text{H.c.})\\ &\quad + \hbar\Omega_1\cos(kz+\phi)\,(|1\rangle\langle 3| + \text{H.c.})\\ &\quad + \hbar\delta_2|2\rangle\langle 2| + \hbar\delta_1|1\rangle\langle 1|. \end{aligned} \tag{1}$$

The usual formalism used to compute the atom's dynamics is to consider the light force as a Langevin force. Its mean value is $\mathcal{F}(v)$, and the fluctuations around this mean will give rise to diffusion in momentum space, characterized by the diffusion coefficient $\mathcal{D}_p(v) \geqslant 0$. In order to calculate an equilibrium temperature, one needs $\mathcal{F}(v)$ and $\mathcal{D}_p(v)$. In the limit of small velocities the force reads

$$\mathcal{F}(v) \simeq -\alpha\, v, \tag{2}$$

with α the friction coefficient. If $\alpha > 0$ the force is a cooling force; in the opposite case it produces heating. For a cooling force the limiting temperature in this regime is given by

$$k_{\rm B}T \simeq \mathcal{D}_p(0)/\alpha. \tag{3}$$

However, since our model (1) is a gross simplification of the physical system, we do not expect to be able to quantitatively predict a steady-state temperature. Instead, in order to reveal the physical mechanisms in action, we only calculate the force $\mathcal{F}(v)$ and the excited state population ρ_{33}. Restricting our analysis to the force and photon scattering rate, $\Gamma\rho_{33}$, suffices to determine whether the action of the weak repumper serves to heat or cool the atomic ensemble.

From (1) the mean light force on the atoms is computed by taking the quantum average of the gradient of the potential, $F = \langle -\nabla\hat{\mathcal{H}}_{\rm a.l.}\rangle = -{\rm Tr}[\,\hat{\rho}\,\hat{\mathcal{H}}_{\rm a.l.}]$, with ρ the density matrix, yielding the wavelength-averaged force $\mathcal{F}$,

$$\mathcal{F}(v) = \frac{k}{2\pi}\int_0^{\frac{2\pi}{k}} dz\, F(z,v), \tag{4}$$

$$\mathcal{F}(v) = \frac{\hbar k^2}{\pi}\int_0^{\frac{2\pi}{k}} dz\,\sin(kz)(\Omega_2 {\rm Re}\rho_{23} + \Omega_1 {\rm Re}\rho_{12}). \tag{5}$$

The spontaneous emission rate averaged over the standing wave is simply given by the linewidth of the excited state multiplied by its population:

$$\Gamma' = \frac{k}{2\pi}\int_0^{\frac{2\pi}{k}} dz\,\Gamma\,\rho_{33}. \tag{6}$$

So, both the force and the spontaneous emission rate are functions of the density matrix ρ, the evolution of which is given by the OBEs,

$$i\frac{d}{dt}\rho = \frac{1}{\hbar}[\hat{\mathcal{H}}_{\rm AL},\rho] + i\left(\frac{d\rho}{dt}\right)_{\text{spont. emis.}}. \tag{7}$$

As we are focusing on the sub-Doppler regime, we assume

$$v \ll \Gamma/k, \tag{8}$$

with v being the velocity. The inequality holds for $T \ll 13$ mK for lithium. This inequality allows us to replace the full time derivative in the left-hand side of (7) by a partial spatial derivative times the atomic velocity,

$$\frac{d}{dt} \to v\frac{\partial}{\partial z}.$$

Using the notation $\Omega_i(z) = \Omega_i\cos(z+\phi_i)$ and setting $\hbar = k = 1$ from here on,

$$iv\frac{\partial\rho_{22}}{\partial z} = -2i\Omega_2(z)\,{\rm Im}(\rho_{23}) + i\frac{\Gamma}{2}\rho_{33}, \tag{9}$$

$$iv\frac{\partial\rho_{11}}{\partial z} = -2i\Omega_1(z)\,{\rm Im}(\rho_{13}) + i\frac{\Gamma}{2}\rho_{33}, \tag{10}$$

$$iv\frac{\partial\rho_{23}}{\partial z} = \left(\delta_2 - i\frac{\Gamma}{2}\right)\rho_{23} + \Omega_2(z)\,(\rho_{33}-\rho_{22}) - \Omega_1(z)\rho_{21}, \tag{11}$$

$$iv\frac{\partial\rho_{13}}{\partial z} = \left(\delta_1 - i\frac{\Gamma}{2}\right)\rho_{13} + \Omega_1(z)\,(\rho_{33}-\rho_{11}) - \Omega_2(z)\rho_{12}, \tag{12}$$

$$iv\frac{\partial\rho_{21}}{\partial z} = (\delta_2-\delta_1)\rho_{21} + \Omega_2(z)\rho_{31} - \Omega_2(z)\rho_{23}. \tag{13}$$

The solution of these equations yields the expression of $\mathcal{F}(v)$ and Γ'. This semiclassical model is valid only for velocities above the recoil velocity $v_{\rm rec} = \hbar k/m$ (corresponding to a temperature $mv_{\rm rec}/k_B$ of about 6 μK for lithium). Different theoretical studies [17,18,20,22,30,31] as well as experiments [16,32] have been performed on such a Λ configuration in standing waves or similar systems. However, in our ^{7}Li experiment, we have the situation in which the Λ configuration is coupled to a gray molasses scheme which involves a different set of dark states. This fixes the laser light parameters to values that motivate our theoretical exploration. Thus, we

concentrate on the situation corresponding to the conditions of our experiment.

To solve the OBEs (9)–(13), we first introduce a perturbative approach that enables us to point out the relevant physical mechanisms. We further extend the analysis by an exact approach in terms of continued fractions.

B. Perturbative approach

In our perturbative approach we choose a Rabi frequency Ω_2 between 2Γ and 4Γ and $\Omega_1 \ll \Gamma, \Omega_2, \delta_2$ as the ratio of the repumper to principal laser power is very small, typically $(\Omega_1/\Omega_2)^2 \lesssim 0.03$, under our experimental conditions. We further simplify the approach by considering only the in-phase situation $\phi = 0$; any finite phase would lead to divergencies of the perturbative approach at the nodes of wave 1. The validity of these assumptions are discussed in Sec. III C.

We perform an expansion in powers of the Rabi frequency Ω_1 and the atomic velocity such that the complete expansion reads

$$\rho_{ij} = \sum_{n,l} \rho_{i,j}^{(n,l)} (\Omega_1)^n (v)^l. \tag{14}$$

This expansion of ρ allows us to recursively solve the OBEs. Using an expansion similar to Eq. (14) for the force, we find

$$\alpha = -\sum_{n=0}^{\infty} \mathcal{F}^{(n,1)} (\Omega_1)^n. \tag{15}$$

We plug the perturbative solution of the OBEs into Eq. (5) and find, to the lowest order ($n = 2$) in Ω_1,

$$\alpha \simeq -\frac{(\Omega_1)^2}{2\pi} \int_0^{2\pi} dz \sin(z) \left(\Omega_2 \mathrm{Re}\, \rho_{23}^{(2,1)} + \mathrm{Re}\, \rho_{13}^{(1,1)}\right). \tag{16}$$

The spontaneous emission rate to lowest order in v and Ω_1 reads

$$\Gamma' = \Gamma \frac{(\Omega_1)^2}{2\pi} \int_0^{2\pi} dz\, \rho_{33}^{(2,0)}. \tag{17}$$

Figure 4 presents the results from (15) and (17) compared with the experimental data. It shows that indeed a narrow cooling force appears near the Raman resonance condition and that the photon scattering rate vanishes at exact resonance, hinting at an increase of cooling efficiency with respect to the gray molasses Sisyphus cooling mechanism which achieves a temperature near 200 μK over a broad range. The strong heating peak for small, positive repumper detuning is also a consequence of the negative value of α, and the heating peak shifts towards higher frequency and broadens for larger intensities of the principal laser. In contrast, the friction coefficient and scattering rate in the range $-6 \leqslant \delta/\Gamma \leqslant -3$, which correspond to a repumper near resonance, do not seem to significantly affect the measured temperature.

To gain further physical insight into this cooling near the Raman condition, it is useful to work in the dressed-atom picture. Given the weak repumping intensity, we first ignore its effect and consider only the dressing of the states $|2\rangle$ and $|3\rangle$ by the strong pump with Rabi frequency Ω_2. This dressing

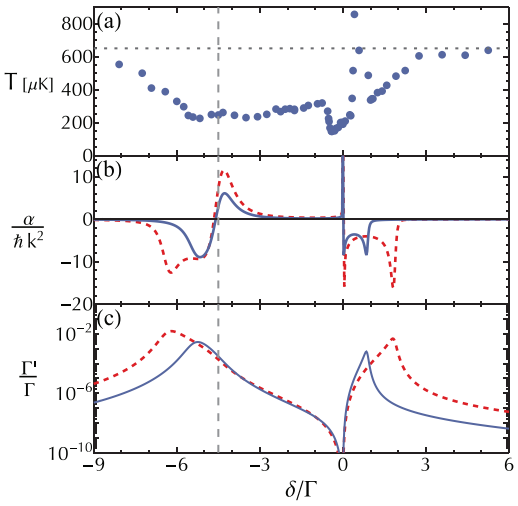

FIG. 4. (Color online) Comparison of experimental data with the perturbative approach results for a detuning of the pump $\delta_2 = 2\pi \times 26.4$ MHz $= 4.5\Gamma$. (a) Temperature versus repumper detuning, experiment; we indicate the MOT temparature by the dotted line. Panels (b) and (c) show, respectively, the friction coefficient α and photon scattering rate Γ' for $\Omega_2 = 3.4\Gamma$ (red dashed curve) and 2.1Γ (blue solid curve). The intensity ratio $(\Omega_1/\Omega_2)^2$ is 0.02. The vertical dashed line indicates the position of $\delta_1 = 0$.

gives rise to an Autler-Townes doublet structure which follows the spatial modulation of the standing wave:

$$|2'\rangle \propto |2\rangle - i\Omega_2(z)/\delta_2 |3\rangle, \tag{18}$$

$$|3'\rangle \propto -i\Omega_2(z)/\delta_2 |2\rangle + |3\rangle. \tag{19}$$

Since the pump is relatively far detuned (in the conditions of Fig. 4 $\Omega_2/\delta_2 \lesssim 0.45$), the broad state $|3'\rangle$ carries little $|2\rangle$ character. Conversely, the narrow state $|2'\rangle$ is mostly state $|2\rangle$. It follows that $|3'\rangle$ has a lifetime $\Gamma^{|3'\rangle} \simeq \Gamma$, while $|2'\rangle$ is relatively long lived with a spatially dependent linewidth $\Gamma^{|2'\rangle} = \Gamma(\Omega_2(z)/\delta_2)^2$, which is always $\leqslant \Gamma/6$ for the parameters chosen here. In order to reintroduce the effects of the repumping radiation, we note that the position in δ of the broad state is $\delta^{|3'\rangle} \simeq -\delta_2 - \Omega_2(z)^2/\delta_2$ and the narrow state $\delta^{|2'\rangle} \simeq \Omega_2(z)^2/\delta_2$. As coherent population transfer between $|1\rangle$ and $|2'\rangle$ does not change the ensemble temperature, we consider only events which couple atoms out of $|2'\rangle$ to $|1\rangle$ through spontaneous decay and therefore scale with $\Gamma_{|2'\rangle}$. The rates of coupling from $|1\rangle$ into the dressed states can be approximated by the two-level absorption rates:

$$\gamma_{|1\rangle \to |2'\rangle} \sim \frac{\Omega_1(z)^2}{2} \frac{\Gamma^{|2'\rangle}(z)}{[\Gamma^{|2'\rangle}(z)/2]^2 + [\delta - \delta^{|2'\rangle}(z)]^2}, \tag{20}$$

$$\gamma_{|1\rangle \to |3'\rangle} \sim \frac{\Omega_1(z)^2}{2} \frac{\Gamma}{(\Gamma/2)^2 + [\delta - \delta^{|3'\rangle}(z)]^2}. \tag{21}$$

Finally, these results are valid only in the limit $|\delta| > \Gamma\Omega_2^2/\delta_2^2$ (see, e.g., [33]) when state $|1\rangle$ is weakly coupled to the radiative cascade. Near the Raman resonance, the dressed state family contains a dark state which bears an infinite lifetime under the assumptions made in this section but is, in reality, limited by

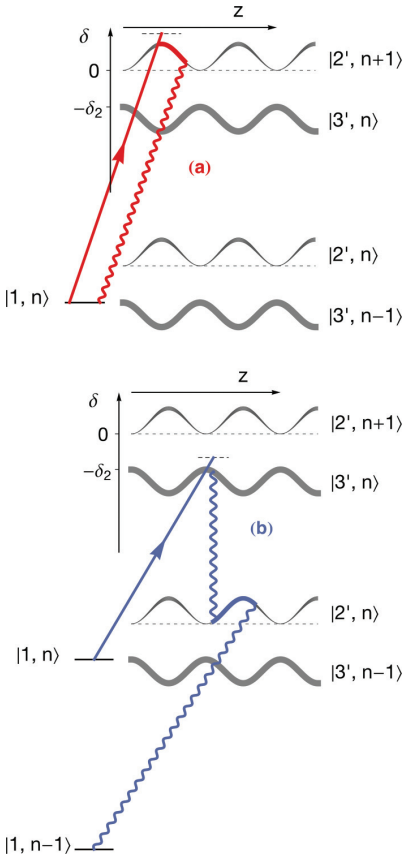

FIG. 5. (Color online) The cascade of levels dressed by transition 2 with a schematical representation of state $|1\rangle$. Traces show typical cycles of atoms pumped from $|1\rangle$ and back depending on the detuning of wave 1. The detuning of the repumper modulates the entry point into the cascade of the dressed states, leading either (a) heating or (b) cooling processes.

off-resonant excitations and motional coupling. This dark state reads

$$|\mathrm{NC}\rangle = (\Omega_2|1\rangle - \Omega_1|2\rangle)/\sqrt{\Omega_1^2 + \Omega_2^2}, \tag{22}$$

which we must add in by hand.

Using this toy model, we now explain the features of Fig. 4 and Fig. 2. Figure 5 represents the cascade of dressed levels where each doublet is separated by one pump photon. It gives rise, for example, to the well-known Mollow triplet. Condition (8) states that if an atom falls in state $|3'\rangle$ it will rapidly decay to $|2'\rangle$ without traveling a significant distance. However, the atom will remain in $|2'\rangle$ long enough to sample the spatial variation of the standing wave and gain or lose energy depending on the difference of light shift between the entry and the departure points, as in most sub-Doppler cooling schemes.

Let us first analyze the spontaneous emission rate shown in Fig. 4(c). It reaches two maxima, the first one for $\delta \sim \delta^{|3'\rangle}$ and the second one for $\delta \sim \delta^{|2'\rangle}$, and it goes to exactly zero at $\delta = 0$. The two maxima are simply due to scattering off the states $|2'\rangle$ and $|3'\rangle$. At $\delta = 0$, Γ' goes to zero due to coherent population trapping in $|\mathrm{NC}\rangle$. It is the presence of this dark state which leads to the reduced scattering rate of photons around $\delta = 0$ and the suppression of the final temperature of the gas in the region around the Raman condition.

The friction coefficient, Fig. 4(b), displays a more complicated structure with variations in δ. It shows a dispersive shape around $\delta^{|3'\rangle}$, remains positive in the range $\delta^{|3'\rangle} < \delta < 0$, diverges at $\delta = 0$, and reaches negative values for $\delta > 0$ up to $\delta^{|2'\rangle}$, where it drops to negligible values. This structure for α can be explained using our toy model. Let us consider the different scenarios corresponding to both sides of δ near 0, they follow formally from Eqs. (20) and (21) and the spatially varying linewidth of $|2'\rangle$.

For the case of the repumper tuned slightly blue of the narrow doublet state, $\delta > \delta^{|2'\rangle}$, shown in Fig. 5(a), the atoms are pumped directly from $|1\rangle$ into $|2'\rangle$. However, this pumping happens preferentially at the antinodes of the standing wave as the repumper intensity is greatest, the linewidth of $|2'\rangle$ is the largest, and the light shift minimizes the detuning of the repumper from the $|1\rangle \rightarrow |2'\rangle$ transition for the $\phi = 0$ case considered here. On average, the atoms exit this state at a point with a smaller light shift through a spontaneous emission process either into the cascade of dressed states or directly back to $|1\rangle$. As a result, we expect heating and $\alpha < 0$ in this region.

For repumper detunings between $\delta^{|3'\rangle}$ and 0, Fig. 5(b), we predict cooling. For this region, the atoms are initially pumped into $|3'\rangle$. Here the light shift modifies the relative detuning, favoring coupling near the nodes of the light. Spontaneous decay drops the atoms near the nodes of the longer-lived $|2'\rangle$, and they travel up the potential hill into regions of larger light shift before decaying, yielding cooling and a positive α. These sign changes of α and the decreased scattering rate due to $|\mathrm{NC}\rangle$ in the vicinity of the Raman condition explain the features of our perturbative model.

We conclude this section by stating that the experimentally observed change of sign of the force close to the Raman condition is well described in our perturbative model. The model further reveals the importance of Raman coherence and the existence of a dark state. The dark state together with the friction coefficient associated with cycles represented in trace 5(b) correspond to a cooling mechanism analogous to that of gray molasses. In this way, the bichromatic system provides an additional gray molasses scheme involving both hyperfine states which complements the gray molasses cooling scheme on the principal transition. On the other hand, when the friction coefficient is negative in the vicinity of the two-photon resonance, it turns into a heating mechanism that overcomes the standard gray molasses operating on the $F = 2 \rightarrow F' = 2$ transition.

The perturbative approach successfully revealed the mechanisms giving rise to the experimentally observed additional cooling. However, it also possesses some shortcomings. First, the divergence of α at $\delta = 0$ is not physical; the assumption that Ω_1 is the smallest scale in the problem breaks down when $\delta \rightarrow 0$. Alternatively, it can be seen as the failure of our model based on nondegenerate perturbative theory in the region where $|1\rangle$ and $|2\rangle$ become degenerate when dressed with ω_1 and ω_2, respectively. Second, we have only addressed the $\phi = 0$ case. Since the experiment was done in three dimensions with three pairs of counterpropagating beams, the relative phase

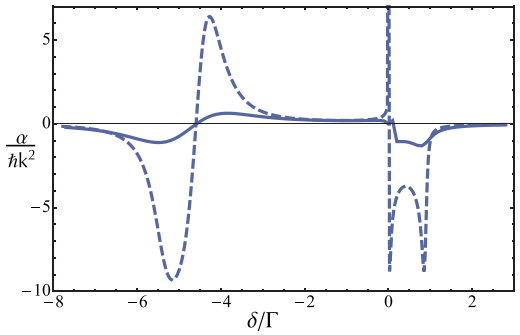

FIG. 6. (Color online) Comparison of results using the perturbative calculation (dashed), and the continued fractions (solid) for the $\phi = 0$ case, with the same parameters as in Fig. 4 and $\Omega_2 = 2.1\Gamma$.

between the two frequencies varies spatially, and we must test if the picture derived at $\phi = 0$ holds when averaging over all phases. In order to address these limitations and confirm the predictions of the perturbative approach, we now present a continued-fractions solution to the OBEs which does not rely on Ω_1 being a small parameter.

C. Continued fractions approach

The limitations listed above can be addressed by using a more general approach, namely, an expansion of the density matrix in Fourier harmonics:

$$\rho_{ij} = \sum_{n=-\infty}^{n=+\infty} \rho_{ij}^{(n)} e^{inkz}. \tag{23}$$

Injecting this expansion in (9)–(13) yields recursive relations between different Fourier components of ρ. Kozachiov *et al.* [17,30] express the solutions of these relations for a generalized Λ system in terms of continued fractions. Here we use their results to numerically solve the Bloch equations. We then compute the force $\mathcal{F}(v)$ to arbitrary order of Ω_1 and extract α by means of a linear fit to the small-v region. We then compute $\mathcal{F}(v)$ and the photon scattering rate Γ' averaged over the phase between the two standing waves.

Figure 6 compares $\alpha(\delta)$ obtained through the continued-fractions approach with the results of the perturbative expansion for the $\phi = 0$ case. The continued-fractions approach has removed the divergence at $\delta = 0$ and α crosses zero linearly. The overall friction coefficient is reduced but the two methods show qualitative agreement in the range of δ considered. At the Raman condition the interaction with light is canceled due to the presence of $|\mathrm{NC}\rangle$; thus, the diffusion coefficient $\mathcal{D}_p$ in momentum space also cancels. To lowest order, the diffusion and friction coefficients scale as

$$\mathcal{D}_p \simeq \delta^2, \tag{24}$$

$$\alpha \simeq \delta; \tag{25}$$

according to (3) the temperature scales as

$$T \simeq \delta. \tag{26}$$

Through this qualitative scaling argument, we show that even though the light action on the atoms is suppressed when approaching the Raman condition, we expect that the temperature will drop when approaching from the $\delta < 0$ side, completing the physical picture derived in the previous section.

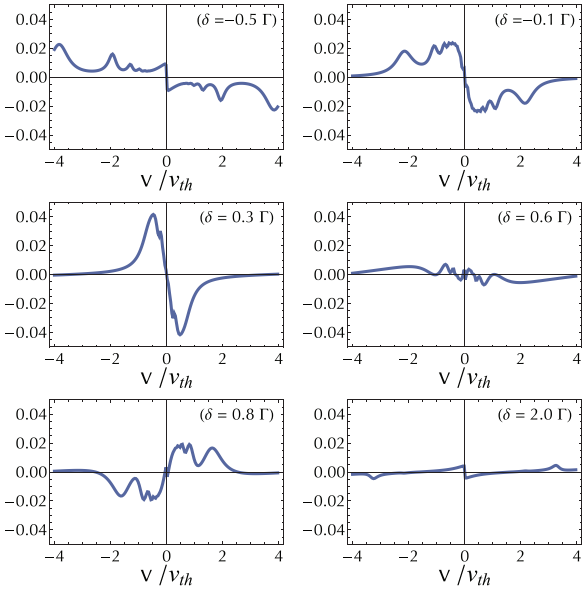

FIG. 7. (Color online) $\langle\mathcal{F}\rangle_\phi$ in units of $1/\hbar k\Gamma$ as a function of v for different values of δ around $\delta = 0$. The horizontal scale is in units of the thermal velocity at $T = 200\,\mu$K, $v_{th} = \sqrt{k_B T/m}$.

Next, we analyze how a randomized phase between the repumping and principal standing waves, ϕ, modifies $\mathcal{F}(v)$. In order to take this into account, we calculate the phase-averaged force:

$$\langle\mathcal{F}(v)\rangle_\phi = \frac{1}{2\pi}\int_0^{2\pi} \mathcal{F}(v,\phi)\,d\phi. \tag{27}$$

In Fig. 7, the phase-averaged force is plotted for various detunings near the Raman condition. It can be seen that a cooling force is present for small detunings, qualitatively in agreement with our perturbative model and with the experimental data. The force, however, changes sign to heating for small blue detuning, close to $\delta = 0.6\,\Gamma$, also in qualitative agreement with the experimental data. We note that the cooling slope very close to zero velocity in the $\delta = 0.8\,\Gamma$ plot corresponds to a velocity on the order of or below the single-photon recoil velocity, i.e., is nonphysical.

Finally, for the $\phi \neq 0$ case, $|\mathrm{NC}\rangle$ varies in space and the motion of the atoms can couple atoms out of $|\mathrm{NC}\rangle$ even at the Raman condition. In Fig. 8 we verify that the rate of photon scattering retains a minimum near the $\delta = 0$ region after averaging over ϕ by plotting $\langle\Gamma'\rangle_\phi = \Gamma\langle\rho_{33}\rangle_\phi$ calculated with the continued fractions approach. Overall, the friction coefficient α and photon scattering rate Γ' confirm the existence of a cooling force associated with a decrease in photon scattering in the vicinity of the Raman condition for the 1D bichromatic standing-wave model. Thus, the continued fractions calculation has confirmed the physical mechanisms revealed by the perturbative expansion and that the lowest

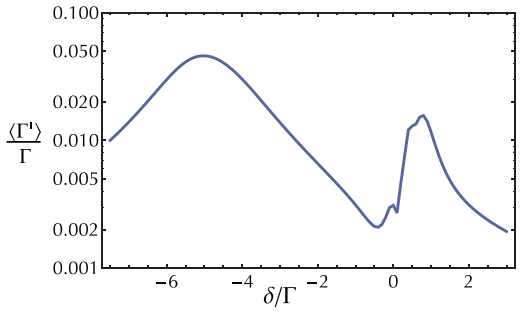

FIG. 8. (Color online) Continued fractions solution of the photon scattering rate $\Gamma' = \Gamma\,\rho_{33}$ averaged over all relative phases of the repumper and principal standing waves as a function of the two-photon detuning δ. Velocity-dependent effects are taken into account here by computing an average of $\langle\Gamma'\rangle_\phi(v)$ weighed by a Maxwell-Boltzmann velocity distribution at 200 μK.

temperatures should be expected close to $\delta = 0$, as seen in the experiment.

IV. CONCLUSION

In this study, using bichromatic laser light near 670 nm, we have demonstrated sub-Doppler cooling of ^{7}Li atoms down to 60 μK with near unity capture efficiency from a magneto-optical trap. Solving the OBEs for a simplified Λ level structure, we have analyzed the detuning dependence of the cooling force and photon scattering rate. Our analysis shows that the lowest temperatures are expected for a detuning of the repumping light near the Raman condition, in agreement with our measurements. There the Λ configuration adds a new set of long-lived dark states that strongly enhance the cooling efficiency. For ^{7}Li, this addition results in a threefold reduction of the steady-state temperature in comparison with an incoherently repumped gray molasses scheme. This atomic cloud at 60 μK is an ideal starting point for direct loading into a dipole trap, where one of the broad Feshbach resonances in the lowest-energy states of ^{7}Li or ^{6}Li could be used to efficiently cool the atoms to quantum degeneracy [15,34]. Alternatively, when the atoms are loaded into a quadrupole magnetic trap, we measure a phase space density of $\simeq 10^{-5}$. This Λ-enhanced sub-Doppler cooling in a D_1 gray molasses is general and should occur in all alkali metals. Notably, we have observed its signature in a number of the alkali-metal isotopes not amenable to polarization gradient cooling: ^{7}Li (this work), ^{40}K [25], and ^{6}Li [35].

ACKNOWLEDGMENTS

We acknowledge fruitful discussions with Y. Castin, J. Dalibard S. Wu, F. Sievers, N. Kretzschmar, D. R. Fernandes, M. Schleier-Smith, and I. Leroux and support from Région Île de France (IFRAF-C'Nano), EU (ERC advanced grant Ferlodim), Institut de France (Louis D. Foundation), and Institut Universitaire de France.

[1] C. Chin, R. Grimm, P. Julienne, and E. Tiesinga, Rev. Mod. Phys. **82**, 1225 (2010).
[2] I. Bloch, J. Dalibard, and W. Zwerger, Rev. Mod. Phys. **80**, 885 (2008).
[3] S. Nascimbène, N. Navon, K. J. Jiang, F. Chevy, and C. Salomon, Nature (London) **463**, 1057 (2010).
[4] N. Navon, S. Piatecki, K. Günter, B. Rem, T. C. Nguyen, F. Chevy, W. Krauth, and C. Salomon, Phys. Rev. Lett. **107**, 135301 (2011).
[5] R. J. Wild, P. Makotyn, J. M. Pino, E. A. Cornell, and D. S. Jin, Phys. Rev. Lett. **108**, 145305 (2012).
[6] B. S. Rem, A. T. Grier, I. Ferrier-Barbut, U. Eismann, T. Langen, N. Navon, L. Khaykovich, F. Werner, D. S. Petrov, F. Chevy *et al.*, Phys. Rev. Lett. **110**, 163202 (2013).
[7] S. Lepoutre, A. Gauguet, G. Trénec, M. Büchner, and J. Vigué, Phys. Rev. Lett. **109**, 120404 (2012).
[8] R. Bouchendira, P. Cladé, S. Guellati-Khélifa, F. Nez, and F. Biraben, Phys. Rev. Lett. **106**, 080801 (2011).
[9] T. Esslinger, Annu. Rev. Condens. Matter Phys. **1**, 129 (2010).
[10] A. Härter, A. Krükow, A. Brunner, W. Schnitzler, S. Schmid, and J. H. Denschlag, Phys. Rev. Lett. **109**, 123201 (2012).
[11] M. Cetina, A. T. Grier, and V. Vuletic, Phys. Rev. Lett. **109**, 253201 (2012).
[12] J. Dalibard and C. Cohen-Tannoudji, J. Opt. Soc. Am. B **6**, 2023 (1989).
[13] P. D. Lett, W. D. Phillips, S. L. Rolston, C. E. Tanner, R. N. Watts, and C. I. Westbrook, J. Opt. Soc. Am. B **6**, 2084 (1989).
[14] D. S. Weiss, E. Riis, Y. Shevy, P. J. Ungar, and S. Chu, J. Opt. Soc. Am. B **6**, 2072 (1989).
[15] P. M. Duarte, R. A. Hart, J. M. Hitchcock, T. A. Corcovilos, T. L. Yang, A. Reed, and R. G. Hulet, Phys. Rev. A **84**, 061406 (2011).
[16] R. Gupta, C. Xie, S. Padua, H. Batelaan, and H. Metcalf, Phys. Rev. Lett. **71**, 3087 (1993).
[17] D. V. Kosachiov, Y. V. Rozhdestvensky, and G. Nienhuis, J. Opt. Soc. Am. B **14**, 535 (1997).
[18] M. Drewsen, Phys. Rev. A **51**, 1407 (1995).
[19] C. F. Roos, D. Leibfried, A. Mundt, F. Schmidt-Kaler, J. Eschner, and R. Blatt, Phys. Rev. Lett. **85**, 5547 (2000).
[20] G. Grynberg and J.-Y. Courtois, Europhys. Lett. **27**, 41 (1994).
[21] G. Morigi and E. Arimondo, Phys. Rev. A **75**, 051404 (2007).
[22] J. W. Dunn, J. W. Thomsen, C. H. Greene, and F. C. Cruz, Phys. Rev. A **76**, 011401 (2007).
[23] A. Aspect, E. Arimondo, R. Kaiser, N. Vansteenkiste, and C. Cohen-Tannoudji, Phys. Rev. Lett. **61**, 826 (1988).
[24] G. Morigi, J. Eschner, and C. H. Keitel, Phys. Rev. Lett. **85**, 4458 (2000).
[25] D. R. Fernandes, F. Sievers, N. Kretzschmar, S. Wu, C. Salomon, and F. Chevy, Europhys. Lett. **100**, 63001 (2012).

[26] M. Weidemüller, T. Esslinger, M. A. Ol'shaniî, A. Hemmerich, and T. W. Hänsch, Europhys. Lett. **27**, 109 (1994).
[27] U. Eismann, F. Gerbier, C. Canalias, A. Zukauskas, G. Trénec, J. Vigué, F. Chevy, and C. Salomon, Appl. Phys. B **106**, 25 (2011).
[28] U. Eismann, A. Bergschneider, F. Sievers, N. Kretzschmar, C. Salomon, and F. Chevy, Opt. Express **21**, 9091 (2013).
[29] M.-O. Mewes, G. Ferrari, F. Schreck, A. Sinatra, and C. Salomon, Phys. Rev. A **61**, 011403 (1999).
[30] D. V. Kosachev and Y. V. Rozhdestvenskii, J. Exp. Theor. Phys. **79**, 856 (1994).
[31] C. Menotti, G. Morigi, J. H. Müller, and E. Arimondo, Phys. Rev. A **56**, 4327 (1997).
[32] N. Malossi, S. Damkjær, P. L. Hansen, L. B. Jacobsen, L. Kindt, S. Sauge, J. W. Thomsen, F. C. Cruz, M. Allegrini, and E. Arimondo, Phys. Rev. A **72**, 051403 (2005).
[33] E. Arimondo, in *Progress in Optics*, Vol. 35 (Elsevier, Amsterdam, 1996), pp. 257–354.
[34] N. Gross and L. Khaykovich, Phys. Rev. A **77**, 023604 (2008).
[35] F. Sievers, N. Kretzschmar, S. Wu, *et al.* (private communication).

C.2 A mixture of Bose and Fermi superfluids

Igor Ferrier-Barbut, Marion Delehaye, Sébastien Laurent, Andrew T. Grier, Matthieu Pierce, Benno S. Rem, Frédéric Chevy, and Christophe Salomon

Science **345**, 1035-1038 (2014)

collisions. An analysis with some similarities to ours for the bright debris disk of HD 172555 (*20*) found that dust created in a hypervelocity impact will have a size slope of ~ −4, in agreement with the fits of (*10*) to the IR spectrum of ID8.

After the exponential decay is removed from the data ("detrending"), the light curves at both wavelengths appear to be quasi-periodic. The regular recovery of the disk flux and lack of extraordinary stellar activity essentially eliminate coronal mass ejection (*21*) as a possible driver of the disk variability. We employed the SigSpec algorithm (*22*) to search for complex patterns in the detrended, post-impact 2013 light curve. The analysis identified two significant frequencies with comparable amplitudes, whose periods are P_1 = 25.4 ± 1.1 days and P_2 = 34.0 ± 1.5 days (Fig. 3A) and are sufficient to qualitatively reproduce most of the observed light curve features (Fig. 3B). The quoted uncertainties (*23*) do not account for systematic effects due to the detrending and thus are lower limits to the real errors. Other peaks with longer periods in the periodogram are aliases or possibly reflect long-term deviation from the exponential decay. These artifacts make it difficult to determine whether there are weak real signals near those frequencies.

We now describe the most plausible interpretation of this light curve that we have found. The two identified periods have a peak-to-peak amplitude of ~6×10^{-3} in fractional luminosity, which provides a critical constraint for models of the ID8 disk. In terms of sky coverage at the disk distance inferred from the IR SED, such an amplitude requires the disappearance and reappearance every ~30 days of the equivalent of an opaque, stellar-facing "dust panel" of radius ~110 Jupiter radii. One possibility is that the disk flux periodicity arises from recurring geometry that changes the amount of dust that we can see. At the time of the impact, fragments get a range of kick velocities when escaping into interplanetary space. This will cause Keplerian shear of the cloud (*24*), leading to an expanding debris concentration along the original orbit (supplementary text). If the ID8 planetary system is roughly edge-on, the longest dimension of the concentration will be parallel to our line of sight at the greatest elongations and orthogonal to the line of sight near conjunctions to the star. This would cause the optical depth of the debris to vary within an orbital period, in a range on the order of 1 to 10 according to the estimated disk mass and particle sizes. Our numerical simulations of such dust concentrations on moderately eccentric orbits are able to produce periodic light curves with strong overtones. P_2 and P_1 should have a 3:2 ratio if they are the first- and second-order overtones of a fundamental, which is consistent with the measurements within the expected larger errors (<2σ or better). In this case, the genuine period should be 70.8 ± 5.2 days (lower-limit errors), a value where it may have been submerged in the periodogram artifacts. This period corresponds to a semimajor axis of ~0.33 astronomical units, which is consistent with the temperature and distance suggested by the spectral models (*10*).

Despite the peculiarities of ID8, it is not a unique system. In 2012 and 2013, we monitored four other "extreme debris disks" (with disk fractional luminosity ≥10^{-2}) around solar-like stars with ages of 10 to 120 My. Various degrees of IR variations were detected in all of them. The specific characteristics of ID8 in the time domain, including the yearly exponential decay, additional more rapid weekly to monthly changes, and color variations, are also seen in other systems. This opens up the time domain as a new dimension for the study of terrestrial planet formation and collisions outside the solar system. The variability of many extreme debris disks in the era of the final buildup of terrestrial planets may provide new possibilities for understanding the early solar system and the formation of habitable planets (*25*).

REFERENCES AND NOTES

1. R. Helled *et al.*, in *Protostars and Planets VI*, H. Beuther, R. Klessen, C. Dullemond, T. Henning, Eds. (Univ. of Arizona Press, Tucson, AZ, 2014), in press; available at http://arxiv.org/abs/1311.1142.
2. M. C. Wyatt, *Annu. Rev. Astron. Astrophys.* **46**, 339–383 (2008).
3. K. Righter, D. P. O'Brien, *Proc. Natl. Acad. Sci. U.S.A.* **108**, 19165–19170 (2011).
4. S. N. Raymond, E. Kokubo, A. Morbidelli, R. Morishima, K. J. Walsh, in *Protostars and Planets VI*, H. Beuther, R. Klessen, C. Dullemond, T. Henning, Eds. (Univ. of Arizona Press, Tucson, AZ, 2014), in press; available at http://arxiv.org/abs/1312.1689.
5. R. M. Canup, *Annu. Rev. Astron. Astrophys.* **42**, 441–475 (2004).
6. M. Ćuk, S. T. Stewart, *Science* **338**, 1047–1052 (2012).
7. R. M. Canup, *Science* **338**, 1052–1055 (2012).
8. H. Y. A. Meng *et al.*, *Astrophys. J.* **751**, L17–L21 (2012).
9. D. R. Soderblom, L. A. Hillenbrand, R. D. Jeffries, E. E. Mamajek, T. Naylor, in *Protostars and Planets VI*, H. Beuther, R. Klessen, C. Dullemond, T. Henning, Eds. (Univ. of Arizona Press, Tucson, AZ, 2014), in press; available at http://arxiv.org/abs/1311.7024.
10. J. Olofsson *et al.*, *Astron. Astrophys.* **542**, 90–115 (2012).
11. P. Artymowicz, *Astrophys. J.* **335**, L79–L82 (1988).
12. G. G. Fazio *et al.*, *Astrophys. J. Suppl. Ser.* **154**, 10–17 (2004).
13. D. Jewitt, H. Matthews, *Astron. J.* **117**, 1056–1062 (1999).
14. J. A. M. McDonnell *et al.*, *Nature* **321**, 338–341 (1986).
15. D. Perez-Becker, E. Chiang, *Mon. Not. R. Astron. Soc.* **433**, 2294–2309 (2013).
16. P. H. Warren, *Geochim. Cosmochim. Acta* **72**, 3562–3585 (2008).
17. B. C. Johnson, H. J. Melosh, *Icarus* **217**, 416–430 (2012).
18. M. C. Wyatt, W. R. F. Dent, *Mon. Not. R. Astron. Soc.* **334**, 589–607 (2002).
19. B. Zuckerman, I. Song, *Astrophys. J.* **758**, 77–86 (2012).
20. B. C. Johnson *et al.*, *Astrophys. J.* **761**, 45–57 (2012).
21. R. Osten *et al.*, *Astrophys. J.* **765**, L44–L46 (2013).
22. P. Reegen, *Astron. Astrophys.* **467**, 1353–1371 (2007).
23. T. Kallinger, P. Reegen, W. W. Weiss, *Astron. Astrophys.* **481**, 571–574 (2008).
24. S. J. Kenyon, B. C. Bromley, *Astron. J.* **130**, 269–279 (2005).
25. S. Elser, B. Moore, J. Stadel, R. Morishima, *Icarus* **214**, 357–365 (2011).
26. T. Naylor *et al.*, *Mon. Not. R. Astron. Soc.* **335**, 291–310 (2002).
27. R. D. Jeffries, T. Naylor, C. R. Devey, E. J. Totten, *Mon. Not. R. Astron. Soc.* **351**, 1401–1422 (2004).

ACKNOWLEDGMENTS

H.Y.A.M, K.Y.L.S., and G.H.R. thank R. Malhotra and A. Gáspár for valuable discussions. This work is based on observations made with the Spitzer Space Telescope, which is operated by the Jet Propulsion Laboratory (JPL), California Institute of Technology, under a contract with NASA. Support for this work was provided by NASA through an award issued by JPL/Caltech and by NASA grant NNX13AE74G. All data are publicly available through the NASA/IPAC Infrared Science Archive.

SUPPLEMENTARY MATERIALS

www.sciencemag.org/content/345/6200/1032/suppl/DC1
Supplementary Text
Figs. S1 to S4
References (*28*–*45*)

23 April 2014; accepted 15 July 2014
10.1126/science.1255153

SUPERFLUIDITY

A mixture of Bose and Fermi superfluids

I. Ferrier-Barbut,* M. Delehaye, S. Laurent, A. T. Grier,† M. Pierce, B. S. Rem,‡ F. Chevy, C. Salomon

Superconductivity and superfluidity of fermionic and bosonic systems are remarkable many-body quantum phenomena. In liquid helium and dilute gases, Bose and Fermi superfluidity has been observed separately, but producing a mixture in which both the fermionic and the bosonic components are superfluid is challenging. Here we report on the observation of such a mixture with dilute gases of two lithium isotopes, lithium-6 and lithium-7. We probe the collective dynamics of this system by exciting center-of-mass oscillations that exhibit extremely low damping below a certain critical velocity. Using high-precision spectroscopy of these modes, we observe coherent energy exchange and measure the coupling between the two superfluids. Our observations can be captured theoretically using a sum-rule approach that we interpret in terms of two coupled oscillators.

In recent years, ultracold atoms have emerged as a unique tool to engineer and study quantum many-body systems. Examples include weakly interacting Bose-Einstein condensates (*1*, *2*), two-dimensional gases (*3*), and the superfluid-Mott insulator transition (*4*) in the case of bosonic atoms, and the crossover between Bose-Einstein condensation (BEC) and fermionic superfluidity described by the the theory of Bardeen, Cooper, and Schrieffer (BCS) for fermionic atoms (*5*). Mixtures of Bose-Einstein condensates were produced shortly after the observation of BEC (*2*), and a BEC mixed with a single-spin state Fermi sea was originally observed in (*6*, *7*). However, realizing a mixture in which both fermionic and bosonic species are superfluid has been experimentally challenging. This has also been a long-sought goal in liquid helium, where superfluidity was achieved separately in both bosonic ^{4}He and fermionic ^{3}He. The double superfluid should undergo a transition

between s-wave and p-wave Cooper pairs as the ^{3}He dilution is varied (*8*). However, because of strong interactions between the two isotopes, ^{3}He-^{4}He mixtures contain only a small fraction of ^{3}He (typically 6%) which, so far, has prevented attainment of simultaneous superfluidity for the two species (*8*, *9*).

Here we report on the production of a Bose-Fermi mixture of quantum gases in which both species are superfluid. Our system is an ultracold gas of fermionic ^{6}Li in two spin states mixed with ^{7}Li bosons and confined in an optical dipole trap. Using radio-frequency pulses, we prepare ^{6}Li atoms in their two lowest hyperfine states $|1_f\rangle$ and $|2_f\rangle$, whereas ^{7}Li is spin polarized in the second-to-lowest state $|2_b\rangle$ (*10*). For this combination of states, in the vicinity of the ^{6}Li Feshbach resonance at a magnetic field of 832 G (*11*), the scattering length of the bosonic isotope $a_b = 70a_0$ (a_0 is the Bohr radius) is positive, preventing collapse of the BEC. The boson-fermion interaction is characterized by a scattering length $a_{bf} = 40.8a_0$ that does not depend on magnetic field in the parameter range studied here. At resonance, the Fermi gas exhibits a unitary limited collision rate, and lowering the optical dipole trap depth leads to extremely efficient evaporation. Owing to a large excess of ^{6}Li atoms with respect to ^{7}Li, the Bose gas is sympathetically driven to quantum degeneracy.

The two clouds reach the superfluid regime after a 4-s evaporation ramp (*10*). As the ^{7}Li Bose gas is weakly interacting, the onset of BEC is detected by the growth of a narrow peak in the density profile of the cloud. From previous studies on atomic Bose-Einstein condensates, we conclude that the ^{7}Li BEC is in a superfluid phase. Superfluidity in a unitary Fermi gas is notoriously more difficult to detect because of the absence of any qualitative modification of the density profile at the phase transition. To demonstrate the superfluidity of the fermionic component of the cloud, we slightly imbalance the two spin populations. In an imbalanced gas, the cloud is organized in concentric layers, with a fully paired superfluid region at its center, where Cooper pairing maintains equal spin populations. This ^{6}Li superfluid core can be detected by the presence of a plateau in the doubly integrated density difference (*12*). Examples of density profiles of the bosonic and fermionic superfluids are shown in Fig. 1, where both the Bose-Einstein condensate (blue circles) and the plateau (black diamonds in the inset) are clearly visible. Our coldest samples contain $N_b = 4 \times 10^4$ ^{7}Li atoms and $N_f = 3.5 \times 10^5$ ^{6}Li atoms. The absence of a thermal fraction in the bosonic cloud indicates a temperature below $0.5T_{c,b}$, where $k_B T_{c,b} = 0.94\hbar\bar{\omega}_b N_b^{1/3}$ is the critical temperature of the ^{7}Li bosons, and $\bar{\omega}_b$ ($\bar{\omega}_f$) is the geometric mean trapping frequency for ^{7}Li (^{6}Li). Combined with the observation of the ^{6}Li plateau, this implies that the Fermi cloud is also superfluid with a temperature below $0.8T_{c,f}$. Here, $T_{c,f}$ is the critical temperature for superfluidity of a spin-balanced, harmonically trapped Fermi gas at unitarity, $T_{c,f} = 0.19T_F$ (*13*), and $k_B T_F = \hbar\bar{\omega}_f(3N_f)^{1/3}$ is the Fermi temperature. The superfluid mixture is very stable, with a lifetime exceeding 7 s for our coldest samples.

As seen in Fig. 1, the Bose-Fermi interaction is too weak to alter significantly the density profiles of the two species (*14*). To probe the interaction between the two superfluids, we study the dynamics of the mass centers of the two isotopes (dipole modes), a scheme used previously for the study of mixtures of Bose-Einstein condensates (*15*, *16*), mixtures of Bose-Einstein condensates and spin-polarized Fermi seas (*17*), spin diffusion in Fermi gases (*18*), or integrability in one-dimensional systems (*19*). In a purely harmonic trap and in the absence of interspecies interactions, the dipole mode of each species is undamped and can therefore be measured over long time spans to achieve a high-frequency resolution and detect small perturbations of the system. We excite the dipole modes by shifting the initial position of the ^{6}Li and ^{7}Li clouds by a displacement d along the weak direction z of the trap (*10*). We then release them and let them evolve during a variable time t, after which we measure their positions. By monitoring the cloud oscillations during up to 4 s, we determine their frequencies with high precision ($\frac{\Delta\omega}{\omega} \lesssim 2 \times 10^{-3}$). In the absence of the other species, the oscillation frequencies of ^{6}Li and ^{7}Li are, respectively, $\omega_f = 2\pi \times 16.80(2)$ Hz and $\omega_b = 2\pi \times 15.27(1)$ Hz. In the axial direction, the confinement is mostly magnetic, and at high magnetic field, both species are in the Paschen-Back regime, where the electronic and nuclear spin degrees of freedom are decoupled. In this regime, the magnetic confinement mostly results from the electronic spin and is therefore almost identical for the two isotopes. The ratio ω_f/ω_b is then very close to the expected value $\sqrt{7/6} \simeq 1.08$ based on the ratio of the atomic masses (*20*).

Contrary to the large damping observed in the Bose-Bose mixtures (*15*), we observe long-lived oscillations of the Bose-Fermi superfluid mixture at frequencies ($\tilde{\omega}_b$, $\tilde{\omega}_f$). These oscillations extend over more than 4 s with undetectable damping (Fig. 2 and fig. S2). This very weak dissipation is only observed when the initial displacement d is below 100 μm, corresponding to a maximum relative velocity $v_{max} = (\tilde{\omega}_b + \tilde{\omega}_f)d$ below 18 mm/s ≃ 0.4 v_F, where $v_F = \sqrt{2k_B T_F/m_f}$. In this situation, the BEC explores only the central part of the much broader Fermi cloud. When $v_{max} > v_c = 0.42^{+0.05}_{-0.11} v_F = 20^{+2}_{-5}$ mm/s, we observe a sharp onset of damping and heating of the BEC compatible with the Landau criterion for breakdown of superfluidity (Fig. 2C) (*10*). For comparison, the sound velocity of an elongated Fermi gas at its center is $v_s' = \xi^{1/4} v_F/\sqrt{5} = 17$ mm/s (*21*), where $\xi = 0.38$ is the Bertsch parameter (*5*, *13*). The measured critical velocity v_c is very close to v_s' and is clearly above the BEC sound velocity of ≃5 mm/s at its center.

Two striking phenomena are furthermore observed. First, whereas the frequency $\tilde{\omega}_f$ of ^{6}Li oscillations is almost unchanged from the value in the absence of ^{7}Li, that of ^{7}Li is downshifted

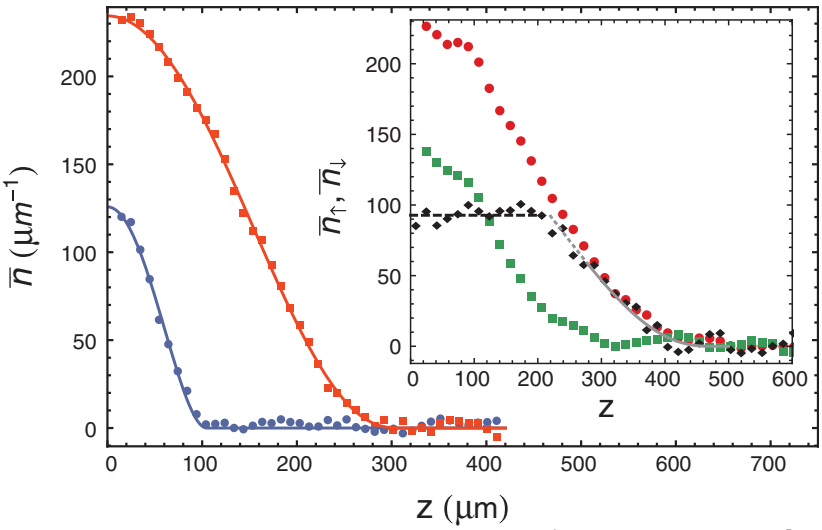

Fig. 1. Density profiles in the double superfluid regime. $N_b = 4 \times 10^4$ ^{7}Li atoms and $N_f = 3.5 \times 10^5$ ^{6}Li atoms are confined in a trap at a temperature below 130 nK. The density profiles $\overline{n}_b$ (blue circles) and $\overline{n}_{f,\uparrow}$ (red squares) are doubly integrated over the two transverse directions. The blue (red) solid line is a fit to the ^{7}Li (^{6}Li) distribution by a mean-field (unitary Fermi gas) EoS in the Thomas-Fermi approximation. Inset: Spin-imbalanced Fermi gas ($N_{f,\uparrow} = 2 \times 10^5$, $N_{f,\downarrow} = 8 \times 10^4$) in thermal equilibrium with a BEC. Red circles: $\overline{n}_{f,\uparrow}$; green squares: $\overline{n}_{f,\downarrow}$; black diamonds: difference $\overline{n}_{f,\uparrow} - \overline{n}_{f,\downarrow}$. The plateau (black dashed line) indicates superfluid pairing (*12*). Gray solid line: Thomas-Fermi profile of a noninteracting Fermi gas for the fully spin-polarized outer shell prolonged by the partially polarized normal phase (gray dashed line).

Laboratoire Kastler-Brossel, École Normale Supérieure, Collège de France, CNRS and UPMC, 24 rue Lhomond, 75005 Paris, France.
*Corresponding author. E-mail: iferrier@lkb.ens.fr †Present address: Van Swinderen Institute, University of Groningen, Faculty of Mathematics and Natural Sciences, Zernikelaan 25, 9747 AA Groningen, Netherlands. ‡Present address: Institut für Laserphysik, Universität Hamburg, Luruper Chaussee 149, Building 69, D-22761 Hamburg, Germany.

to $\tilde{\omega}_b = 2\pi \times 15.00(2)$ Hz. Second, the amplitude of oscillations of the bosonic species displays a beat at a frequency $\simeq(\tilde{\omega}_f - \tilde{\omega}_b)/(2\pi)$, revealing coherent energy transfer between the two clouds (Fig. 2B). To interpret the frequency shift of the ^{7}Li atoms, we note that $N_b \ll N_f$, which allows us to treat the BEC as a mesoscopic impurity immersed in a Fermi superfluid. Similarly to the Fermi polaron case (*22*), the effective potential seen by the bosons is the sum of the trapping potential $V(r)$ and the mean-field interaction $g_{bf}n_f(r)$, where n_f is the total fermion density, $g_{bf} = 2\pi\hbar^2 a_{bf}/m_{bf}$, and $m_{bf} = \frac{m_b m_f}{m_b+m_f}$ is the ^{6}Li/^{7}Li reduced mass. Neglecting at first the back-action of the bosons on the fermions, we can assume that n_f is given by the local-density-approximation result $n_f(r) = n_f^{(0)}(\mu_f^0 - V(r))$, where $n_f^{(0)}(\mu)$ is the stationary equation of state (EoS) of the Fermi gas. Because the Bose-Einstein condensate is much smaller than the Fermi cloud (Fig. 2A), $V(r)$ is smaller than μ_f^0 over the BEC volume. We can thus expand $n_f^{(0)}$, and we get

$$V_{\text{eff}}(r) = g_{bf}n_f(0) + V(r)\left[1 - g_{bf}\left(\frac{dn_f^{(0)}}{d\mu_f}\right)_{r=0}\right] \quad (1)$$

We observe that the effective potential is still harmonic and the rescaled frequency is given by

$$\tilde{\omega}_b \simeq \omega_b\left(1 - \frac{1}{2}g_{bf}\left(\frac{dn_f^{(0)}}{d\mu_f}\right)_{r=0}\right) \quad (2)$$

For a unitary Fermi gas, the chemical potential is related to the density by $\mu_f = \xi\hbar^2(3\pi^2 n_f)^{2/3}/2m_f$. In the weakly coupled limit, we get $\frac{\delta\omega_b}{\omega_b} = \frac{\omega_b - \tilde{\omega}_b}{\omega_b} = \frac{13k_F a_{bf}}{7\pi\xi^{5/4}}$, where $\hbar k_F = \sqrt{2\hbar m_f \bar{\omega}_f (3N_f)^{1/3}}$ is the Fermi momentum of a noninteracting harmonically trapped Fermi gas. Using our experimental parameters $k_F = 4.6 \times 10^6$ m^{-1}, we predict a value $\tilde{\omega}_b \simeq 2\pi \times 14.97$ Hz, in very good agreement with the observed value 15.00(2)Hz.

To understand the amplitude modulation, we now take into account the back-action on the fermions. A fully quantum formalism using a sum-rule approach (*23*–*25*) leads to a coupled oscillator model in which the positions of the two clouds obey the following equations (*10*)

$$M_f\ddot{z}_f = -K_f z_f - K_{bf}(z_f - z_b) \quad (3)$$

$$M_b\ddot{z}_b = -K_b z_b - K_{bf}(z_b - z_f) \quad (4)$$

where $M_b = N_b m_b$ ($M_f = N_f m_f$) is the total mass of the ^{7}Li (^{6}Li) cloud, $K_b = M_b\omega_b^2$ ($K_f = M_f\omega_f^2$) is the spring constant of the axial magnetic confinement, and K_{bf} is a phenomenological (weak) coupling constant describing the mean-field interaction between the two isotopes. To recover the correct frequency shift (Eq. 2), we take $K_{bf} = 2K_b\frac{\delta\omega_b}{\omega_b}$. Solving these equations with the initial condition $z_f(0) = z_b(0) = d$, and defining $\rho = N_b/N_f$ and $\varepsilon = \frac{2m_b}{m_b - m_f}\left(\frac{\tilde{\omega}_b - \omega_b}{\omega_b}\right)$, in the limit $\rho, \varepsilon \ll 1$ we get

$$z_f = d[(1 - \varepsilon\rho)\cos(\tilde{\omega}_f t) + \varepsilon\rho\cos(\tilde{\omega}_b t)] \quad (5)$$

$$z_b = d[-\varepsilon\cos(\tilde{\omega}_f t) + (1 + \varepsilon)\cos(\tilde{\omega}_b t)] \quad (6)$$

The predictions of Eqs. 5 and 6 agree well with experiment (Fig. 2B). Interestingly, the peak-to-peak modulation of the amplitude of ^{7}Li is much larger than the relative frequency shift, a consequence of the almost exact tuning of the two oscillators (up to a factor $\sqrt{6/7}$). Thus, the mass prefactor in the expression for ε is large (=14) and leads to $\varepsilon \simeq 0.25$ at unitarity. This results in efficient energy transfer between the two modes despite their weak coupling, as observed.

We now extend our study of the Bose-Fermi superfluid mixture to the BEC-BCS crossover by tuning the magnetic field away from the resonance value $B_f = 832$ G. We explore a region from 860 G down to 780 G where $1/k_F a_f$ spans the interval $[-0.4, +0.8]$. In this whole domain, except in a narrow region between 845 and 850 G where the boson-boson scattering length

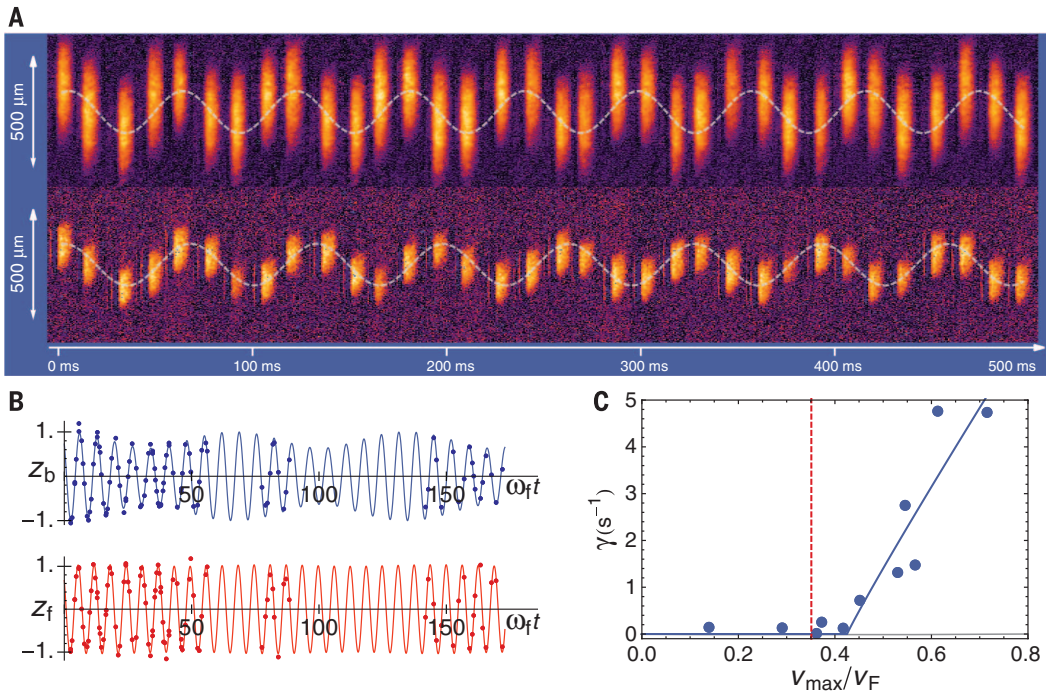

Fig. 2. Coupled oscillations of the superfluid mixture. (**A**) Center-of-mass oscillations. The oscillations are shown over the first 500 ms at a magnetic field of 835 G for a Fermi superfluid (top) and a Bose superfluid (bottom).The oscillation period of ^{6}Li (^{7}Li) is 59.7(1) ms [66.6(1) ms], leading to a dephasing of π near 300 ms. These oscillations persist for more than 4 s with no visible damping. The maximum relative velocity between the two clouds is 1.8 cm/s. (**B**) Coupled oscillations. Symbols: Center-of-mass oscillation of ^{7}Li (top) and ^{6}Li (bottom) displaying coherent energy exchange between both superfluids. Solid lines: Theory for an initial displacement d of 100 μm at a magnetic field of 835 G; see text. (**C**) Critical damping. Symbols: Damping rate (blue circles) of the amplitude of the center-of-mass oscillations of the ^{7}Li BEC as a function of the maximal relative velocity between the two superfluids normalized to the Fermi velocity of the ^{6}Li gas. Data taken at 832 G. From these data and using a fit function given in (*10*) (solid line), we extract $v_c = 0.42^{+0.05}_{-0.11}v_F$. The red dashed line shows the speed of sound of an elongated unitary Fermi superfluid $v_s' = \xi^{1/4}v_F/\sqrt{5} = 0.35v_F$ (*20*).

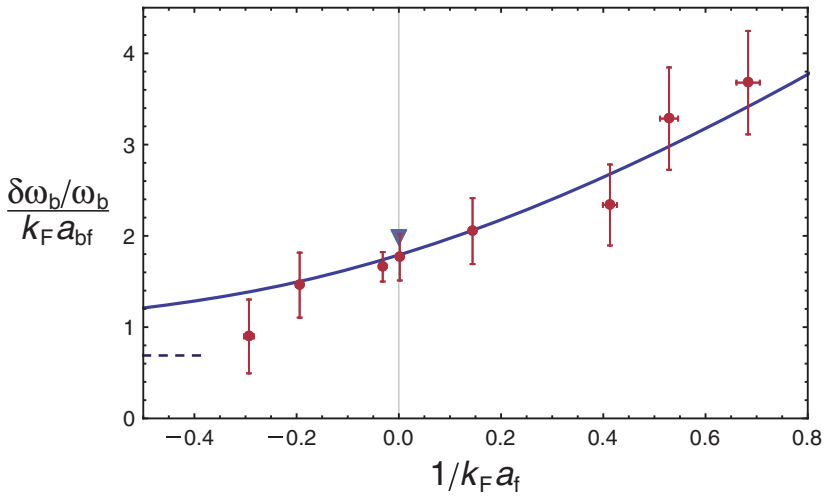

Fig. 3. Dipole mode frequency shift in the BEC-BCS crossover. Red circles: Experiment. Blue line: zero-temperature prediction from the equation of state of (*26*); dashed line: ideal Fermi gas. Blue triangle: prediction from (*13*). Error bars include systematic and statistical errors at 1 SD.

is negative, the mixture is stable and the damping extremely small.

The frequency shift of the BEC (Eq. 2) now probes the derivative of the EoS $n_f(\mu_f)$ in the BEC-BCS crossover. In the zero-temperature limit and under the local density approximation, Eq. 2 obeys the universal scaling $\frac{\delta\omega_b}{\omega_b} = k_F a_{bf} f\left(\frac{1}{k_F a_f}\right)$

In Fig. 3, we compare our measurements to the prediction for the function f obtained from the zero-temperature EoS measured in (*26*). On the BCS side, $(1/k_F a_f < 0)$, the frequency shift is reduced and tends to that of a noninteracting Fermi gas. Far on the BEC side $(1/k_F a_f \gg 1)$, we can compute the frequency shift using the EoS of a weakly interacting gas of dimers. Within the mean-field approximation, we have $\frac{dn_f}{d\mu_f} = \frac{2m_f}{\pi\hbar^2 a_{dd}}$, where $a_{dd} = 0.6a_f$ is the dimer-dimer scattering length. This expression explains the increase in the frequency shift when a_f is reduced, i.e., moving toward the BEC side [see (*10*) for the effect of Lee-Huang-Yang quantum correction].

The excellent agreement between experiment and our model confirms that precision measurements of collective modes are a sensitive dynamical probe of equilibrium properties of many-body quantum systems (*27*). Our approach can be extended to the study of higher-order excitations. In particular, although there are two first sound modes, one for each atomic species, we expect only one second sound for the superfluid mixture (*28*) if cross-thermalization is fast enough. In addition, the origin of the critical velocity for the relative motion of Bose and Fermi superfluids is an intriguing question that can be further explored in our system. Finally, a richer phase diagram may be revealed when N_b/N_f is increased (*29*) or when the superfluid mixture is loaded in an optical lattice (*30*).

REFERENCES AND NOTES

1. W. Ketterle, *Rev. Mod. Phys.* **74**, 1131–1151 (2002).
2. E. A. Cornell, C. E. Wieman, *Rev. Mod. Phys.* **74**, 875–893 (2002).
3. Z. Hadzibabic, P. Krüger, M. Cheneau, B. Battelier, J. Dalibard, *Nature* **441**, 1118–1121 (2006).
4. M. Greiner, O. Mandel, T. Esslinger, T. W. Hänsch, I. Bloch, *Nature* **415**, 39–44 (2002).
5. W. Zwerger, Ed., *The BCS-BEC Crossover and the Unitary Fermi Gas*, vol. 836 of *Lecture Notes in Physics* (Springer, Berlin, 2012).
6. F. Schreck *et al.*, *Phys. Rev. Lett.* **87**, 080403 (2001).
7. A. G. Truscott, K. E. Strecker, W. I. McAlexander, G. B. Partridge, R. G. Hulet, *Science* **291**, 2570–2572 (2001).
8. J. Rysti, J. Tuoriniemi, A. Salmela, *Phys. Rev. B* **85**, 134529 (2012).
9. J. Tuoriniemi *et al.*, *J. Low Temp. Phys.* **129**, 531–545 (2002).
10. See supplementary materials on *Science* Online.
11. G. Zürn *et al.*, *Phys. Rev. Lett.* **110**, 135301 (2013).
12. T. De Silva, E. Mueller, *Phys. Rev. A* **73**, 051602 (2006).
13. M. J. H. Ku, A. T. Sommer, L. W. Cheuk, M. W. Zwierlein, *Science* **335**, 563–567 (2012).
14. K. Mølmer, *Phys. Rev. Lett.* **80**, 1804–1807 (1998).
15. D. S. Hall, M. R. Matthews, J. R. Ensher, C. E. Wieman, E. A. Cornell, *Phys. Rev. Lett.* **81**, 1539–1542 (1998).
16. P. Maddaloni, M. Modugno, C. Fort, F. Minardi, M. Inguscio, *Phys. Rev. Lett.* **85**, 2413–2417 (2000).
17. F. Ferlaino *et al.*, *J. Opt. B Quantum Semiclassical Opt.* **5**, S3–S8 (2003).
18. A. Sommer, M. Ku, G. Roati, M. W. Zwierlein, *Nature* **472**, 201–204 (2011).
19. T. Kinoshita, T. Wenger, D. S. Weiss, *Nature* **440**, 900–903 (2006).
20. Because of a slight deviation from the Paschen-Back regime for ^{7}Li, this ratio is 1.1 instead of 1.08.
21. Y. Hou, L. Pitaevskii, S. Stringari, *Phys. Rev. A* **88**, 043630 (2013).
22. C. Lobo, A. Recati, S. Giorgini, S. Stringari, *Phys. Rev. Lett.* **97**, 200403 (2006).
23. S. Stringari, *J. Phys. IV France* **116**, 47–66 (2004).
24. T. Miyakawa, T. Suzuki, H. Yabu, *Phys. Rev. A* **62**, 063613 (2000).
25. A. Banerjee, *Phys. Rev. A* **76**, 023611 (2007).
26. N. Navon, S. Nascimbène, F. Chevy, C. Salomon, *Science* **328**, 729–732 (2010).
27. M. K. Tey *et al.*, *Phys. Rev. Lett.* **110**, 055303 (2013).
28. G. Volovik, V. Mineev, I. Khalatnikov, *Sov. Phys. JETP* **69**, 675 (1975).
29. T. Ozawa, A. Recati, S. Stringari, http://arxiv.org/abs/1405.7187 (2014).
30. A. B. Kuklov, B. V. Svistunov, *Phys. Rev. Lett.* **90**, 100401 (2003).

ACKNOWLEDGMENTS

We thank S. Stringari and Y. Castin for fruitful discussions and S. Balibar, J. Dalibard, F. Gerbier, S. Nascimbène, C. Cohen-Tannoudji, and M. Schleier-Smith for critical reading of the manuscript. We acknowledge support from the European Research Council Ferlodim and Thermodynamix, the Ile de France Nano-K (contract Atomix), and Institut de France Louis D. Prize.

SUPPLEMENTARY MATERIALS

www.sciencemag.org/content/345/6200/1035/suppl/DC1
Materials and Methods
Figs. S1 to S4
References (*31–34*)

29 April 2014; accepted 30 June 2014
Published online 17 July 2014;
10.1126/science.1255380

EARTHQUAKE DYNAMICS

Strength of stick-slip and creeping subduction megathrusts from heat flow observations

Xiang Gao[1] and Kelin Wang[2,3]*

Subduction faults, called megathrusts, can generate large and hazardous earthquakes. The mode of slip and seismicity of a megathrust is controlled by the structural complexity of the fault zone. However, the relative strength of a megathrust based on the mode of slip is far from clear. The fault strength affects surface heat flow by frictional heating during slip. We model heat-flow data for a number of subduction zones to determine the fault strength. We find that smooth megathrusts that produce great earthquakes tend to be weaker and therefore dissipate less heat than geometrically rough megathrusts that slip mainly by creeping.

Subduction megathrusts that primarily exhibit stick-slip behavior can produce great earthquakes, but some megathrusts are observed to creep while producing small and moderate-size earthquakes. The relationship between seismogenesis and strength of subduction megathrust is far from clear. Faults that produce great earthquakes are commonly thought of as being stronger than those that creep (*1*). Megathrusts that are presently locked to build up stress for future great earthquakes are thus described as being "strongly coupled." However, some studies have proposed strong creeping megathrusts because of the geometric irregularities of very rugged subducted sea floor (*2*, *3*).

Contrary to a widely held belief, geodetic and seismic evidence shows that very rough subducting sea floor promotes megathrust creep (*2*). All

Supplementary material to A Mixture of Bose and Fermi Superfluids

I. Ferrier-Barbut, M. Delehaye, S. Laurent, A. T. Grier, M. Pierce, B. S. Rem, F. Chevy, and C. Salomon
Laboratoire Kastler-Brossel, École Normale Supérieure,
Collège de France, CNRS and UPMC, 24 rue Lhomond, 75005 Paris, France

Feshbach Resonances

The Bose-Fermi mixture is composed of a ^{7}Li cloud prepared in the $|2_\mathrm{b}\rangle$ state, which connects to the $|F=1, m_\mathrm{f}=0\rangle$ state at low field, together with a ^{6}Li gas in the two lowest energy states $|1_\mathrm{f}\rangle$ and $|2_\mathrm{f}\rangle$ connecting to $|F=1/2, m_\mathrm{f}=1/2\rangle$ and $|F=1/2, m_\mathrm{f}=-1/2\rangle$ respectively.
In Fig. S1 we present the relevant s-wave scattering lengths characterizing the ^{7}Li-^{7}Li, ^{6}Li-^{6}Li and ^{6}Li-^{7}Li interactions in the 700 G-1000 G magnetic field region of interest. ^{7}Li, $|2_\mathrm{b}\rangle$ exhibits two Feshbach resonances located at 845.5 G and 894 G. For fermionic ^{6}Li, the two spin-states $|1_\mathrm{f}\rangle$, $|2_\mathrm{f}\rangle$ exhibit one very broad s-wave resonance at 832.18 G. Note the 1/100 vertical scale for ^{6}Li in Fig. S1. The scattering lengths are taken from (*11,31*) in units of Bohr radius a_0 as a function of magnetic field B in gauss:

$$a_\mathrm{f}(B) = -1582\left(1-\frac{-262.3}{B-832.18}\right) \tag{S1}$$

$$a_\mathrm{b}(B) = -18.24\left(1-\frac{-237.8}{B-893.95}\right)\left(1-\frac{4.518}{B-845.54}\right) \tag{S2}$$

For the inter-isotope interaction, coupled-channel calculations by S. Kokkelmans provide a scattering length $a_\mathrm{bf} = 40.8\,a_0$ independent of the magnetic field in this region.

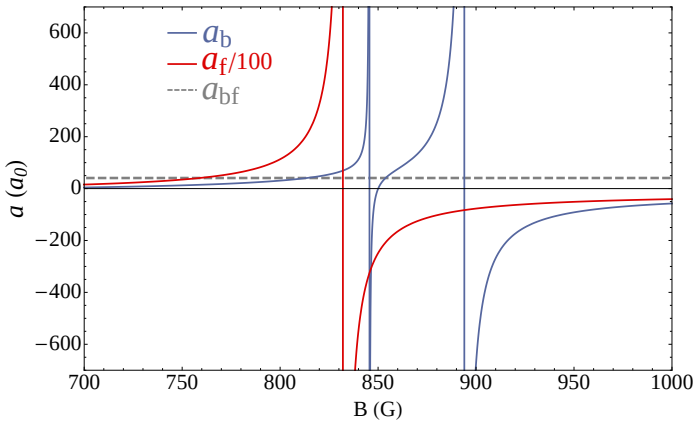

Figure S1: Magnetic field dependence of the different scattering lengths a_b (blue), a_f (red), and a_bf (dashed gray). $a_\mathrm{bf} = 40.8\,a_0$ is independent of B. Note the 1/100 vertical scale for ^{6}Li.

Experimental set-up, mixture preparation

The apparatus and early stages of our experiment have been described in (*32*). Initially ^{7}Li (resp. ^{6}Li) atoms are cooled to $40\,\mu$K in a Ioffe-Pritchard trap in the $|F=2, m_\mathrm{f}=2\rangle$ (resp. $|F=3/2, m_\mathrm{f}=3/2\rangle$) states at a bias field of 12.9 G. The trapping potential for the mixture is a hybrid trap composed of an optical dipole trap (wavelength $1.07\,\mu m$) with waist 27μm superimposed with a magnetic curvature in which the bias magnetic field remains freely adjustable. About 3×10^5 ^{7}Li and 2×10^6 ^{6}Li atoms are transferred in a $300\,\mu$K deep optical dipole trap. They are then transferred to their absolute ground state $|F=1, m_\mathrm{f}=1\rangle$ and $|F=1/2, m_\mathrm{f}=1/2\rangle$ by a rapid adiabatic passage (RAP) using two 50 ms radio-frequency (RF) pulses and a sweep of the magnetic bias down to 4.3 G. These states connect at high magnetic field respectively to $|1_\mathrm{b}\rangle$ and $|1_\mathrm{f}\rangle$. We revert the magnetic curvature in order to provide an axial confining potential, the ground states being high-field-seeking states. The bias field is ramped in 100 ms to 656 G where we transfer ^{7}Li to the state $|2_\mathrm{b}\rangle$ by a RAP done by an RF pulse with a frequency sweep from 170.9 MHz to 170.7 MHz in 5 ms. The field is ramped in 100 ms to 835 G where a mixture of ^{6}Li in its two lowest energy states $|1_\mathrm{f}\rangle$ and $|2_\mathrm{f}\rangle$ is prepared with an RF sweep between 76.35 MHz and 76.25 MHz. The duration of this sweep varies the Landau-Zener efficiency of the transfer offering control of the spin polarization of the ^{6}Li mixture. Initial conditions for evaporation at this field are 1.5×10^5 ^{7}Li and 1.5×10^6 ^{6}Li at $30\,\mu$K in a $300\,\mu$K deep trap. The evaporation of the mixture is done near unitarity for the fermions providing high collision rate. In 3 s the laser power is reduced by a factor 100 and ^{7}Li is sympathetically cooled by ^{6}Li with high efficiency; the phase-space density increases to BEC by a factor $\sim 2\times10^4$ for a factor of ten loss in ^{7}Li atoms. To confirm this sympathetic cooling scheme we have also performed the evaporation at 850 G where the ^{7}Li scattering length vanishes, demonstrating that ^{7}Li can be cooled down solely by thermalisation with ^{6}Li. At the end of evaporation, we typically wait 700 ms at constant dipole trap power to ensure thermal equilibrium between both species.

The trapping potential is cylindrically symmetric, with axial (transverse) frequency ω_z (ω_ρ). The BEC phase transition is observed at a temperature of 700 nK. Our studies are performed in a shallow trap with frequencies:

- $\omega_{\rho,\mathrm{b}} = 2\pi\times550(20)$ Hz, $\omega_{\rho,\mathrm{f}} = 2\pi\times595(20)$ Hz
- $\omega_{z,\mathrm{b}} = 2\pi\times15.27$ Hz, $\omega_{z,\mathrm{f}} = 2\pi\times16.8$ Hz.

These frequencies are measured by single species center-of-mass oscillations at a field of 832G.

Typical atoms numbers are $N_\mathrm{b} = 4\times10^4$ ^{7}Li atoms and $N_\mathrm{f} = 3.5\times10^5$ ^{6}Li in a spin-balanced mixture. The critical temperature for ^{7}Li Bose-Einstein condensation is $T_{\mathrm{c,b}} = \frac{\hbar\bar{\omega}_\mathrm{b}}{k_\mathrm{B}}\left(N_\mathrm{b}/\zeta(3)\right)^{1/3} = 260$ nK and the Fermi temperature for ^{6}Li $T_\mathrm{F} = \frac{\hbar\bar{\omega}_\mathrm{f}}{k_\mathrm{B}}\left(3N_\mathrm{f}\right)^{1/3} = 880$ nK. To our experimental precision, the condensed fraction $\frac{N_0}{N}$ is higher than 0.8, implying $\frac{T_\mathrm{b}}{T_{\mathrm{c,b}}} \lesssim 0.5$. With $T_\mathrm{f} \lesssim T_\mathrm{b}$, we have $\frac{T_\mathrm{f}}{T_\mathrm{F}} \lesssim 0.15 = 0.8\,T_{\mathrm{c,f}}$. This temperature upper bound indicates fermionic superfluidity, in agreement with the direct observation of the superfluid core in the spin-imbalanced gas shown in Fig. 1 in the main text and the extremely low damping observed for small relative oscillations between both isotopes.

The large imbalance in isotope population $N_\mathrm{f}/N_\mathrm{b} \simeq 10$ results from our cooling strategy. At the cost of a small loss in ^{6}Li numbers, we can also get samples containing $N_\mathrm{b} \simeq N_{\mathrm{f},\uparrow} \simeq N_{\mathrm{f},\downarrow} \simeq 10^5$.

To excite the dipole mode of the two superfluids, we take advantage of the fact that the axial position of the waist of the dipole trap laser beam is slightly off-centered with respect to the minimum of the axial magnetic confinement. In order to displace the center of the atomic clouds, we slowly increase the laser power of the dipole trap by a variable factor (between 1.1 and 2). This results in axial displacement and radial compression of both clouds. The intensity ramp is done in $t_\mathrm{up} = 150$ ms, i.e slow compared to the

trap periods. We then return the laser power to its initial value in $t_{\rm down} = 20$ ms, fast compared to the axial trap period but slow compared to the radial period, avoiding excitation of radial collective modes. The center of mass positions of both clouds are measured by recording in situ images at variable delays after the axial excitation, up to 4 seconds. Examples of center-of-mass oscillations over a time span of more than 3.5 s are shown in Fig S2.

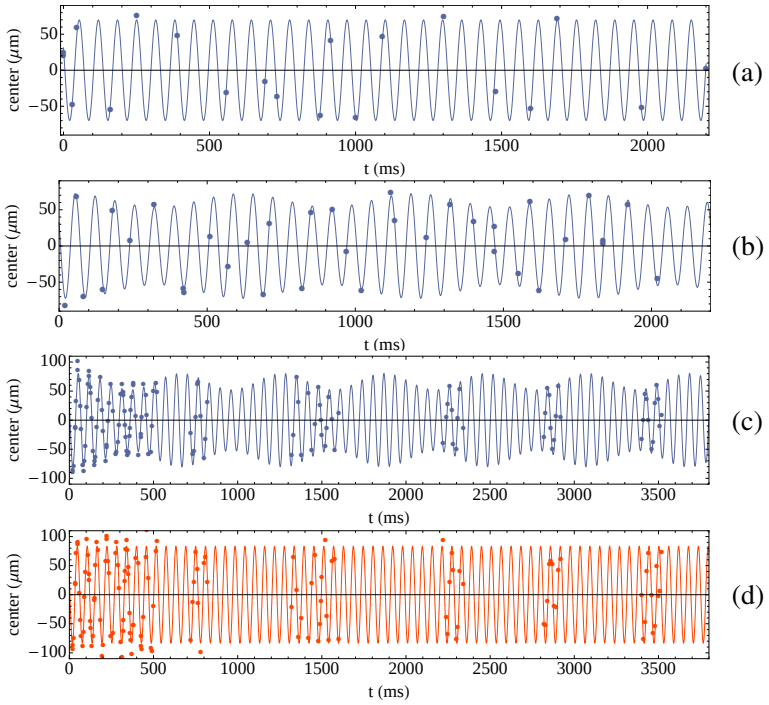

Figure S2: Examples of center-of-mass oscillations. ^{7}Li bosons alone at 832 G (a), ^{7}Li bosons in the presence of ^{6}Li fermions at 832G (b). 4 second time span for the evolution of ^{7}Li bosons (c) mixed with ^{6}Li fermions (d) at 835 G. The coherent energy exchange between ^{7}Li and ^{6}Li superfluids with no detectable damping is clearly visible.

Critical velocity measurement

When we increase the initial amplitude d_0 of the oscillations above $\simeq 100\,\mu$m, we observe first strong damping of the ^{7}Li BEC oscillations inside the Fermi cloud followed by long-lived oscillations at a lower amplitude, as shown in Fig. S3. To verify that this damping is not due to trap anharmonicity for large displacements, we measured oscillations of the BEC in the absence of fermions. For a displacement of $d = 120\,\mu$m, which corresponds to a velocity of $v \simeq 0.45 v_{\rm F}$ in the presence of the Fermi cloud, we found a characteristic damping rate of $\gamma = 0.05\,{\rm s}^{-1}$. For a much larger initial displacement $d = 275\,\mu$m ($v \simeq v_{\rm F}$) we observe an influence of trap anharmonicity with an effective damping rate $\gamma = 0.26\,{\rm s}^{-1}$. Both of these rates are much smaller than the measured rates in presence of the Fermi cloud for velocities above $0.4\,v_{\rm F}$ as shown in Fig. 2(c) in main text.

The observed behavior is compatible with a critical velocity $v_{\rm c}$ for relative motion, resulting in damping for velocities above $v_{\rm c}$ at early times and then undamped oscillations when the velocity is smaller than

v_c. We fit our data with Eq. (7) from main text and an amplitude $d = d_0 \exp(-\gamma t) + d'$ where d' is the amplitude for the long-lived final oscillations. γ is then a damping rate extracted from each data set. Its variation against maximal relative velocity between the two clouds is shown in Fig. 2(c) of main text. To extract a critical velocity we use a simple model:

$$\gamma(v) = \Theta(v - v_c)\, A\, ((v - v_c)/v_F)^\alpha \tag{S3}$$

where $\Theta(x)$ is the Heaviside function, A and α are free parameters. By fitting Eq. (S3), we obtain a critical velocity $v_c = 0.42^{+0.05}_{-0.11}\, v_F$, an exponent $\alpha = 0.95^{+0.8}_{-0.3}$, close to 1, and $A = 17(9)\,\mathrm{s}^{-1}$. This function is plotted in solid blue curve in Fig. 2(c) of main text. v_c is very close to the sound velocity of an elongated Fermi gas $v_s' = \frac{\xi^{1/4}}{\sqrt{5}} v_F = 0.35\, v_F$ (*21*). For comparison, in a nearly isotropic trap and a moving 1D lattice, the MIT group found a critical velocity $v_c = 0.32\, v_F$ (*33*).

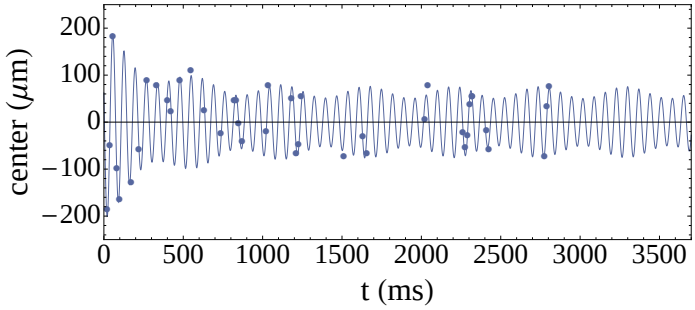

Figure S3: Example of dipole oscillations of the ^{7}Li BEC for a large initial amplitude (blue circles). The blue solid line is a fit to equation (7) from main text with a phenomenological damping rate $\gamma = 3.1\mathrm{s}^{-1}$.

BEC mean-field and Lee-Huang-Yang limit

Here we evaluate the frequency shift $\delta\omega_b/\omega_b$ given by

$$\frac{\delta\omega_b}{\omega_b} \simeq \frac{1}{2} g_{bf} \left(\frac{dn_f^{(0)}}{d\mu_f}\right)_{r=0}, \tag{S4}$$

in the limit where the Fermi superfluid is a molecular BEC of composite Fermi-Fermi dimers. The dimers have a mass $m_d = 2m_f$ and a binding energy $E_d = \hbar^2/m_d a_d^2$, where $a_d = 0.6\, a_f$ is the dimer-dimer scattering length (*34*). The Lee-Huang-Yang EoS for the molecular BEC reads

$$n_d = \frac{\mu_d}{g_d}\left(1 - \frac{32}{3\sqrt{\pi}}\sqrt{\frac{\mu_d a_d^3}{g_{dd}}}\right) \tag{S5}$$

where $n_d = n_f/2$ is the density of dimers, $\mu_d = 2\mu_f + E_d$ their chemical potential, and $g_{dd} = 4\pi\hbar^2 a_d/m_d$ the coupling constant for the dimer-dimer interaction. Then we have $\frac{d}{d\mu_f} = 2\frac{d}{d\mu_d}$ and thus

$$\frac{dn_f^{(0)}}{d\mu_f} = \frac{4}{g_d}\left(1 - \frac{16}{\sqrt{\pi}}\sqrt{\frac{\mu_d a_d^3}{g_{dd}}}\right). \tag{S6}$$

This quantity must be evaluated in the center of the trap ($r = 0$) to infer the frequency shift (S4). The second term in (S6) is of first order in $\sqrt{n_{\rm d} a_{\rm d}}$. We then evaluate its argument in the mean-field approximation which gives the usual expression for the chemical potential of a BEC in a harmonic trap:

$$(\mu_{\rm d})_{r=0} = \frac{\hbar\bar{\omega}_{\rm f}}{2}\left(15 N_{\rm d} a_{\rm d}\sqrt{\frac{m_{\rm d}\bar{\omega}_{\rm f}}{\hbar}}\right)^{2/5}. \tag{S7}$$

Using (S7) and the expression of the Fermi wave-vector:

$$k_{\rm F} = \sqrt{\frac{m_{\rm d}\bar{\omega}_{\rm f}}{\hbar}}(6N_{\rm d})^{1/6}, \tag{S8}$$

with $N_{\rm f} = 2N_{\rm d}$, we can recast our expression for the frequency shift (S6) in the universal units used in the main text (Eq. (10)):

$$\left(\frac{\mu_{\rm d} a_{\rm d}^3}{g_{\rm d}}\right)_{r=0} = \frac{1}{8\pi}\left(\frac{5}{2}\right)^{2/5}(a_{\rm d} k_{\rm F})^{12/5} \tag{S9}$$

$$\left(\frac{dn_{\rm f}^{(0)}}{d\mu_{\rm f}}\right)_{r=0} \simeq \frac{2m_{\rm f}}{0.6\pi\hbar^2 a_{\rm f}}\left(1 - 1.172\,(k_{\rm F} a_{\rm f})^{6/5}\right) \tag{S10}$$

$$\frac{\delta\omega_{\rm b}}{\omega_{\rm b}}\frac{1}{k_{\rm F} a_{\rm bf}} \simeq 6.190\frac{1}{k_{\rm F} a_{\rm f}}\left(1 - 1.172\,(k_{\rm F} a_{\rm f})^{6/5}\right) \tag{S11}$$

This limit is shown in green in Fig. S4. The mean-field approximation (red curve in Fig. S4) corresponds to the first term in Eq. (S11).

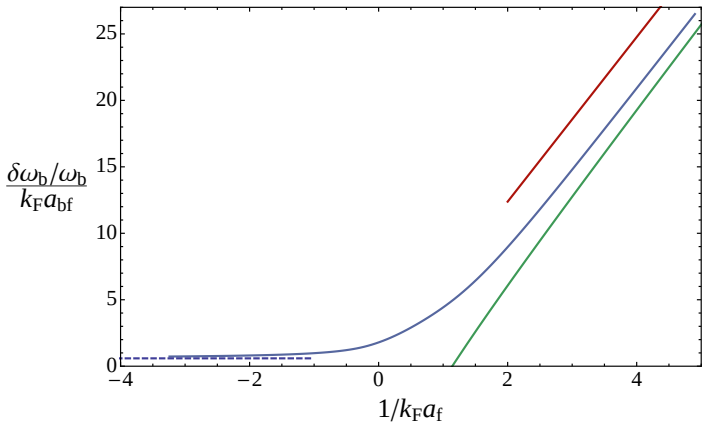

Figure S4: Predicted frequency shift (blue line) over a broad range of $1/k_{\rm F} a_{\rm f}$. The dashed blue line shows the ideal Fermi gas limit. On the BEC side the green line shows the Lee-Huang-Yang prediction (S11) and the red line the mean-field prediction.

Derivation of the coupled oscillator model using the sum-rule approach

We describe the dynamics of the system by a Hamiltonian

$$\widehat{H} = \sum_{i,\alpha} \left[\frac{\widehat{p}_{\alpha,i}^2}{2m_\alpha} \right] + U(\boldsymbol{r}_{\alpha,i}), \tag{S12}$$

where $\alpha = \mathrm{b}, \mathrm{f}$ labels the isotopes, and U describes the total (trap+interaction) potential energy of the cloud.

Consider the operators $\widehat{F}_\alpha = \sum_{i=1}^{N_\alpha} \widehat{z}_{\alpha,i}$, where $z_{\alpha,i}$ is the position along z of the i-th atom of species $\alpha = \mathrm{b}, \mathrm{f}$ and take $\widehat{F}(a_\mathrm{f}, a_\mathrm{b}) = \sum_\alpha a_\alpha \widehat{F}_\alpha$ an excitation operator depending on two mixing coefficients (a_α). We introduce the moments S_p defined by

$$S_p = \sum_n (E_n - E_0)^p \left| \langle n|\widehat{F}|0\rangle \right|^2,$$

where $|n\rangle$ and E_n are the eigenvectors and the eigenvalues of the Hamiltonian $\widehat{H}$ (by definition $|0\rangle$ is the ground state and E_0 is its energy). Using the Closure Relation and first order perturbation theory, S_1 and S_{-1} can be calculated exactly and we have

$$S_1 = -\sum_\alpha \frac{\hbar^2}{m_\alpha} N_\alpha a_\alpha^2 \tag{S13}$$

$$S_{-1} = -\frac{1}{k} \sum_{\alpha,\beta} a_\alpha a_\beta N_\alpha \frac{\partial \langle z_\alpha \rangle}{\partial b_\beta} \tag{S14}$$

where k is the restoring force of the axial magnetic trap and $\langle z_\alpha \rangle$ is the center of mass position of atoms α in the presence of a perturbing potential $-k \sum_\beta b_\beta \widehat{F}_\alpha$ corresponding to a shift of the trapping potential of species β by a distance b_β. $\langle z_\alpha \rangle$ satisfies two useful conditions. First, using Hellmann-Feynman's theorem, the matrix $N_\alpha \partial_{b_\beta} \langle z_\alpha \rangle = \partial^2_{b_\alpha b_\beta} \widehat{H}$ is symmetric. Secondly, if we shift the two traps by the same quantify $b_\beta = b$, the center of mass of the two clouds move by $\langle z_\alpha \rangle = b$. Differentiating this constraint with respect to b yields the condition $\sum_\beta \partial_{b_\beta} \langle z_\alpha \rangle = 1$.

Experimentally, we observe that only two modes are excited by the displacement of the trap center. We label $|n = 1\rangle$ and $|n = 2\rangle$ the corresponding modes and we take $\hbar\omega_n = E_n - E_0$, with, by convention, $\omega_1 \leq \omega_2$. We thus have for any set of mixing parameters $(a_\mathrm{f}, a_\mathrm{b})$,

$$\hbar^2 \omega_1^2 \leq \frac{S_1}{S_{-1}} \leq \hbar^2 \omega_2^2. \tag{S15}$$

To find the values of the two frequencies ω_1 and ω_2, one thus simply has to find the extrema of S_1/S_{-1} with respect to a_f and a_b. Using the sum rules (S13) and (S14), we see that

$$\frac{S_1}{S_{-1}} = \hbar^2 k \frac{\sum_\alpha N_\alpha / m_\alpha a_\alpha^2}{\sum_{\alpha,\beta} N_\alpha a_\alpha a_\beta \frac{\partial \langle z_\alpha \rangle}{\partial b_\beta}}. \tag{S16}$$

This expression can be formally simplified by taking $a'_\alpha = a_\alpha \sqrt{N_\alpha / m_\alpha}$ and $\psi = (a'_\mathrm{f}, a'_\mathrm{b})$. We then have

$$\frac{S_1}{S_{-1}} = \hbar^2 k \frac{\langle \psi | \psi \rangle}{\langle \psi | \mathcal{M} \psi \rangle}, \tag{S17}$$

where the scalar product is defined by $\langle\psi|\psi'\rangle = \sum_\alpha \psi_\alpha \psi'_\alpha$ and the effective-mass operator is given by

$$\mathcal{M}_{\alpha\beta} = \sqrt{m_\alpha m_\beta}\sqrt{\frac{N_\alpha}{N_\beta}}\frac{\partial\langle z_\alpha\rangle}{\partial b_\beta}. \tag{S18}$$

With these notations, the frequencies $\omega_{i=1,2}$ are given by $\omega_i = \sqrt{k/\tilde{m}_i}$, where $\tilde{m}_i$ is an eigenvalue of $\mathcal{M}$.

In the weak-coupling limit, the cross-terms $\partial_{b_\beta}\langle z_\alpha\rangle$ ($\alpha \neq \beta$) are small and using their symmetry properties, we can write $\mathcal{M}$ as $\mathcal{M}_0 + \mathcal{M}_1$ with

$$\mathcal{M}_0 = \begin{pmatrix} m_\mathrm{f} & 0 \\ 0 & m_\mathrm{b} \end{pmatrix} \tag{S19}$$

$$\mathcal{M}_1 = \begin{pmatrix} -m_\mathrm{f}\frac{\partial\langle z_\mathrm{f}\rangle}{\partial b_\mathrm{b}} & \sqrt{m_\mathrm{f} m_\mathrm{b}}\sqrt{\frac{N_\mathrm{b}}{N_\mathrm{f}}}\frac{\partial\langle z_\mathrm{b}\rangle}{\partial b_\mathrm{f}} \\ \sqrt{m_\mathrm{f} m_\mathrm{b}}\sqrt{\frac{N_\mathrm{b}}{N_\mathrm{f}}}\frac{\partial\langle z_\mathrm{b}\rangle}{\partial b_\mathrm{f}} & -m_\mathrm{b}\frac{\partial\langle z_\mathrm{b}\rangle}{\partial b_\mathrm{f}} \end{pmatrix} \tag{S20}$$

Since the matrix $\mathcal{M}$ is symmetric we can use the usual perturbation theory to calculate its eigenvalues and eigenvectors. We have to first order

$$\tilde{m}_1 = m_\mathrm{f}\left(1 - \frac{\partial\langle z_\mathrm{f}\rangle}{\partial b_\mathrm{b}}\right) \tag{S21}$$

$$\tilde{m}_2 = m_\mathrm{b}\left(1 - \frac{\partial\langle z_\mathrm{b}\rangle}{\partial b_\mathrm{f}}\right) \tag{S22}$$

Using the symmetry of $N_\alpha\partial_{b_\beta}\langle z_\alpha\rangle$, we see that in the experimentally relevant limit $N_\mathrm{f} \gg N_\mathrm{b}$, we have $\partial_{b_\mathrm{f}}\langle z_\mathrm{b}\rangle \gg \partial_{b_\mathrm{b}}\langle z_\mathrm{f}\rangle$. Thus the frequency of ^{6}Li is essentially not affected by the coupling between the two species. To leading order, we can identify ω_1 (ω_2) with $\tilde{\omega}_\mathrm{b}$ ($\tilde{\omega}_\mathrm{f}$) and we have

$$\tilde{\omega}_\mathrm{f} \simeq \omega_\mathrm{f} \tag{S23}$$

$$\tilde{\omega}_\mathrm{b} \simeq \omega_\mathrm{b}\left(1 + \frac{1}{2}\frac{\partial\langle z_\mathrm{b}\rangle}{\partial b_\mathrm{f}}\right) \tag{S24}$$

To calculate the frequency $\tilde{\omega}_\mathrm{b}$ we need to know the crossed-susceptibility $\partial_{b_\mathrm{f}}\langle z_\mathrm{b}\rangle$. Since this is in equilibrium quantity, we can calculate it using the local-density approximation. We then obtain

$$\frac{\partial\langle z_\mathrm{b}\rangle}{\partial b_\mathrm{f}} = \frac{k g_\mathrm{bf}}{N_\mathrm{b}}\int d^3\boldsymbol{r}\, z^2\left(\frac{\partial n_\mathrm{f}}{\partial\mu_\mathrm{f}}\right)\left(\frac{\partial n_\mathrm{b}}{\partial\mu_\mathrm{b}}\right) \tag{S25}$$

In the limit $N_\mathrm{b} \ll N_\mathrm{f}$, the bosonic cloud is much smaller than the fermionic cloud. We can therefore approximate this expression by

$$\frac{\partial\langle z_\mathrm{b}\rangle}{\partial b_\mathrm{f}} \simeq \frac{k g_\mathrm{bf}}{N_\mathrm{b}}\left(\frac{\partial n_\mathrm{f}}{\partial\mu_\mathrm{f}}\right)_0\int d^3\boldsymbol{r}\, z^2\left(\frac{\partial n_\mathrm{b}}{\partial\mu_\mathrm{b}}\right) \tag{S26}$$

where the index zero indicates that the derivative is calculated at the center of the trap. The integral can be calculated exactly and we finally obtain

$$\frac{\partial\langle z_\mathrm{b}\rangle}{\partial b_\mathrm{f}} = g_\mathrm{bf}\left(\frac{\partial n_\mathrm{f}}{\partial\mu_\mathrm{f}}\right)_0, \tag{S27}$$

where we recover Eq. (2) from main text.

To get the dynamics of the system after the excitation, we need to calculate the eigenvectors of the matrix $\mathcal{M}$. Note $\psi_i' = (a_{i,\mathrm{f}}', a_{i,\mathrm{b}}')$ the eigenvector associated to the eigenvalue ω_i. Using once more first order perturbation theory, we have

$$\psi_1' = \begin{pmatrix} 1 \\ \frac{\sqrt{m_\mathrm{f} m_\mathrm{b}}}{m_\mathrm{f}-m_\mathrm{b}} \sqrt{\frac{N_\mathrm{b}}{N_\mathrm{f}}} \frac{\partial \langle z_\mathrm{b} \rangle}{\partial b_\mathrm{f}} \end{pmatrix} \tag{S28}$$

$$\psi_2' = \begin{pmatrix} \frac{\sqrt{m_\mathrm{f} m_\mathrm{b}}}{m_\mathrm{b}-m_\mathrm{f}} \sqrt{\frac{N_\mathrm{b}}{N_\mathrm{f}}} \frac{\partial \langle z_\mathrm{b} \rangle}{\partial b_\mathrm{f}} \\ 1 \end{pmatrix}, \tag{S29}$$

from which we deduce the vectors $\psi_{i=1,2} = (a_{i,\mathrm{f}}, a_{i,\mathrm{b}})$ giving the excitation operator $\widehat{F}(a_{i,\mathrm{f}}, a_{i,\mathrm{b}})$. More precisely

$$\psi_1 = \sqrt{\frac{m_\mathrm{f}}{N_\mathrm{f}}} \begin{pmatrix} 1 \\ \frac{m_\mathrm{b}}{m_\mathrm{f}-m_\mathrm{b}} \frac{\partial \langle z_\mathrm{b} \rangle}{\partial b_\mathrm{f}} \end{pmatrix} \tag{S30}$$

$$\psi_2 = \sqrt{\frac{m_\mathrm{b}}{N_\mathrm{b}}} \begin{pmatrix} \frac{m_\mathrm{f}}{m_\mathrm{b}-m_\mathrm{f}} \frac{N_\mathrm{b}}{N_\mathrm{f}} \frac{\partial \langle z_\mathrm{b} \rangle}{\partial b_\mathrm{f}} \\ 1 \end{pmatrix}. \tag{S31}$$

Note d the initial displacement of the two species and expand the initial condition $Z = (z_\mathrm{f}(0), z_\mathrm{b}(0)) = (d, d)$ over the basis $\{\psi_1, \psi_2\}$ as $Z = \sum_i c_i \psi_i$. Since by construction the operator $\widehat{F}(a_{i,\mathrm{f}}, a_{i,\mathrm{b}})$ excites solely the mode ω_i we must have at time t $Z(t) = \sum_i c_i \cos(\omega_i t)\psi_i$ (we assume that the initial velocities are zero). After a straightforward calculation, we get

$$z_\mathrm{f}(t) = d\left[\frac{(1-\varepsilon\rho\eta)\cos(\omega_1 t) + \eta\rho\varepsilon(1+\varepsilon)\cos(\omega_2 t)}{1+\varepsilon^2\rho\eta}\right] \tag{S32}$$

$$z_\mathrm{b}(t) = d\left[\frac{-\varepsilon(1-\varepsilon\rho\eta)\cos(\omega_1 t) + (1+\varepsilon)\cos(\omega_2 t)}{1+\varepsilon^2\rho\eta}\right] \tag{S33}$$

with $\rho = N_\mathrm{b}/N_\mathrm{f}$, $\varepsilon = m_\mathrm{b}/(m_\mathrm{b}-m_\mathrm{f})\partial_{b_\mathrm{f}}\langle z_\mathrm{b}\rangle$ and $\eta = m_\mathrm{f}/m_\mathrm{b}$. In experimentally relevant situations, we have $\varepsilon \ll 1$, $\rho \ll 1$ and $\eta \simeq 1$. We can thus approximate the previous equations by

$$z_\mathrm{f}(t) \simeq d\left[(1-\varepsilon\rho)\cos(\tilde{\omega}_\mathrm{f} t) + \rho\varepsilon\cos(\tilde{\omega}_\mathrm{b} t)\right] \tag{S34}$$

$$z_\mathrm{b}(t) \simeq d\left[-\varepsilon\cos(\tilde{\omega}_\mathrm{f} t) + (1+\varepsilon)\cos(\tilde{\omega}_\mathrm{b} t)\right], \tag{S35}$$

and where according to Eq. (S24), we can take

$$\varepsilon = \frac{2m_\mathrm{b}}{m_\mathrm{b}-m_\mathrm{f}}\left(\frac{\tilde{\omega}_\mathrm{b}-\omega_\mathrm{b}}{\omega_\mathrm{b}}\right). \tag{S36}$$

References

31. N. Gross, Z. Shotan, O. Machtey, S. Kokkelmans, L. Khaykovich, *Comptes Rendus Physique* **12**, 4 (2011).

32. S. Nascimbène, *et al.*, *Phys. Rev. Lett.* **103**, 170402 (2009).

33. D. Miller, *et al.*, *Phys. Rev. Lett.* **99**, 070402 (2007).

34. D. Petrov, C. Salomon, G. Shlyapnikov, *Phys. Rev. Lett.* **93**, 090404 (2004).

C.3 Chandrasekhar-Clogston limit and critical polarization in a Fermi-Bose superfluid mixture

Tomoki Ozawa, Alessio Recati, Marion Delehaye, Frédéric Chevy, and Sandro Stringari

Physical Review A **90**, 043608 (2014)

PHYSICAL REVIEW A **90**, 043608 (2014)

Chandrasekhar-Clogston limit and critical polarization in a Fermi-Bose superfluid mixture

Tomoki Ozawa,[1] Alessio Recati,[1] Marion Delehaye,[2] Frédéric Chevy,[2] and Sandro Stringari[1]
[1]*INO-CNR BEC Center and Dipartimento di Fisica, Università di Trento, I-38123 Povo, Italy*
[2]*Laboratoire Kastler-Brossel, École Normale Supérieure, CNRS and UPMC, 24 rue Lhomond, 75005 Paris, France*
(Received 28 May 2014; published 8 October 2014)

We study mixtures of a population-imbalanced, strongly interacting Fermi gas and of a Bose-Einstein condensed gas at zero temperature. In the homogeneous case, we find that the Chandrasekhar-Clogston critical polarization for the onset of instability of Fermi superfluidity is enhanced due to the interaction with the bosons. Predictions for the critical polarization are also given in the trapped case, with a special focus on the situation of equal Fermi-Bose and Bose-Bose coupling constants, where the density of fermions becomes flat in the center of the trap. This regime can be realized experimentally using Feshbach resonances and is well suited to investigate the emergence of exotic configurations, such as the occurrence of spin domains or the Fulde-Ferrell-Larkin-Ovchinnikov (FFLO) phase.

DOI: 10.1103/PhysRevA.90.043608 PACS number(s): 67.85.Pq, 03.75.Mn, 03.75.Ss, 05.30.Fk

I. INTRODUCTION

The property of fermions interacting with a Bose fluid has been a longstanding subject of research in condensed matter physics, dating back to the study of ^{3}He $-^4$He mixtures [1]. With the recent development of research activity in ultracold gases, it is now possible to experimentally create mixtures of degenerate bosonic and fermionic atomic gases [2–11]. Very recently, the first experimental realization of a superfluid Bose-Fermi mixture was reported [12], the Fermi gas being at the unitarity limit.

There are several theoretical works on mixtures of superfluid Bose gases interacting with spin-1/2 Fermi gases [13–17], but the behavior of coexisting superfluid Fermi and Bose gases in the case of strong Fermi-Fermi interaction has not yet been considered in the literature. Furthermore, since spin-imbalanced fermions are predicted to give rise to exotic phases such as the Fulde-Ferrell-Larkin-Ovchinnikov (FFLO) phase [18–20], it is of great interest to investigate how their behavior is modified by the interaction with bosons.

In this paper, we show that in a homogeneous configuration the Chandrasekhar-Clogston critical polarization for the breakdown of superfluidity is larger than in the absence of the bosonic component [21]. We then consider the case of a harmonically trapped configuration: when the Bose-Bose and Bose-Fermi interactions are equal, the fermionic density in the region of coexistence with bosons becomes flat, because the interaction with bosons exactly compensates the external trapping potential [22]. We investigate the phase diagram of the trapped gas when the fermion imbalance is varied and show that, for a finite range of polarization, the fermionic density in the Bose-Fermi coexistence region can become inhomogeneous.

II. HOMOGENEOUS SYSTEM

The balanced unitary Fermi gas is known to be fully superfluid at zero temperature. As one increases the polarization, it has been observed that the system phase separates into a balanced superfluid phase and an imbalanced normal phase [23]. The two phases have different densities, and the equilibrium conditions between the two phases fix the ratio x between the density of the minority species over the density of the majority species in the normal phase, which determines the Chandrasekhar-Clogston limit. At zero temperature, this critical ratio turns out to be, at unitarity, $x \approx 0.4$ [21,24,25]. As we show, this value is modified by the interaction with bosons. We assume that the Fermi gas is phase separated into a superfluid phase with density n_s for both species and a normal phase with density $n_\uparrow$ and $n_\downarrow$ for the spin-up (majority) and spin-down (minority) fermions, respectively. The density of the coexisting bosons in the Fermi superfluid phase is n_{bs} and that in the normal phase is n_{bn}. Later we discuss the stability conditions for such configurations. We assume that both the bosonic and fermionic species can be described within the local density approximation and both the Bose-Bose and the Bose-Fermi interactions are weak enough to be treated within the mean-field approximation. Then the energy density in the superfluid phase (E_s) and in the normal phase (E_n) takes the form

$$\begin{aligned} E_s &= \frac{g_{bb}}{2} n_{bs}^2 + 2 g_{bf} n_{bs} n_s + e_s[n_s], \\ E_n &= \frac{g_{bb}}{2} n_{bn}^2 + g_{bf} n_{bn} (n_\uparrow + n_\downarrow) + e_n[n_\uparrow, n_\downarrow], \end{aligned} \tag{1}$$

where $g_{bb} \equiv 4\pi\hbar^2 a_{bb}/m_b$, assumed to be positive, and $g_{bf} \equiv 2\pi\hbar^2 a_{bf}/m_r$ are, respectively, the Bose-Bose and spin-independent Bose-Fermi interaction coupling constants. The Bose-Bose and Bose-Fermi scattering lengths are a_{bb} and a_{bf}, respectively, and $m_r \equiv m_b m_f/(m_b + m_f)$, where m_b and m_f are the boson and fermion masses, respectively. The Fermi energy density in the superfluid phase is given by the universal form

$$e_s[n_s] \equiv \xi \frac{6}{5} \frac{\hbar^2}{2m_f} (6\pi^2 n_s)^{2/3} n_s, \tag{2}$$

where $\xi = 0.370$ [25–27] is the Bertsch parameter. For the normal phase we use the expansion in the parameter $x \equiv n_\downarrow/n_\uparrow$ introduced in [21]:

$$\begin{aligned} e_n[n_\uparrow, n_\downarrow] &\equiv \frac{3}{5} \epsilon_{F\uparrow} n_\uparrow \left(1 - \frac{5}{3} A x + \frac{m_f}{m^*} x^{5/3} + F x^2\right) \\ &\equiv \frac{3}{5} \epsilon_{F\uparrow} n_\uparrow \epsilon(x), \end{aligned} \tag{3}$$

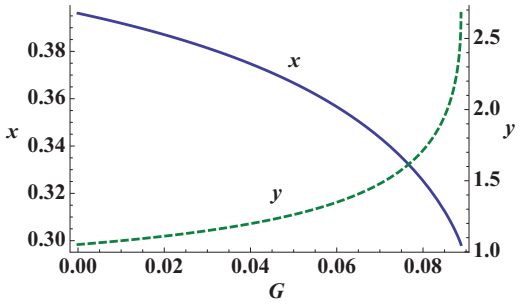

FIG. 1. (Color online) Critical ratios $x \equiv n_\downarrow/n_\uparrow$ (solid blue line with left axis) and $y \equiv n_s/n_\uparrow$ (dotted green line with right axis) as a function of $G \equiv n_\uparrow g_{bf}^2/\epsilon_{F\uparrow} g_{bb}$.

where $\epsilon_{F\uparrow} \equiv (\hbar^2/2m_f)(6\pi^2 n_\uparrow)^{2/3}$ is the noninteracting Fermi energy of the majority species, and for the parameters in $\epsilon(x)$ we use $A = 0.615$, $m^*/m_f = 1.20$, and $F = (5/9)A^2$, determined by diagramatic methods and Monte-Carlo calculations [28–30]. Using different sets of parameters would not change our results significantly. The equilibrium between the two phases is determined by matching the pressure and the chemical potentials for both bosons and fermions at the interface, which leads to the following conditions for x and $y \equiv n_s/n_\uparrow$:

$$\xi y^{2/3} - 2Gy - \frac{1}{2}\epsilon(x) - \frac{3}{10}\epsilon'(x)(1-x) + G(1+x) = 0,$$
$$2Gy^2 - \frac{4}{5}\xi y^{5/3} - G\frac{(1+x)^2}{2} + \frac{2}{5}\epsilon(x) = 0, \tag{4}$$

where $\epsilon'(x) \equiv d\epsilon(x)/dx$ and $G \equiv n_\uparrow g_{bf}^2/(\epsilon_{F\uparrow} g_{bb})$ is a dimensionless parameter independent of the bosonic density. As a consequence, also the critical ratios x and y are independent of the boson density, provided there are background bosons with nonzero densities in both phases. The parameter G has an important physical meaning, corresponding to the ratio between the change in the energy of fermions caused by the induced interaction $-g_{bf}^2/g_{bb}$ in the static limit and the noninteracting Fermi energy. The existence of two real solutions for x and y for (4) is ensured for $0 \leqslant G \leqslant G_{\max} \approx 0.089$, and in Fig. 1 we plot the resulting values of x and y as a function of G. When $G = 0$, the critical ratio $x \approx 0.40$ coincides with the value obtained in the absence of Bose-Fermi interaction ($g_{bf} = 0$). As G becomes larger, the value of x decreases, reaching the minimum value of $x \approx 0.30$, which means that the superfluid phase of fermions is stabilized by the interaction with bosons. The ratio y, on the other hand, increases with G, reaching the maximum value of $y \approx 2.68$, which implies that the density jump at the interface of the two phases becomes larger; the maximum value of the jump, corresponding to $G = G_{\max}$, is $2n_s/(n_\uparrow + n_\downarrow) \approx 4.1$, to be compared with the value $\approx$1.5 when $G = 0$.

The nonexistence of real solutions when $G > G_{\max}$ is related to the occurrence of dynamical instability in the fermionic superfluid phase caused by the interaction with bosons. The dynamical stability of the superfluid phase requires that the following inequality be obeyed [31]:

$$\frac{\delta^2 e_s[n_s]}{\delta n_s^2} - 4\frac{g_{bf}^2}{g_{bb}} > 0, \tag{5}$$

which is equivalent to imposing $\xi/3y^{1/3} > G$. We have checked that the condition for having real solutions for x and y coincides with the one ensuring dynamical stability. If G becomes larger than $G_{\max}$, the superfluid Fermi gas and the Bose gas are expected to phase separate.

III. TRAPPED SYSTEM

Let us now consider the case of a trapped quantum mixture. In the absence of bosons, it is known that as one introduces a small imbalance between the two species, the central part of the trap remains superfluid and the outer shell is turned into a normal state [21,23]. When the imbalance is large enough, the whole Fermi gas is in the normal state.

In the presence of bosons, the situation can change significantly. The energy of a highly polarized Fermi gas interacting with a BEC gas is given, within the local density approximation (LDA), by

$$\begin{aligned} E = &\int_{r<R_b} d^3r \Big\{ \frac{g_{bb}}{2} n_b^2(r) + [V_b(r) - \mu_b] n_b(r) \\ &+ g_{bf} n_b(r)[n_\uparrow(r) + n_\downarrow(r)] + e_n[n_\uparrow(r), n_\downarrow(r)] \\ &+ [V_f(r) - \mu_\uparrow] n_\uparrow(r) + [V_f(r) - \mu_\downarrow] n_\downarrow(r) \Big\} \\ &+ \int_{R_b<r} d^3r \{ e_n[n_\uparrow(r), n_\downarrow(r)] + [V_f(r) - \mu_\uparrow] n_\uparrow(r) \\ &+ [V_f(r) - \mu_\downarrow] n_\downarrow(r) \}, \end{aligned} \tag{6}$$

where R_b is the radius at which the boson density vanishes, and $V_b(r)$ and $V_f(r)$ are the harmonic traps for bosons and fermions, respectively [32]. The densities of boson, spin-up fermion, and spin-down fermion are $n_b(r)$, $n_\uparrow(r)$, and $n_\downarrow(r)$, respectively, and the corresponding chemical potentials are labeled, respectively, with μ_b, $\mu_\uparrow$, and $\mu_\downarrow$.

Taking the variation of the energy with respect to $n_b(r)$, $n_\uparrow(r)$, and $n_\downarrow(r)$ in the Bose-Fermi coexistence region $r < R_b$, which is hereafter referred to as the "core" region, one obtains the following equations:

$$\begin{aligned} &n_b(r) = \{\mu_b - V_b(r) - g_{bf}[n_\uparrow(r) + n_\downarrow(r)]\}/g_{bb}, \\ &\frac{\delta e_n}{\delta n_\sigma} + V_f(r) - \frac{g_{bf}}{g_{bb}} V_b(r) + \frac{g_{bf}}{g_{bb}}\mu_b - \mu_\sigma \\ &\quad - \left(g_{bf}^2/g_{bb}\right)[n_\uparrow(r) + n_\downarrow(r)] = 0, \end{aligned} \tag{7}$$

where $\sigma = \uparrow, \downarrow$. The second equation explicitly reveals that, if $g_{bf} V_b(r) = g_{bb} V_f(r)$, the fermion densities are not affected by the presence of the trap and take a constant value inside the core [22]. This follows from the fact that the effect of the trap on the fermions is exactly canceled by the mean-field interaction with bosons [33]. Conversely, the bosonic density is not affected by the presence of fermions and, choosing an external potential of harmonic form, the bosonic density, for $r < R_b$, takes an inverted parabola profile, whose shape is solely determined by the total number of bosons and the

Bose-Bose coupling constant g_{bb}. If instead $g_{bf}V_b > g_{bb}V_f$, the fermions feel an antitrapping potential in the core region and their density will increases when one moves away from the center.

When the imbalance is small, most of the fermions are in the superfluid phase and one can write down a similar energy functional as (6), but the region $r < R_b$ is filled with the superfluid phase, while the region $r > R_b$ is divided into an inner superfluid phase and an outer normal phase. One obtains the following conditions analogous to Eq. (7):

$$n_b(r) = [\mu_b - V_b(r) - 2g_{bf}n_s(r)]/g_{bb},$$
$$\frac{\delta e_s}{\delta n_s} + 2\left(V_f(r) - \frac{g_{bf}}{g_{bb}}V_b(r)\right) + 2\frac{g_{bf}}{g_{bb}}\mu_b - (\mu_\uparrow + \mu_\downarrow) - 4(g_{bf}^2/g_{bb})n_s(r) = 0, \quad (8)$$

in the core. As in the highly polarized case, one can see that in this region the fermions exhibit a flat density distribution when $g_{bf}V_b(r) = g_{bb}V_f(r)$. The equilibrium between the superfluid phase and the normal phase in the tail is determined by matching the pressure and the chemical potentials at the interface, and the critical ratio $x = n_\downarrow/n_\uparrow$ is equal to 0.40, which is the value predicted in the absence of bosons [21,24,25].

For concreteness we provide predictions for the mixture of ^{7}Li bosons and ^{6}Li fermions reported in [12] where $V(r) \equiv V_b(r) = V_f(r)$, and we focus on the special case $g_{bf} = g_{bb}$. This condition $g_{bb} = g_{bf}$ [corresponding to $a_{bb}/a_{bf} = (m_b + m_f)/2m_f$], together with that of unitarity for the Fermi component, are achievable for a magnetic field of $B = 817$ G, leading to a fermion-fermion scattering length of $25800a_B$ and to a boson-boson scattering length $a_{bb} = 44.2a_B$, the average Fermi momentum being $k_F = 10^6 \sim 10^7\text{m}^{-1}$.

The density profile of the fermions (both inside and outside the core) can be obtained by solving (7) or (8) and similar equations for the region $r > R_b$. In Fig. 2, we plot two density distributions for fixed values of $N_b = 10^5$ and $N_\uparrow = 1.5 \times 10^5$ but with two different values of $N_\downarrow$. We choose $a_{bb} = 10^{-3}l_{\text{ho}}m_b/m_f$, where $l_{\text{ho}} \equiv \sqrt{\hbar/m_f\omega_f}$ is the harmonic

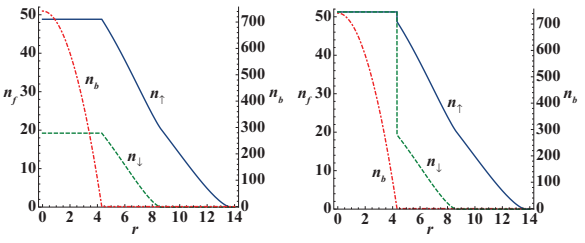

(a)The whole system is normal (b)The core is all superfluid

FIG. 2. (Color online) Local 3D density profile of the two opposite limits where the inhomogeneous phase in the core is about to appear. We fix $N_b = 10^5$ and $N_\uparrow = 1.5 \times 10^5$. The solid (blue) lines are spin-up fermions, the dotted (green) lines are spin-down fermions, and the dash-dotted (red) lines are bosons. The left axis is for the fermion densities and the right axis is for the boson density. The number of spin-down fermions is (a) $N_\downarrow = 0.22 \times 10^5$ and (b) $N_\downarrow = 0.33 \times 10^5$. The length is in units of l_{ho}, and the density of particles is in units of $1/l_{\text{ho}}^3$.

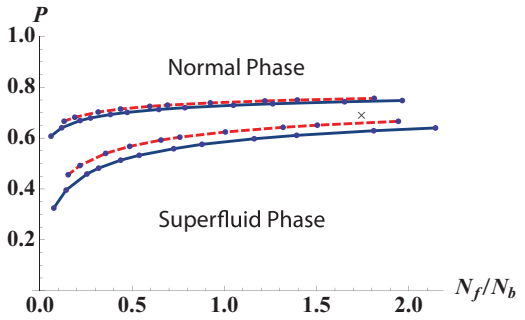

FIG. 3. (Color online) Critical polarizations for entering the inhomogeneous core as a function of N_f/N_b for $N_b = 10^5$ (solid blue lines) and $N_b = 10^4$ (dashed red lines). The cross corresponds to the situation of Fig. 4.

oscillator length corresponding to a fermionic trap frequency $\omega_f = 2\pi \times 420$ Hz. Figure 2(a) corresponds to the smallest value of total polarization of the gas [$P \equiv (N_\uparrow - N_\downarrow)/(N_\uparrow + N_\downarrow) = 0.74$] compatible with the absence of superfluidity, where the ratio $n_\downarrow/n_\uparrow$ in the core is equal to the critical value determined by Eq. (4) for the value of G in the core region. A smaller value of P would correspond to the onset of a superfluid region in the core. Figure 2(b) instead corresponds to the largest value of total polarization ($P = 0.63$) compatible with the presence of a superfluid phase occupying the whole core region. A larger value of P would correspond to the onset of a normal region in the core (see also Fig. 3).

For intermediate values of the population imbalance, coexistence of the superfluid and the normal phase takes place in the core region, giving rise to inhomogeneity and new interesting physics. Inhomogeneity in the core can be reached either by starting with a balanced superfluid gas and gradually decreasing the number of minority fermions until the normal part enters the core, or by starting with a completely polarized gas and gradually increasing the number of minority fermions until a superfluid phase region in the core is favorable. In Fig. 3, the two critical polarizations for entering the inhomogeneous core phase are plotted as a function of N_f/N_b, where $N_f \equiv N_\uparrow + N_\downarrow$, for two different values of N_b. The upper region corresponds to the phase with the whole system being normal [Fig. 2(a)], and the lower region corresponds to the whole core being superfluid [Fig. 2(b)]. The region between the lines represents the inhomogeneous core phase. We observe that the critical polarization as a function of N_f/N_b is not very sensitive to the number of bosons. The two critical polarization lines approach the value 0.8 as $N_f/N_b \to \infty$. This asymptotic value corresponds to the critical polarization for the onset of superfluidity in the absence of bosons [24].

We now discuss the possible scenarios characterizing the inhomogeneous phase for intermediate values of population imbalance (see Fig. 3). The simplest possibility, hereafter called the superfluid-normal (S-N) scenario, is that the core is phase separated into a central superfluid and an outer normal phase. The equilibrium condition between the superfluid phase and the normal phase turns out to be determined by the same conditions (4) holding for the homogeneous mixture. Another

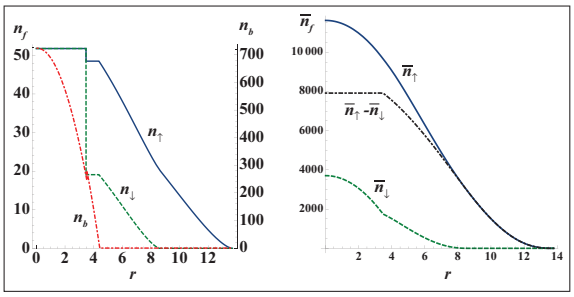

(a)Local (left) and doubly integrated (right) density for the S-N scenario (see text)

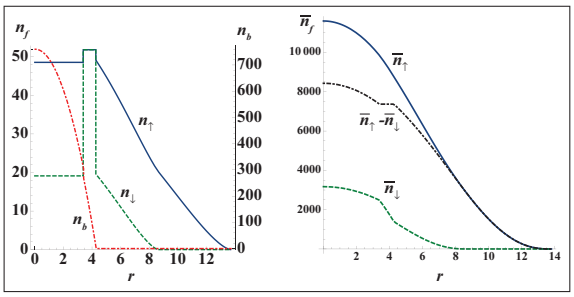

(b)Local (left) and doubly integrated (right) density for the N-S-N scenario (see text)

FIG. 4. (Color online) Local 3D density and doubly integrated density profiles for two different configurations for the core, corresponding to the S-N and N-S-N scenarios in the text. We have chosen $N_b = 10^5$ and $N_\uparrow = 1.5 \times 10^5$ as in Fig. 2. The value of $N_\downarrow$ is instead 0.28×10^5, corresponding to $P = 0.69$ and $N_f/N_b = 1.78$, i.e., to the inhomogeneous core region of Fig. 3. The solid (blue) lines are for spin-up fermions and the dotted (green) lines are for spin-down fermions. The dash-dotted (red) lines are for bosons for the local density, and the dash-dotted (black) lines are the difference $\bar{n}_\uparrow - \bar{n}_\downarrow$ for the doubly integrated density. For the local density, the left axis is for fermions and the right axis is for bosons. Lengths are in units of $l_{\rm ho}$.

possibility, hereafter called the normal-superfluid-normal (N-S-N) scenario, is that the core is phase separated into a central normal phase and an outer superfluid phase, while the tail is normal. The two scenarios have very similar energies and can be easily distinguished in experiments [34] by measuring the doubly integrated column density $\bar{n}_\sigma(z) \equiv \int dx dy\, n_\sigma(x,y,z)$, because the superfluid region appears as a flat profile in the difference $\bar{n}_\uparrow(z) - \bar{n}_\downarrow(z)$ [35]. This flat, doubly integrated density profile is due to pairing and should not be confused with the three-dimensional (3D) flat density profile that is caused by the Fermi-Bose interaction. Typical density distributions and corresponding doubly integrated column densities are plotted in Fig. 4. Another interesting feature of this inhomogeneous core phase is that the boson density is not a simple inverse parabola but has a small jump (not visible in the figure) at the phase boundary between the superfluid and normal fermion. The two scenarios of Fig. 4 can be energetically separated by changing the value of g_{bb} as compared to g_{bf}. If, e.g., $g_{bb} \lesssim g_{bf}$, the fermions are affected by a small antitrapping potential in the core and the second scenario, Fig. 4(b), will take place. The difference should be clearly visible experimentally, as shown in the doubly integrated densities in Fig. 4.

The emergence of the inhomogeneous phase is also compatible with other more exotic possibilities, such as the emergence of the FFLO phase [18–20]. Indeed, the local chemical potential for fermions is constant over the flat region; therefore phases which can exist only within a narrow range in the chemical potential could be observed in the core.

ACKNOWLEDGMENTS

We thank Igor Ferrier-Barbut and Christophe Salomon for useful discussions. We also thank Stefano Giorgini for insightful comments. This work was supported by the ERC through the QGBE grant and by Provincia Autonoma di Trento, and by the ERC Ferlodim and Thermodynamix, the Ile de France Nano-K (Contract Atomix), and by an Institut de France Louis D. Prize.

[1] J. Bardeen, G. Baym, and D. Pines, Phys. Rev. **156**, 207 (1967).
[2] F. Schreck, L. Khaykovich, K. L. Corwin, G. Ferrari, T. Bourdel, J. Cubizolles, and C. Salomon, Phys. Rev. Lett **87**, 080403 (2001).
[3] Z. Hadzibabic, C. A. Stan, K. Dieckmann, S. Gupta, M. W. Zwierlein, A. Görlitz, and W. Ketterle, Phys. Rev. Lett. **88**, 160401 (2002).
[4] S. Inouye, J. Goldwin, M. L. Olsen, C. Ticknor, J. L. Bohn, and D. S. Jin, Phys. Rev. Lett. **93**, 183201 (2004).
[5] K. Günter, T. Stöferle, H. Moritz, M. Köhl, and T. Esslinger, Phys. Rev. Lett. **96**, 180402 (2006).
[6] C. Ospelkaus, S. Ospelkaus, L. Humbert, P. Ernst, K. Sengstock, and K. Bongs, Phys. Rev. Lett. **97**, 120402 (2006).
[7] M. Zaccanti, C. D'Errico, F. Ferlaino, G. Roati, M. Inguscio, and G. Modugno, Phys. Rev. A **74**, 041605(R) (2006).
[8] Th. Best, S. Will, U. Schneider, L. Hackermüller, D. van Oosten, I. Bloch, and D.-S. Lühmann, Phys. Rev. Lett. **102**, 030408 (2009).
[9] S. Sugawa, K. Inaba, S. Taie, R. Yamazaki, M. Yamashita, and Y. Takahashi, Nat. Phys. **7**, 642 (2011).
[10] C.-H. Wu, I. Santiago, J. W. Park, P. Ahmadi, and M. W. Zwierlein, Phys. Rev. A **84**, 011601(R) (2011).
[11] S. Stellmer, R. Grimm, and F. Schreck, Phys. Rev. A **87**, 013611 (2013).
[12] I. Ferrier-Barbut, M. Delehaye, S. Laurent, A. T. Grier, M. Pierce, B. S. Rem, F. Chevy, and C. Salomon, arXiv:1404.2548.
[13] S. Modak, S.-W. Tsai, and K. Sengupta, Phys. Rev. B **84**, 134508 (2011).
[14] A. Yamamoto and T. Hatsuda, Phys. Rev. A **86**, 043627 (2012).
[15] M. Bukov and L. Pollet, Phys. Rev. B **89**, 094502 (2014).
[16] K. Maeda, G. Baym, and T. Hatsuda, Phys. Rev. Lett. **103**, 085301 (2009).
[17] B. Ramachandhran, S. G. Bhongale, and H. Pu, Phys. Rev. A **83**, 033607 (2011).
[18] H. Hu and X.-J. Liu, Phys. Rev. A **73**, 051603(R) (2006).

[19] A. Bulgac and M. McNeil Forbes, Phys. Rev. Lett. **101**, 215301 (2008).
[20] L. Radzihovsky and D. E. Sheehy, Rep. Prog. Phys. **73**, 076501 (2010).
[21] A. Recati, C. Lobo, and S. Stringari, Phys. Rev. A **78**, 023633 (2008).
[22] K. Mølmer, Phys. Rev. Lett. **80**, 1804 (1998).
[23] Y. Shin, C. H. Schunck, A. Schirotzek, and W. Ketterle, Nature (London) **451**, 689 (2008).
[24] C. Lobo, A. Recati, S. Giorgini, and S. Stringari, Phys. Rev. Lett. **97**, 200403 (2006).
[25] *The BCS-BEC Crossover and the Unitary Fermi Gas*, edited by W. Zwerger (Springer-Verlag, Berlin, 2012).
[26] M. J. H. Ku, A. T. Sommer, L. W. Cheuk, and M. W. Zwierlein, Science **335**, 563 (2012).
[27] G. Zürn, T. Lompe, A. N. Wenz, S. Jochim, P. S. Julienne, and J. M. Hutson, Phys. Rev. Lett. **110**, 135301 (2013).
[28] N. Prokof'ev and B. Svistunov, Phys. Rev. B **77**, 020408(R) (2008).
[29] R. Combescot and S. Giraud, Phys. Rev. Lett. **101**, 050404 (2008).
[30] C. Mora and F. Chevy, Phys. Rev. Lett. **104**, 230402 (2010).
[31] L. Viverit, C. J. Pethick, and H. Smith, Phys. Rev. A **61**, 053605 (2000).
[32] In the following, without loss of generality, we use an isotropic potential.
[33] The cancellation effect disappears when the number of bosons is not large enough to apply LDA.
[34] An experimental measurement of the local 3D density would require a more sophisticated 3D reconstruction of the density based on inverse Abel transformation [23].
[35] T. N. De Silva and E. J. Mueller, Phys. Rev. A **73**, 051602 (2006).

C.4 Critical velocity and dissipation of an ultracold Bose-Fermi counterflow

Marion Delehaye, Sébastien Laurent, Igor Ferrier-Barbut, Shuwei Jin, Frédéric Chevy, and Christophe Salomon

Physical Review Letters **115**, 265303 (2015)

Critical Velocity and Dissipation of an Ultracold Bose-Fermi Counterflow

Marion Delehaye, Sébastien Laurent, Igor Ferrier-Barbut,* Shuwei Jin, Frédéric Chevy, and Christophe Salomon
Laboratoire Kastler Brossel, ENS-PSL, CNRS, UPMC-Sorbonne Universités, and Collège de France, 75005 Paris, France
(Received 10 October 2015; revised manuscript received 19 November 2015; published 23 December 2015)

We study the dynamics of counterflowing bosonic and fermionic lithium atoms. First, by tuning the interaction strength we measure the critical velocity v_c of the system in the BEC-BCS crossover in the low temperature regime and we compare it to the recent prediction of Castin *et al.*, C. R. Phys. 16, 241 (2015). Second, raising the temperature of the mixture slightly above the superfluid transitions reveals an unexpected phase locking of the oscillations of the clouds induced by dissipation.

DOI: 10.1103/PhysRevLett.115.265303 PACS numbers: 67.85.-d, 03.75.Kk, 03.75.Ss, 37.10.Gh

Superconductivity and superfluidity are spectacular macroscopic manifestations of quantum physics at low temperature. Besides liquid helium 4 and helium 3, dilute quantum gases have emerged over the years as a versatile tool to probe superfluid properties in diverse and controlled situations. Frictionless flows have been observed with both bosonic and fermionic atomic species, in different geometries and in a large range of interaction parameters from the weakly interacting Bose gas to strongly correlated fermionic systems [1–6]. Several other hallmarks of superfluidity such as quantized vortices or second sound were also observed in cold atoms [7–9].

A peculiar feature of superfluid flows is the existence of a critical velocity above which dissipation arises. In Landau's original argument, this velocity is associated with the threshold for creation of elementary excitations in the superfluid: for a linear dispersion relation, it predicts that the critical velocity is simply given by the sound velocity in the quantum liquid. This critical velocity has been measured both in superfluid helium [10] and ultracold atoms [1,4–6,11]. However, the recent production of a Bose-Fermi double superfluid [12] raised new questions on Bose-Fermi mixtures [13–16] and interrogations on the validity of Landau's argument in the case of superfluid counterflow [17–22].

In this Letter, we study the dynamics of a Bose-Fermi superfluid counterflow in the crossover between the Bose-Einstein condensate (BEC) and Bardeen-Cooper-Schrieffer (BCS) regimes and at finite temperature. We show how friction arises when the relative velocity of the Bose and Fermi clouds increases and we confirm that damping occurs only above a certain critical relative velocity v_c. We compare our measurements to Landau's prediction and its recent generalization $v_c = c_s^F + c_s^B$, where c_s^F and c_s^B are the sound velocities of the fermionic and bosonic components, respectively [18]. Finally, we study finite temperature damping of the counterflow and we show that the system can be mapped onto a Caldeira-Leggett-like model [23] of two quantum harmonic oscillators coupled to a bath of excitations. This problem has been recently studied as a toy model for decoherence in quantum networks [24] or for heat transport in crystals [25] and we show here that the emergence of dissipation between the two clouds leads to a Zeno-like effect which locks their relative motions.

Our Bose and Fermi double-superfluid setup was previously described in [12]. We prepare vapors of bosonic (B) ^{7}Li atoms spin polarized in the second-to-lowest energy state and fermionic (F) ^{6}Li atoms prepared in a balanced mixture of the two lowest spin states noted $|\uparrow\rangle$, $|\downarrow\rangle$. The two species are kept in the same cigar-shaped hybrid magnetic-optical trap in which evaporative cooling is performed in the vicinity of the 832 G ^{6}Li Feshbach resonance [26]. The final number of fermions $N_F = 2.5 \times 10^5$ greatly exceeds that of the bosons $N_B \sim 2.5 \times 10^4$ and the temperature of the sample is adjusted by stopping the evaporation at different trap depths. The thermal pedestal surrounding the ^{7}Li BEC provides a convenient low temperature thermometer for both species after sufficiently long thermalization time ($\sim$1 sec). The lowest temperature achieved in this study corresponds to almost entirely superfluid clouds with $T/T_{c,\alpha=B,F} \leq 0.5$, where $T_{c,\alpha}$ is the superfluidity transition temperature of species α.

The magnetic field values used in the experiment (780–880 G) enable us to scan the fermion-fermion interaction within a range $-0.5 \leq 1/k_F a_F \leq 1$. Here, a_F is the s-wave scattering length between $|\uparrow\rangle$ and $|\downarrow\rangle$ fermions and the Fermi momentum k_F is defined by $\hbar^2 k_F^2/2m_F = \hbar\bar{\omega}(3N_F)^{1/3}$ with $\bar{\omega}$ the geometric mean of the trap frequencies, and N_F the total number of fermions of mass m_F. In our shallowest traps, typical trap frequencies for ^{6}Li are $\omega_x = \omega_y = 2\pi \times 550$ Hz and $\omega_z = 2\pi \times 17$ Hz. Since the bosonic and fermionic isotopes experience the same trapping potentials, the oscillation frequencies of the two species are within a ratio $\sqrt{6/7} \simeq 0.9$.

We excite the dipole modes of the system by displacing adiabatically the centers of mass of the clouds from their initial position by a distance z_0 along the weakly confined z direction, and abruptly releasing them in the trap. The two clouds evolve for a variable time t before *in situ* absorption

images perpendicular to the z direction are taken. The measurement of their doubly integrated density profiles gives access to axial positions and atom numbers of both species. Typical time evolutions of the centers of mass are shown in Fig. 1 for different parameter values. Since the Bose and Fermi components oscillate at different frequencies, they oscillate in quadrature after a few periods. By changing z_0, we can thus tune the maximum relative velocity between the two clouds and probe the critical superfluid counterflow.

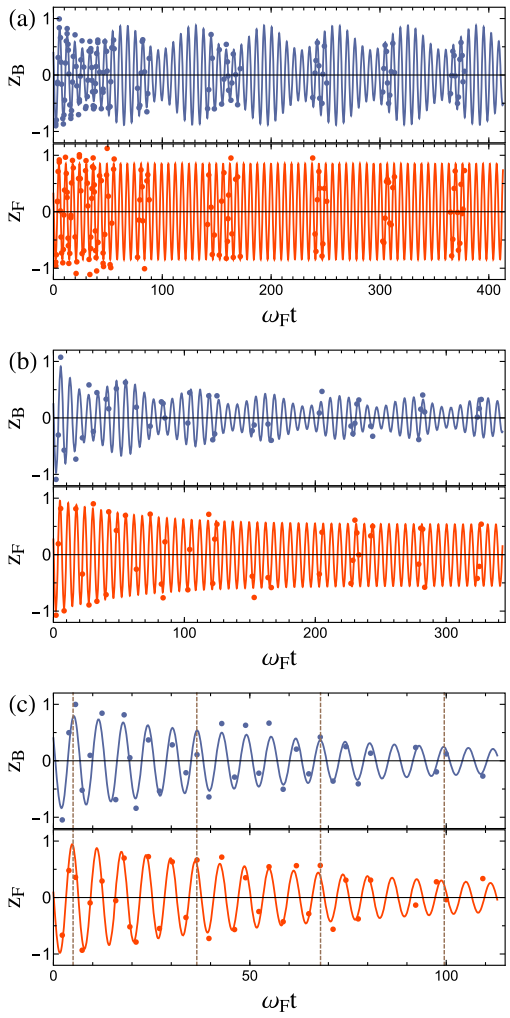

FIG. 1 (color online). Center-of-mass oscillations of bosons (blue, top) and fermions (red, bottom), for different sets of parameters at unitarity. Solid lines: fits using Eq. (1) for the bosons and a similar equation for the fermions. (a) $T/T_F = 0.03$, $T/T_{c,b} \leq 0.5$, $z_0 = 10$ μm. Superfluid regime, no damping is observed and $\omega_B = 2\pi \times 15.41(1)$ Hz $\approx \sqrt{6/7}\omega_F$. The observed beating at $\omega_F - \omega_B$ is due to coherent energy exchange between the clouds. (b) $T/T_F = 0.03$ and $z_0 = 150$ μm. For a larger initial displacement, initial damping ($\gamma_B = 2.4$ s^{-1}) is followed by steady-state evolution. $\omega_B = 2\pi \times 14.2(1)$ Hz $\approx \sqrt{6/7}\omega_F$. (c) $T/T_F = 0.4$ and $z_0 = 80$ μm. At higher temperature, phase locking of the two frequencies is observed with $\omega_F \approx \omega_B = 2\pi \times 17.9(3)$ Hz and $\gamma_B = \gamma_F = 1.4(5)$ s^{-1}.

As shown in Fig. 1(a), the superfluid counterflow exhibits no visible damping on a $\simeq$5 s time scale for very low temperature and small initial displacement. A striking feature is the beat note on the ^{7}Li oscillation amplitude due to the coherent mean-field coupling to the ^{6}Li cloud [12]. For larger relative velocities, ^{7}Li oscillations are initially damped [Fig. 1(b)] until a steady-state regime as in Fig. 1(a) is reached. We fit the time evolution of the cloud position using the phenomenological law

$$z_B(t) = d(t)[a\cos(\omega_B t) + b\cos(\omega_F t)],$$
$$d(t) = d_1 + d_2\exp(-\gamma_B t). \quad (1)$$

We measure the damping rate γ_B as a function of relative velocity for six different values of magnetic field, exploring a large region of the crossover going from the BCS ($1/k_F a_F = -0.42$, $B = 880$ G) to the BEC side ($1/k_F a_F = 0.68$, $B = 780$ G), see Fig. 2. For these magnetic field values, the Bose gas remains in the weakly interacting (repulsive) regime and the Bose-Fermi scattering length is $a_{BF} \simeq 41 a_0$, constant in this magnetic field range, and equal for both $|\uparrow\rangle$ and $|\downarrow\rangle$ spin states.

We extract the critical velocity v_c using an *ad hoc* power-law fitting function $\gamma_B = A\Theta(v - v_c)[(v - v_c)/v_F]^\alpha$, where Θ is the Heaviside function and v_F is the Fermi velocity given by $v_F = \hbar k_F/m_F$. For details, see [27]. v_c in the BEC-BCS crossover is displayed in Fig. 3 (red dots) and compared to the predictions of Landau and Castin *et al.* [18]. In this latter work, dissipation arises by the creation of excitation pairs and yields a critical velocity

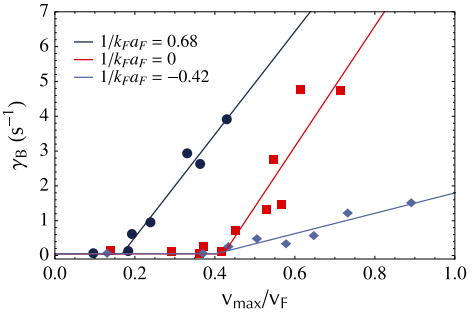

FIG. 2 (color online). Damping rate of the center-of-mass oscillations versus maximal relative velocity in the BEC-BCS crossover in units of the Fermi velocity v_F. Dark blue dots, BEC side (780 G) $1/k_F a_F = 0.68$; red squares, unitarity (832.2 G) $1/k_F a_F = 0$; light blue diamonds, BCS side (880 G) $1/k_F a_F = -0.42$. Power law fits with thresholds provide the critical velocity (solid lines).

$v_c = \min_{\substack{p \\ \sigma=f,b}}\{[\epsilon^B(\boldsymbol{p}) + \epsilon^F_\sigma(\boldsymbol{p})]/[p]\}$. In this expression, $\epsilon^B(\boldsymbol{p})$ denotes the dispersion relation of excitations in the BEC and $\epsilon^F_\sigma(\boldsymbol{p})$ refers to the two possible branches of the Fermi superfluid, phononlike ($\sigma = b$), and threshold for pair breaking excitations ($\sigma = f$) [28]. For homogeneous gases, at unitarity and on the BEC side of the crossover, this critical relative velocity turns out to be simply the sum of the respective sound velocities of the Bose and Fermi superfluids, $v_c = c_s^F + c_s^B$. We thus plot in Fig. 3 the calculated sound velocities of both superfluids in an elongated geometry obtained by integration over the transverse direction [29–33] (red dashed line c_s^F, blue bars c_s^B). Typically, c_s^B contributes $\simeq$20%–25% to the sum shown as green squares in Fig. 3. Around unitarity and on the BCS side of the resonance, our experimental data are consistent with this interpretation as well as with a critical velocity $v_c = c_s^F$ that one would expect by considering the BEC as a single impurity moving inside the fermionic superfluid. By contrast, we clearly exclude the bosonic sound velocity as a threshold for dissipation.

Our measured critical velocities are significantly higher than those previously reported in pure fermionic systems which, for all interaction strengths, were lower than Landau's criterion [4,6]. The main difference with our study is the use of focused laser beams instead of a BEC as a moving obstacle. In [6], the laser beam is piercing the whole cloud including its nonsuperfluid part where the density is low, and its potential may create a strong density modulation of the superfluid. These effects make a direct comparison to Landau criterion difficult [35]. On the contrary, in our system the size of the BEC (Thomas Fermi radii of 73, 3, 3 μm) is much smaller than the typical size of the Fermi cloud (350, 13, 13 μm around unitarity). For oscillation amplitudes up to ± 200 μm the BEC probes only the superfluid core of the fermionic cloud. During its oscillatory motion along z the Bose gas may explore the edges of the Fermi superfluid where the density is smaller. However, it is easy to check that the ratio v/c_s^F is maximum when the centers of the two clouds coincide [27]. Finally, as the mean-field interaction between the two clouds is very small [27] our BEC acts as a weakly interacting local probe of the Fermi superfluid.

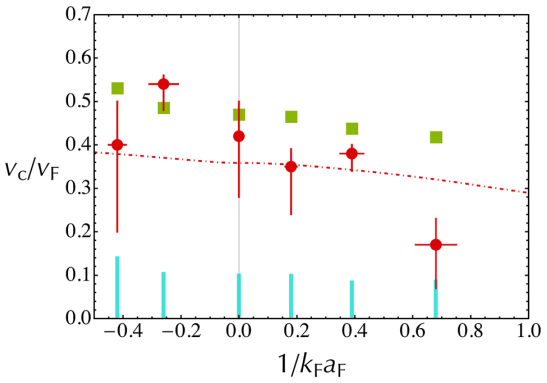

FIG. 3 (color online). Critical velocity of the Bose-Fermi superfluid counterflow in the BEC-BCS crossover normalized to the Fermi velocity v_F. Red dots, measurements. Red dot-dashed line, sound velocity c_s^F of an elongated homogeneous Fermi superfluid calculated from its equation of state [29,30] after integration of the density in the transverse plane, and also measured in [34]. Blue bars, calculated sound velocity c_s^B of the elongated ^{7}Li BEC for each magnetic field (880, 860, 832, 816, 800, 780 G). Green squares indicate the prediction $v_c = c_s^F + c_s^B$. Error bars and c_s^B are discussed in [27].

On the BEC side of the resonance (780 G), however, we observe a strong reduction of the measured critical velocity compared to the predicted values. The effect is strikingly seen in Fig. 2, dark blue dots (see also Supplemental Material [27]). This anomalously small value for positive scattering lengths is consistent with previous measurements [4,6]. Its origin is still unclear but several explanations can be put forward [35]. First, it is well known that vortex shedding can strongly reduce superfluid critical velocity. However, this mechanism requires a strong perturbation. The density of the Bose gas and the mean-field interaction between the two clouds are probably too small for vortex generation through a collective nucleation process. Second, inelastic losses increase on the BEC side of a fermionic Feshbach resonance and heat up the system [36]. This hypothesis is supported by the presence of a clearly visible pedestal in the density profiles of the BEC taken at 780 G. At this value of the magnetic field, we measure a $\simeq$60% condensed fraction, corresponding to a temperature $T/T_{c,B} \simeq 0.5$. Even though the two clouds are still superfluids as demonstrated by the critical behavior around v_c, the increased temperature could be responsible for the decrease of v_c.

We now present results of experiments performed at a higher temperature ($0.03 \lesssim T/T_F \lesssim 0.5$) for $B = 835$ G. For low temperatures ($T/T_F \leq 0.2$), the two clouds remain weakly coupled and, as observed in Fig. 4, the bosonic and fermionic components oscillate at frequencies in the expected ratio $\simeq 0.9 \simeq \sqrt{6/7}$. A new feature emerges for $T \gtrsim T_{c,B} \approx 0.34 T_F > T_{c,F}$ where both gases are in the normal phase. In this "high" temperature regime, the two clouds are locked in phase: ^{7}Li oscillates at ^{6}Li frequency (Fig. 4) and the two components are equally damped [Fig. 1(c)]. This remarkable behavior can be understood as a Zeno effect arising from the increased dissipation between the two components. Indeed, the system can be described as a set of two harmonic oscillators describing, respectively, the macroscopic motion of the global center of mass of the system (Kohn's mode [37]) and the relative motion of the two clouds [27]. These two degrees of freedom are themselves coupled to the "bath" of

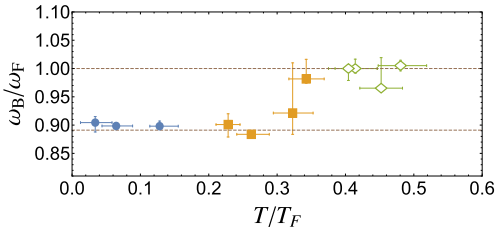

FIG. 4 (color online). Ratio ω_B/ω_F versus temperature of the cloud. Blue circles, the two clouds are superfluids. Yellow squares, only the bosonic component is superfluid. Green open diamonds, the two components are normal. Above $T \approx T_{c,B} \approx 0.34T_F > T_{c,F}$, oscillations of the Bose and Fermi clouds become locked together at ω_F. Oscillations frequencies are obtained using a Lomb-Scargle algorithm [27]. The lower dashed line is the prediction of a low temperature mean field model [12].

the internal excitations of the two clouds (breathing mode, quadrupole modes, pair breaking excitations…).

In the spirit of the dressed-atom picture, we can represent the state of the two harmonic oscillators by the "radiative" cascade of Fig. 5. Here the states $|N, n\rangle$ are labeled by the quantum numbers associated to Kohn's mode (N) and relative motion (n) of the two clouds and we trace out the degrees of freedom of the bath. On the one hand, Kohn's mode is not an eigenstate of the system for fermions and bosons of different masses; center-of-mass and relative-motion modes are coupled and this coherent coupling is responsible for the dephasing of the oscillations of the two clouds in the weakly interacting regime. On the other hand, interspecies interactions do not act on the center of mass of the whole system, owing to Kohn's theorem, but on the contrary lead to an irreversible "radiative" decay of the *relative* motion at a rate γ.

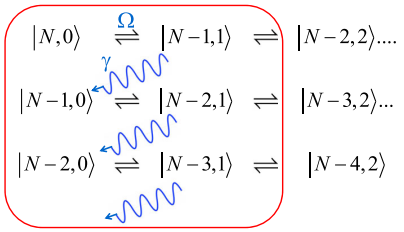

FIG. 5 (color online). Radiative cascade of the center-of-mass motion. In $|N, n\rangle$, N (respectively, n) refers to the center-of-mass (respectively, relative) motion of the two clouds (see text). When the decay rate of the relative motion is larger than the oscillation frequency difference between the two species, the dynamics is restricted to the center-of-mass degree of freedom: in this Zeno-like process, dissipation prevents excitation of the relative motion and the center-of-mass modes of the Bose and Fermi gases do not dephase.

In our experiments, the initial state is a pure center-of-mass excitation $|N, 0\rangle$. If we neglect the interspecies coupling, the system evolves in the subspace spanned by $|N-n, n\rangle_{n=0,\ldots,N}$ of the two coupled oscillators and the system oscillates at a frequency $\delta\omega \simeq \omega_B - \omega_F$ as the centers of mass of the Bose and Fermi clouds dephase. If we now consider the opposite limit where the decay rate γ is larger than the dephasing frequency $\delta\omega$, the strong coupling to the bath prevents the conversion of the center-of-mass excitations into relative motion. As soon as the system is transferred into $|N-1, 1\rangle$ it decays towards state $|N-1, 0\rangle$. Similarly to optical pumping in quantum optics, we can eliminate adiabatically the excited states of the relative motion and restrict the dynamics of the system to the subspace $|N, 0\rangle_{N=0,\ldots,\infty}$ of Kohn's excitations. This situation is reminiscent of the synchronization of two spins immersed in a thermal bath predicted in [38] or to phenomenological classical two-coupled oscillators model.

In this Letter, we have investigated how a Bose-Fermi superfluid flow is destabilized by temperature or relative velocity between the two clouds. In the limit of very low temperature the measured critical velocity for superfluid counterflow slightly exceeds the speed of sound of the elongated Fermi superfluid and decreases sharply towards the BEC side of the BEC-BCS crossover. In a future study, we will investigate the role of temperature, of the confining potential, and of the accelerated motion of the two clouds [35] that should provide a more accurate model for the damping rate versus velocity and more insights on the nature of the excitations. In particular, the *ab initio* calculation of the damping rate will require clarification of the dissipation mechanism at play in a trapped system where the bandwidth of the excitation spectrum is narrow, in contrast to a genuine Caldeira-Leggett model [39].

The authors acknowledge support from Institut Francilien de Recherche sur les Atomes Froids (Atomix Project), ERC (ThermoDynaMix Project), and Institut de France (Louis D. Prize). They thank I. Danaila, N. Proukakis, K. L. Lee, and M. Pierce for insightful comments and discussions, and J. Dalibard, Y. Castin, S. Nascimbène, and T. Yefsah for critical reading of the manuscript.

M. D. and S. L. contributed equally to this work.

*Present Address: 5. Physikalisches Institut and Center for Integrated Quantum Science and Technology, Universität Stuttgart, Pfaffenwaldring 57, 70550 Stuttgart, Germany.

[1] C. Raman, M. Köhl, R. Onofrio, D. S. Durfee, C. E. Kuklewicz, Z. Hadzibabic, and W. Ketterle, Phys. Rev. Lett. **83**, 2502 (1999).

[2] A. P. Chikkatur, A. Görlitz, D. M. Stamper-Kurn, S. Inouye, S. Gupta, and W. Ketterle, Phys. Rev. Lett. **85**, 483 (2000).

[3] C. Ryu, M. F. Andersen, P. Cladé, V. Natarajan, K. Helmerson, and W. D. Phillips, Phys. Rev. Lett. **99**, 260401 (2007).
[4] D. E. Miller, J. K. Chin, C. A. Stan, Y. Liu, W. Setiawan, C. Sanner, and W. Ketterle, Phys. Rev. Lett. **99**, 070402 (2007).
[5] R. Desbuquois, L. Chomaz, T. Yefsah, J. Léonard, J. Beugnon, C. Weitenberg, and J. Dalibard, Nat. Phys. **8**, 645 (2012).
[6] W. Weimer, K. Morgener, V. P. Singh, J. Siegl, K. Hueck, N. Luick, L. Mathey, and H. Moritz, Phys. Rev. Lett. **114**, 095301 (2015).
[7] K. W. Madison, F. Chevy, W. Wohlleben, and J. Dalibard, Phys. Rev. Lett. **84**, 806 (2000).
[8] M. Zwierlein, J. Abo-Shaeer, A. Schirotzek, C. Schunck, and W. Ketterle, Nature (London) **435**, 1047 (2005).
[9] L. A. Sidorenkov, M. K. Tey, R. Grimm, Y.-H. Hou, L. Pitaevskii, and S. Stringari, Nature (London) **498**, 78 (2013).
[10] J. Wilks and D. Betts, *An Introduction to Liquid Helium* (Oxford Science Publications, Clarendon Press, Oxford, 1987).
[11] D. Dries, S. E. Pollack, J. M. Hitchcock, and R. G. Hulet, Phys. Rev. A **82**, 033603 (2010).
[12] I. Ferrier-Barbut, M. Delehaye, S. Laurent, A. T. Grier, M. Pierce, B. S. Rem, F. Chevy, and C. Salomon, Science **345**, 1035 (2014).
[13] T. Ozawa, A. Recati, M. Delehaye, F. Chevy, and S. Stringari, Phys. Rev. A **90**, 043608 (2014).
[14] R. Zhang, W. Zhang, H. Zhai, and P. Zhang, Phys. Rev. A **90**, 063614 (2014).
[15] X. Cui, Phys. Rev. A **90**, 041603 (2014).
[16] J. J. Kinnunen and G. M. Bruun, Phys. Rev. A **91**, 041605 (2015).
[17] M. Abad, A. Recati, S. Stringari, and F. Chevy, Eur. Phys. J. D **69**, 126 (2015).
[18] Y. Castin, I. Ferrier-Barbut, and C. Salomon, C.R. Phys. **16**, 241 (2015).
[19] W. Zheng and H. Zhai, Phys. Rev. Lett. **113**, 265304 (2014).
[20] L. Wen and J. Li, Phys. Rev. A **90**, 053621 (2014).
[21] F. Chevy, Phys. Rev. A **91**, 063606 (2015).
[22] H. Shen and W. Zheng, Phys. Rev. A **92**, 033620 (2015).
[23] A. O. Caldeira and A. J. Leggett, Physica (Amsterdam) **121A**, 587 (1983).
[24] C.-H. Chou, T. Yu, and B. L. Hu, Phys. Rev. E **77**, 011112 (2008).
[25] U. Zürcher and P. Talkner, Phys. Rev. A **42**, 3267 (1990).
[26] G. Zürn, T. Lompe, A. N. Wenz, S. Jochim, P. S. Julienne, and J. M. Hutson, Phys. Rev. Lett. **110**, 135301 (2013).
[27] See Supplemental Material at http://link.aps.org/supplemental/10.1103/PhysRevLett.115.265303 for extra comments and discussion.
[28] R. Combescot, M. Y. Kagan, and S. Stringari, Phys. Rev. A **74**, 042717 (2006).
[29] N. Navon, S. Nascimbène, F. Chevy, and C. Salomon, Science **328**, 729 (2010).
[30] G. Astrakharchik, Ph.D thesis, University of Trento, 2004, arXiv:1412.4529.
[31] S. Stringari, Phys. Rev. A **58**, 2385 (1998).
[32] P. Capuzzi, P. Vignolo, F. Federici, and M. P. Tosi, Phys. Rev. A **73**, 021603 (2006).
[33] L. Luo, B. Clancy, J. Joseph, J. Kinast, and J. E. Thomas, Phys. Rev. Lett. **98**, 080402 (2007).
[34] J. Joseph, B. Clancy, L. Luo, J. Kinast, A. Turlapov, and J. E. Thomas, Phys. Rev. Lett. **98**, 170401 (2007).
[35] V. P. Singh, W. Weimer, K. Morgener, J. Siegl, K. Hueck, N. Luick, H. Moritz, and L. Mathey, arXiv:1509.02168.
[36] C. A. Regal, M. Greiner, and D. S. Jin, Phys. Rev. Lett. **92**, 083201 (2004).
[37] W. Kohn, Phys. Rev. **123**, 1242 (1961).
[38] P. P. Orth, D. Roosen, W. Hofstetter, and K. Le Hur, Phys. Rev. B **82**, 144423 (2010).
[39] R. Onofrio and B. Sundaram, Phys. Rev. A **92**, 033422 (2015).

SUPPLEMENTAL INFORMATION

DAMPING RATES IN THE BEC-BCS CROSSOVER

All the center of mass (CoM) damping rates measured in the BEC-BCS crossover and their respective fitting functions to extract v_c are shown in Fig. 1. As indicated in the main text the fit function is $\gamma_B = A\Theta(v - v_c)((v - v_c)/v_F)^\alpha$, where Θ is the Heaviside function and v_F is the Fermi velocity. The χ^2 test reveals that most of our data is consistent with $\alpha = 1$ as in [1, 2]. Due to the current absence of theoretical prediction for α in a trapped system, we allow α to vary between 0.5 and 2, and this induces a systematic correlation between the extracted α and v_c that we include in our error bars on v_c shown in Fig. 3 of main text. The fit results for $\alpha = 1$ are displayed in Tab. I along with experimental parameters to produce Fig. 3 of main text. The error bars given for v_c give the span of v_c when changing α from 0.5 to 2 in the fit function. Note the strong decrease of the damping rate towards the BCS regime.

In addition, c_s^B depends on the Bose-Bose scattering length which varies with magnetic field and in particular diverges for a magnetic field of 845.5 G (corresponding to $1/k_F a_F = -0.13$). We therefore show only the values of c_s^B at the six magnetic field values used in our experiments.

Following [3] the Bose-Fermi coupling can be characterized by the quantity $\Delta = \sqrt{\frac{\partial\mu_B}{\partial n_F}\frac{\partial\mu_F}{\partial n_B}/\frac{\partial\mu_B}{\partial n_B}\frac{\partial\mu_F}{\partial n_F}}$. As Δ increases, the interspecies interactions affect more and more the properties of the system and for $\Delta = 1$, the mixture is dynamically unstable at rest and demixes. For measurements presented here we typically have $\Delta \simeq 15\%$.

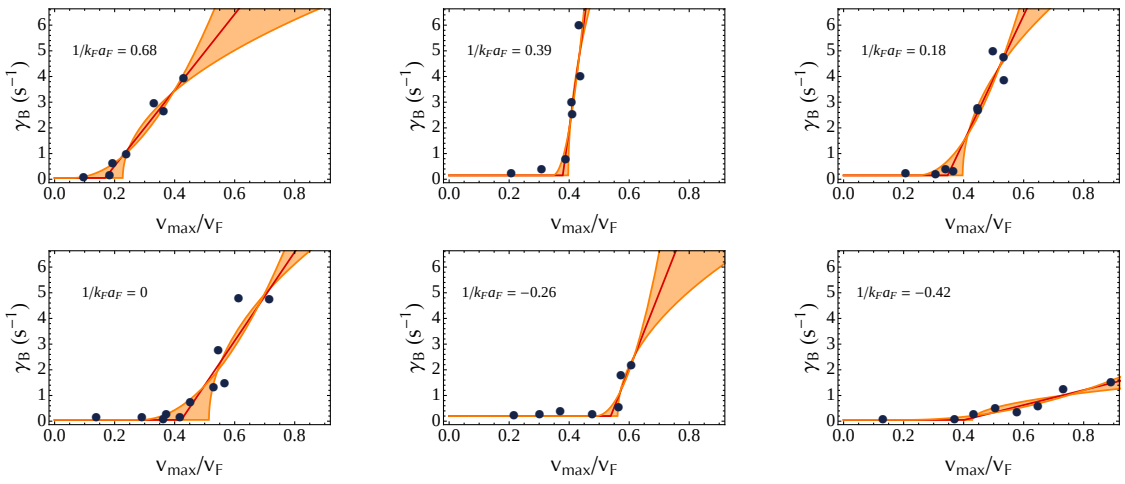

FIG. 1: Damping rates of the center of mass oscillations versus maximal relative velocity in the BEC-BCS crossover in unit of the Fermi velocity v_F. Red line: fit with $\alpha = 1$. Orange zone: region spanned by the fitting function when varying α from 0.5 to 2.

B (G)	780	800	816	832	860	880
$a_{\rm F}(a_0)$	6.4×10^3	11.3×10^3	24.0×10^3	∞	-16.5×10^3	-10.3×10^3
$1/k_{\rm F}a_{\rm F}$	0.68 ± 0.07	0.39 ± 0.01	0.18 ± 0.02	0 ± 0.002	-0.26 ± 0.05	-0.42 ± 0.03
$a_B(a_0)$	21.3	30.8	43.3	69.5	76.0	259
$c_{\rm B}(10^{-2}v_{\rm F})$	9.6 ± 1.4	9.4 ± 0.14	11.0 ± 1.6	11.1 ± 1.7	11.4 ± 1.7	15.1 ± 2.2
$v_{\rm c}/v_{\rm F}$	$0.17^{+0.06}_{-0.10}$	$0.38^{+0.02}_{-0.04}$	$0.35^{+0.04}_{-0.11}$	$0.42^{+0.08}_{-0.14}$	$0.54^{+0.02}_{-0.06}$	$0.40^{+0.10}_{-0.20}$
$A(s^{-1})$	14.8 ± 1.4	85 ± 32	24.6 ± 4.3	17.3 ± 3.6	30 ± 11	2.9 ± 0.5
$v_{\rm c}/c_{\rm s}^{\rm F}$	$0.53^{+0.19}_{-0.31}$	$1.11^{+0.06}_{-0.12}$	$0.99^{+0.11}_{-0.31}$	$1.17^{+0.22}_{-0.39}$	$1.46^{+0.05}_{-0.16}$	$1.05^{+0.26}_{-0.53}$

TABLE I: Experimental parameters, sound velocity at the center of the Bose gas in an elongated geometry $c_B=\sqrt{\mu_{\rm B}/2m_{\rm B}}$, critical velocity $v_{\rm c}/v_{\rm F}$, damping rate $A(s^{-1})$, and $v_{\rm c}/c_{\rm s}^{\rm F}$ for $\alpha=1$ in the BEC-BCS crossover. The typical number of bosons and fermions are constant in the crossover and are respectively $2.5\pm0.5\times10^4$ and $2.5\pm0.5\times10^5$.

EVOLUTION OF THE VELOCITIES IN THE TRAP

We demonstrate here that for a Bose-Fermi superfluid mixture oscillating in a harmonic trap, the ratio $v/c_{\rm s}^{\rm F}$ is maximum when the centers of two clouds coincide. This can be demonstrated in the general case using the equation of state in the BEC-BCS crossover [4], but we will derive it here for the simpler case of a polytropic equation of state.

In the frame of the Fermi cloud, we can describe the trajectory of the BEC by the simple harmonic oscillation

$$z_{\rm B}(t)=Z_0\cos(\omega_{\rm B}t), \tag{1}$$

where we have omitted the slow beating of the amplitude Z_0 due to the oscillation-frequency difference between bosons and fermions. The velocity of the BEC is then $v(z)=-Z_0\omega_{\rm B}\sin(\omega_{\rm B}t)$, hence

$$\left(\frac{v(z)}{v(z=0)}\right)^2=\left(1-\frac{z^2}{Z_0^2}\right), \tag{2}$$

For a polytropic equation of state, the local sound velocity in the Fermi cloud is given by [5]

$$c_{\rm s}^{\rm F}(z)^2 = \frac{\gamma}{\gamma+1}\frac{\mu_{\rm F}(z)}{m_{\rm F}} \tag{3}$$

$$c_{\rm s}^{\rm F}(z)^2 = \frac{\gamma}{\gamma+1}\frac{\mu_{\rm F}(0)}{m_{\rm F}}\left(1-\frac{z^2}{z_{\rm TF}^2}\right), \tag{4}$$

where $z_{\rm TF}$ is the Thomas-Fermi radius of the cloud, and the local chemical potential $\mu_{\rm F}(z)$ was obtained using the local density approximation. Combining equations 2 and 4, we then obtain

$$\frac{v(z)^2}{c_{\rm s}^{\rm F}(z)^2}=\frac{v(z=0)^2}{c_{\rm s}^{\rm F}(z=0)^2}\frac{1-z^2/Z_0^2}{1-z^2/z_{\rm TF}^2}, \tag{5}$$

which is maximum for $z=0$ when $Z_0\leq z_{\rm TF}$.

LOMB-SCARGLE ALGORITHM

We use the fit-free Lomb-Scargle periodogram - or Least Square Spectral Analysis - to extract the spectral components of the oscillations for different temperatures [6, 7]. This method is an adaptation of the Fourier transform to the case of unevenly spaced data. For N data points $\{h_i=h(t_i)\}_{i=1,\ldots,N}$ taken at times $\{t_i\}$, the periodogram is defined as

$$P_N(\omega)=\frac{1}{2\sigma^2}\left\{\frac{[\sum_j(h_j-\bar{h})\cos\omega(t_j-\tau)]^2}{\sum_j\cos^2\omega(t_j-\tau)} + \frac{[\sum_j(h_j-\bar{h})\sin\omega(t_j-\tau)]^2}{\sum_j\sin^2\omega(t_j-\tau)}\right\} \tag{6}$$

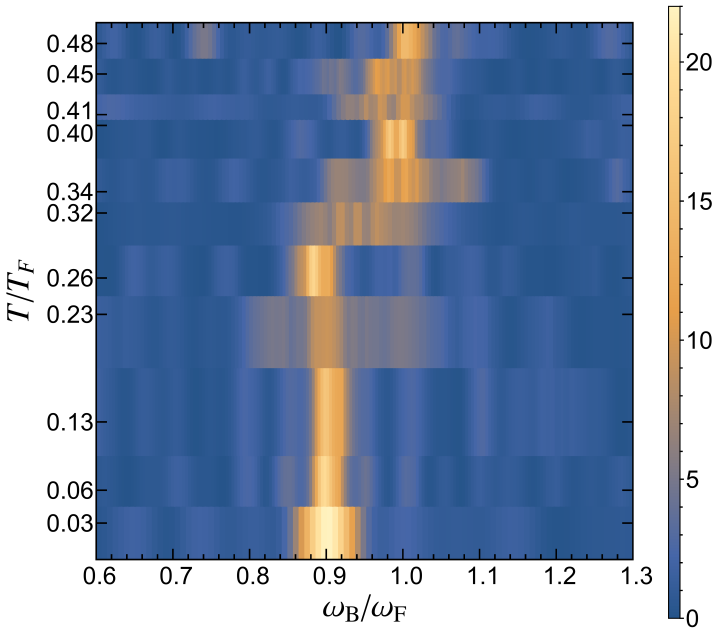

FIG. 2: Power spectrum of the oscillations for different temperatures, obtained using the Lomb-Scargle algorithm of the center-of-mass displacement. Above $T \approx T_{c,B} \approx 0.34\,T_F > T_{c,F}$, oscillations of the Bose and Fermi clouds become locked together at ω_F. A value of 10 for the power represents typically a significance of 0.002.

where τ is given by $\tan(2\omega\tau) = \frac{\sum_j \sin 2\omega t_j}{\sum_j \cos 2\omega t_j}$ making the periodogram independent of the time origin. $\bar{h} = \frac{1}{N}\sum_{i=1}^{N} h_i$ and $\sigma = \frac{1}{N-1}\sum_{i=1}^{N}(h_i - \bar{h})^2$ are the mean and the variance of $\{h_i\}_i$. The periodogram, or power spectrum (see Fig. 2), gives access to the statistical significance (*ie* the probability of rejecting the null hypothesis when it is true) of each of the evaluated frequencies: noting $P_{\max} = \max_{\omega} P_N(\omega)$, the signifiance is proportional to $e^{-P_{\max}}$, and here a value of 10 for the power represents typically a significance of 0.002. Fig. **??** of the main text displays the set of maxima of Fig. 2; error bars correspond to a significance increased by a factor of 10.

RADIATIVE CASCADE MODEL

Consider a mixture of two atomic species labeled by $\alpha = 1, 2$ of identical masses m and confined in identical harmonic traps. According to Kohn's theorem [8], the single-species Hamiltonian can always be written as

$$H_\alpha = \frac{P_\alpha^2}{2M_\alpha} + \frac{M_\alpha \omega^2 X_\alpha^2}{2} + H_{\rm int}^{(\alpha)}, \tag{7}$$

where P_α is the total momentum of cloud α, X_α the position of its center of mass and $M_\alpha = N_\alpha m$ its total mass (N_α being the number of atoms). $H_{\rm int}^{(\alpha)}$ acts only on the internal excitation modes of the cloud and commutes with the center-of-mass variables.

Neglecting interspecies interactions, the total Hamiltonian of the system can be written as $H = H_1 + H_2$. Introducing the center of mass/relative variables, we have then

$$H = H_1 + H_2 = \frac{P^2}{2M} + \frac{M\omega^2 X^2}{2} + \frac{p^2}{2\mu} + \frac{\mu\omega^2 x^2}{2} + H_{\rm int}^{(1)} + H_{\rm int}^{(2)}, \tag{8}$$

with the usual definitions $P = P_1 + P_2$, $X = (M_1X_1 + M_2X_2)/M$, $p = \mu(P_1/M_1 - P_2/M_2)$, $x = x_1 - x_2$, $M = M_1 + M_2$ and $\mu = M_1M_2/M$. The dynamics of the center of mass and relative variables are described by independent harmonic oscillators decoupled from the internal degrees of freedom. The decoupled base can therefore be written as $|N, n, \varphi\rangle$, where N (resp. n) is the excitation number of the center-of-mass (resp. relative) motion, and φ describes the state of the internal excitation modes.

Let's now add the interspecies interactions and the mass difference between the two species.

1. *Interspecies coupling*: interactions between the two species are described by the Hamiltonian

$$H_{1,2} = \sum_{i \leq N_1, j \leq N_2} U(x_{1,i} - x_{2,j}). \tag{9}$$

   where $x_{i,\alpha}$ is the position of the i-th particle of species α and U is the interspecies interaction potential.

   Owing to Kohn's theorem, this Hamiltonian commutes with P and X and therefore couples the internal degrees of freedom only to the relative variables (x, p).

2. *Mass difference*: assume that species α has a mass $m_\alpha = m + \epsilon_\alpha \delta m/2$, with $\epsilon_1 = 1$ and $\epsilon_2 = -1$. This mass difference adds to the kinetic energy a term

$$\delta H_{\rm K} = -\frac{\delta m}{2m} \sum_{i,\alpha} \epsilon_\alpha \frac{p_{i,\alpha}^2}{2m}. \tag{10}$$

   As before, we can isolate the center of mass contribution and write

$$\delta H_{\rm K} = -\frac{\delta m}{2m} \left[\frac{P_1^2}{2M_1} - \frac{P_2^2}{M_2} \right] + \delta H_{K,\rm int}, \tag{11}$$

   where $\delta H_{K,\rm int}$ contributes to the internal energies of the clouds and commutes with the center-of-mass degrees of freedom.

Let's now insert these two contributions in the total Hamiltonian. We have

$$H = H_{\rm CoM} + H_{\rm rel} + H'_{\rm int} + H_{1,2} + H_{\rm coh}. \tag{12}$$

with

$$H_{\rm CoM} = \frac{P^2}{2M}(1 - \rho\frac{\delta m}{2m}) + \frac{M\omega^2}{2}X^2 \tag{13}$$

$$H_{\rm rel} = \frac{p^2}{2\mu}(1 + \rho\frac{\delta m}{2m}) + \frac{\mu\omega^2}{2}x^2 \tag{14}$$

$$H'_{\rm int} = H_{\rm int}^{(1)} + H_{\rm int}^{(2)} + \delta H_{K,\rm int}, \tag{15}$$

$$H_{\rm coh} = \frac{\delta m}{m}\left(\frac{P \cdot p}{M}\right), \tag{16}$$

and $\rho = (M_1 - M_2)/M$.

This hamiltonian describes two harmonic oscillators ($H_{\rm CoM}$ and $H_{\rm rel}$) coupled to a thermal bath ($H'_{\rm int}$). The coupling is ensured by the $P \cdot p$ terms which couples only the center-of-mass and relative degrees of freedom, and $H_{1,2}$ that commutes with $H_{\rm CoM}$, owing to Kohn's theorem, and couples the relative motion to the internal degrees of freedom of the two clouds.

The interaction between the relative degrees of freedom and the internal thermal bath described by $H_{\rm int}^{1,2}$ leads to an irreversible decay of the relative motion. By contrast, $H_{\rm coh}$ reflects the coherent beating existing between the relative oscillations of the two species due to their oscillation-frequency difference. It can be expressed using the annihilation operators a and b for the center of mass and relative motions respectively. We have then

$$H_{\rm coh} = -\frac{\delta m}{m}\hbar\omega\sqrt{\frac{\mu}{M}}\left(a - a^\dagger\right)\left(b - b^\dagger\right). \tag{17}$$

Using the rotating wave approximation, one can eliminate the non resonant terms and one finally gets

$$H_{\rm coh} \simeq \frac{\delta m}{2m}\hbar\omega\sqrt{\frac{\mu}{M}}\left(a^\dagger b + a b^\dagger\right). \tag{18}$$

This Hamiltonian is similar to the generalized Caldeira-Leggett model [9] used in solid state physics to study heat transport by phonons in a crystal. The absence of coupling between the bath and Kohn's mode generalizes to the decomposition used in [10] for a bilinear coupling between the harmonic oscillators and the bath.

In the experiment, we excite the center of mass motion and the initial state is $|N, 0, \varphi\rangle$. The coherent coupling transfers the system to the state $|N-1, 1, \varphi\rangle$. If the coupling to the bath is strong, the relative motion decays very fast and the system falls into a state $|N-1, 0, \varphi'\rangle$ (actually, since several states of the bath are involved, it is more appropriate to describe the state of the two harmonic oscillators by a density matrix rather than a well-defined quantum state). In this case, just like for optical pumping, we can adiabatically eliminate the intermediate state $|N-1, 1, \varphi\rangle$ and consider that the dynamics occurs only in the sub-space $|N, 0, \varphi\rangle$, where the relative motion is never excited and the centers of mass of the two clouds are locked. In some sense, this freezing of the system state in a pure motion of its center of mass can be considered as a manifestation of the quantum Zeno effect.

[1] D. E. Miller, J. K. Chin, C. A. Stan, Y. Liu, W. Setiawan, C. Sanner, and W. Ketterle, Phys. Rev. Lett. **99**, 070402 (2007), URL http://link.aps.org/doi/10.1103/PhysRevLett.99.070402.

[2] W. Weimer, K. Morgener, V. P. Singh, J. Siegl, K. Hueck, N. Luick, L. Mathey, and H. Moritz, Phys. Rev. Lett. **114**, 095301 (2015), URL http://link.aps.org/doi/10.1103/PhysRevLett.114.095301.

[3] M. Abad, A. Recati, S. Stringari, and F. Chevy, Eur. Phys. J. D **69**, 126 (2015), URL http://dx.doi.org/10.1140/epjd/e2015-50851-y.

[4] N. Navon, S. Nascimbène, F. Chevy, and C. Salomon, Science **328**, 729 (2010), http://www.sciencemag.org/content/328/5979/729.full.pdf, URL http://www.sciencemag.org/content/328/5979/729.abstract.

[5] P. Capuzzi, P. Vignolo, F. Federici, and M. P. Tosi, Phys. Rev. A **73**, 021603 (2006), URL http://link.aps.org/doi/10.1103/PhysRevA.73.021603.

[6] N. Lomb, Astrophysics and Space Science **39**, 447 (1976), ISSN 0004-640X, URL http://dx.doi.org/10.1007/BF00648343.

[7] J. Scargle, Astrophysical Journal **263**, 835 (1982), URL http://articles.adsabs.harvard.edu/full/1982ApJ...263..835S.

[8] W. Kohn, Phys. Rev. **123**, 1242 (1961), URL http://link.aps.org/doi/10.1103/PhysRev.123.1242.

[9] A. O. Caldeira and A. J. Leggett, Physica A: Statistical mechanics and its Applications **121**, 587 (1983).

[10] C.-H. Chou, T. Yu, and B. L. Hu, Phys. Rev. E **77**, 011112 (2008), URL http://link.aps.org/doi/10.1103/PhysRevE.77.011112.

C.5 Universal loss dynamics in a unitary Bose gas

Ulrich Eismann, Lev Khaykovich, Sébastien Laurent, Igor Ferrier-Barbut, Benno S. Rem, Andrew T. Grier, Marion Delehaye, Frédéric Chevy, Christophe Salomon, Li-Chung Ha, and Cheng Chin

Submitted to Physical Review X

Universal Loss Dynamics in a Unitary Bose Gas

Ulrich Eismann[1,3],* Lev Khaykovich[1,2],† Sébastien Laurent[1], Igor Ferrier-Barbut[1],‡ Benno S. Rem[1],§
Andrew T. Grier[1],¶ Marion Delehaye[1], Frédéric Chevy[1], Christophe Salomon[1], Li-Chung Ha[3], and Cheng Chin[3]
[1]*Laboratoire Kastler Brossel, ENS-PSL Research University, CNRS, UPMC, Collège de France, 24 rue Lhomond, 75005, Paris, France*
[2]*Department of Physics, Bar-Ilan University, Ramat-Gan 52900, Israel and*
[3]*James Franck Institute, Enrico Fermi Institute and Department of Physics, University of Chicago, Chicago, IL 60637, USA*
(Dated: May 29, 2015)

The low temperature unitary Bose gas is a fundamental paradigm in few-body and many-body physics, attracting wide theoretical and experimental interest. Here we first present a theoretical model that describes the dynamic competition between two-body evaporation and three-body recombination in a harmonically trapped unitary atomic gas above the condensation temperature. We identify a universal magic trap depth where, within some parameter range, evaporative cooling is balanced by recombination heating and the gas temperature stays constant. Our model is developed for the usual three-dimensional evaporation regime as well as the 2D evaporation case. Experiments performed with unitary ^{133}Cs and ^{7}Li atoms fully support our predictions and enable quantitative measurements of the 3-body recombination rate in the low temperature domain. In particular, we measure for the first time the Efimov inelasticity parameter $\eta_* = 0.098(7)$ for the 47.8-G d-wave Feshbach resonance in ^{133}Cs. Combined ^{133}Cs and ^{7}Li experimental data allow investigations of loss dynamics over two orders of magnitude in temperature and four orders of magnitude in three-body loss. We confirm the $1/T^2$ temperature universality law up to the constant η_*.

PACS numbers: 05.30.Jp Boson systems
05.70.Ln Nonequilibrium and irreversible thermodynamics
34.50.-s Scattering of atoms and molecules
51.30.+i Thermodynamic properties, equations of state

I. INTRODUCTION

Resonantly interacting Bose systems realized in ultracold atomic gases are attracting growing attention thanks to being among the most fundamental systems in nature and also among the least studied. Recent theoretical studies have included hypothetical BEC-BCS type transitions [1–5] and, at unitarity, calculations of the universal constant connecting the total energy of the system with the only energy scale left when the scattering length diverges: $E_n = \hbar^2 n^{2/3}/m$ [6–9]. The latter assumption itself remains a hypothesis as the Efimov effect might break the continuous scaling invariance of the unitary Bose gas and introduce another relevant energy scale to the problem. A rich phase diagram of the hypothetical unitary Bose gas at finite temperature has also been predicted [10, 11].

In experiments, several advances in the study of the resonantly interacting Bose gas have recently been made using the tunability of the s-wave scattering length a near a Feshbach resonance. The JILA group showed signatures of beyond-mean-field effects in two-photon Bragg spectroscopy performed on a ^{85}Rb BEC [12], and the ENS group quantitatively studied the beyond mean-field Lee-Huang-Yang corrections to the ground state energy of the Bose-Einstein condensate [13]. Logarithmic behavior of a strongly interacting 2D superfluid was also reported by the Chicago group [14]. Experiments have also started to probe the regime of unitarity ($1/a = 0$ directly. Three-body recombination rates in the non-degenerate regime have been measured in two different species, ^{7}Li [15] and ^{39}K [16], and clarified the temperature dependence of the unitary Bose gas lifetime. In another experiment, fast and non-adiabatic projection of the BEC on the regime of unitarity revealed the establishment of thermal quasi-equilibrium on a time scale faster than inelastic losses [17].

In a three-body recombination process three atoms collide and form a dimer, the binding energy of which is transferred into kinetic energies of the colliding partners. The binding energy is usually larger than the trap depth and thus leads to the loss of all three atoms. Because three-body recombination occurs more frequently at the center of the trap, this process is associated with "anti-evaporative" heating (loss of atoms with small potential energy) which competes with two-body evaporation and leads to a non trivial time dependence for the sample temperature. In this paper, we develop a theoretical model that describes these atom loss dynamics. We si-

*Present Address: Toptica Photonics AG, Lochhamer Schlag 19, 82166 Gräfelfing, Germany; These authors contributed equally to this work.
†These authors contributed equally to this work.
‡Present Address: 5. Physikalisches Institut and Center for Integrated Quantum Science and Technology, Universität Stuttgart, Pfaffenwaldring 57, 70550 Stuttgart, Germany
§Present Address: Institut für Laserphysik, Universitt Hamburg, Luruper Chaussee 149, Building 69, D-22761 Hamburg, Germany
¶Present address: Department of Physics, Columbia University, 538 West 120th Street, New York, NY 10027-5255, USA

multaneously take into account two and three-body losses to quantitatively determine each of these contributions. We predict the existence of a magic value for the trap-depth-over-temperature ratio where residual evaporation compensates for three-body loss heating and maintains the gas temperature constant within some range of parameters. We then apply our model to analyze the loss dynamics of ^{133}Cs and ^{7}Li unitary Bose gases prepared at various temperatures and atom numbers. Comparing measurements in these two different atomic species we find the dynamics to be universal, i.e. in both systems the three-body loss rate is found to scale universally with temperature. Excellent agreement between theory and experiment confirms that the dynamic evolution of the unitary Bose gas above the condensation temperature can be well modelled by the combination of two and three-body interaction processes.

II. MODEL

A former study developed for measuring three-body decay in trapped ^{133}Cs [18] atoms has proposed a model to describe the time evolution of the atom number N and the temperature T taking into account the three-body recombination induced loss and the heating associated with it. This model is valid in the limit of deep trapping potentials (trapping depth much larger than the atom's temperature) and for temperature independent losses. Here we generalize this model to include evaporation induced cooling and the associated atom loss, as well as the temperature dependence of the three-body loss rate.

A. Rate equation for atom number

The locally defined three-body recombination rate $L_3 n^3(r)/3$ leads, through integration over the whole volume, to the loss rate of atoms:

$$\frac{\mathrm{d}N}{\mathrm{d}t} = -3\int \frac{L_3 n^3(r)}{3}\mathrm{d}^3 r = -L_3\langle n^2\rangle N, \tag{1}$$

where the factor of 3 in front on the integral reflects the fact that all 3 atoms are lost per each recombination event. In the following, we neglect single-atom losses due to collisions with the background gas and we assume that two-body inelastic collisions are forbidden, a condition which is fulfilled for atoms polarized in the absolute ground state.

An expression for the three-body recombination loss coefficient at unitarity for a non-degenerate gas has been developed in Ref. [15]. Averaged over the thermal distribution it reads:

$$L_3 = \frac{72\sqrt{3}\pi^2\hbar\left(1-e^{-4\eta_*}\right)}{m k_{\mathrm{th}}^6} \times \int_0^\infty \frac{\left(1-|s_{11}|^2\right)e^{-k^2/k_{\mathrm{th}}^2}k\,\mathrm{d}k}{|1+(kR_0)^{-2is_0}e^{-2\eta_*}s_{11}|^2}, \tag{2}$$

where $k_{\mathrm{th}} = \sqrt{mk_{\mathrm{B}}T}/\hbar$, R_0 is the three-body parameter, and the Efimov inelasticity parameter η_* characterizes the strength of the short range inelastic processes. Here, $\hbar$ is the reduced Planck's constant, k_{B} is the Boltzmann's constant, and $s_0 = 1.00624$ for three identical bosons [19]. The matrix element s_{11} relates the incoming to outgoing wave amplitudes in the Efimov scattering channel and shows the emerging discrete scaling symmetry in the problem (see for example Ref. [20]). Details are given in the supplementary material to Ref. [15] for the calculation of $s_{11}(ka)$, where a is the scattering length and k is the relative wavenumber of the colliding partners. Because of its numerically small value for three identical bosons at unitarity, we can set $|s_{11}| = 0$ and L_3 is well approximated by:

$$L_3 \approx \frac{\hbar^5}{m^3}36\sqrt{3}\pi^2\frac{1-e^{-4\eta_*}}{(k_{\mathrm{B}}T)^2} = \frac{\lambda_3}{T^2}, \tag{3}$$

where λ_3 is a temperature-independent constant. Assuming a harmonic trapping potential, we directly express the average square density $\langle n^2\rangle$ through N and T. In combination with Eq. (3), Eq. (1) is represented as:

$$\frac{\mathrm{d}N}{\mathrm{d}t} = -\gamma_3\frac{N^3}{T^5}, \tag{4}$$

where

$$\gamma_3 = \lambda_3\left(\frac{m\bar{\omega}^2}{2\sqrt{3}\pi k_{\mathrm{B}}}\right)^3, \tag{5}$$

with $\bar{\omega}$ being the geometric mean of the angular frequencies in the trap.

To model the loss of atoms induced by evaporation, we consider time evolution of the phase-space density distribution of a classical gas:

$$f(\mathbf{r},\mathbf{p}) = \frac{n_0{\lambda_{\mathrm{dB}}}^3}{(2\pi\hbar)^3}e^{-U(\mathbf{r})/k_{\mathrm{B}}T}e^{-p^2/2mk_{\mathrm{B}}T}, \tag{6}$$

which obeys the Boltzmann equation. Here n_0 is the central peak density of atoms, $\lambda_{\mathrm{dB}} = (2\pi\hbar^2/mk_{\mathrm{B}}T)^{1/2}$ is the thermal de Broglie wavelength, and $U(\mathbf{r})$ is the external trapping potential. The normalization constant is fixed by the total number of atoms, such that $\int f(\mathbf{r},\mathbf{p})\mathrm{d}^3p\,\mathrm{d}^3r = N$.

If the gas is trapped in a 3-D trap with a potential depth U, the collision integral in the Boltzmann equation can be evaluated analytically [21]. Indeed, the low-energy collisional cross-section

$$\sigma(k) = \frac{8\pi}{k^2+a^{-2}} \tag{7}$$

reduces at unitarity to a simple dependence on the relative momentum of colliding partners: $\sigma(k) = 8\pi/k^2$. However, not every collision leads to a loss of atoms due to evaporation. Consider

$$\eta = U/k_{\mathrm{B}}T. \tag{8}$$

In the case of $\eta \gg 1$, such loss is associated with a transfer of large amount of energy to the atom which ultimately leads to the energy independent cross-section. This can be understood with a simple argument [22]. Assume that two atoms collide with the initial momenta $\boldsymbol{p_1}$ and $\boldsymbol{p_2}$. After the collision they emerge with the momenta $\boldsymbol{p_3}$ and $\boldsymbol{p_4}$, and if one of them acquires a momentum $|\boldsymbol{p_3}| \gtrsim \sqrt{2mU}$. Then, $|\boldsymbol{p_4}|$ is necessarily smaller than the most probable momentum of atoms in the gas and $|\boldsymbol{p_3}| \gg |\boldsymbol{p_4}|$. In the center of mass coordinates the absolute value of the relative momentum is preserved, so that $\frac{1}{2}|\boldsymbol{p_1} - \boldsymbol{p_2}| = \frac{1}{2}|\boldsymbol{p_3} - \boldsymbol{p_4}| \approx \frac{1}{2}|\boldsymbol{p_3}|$. Assuming $|\boldsymbol{p_3}| = \sqrt{2mU}$, we get $|\boldsymbol{p_1} - \boldsymbol{p_2}| = \sqrt{2mU}$. Substituting the relative momentum in the center of mass coordinate, $\hbar\boldsymbol{k} = \frac{1}{2}(\boldsymbol{p_1} - \boldsymbol{p_2})$, to the unitary form of the collisional cross-section, we find the latter is energy independent:

$$\sigma_U = \frac{16\pi\hbar^2}{mU}, \tag{9}$$

and the rate-equation for the atom number can be written as:

$$\frac{\mathrm{d}N}{\mathrm{d}t} = -\Gamma_{\mathrm{ev}} N, \quad \Gamma_{\mathrm{ev}} = n_0 \sigma_U \bar{v} e^{-\eta} \frac{V_{\mathrm{ev}}}{V_{\mathrm{e}}}. \tag{10}$$

The peak density is $n_0 = N/V_{\mathrm{e}}$, where V_e is the effective volume of the sample. In the harmonic trap V_e can be related to $\overline{\omega}$ and the temperature T: $V_e = \left(\frac{2\pi k_{\mathrm{B}} T}{m\overline{\omega}^2}\right)^{3/2}$. The ratio of the evaporative and effective volumes is defined by [21]:

$$\frac{V_{\mathrm{ev}}}{V_{\mathrm{e}}} = \eta - 4R\left(3, \eta\right), \tag{11}$$

where $R(a,\eta) = \frac{P(a+1,\eta)}{P(a,\eta)}$ and $P(a,\eta)$ is the incomplete Gamma function

$$P(a,\eta) = \frac{\int_0^\eta u^{a-1} e^{-u} \mathrm{d}u}{\int_0^\infty u^{a-1} e^{-u} \mathrm{d}u}.$$

Finally, taking into account both three-body recombination loss (see Eqs. (4),(5)) and evaporative loss, we can express the total atom number loss rate equation as:

$$\frac{\mathrm{d}N}{\mathrm{d}t} = -\gamma_3 \frac{N^3}{T^5} - \gamma_2 e^{-\eta} \frac{V_{\mathrm{ev}}}{V_{\mathrm{e}}} \frac{N^2}{T}, \tag{12}$$

where

$$\gamma_2 = \frac{16}{\pi} \frac{\hbar^2 \overline{\omega}^3}{k_{\mathrm{B}} U}. \tag{13}$$

Note that η and the ratio of the evaporative and effective volumes explicitly depend on temperature and γ_2 is temperature independent.

B. Rate equation for temperature

1. 'Anti-evaporation' and recombination heating

Ref. [18] points out that in each three-body recombination event a loss of an atom is associated with an excess of $k_{\mathrm{B}}T$ of energy that remains in the sample. This mechanism is caused by the fact that recombination events occur mainly at the center of the trap where the density of atoms is highest and it is known as 'anti-evaporation' heating. We now show that the unitary limit is more 'anti-evaporative' than the regime of finite scattering lengths considered in ref. [18] where L_3 is temperature independent. We separate center of mass and relative motions of the colliding atoms and express the total loss of energy per three-body recombination event as following:

$$\dot{E}_{3\mathrm{b}} = -\int \left\{ \frac{L_3 n^3(\boldsymbol{r})}{3} \left(\langle E_{\mathrm{cm}}\rangle + 3U(\mathbf{r})\right) + \frac{n^3(\boldsymbol{r})}{3} \langle L_3(k) E_k \rangle \right\} \mathrm{d}^3 r. \tag{14}$$

The first two terms in the parenthesis represent the mean center-of-mass kinetic energy $\langle E_{\mathrm{cm}}\rangle = \langle P_{\mathrm{cm}}^2\rangle/2M$ and the local potential energy $3U(\mathbf{r})$ per each recombination triple. $M = 3m$ is the total mass of the three-body system. The last term stands for thermal averaging of the three-body coefficient over the relative kinetic energy $E_k = (\hbar k)^2/2\mu$ where μ is the reduced mass.

Averaging the kinetic energy of the center of mass motion over the phase space density distribution (Eq. (6)) gives $\langle E_{\mathrm{cm}}\rangle = \frac{3}{2} k_{\mathrm{B}} T$. Then the integration over this term is straightforward and using Eq. (1) we have:

$$-\int \frac{L_3 n^3(\mathbf{r})}{3} \langle E_{\mathrm{cm}}\rangle \mathrm{d}^3 r = \frac{1}{2} k_{\mathrm{B}} T \dot{N} \tag{15}$$

The integration over the second term can be easily evaluated as well:

$$-\int \frac{3L_3}{3} n^3(\mathbf{r}) U(\mathbf{r}) \mathrm{d}^3 r = \frac{1}{2} k_{\mathrm{B}} T \dot{N} \tag{16}$$

To evaluate the third term we recall the averaged over the thermal distribution expression of the three-body recombination rate in Eq. (2). Now its integrand has to be supplemented with the loss of the relative kinetic energy per recombination event E_k. Keeping the limit of Eq. (3) this averaging can be easily evaluated to give $\langle L_3(k) E_k\rangle = L_3 k_{\mathrm{B}} T$. Finally, the last term in Eq. (14) gives:

$$-\int \frac{n^3(\mathbf{r})}{3} \langle L_3(k) E_k\rangle \mathrm{d}^3 r = \frac{1}{3} k_{\mathrm{B}} T \dot{N} \tag{17}$$

Finally, getting together all the terms, the lost energy per lost atom in a three-body recombination event becomes:

$$\frac{\dot{E}_{3\mathrm{b}}}{\dot{N}} = \frac{4}{3} k_{\mathrm{B}} T. \tag{18}$$

This expression shows that unitarity limit is more 'anti-evaporative' than the regime of finite scattering length ($k|a| \leq 1$). As the mean energy per atom in the harmonic trap is $3k_{\rm B}T$, at unitarity each escaped atom leaves behind $(3-4/3)k_{\rm B}T = (5/3)k_{\rm B}T$ of the excess energy as compared to $1k_{\rm B}T$ when L_3 is energy independent. In the latter case, thermal averaging of the relative kinetic energy gives $\langle E_k \rangle = 3k_{\rm B}T$, thus $\dot{E}_{3\rm b}/\dot{N} = 2k_{\rm B}T$.

Eq. (18) is readily transformed into the rate equation for the rise of temperature per lost atom using the fact that $E_{3\rm b} = 3Nk_{\rm B}T$ in the harmonic trap and Eq. (4):

$$\frac{{\rm d}T}{{\rm d}t} = \frac{5}{3}\frac{T}{3}\gamma_3\frac{N^2}{T^5}. \tag{19}$$

Another heating mechanism pointed out in Ref. [18] is associated with the creation of weakly bound dimers whose binding energy is smaller than the depth of the potential. In such a case, the three-body recombination products stay in the trap and the binding energy is converted into heat.

In the unitary limit, this mechanism causes no heating. In fact in this regime, as shown in the supplementary material to Ref. [15], the atoms and dimers are in chemical equilibrium with each other, e.g. the rate of dimer formation is equal to the dissociation rate. We therefore exclude this mechanism from our considerations.

2. *Evaporative cooling*

"Anti-evaporative" heating can be compensated by evaporative cooling. The energy loss per evaporated atom is expressed as:

$$\dot{E} = \dot{N}\left(\eta + \tilde{\kappa}\right)k_{\rm B}T \tag{20}$$

where $\tilde{\kappa}$ in a harmonic trap is [21]:

$$\tilde{\kappa} = 1 - \frac{P\left(5,\eta\right)}{P\left(3,\eta\right)}\frac{V_{\rm e}}{V_{\rm ev}}, \tag{21}$$

with $0 < \tilde{\kappa} < 1$.

In a harmonic trap, the average energy per atom is $3k_{\rm B}T = \frac{E}{N}$. Taking the derivative of this equation and combining it with Eq. (20) we get:

$$3\frac{\dot{T}}{T} = \frac{\dot{N}}{N}\left(\eta + \tilde{\kappa} - 3\right). \tag{22}$$

From Eqs. (10) and (22), evaporative cooling is expressed as:

$$3\frac{{\rm d}T}{{\rm d}t} = -\Gamma_{\rm ev}\left(\eta + \tilde{\kappa} - 3\right)T, \tag{23}$$

This equation can be presented in a similar manner as in the previous section:

$$\frac{{\rm d}T}{{\rm d}t} = -\gamma_2 e^{-\eta}\frac{V_{\rm ev}}{V_{\rm e}}\left(\eta + \tilde{\kappa} - 3\right)\frac{N}{T}\frac{T}{3}, \tag{24}$$

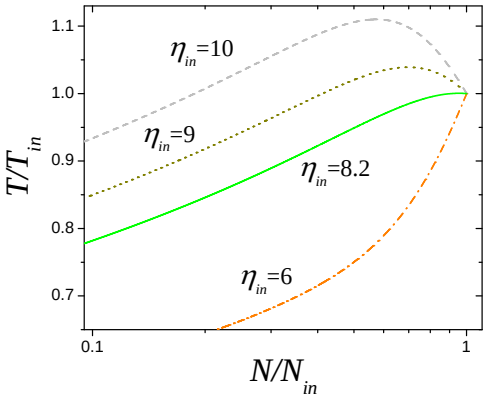

FIG. 1: N-T phase space representation of 'anti-evaporation' heating and evaporative cooling dynamics for different values of the initial $\eta_{\rm in}$ parameter. The "magic" $\eta_{\rm m}$ satisfies the condition ${\rm d}T/{\rm d}N = 0$. For lower values of $\eta_{\rm in}$ the "magic" $\eta_{\rm m}$ is not reached during the evolution of the gas.The figure is drawn for experimental parameters of ^{133}Cs atoms presented in Sec. III. For these conditions $\eta_{\rm m}$ coincides with $\eta_{\rm in} \approx 8$.

where, as before, the temperature dependence remains in η.

Finally, combining the two processes of recombination heating (Eq. (19)) and evaporative cooling (Eq. (24)) we get:

$$\frac{{\rm d}T}{{\rm d}t} = \frac{T}{3}\left(\frac{5}{3}\gamma_3\frac{N^2}{T^5} - \gamma_2 e^{-\eta}\frac{V_{\rm ev}}{V_{\rm e}}\left(\eta + \tilde{\kappa} - 3\right)\frac{N}{T}\right). \tag{25}$$

Eqs. (12) and (25) form a set of coupled rate equations that describe the atom loss dynamics.

C. N-T dynamics and the "magic" $\eta_{\rm m}$

To study atom number and temperature dynamics we solve Eqs. (12) and (25) numerically for different initial values of η, referred to as $\eta_{\rm in}$ from here on. As an illustration, γ_2 and γ_3 are evaluated based on parameters of the ^{133}Cs experiment discussed in Sec. III. The system dynamics in $N-T$ phase space is represented in Fig. 1. All represented values of $\eta_{\rm in}$ lead to a decrease in temperature for small atom numbers indicating that evaporative cooling always wins for asymptotic times where the atom density becomes small. This weakens the three-body recombination event rate and effectively extinguishes the heating mechanism altogether. Large values of the initial $\eta_{\rm in}$ cause initial heating of the system which is followed by a flattening of the temperature dependence at a certain atom number (grey dashed and dark yellow dotted lines) that defines the "magic" $\eta_{\rm m}$. In Fig. 1 the solid

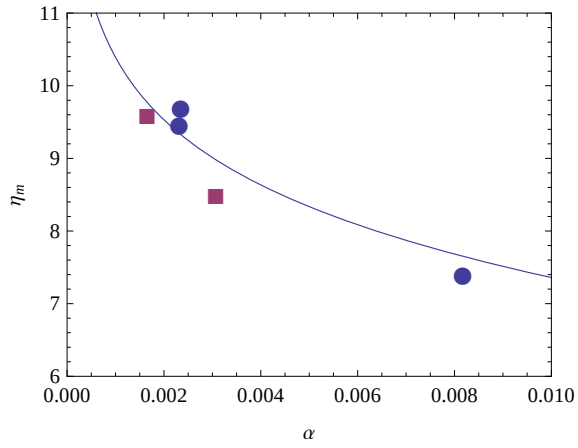

FIG. 2: Universal plot $\eta_{\rm m}$ vs $\alpha = N(\hbar\bar{\omega}/k_BT)^3(1-e^{-4\eta_*})$ (bue curve). The blue solid circles correspond to the results obtained for ^{133}Cs in Fig. 3(a) with $\eta_* = 0.098$. The red solid squares correspond to the ^{7}Li data of Fig. 3(c) with $\eta_* = 0.21$.

green line represents the special case when $\eta_{\rm m} = \eta_{\rm in}$. Experimentally, $\eta(T,N)$ is tuned to satisfy this special case for a given initial temperature and atom number. As it is seen in Fig. 1, lower initial values of $\eta_{\rm in}$ can never reach the necessary condition for $\eta_{\rm m}$ in their subsequent dynamics (orange dotted-dashed line).

The value of $\eta_{\rm m}(T,N)$ is found by solving the equation $\mathrm{d}T/\mathrm{d}N = 0$, i.e. when $T(N)$ becomes independent on the atom number up to the first order in N. From the general structure of this equation, we see that $\eta_{\rm m}$ is solely function of the dimensionless parameter

$$\alpha = N\left(\frac{\hbar\bar{\omega}}{k_BT}\right)^3\left(1-e^{-4\eta_*}\right). \tag{26}$$

Up to a factor $(1-e^{-4\eta_*})$, $\eta_{\rm m}$ depends only on the phase-space density $N(\hbar\bar{\omega}/k_BT)^3$ of the cloud. We plot in Fig. 2 the dependence of $\eta_{\rm m}$ vs α. Since our approach is valid only in the non-quantum degenerate regime where the momentum distribution is a Gaussian, we restricted the plot to small (and experimentally relevant) values of α.

D. 2D evaporation

The above model was developed to explain 3D isothermal evaporation in a harmonic trap and experiments with ^{133}Cs presented below correspond to this situation. Our model can also be extended to 2D isothermal evaporation, as realized in the ^{7}Li gas studied in Ref. [15] and presented below. In this setup, the atoms were trapped in a combined trap consisting of optical confinement in the radial direction and magnetic confinement in the axial direction. Evaporation was performed by lowering the laser beam power which did not lower the axial (essentially infinite) trap depth due to the magnetic confinement. Such a scenario realizes a 2D evaporation scheme. Here, we explore the consequences of having 2D evaporation. In the experimental section we will show the validity of these results with the evolution of a unitary ^{7}Li gas.

Lower dimensional evaporation is, in general, less efficient than its 3D counterpart. 1D evaporation can be nearly totally solved analytically and it has been an intense subject of interest in the context of evaporative cooling of magnetically trapped hydrogen atoms [21, 23, 24]. In contrast, analytically solving the 2D evaporation scheme is infeasible in practice. It also poses a rather difficult questions considering ergodicity of motion in the trap [25]. The only practical way to treat 2D evaporation is Monte Carlo simulations which were performed in Ref. [25] to describe evaporation of an atomic beam. However, as noted in Ref. [25], these simulations follow amazingly well a simple theoretical consideration which leaves the evaporation dynamics as in 3D but introduces an 'effective' η parameter to take into account its 2D character.

The consideration is as following. In the 3D evaporation model, the cutting energy $\epsilon_{\rm c}$ is introduced in the Heaviside function that is multiplied with the classical phase-space distribution of Eq. (6) [21]. For the 2D scheme this Heaviside function is $Y(\epsilon_{\rm c}-\epsilon_\perp)$, where $\epsilon_{\rm c}$ is the 2D truncation energy and $\epsilon_\perp$ is the radial energy of atoms in the trap, the only direction in which atoms can escape. Now we simply add and subtract the axial energy of atoms in the trap and introduce an effective 3D truncation energy as following:

$$Y(\epsilon_{\rm c}-\epsilon_\perp) = Y((\epsilon_{\rm c}+\epsilon_z)-(\epsilon_\perp+\epsilon_z)) = Y(\epsilon_{\rm c}^{\rm eff}-\epsilon_{\rm tot}), \tag{27}$$

where $\epsilon_{\rm tot}$ is the total energy of atoms in the trap and the effective truncation energy is given $\epsilon_{\rm c}^{\rm eff} = \epsilon_{\rm c}+\epsilon_z \simeq \epsilon_{\rm c}+k_{\rm B}T$ where we replaced ϵ_z by its mean value $k_{\rm B}T$ in a harmonic trap. The model then suggests that the evaporation dynamics follows the same functional form as the well established 3D model, but requires a modification of the evaporation parameter (8):

$$\eta^{\rm eff} = \eta + 1, \tag{28}$$

Then, the experimentally provided 2D η should be compared with the theoretically found 3D $\eta^{\rm eff}$ reduced by 1 (i.e. $\eta^{\rm eff}-1$).

III. EXPERIMENTS

In this section, we present experimental $T(N)$ trajectories of unitary ^{133}Cs and ^{7}Li gases, and show that their dynamics are given by the coupled Eqns. (12) and (25). The ^{133}Cs Feshbach resonance at 47.8 Gauss and the ^{7}Li Feshbach resonance at 737.8 Gauss have very similar resonance strength parameter $s_{\rm res} = 0.67$ and 0.80

respectively [26, 27]) and are in the intermediate coupling regime (neither in the broad nor narrow resonance regime). We first confirm the existence of a "magic" $\eta_{\rm m}$ for unitarity-limited losses for both species, with either 3D or 2D evaporation. Then we will use the unitarity-limited three-body loss and the theory presented here to determine the Efimov inelasticity parameter of the narrow 47.8-G resonance in ^{133}Cs which was not measured before.

A. $N-T$ fits

We prepare the initial samples at $T_{\rm in}$ and $N_{\rm in}$ as described in the Supplementary Materials. We measure the atom number $N(t)$ and the temperature $T(t)$ from *in-situ* absorption images taken after a variable hold time t. In Fig. 3(a), we present typical results for the evolution $T(N)$ of the atom number and temperature of the gases, and we furthermore treat the hold time t as a parameter. We also plot the relative temperature $T/T_{\rm in}$ as a function of the relative atom number $N/N_{\rm in}$ for the same data in Fig. 3(b), and for ^{7}Li in Fig. 3(c). We then perform a coupled least-squares fit of the atom number and temperature trajectories, Eqs. (12) and (25), to the data. We note that with our independent knowledge of the geometric mean of the trapping frequencies, $\bar{\omega}$, the only free fit parameters apart from initial temperature and atom number are the trap depth U and the temperature-independent loss constant λ_3. The solid lines are the fits (see Supplementary Materials) to our theory model, which describe the experimental data well for a large variety of initial temperatures, atom numbers and relative trap depth. We are able to experimentally realize the full predicted behavior of rising, falling and constant-to-first-order temperatures.

B. Magic η

The existence of maxima in the $T-N$ plots confirms the existence of a "magic" relative trap depth $\eta_{\rm m}$, where the first-order time derivative of the sample temperature vanishes. Using the knowledge of η_* for both ^{133}Cs and ^{7}Li, we can compare the observed values of $\eta_{\rm m}$ to the prediction of Fig. 2 (note that in the case of ^{7}Li, we plot $\eta_{\rm m}^{\rm eff}$ that enters into the effective 3D evaporation model). We see that for both the 3D evaporation ^{133}Cs data and 2D evaporation ^{7}Li data, the agreement between experiment and theory is remarkable.

Furthermore, in the Supplemental Materials we show that from the three-body loss coefficients and the evaporation model, we can predict the trap depth, which is found in good agreement with the value deduced from the laser power, beam waist, and atom polarizability.

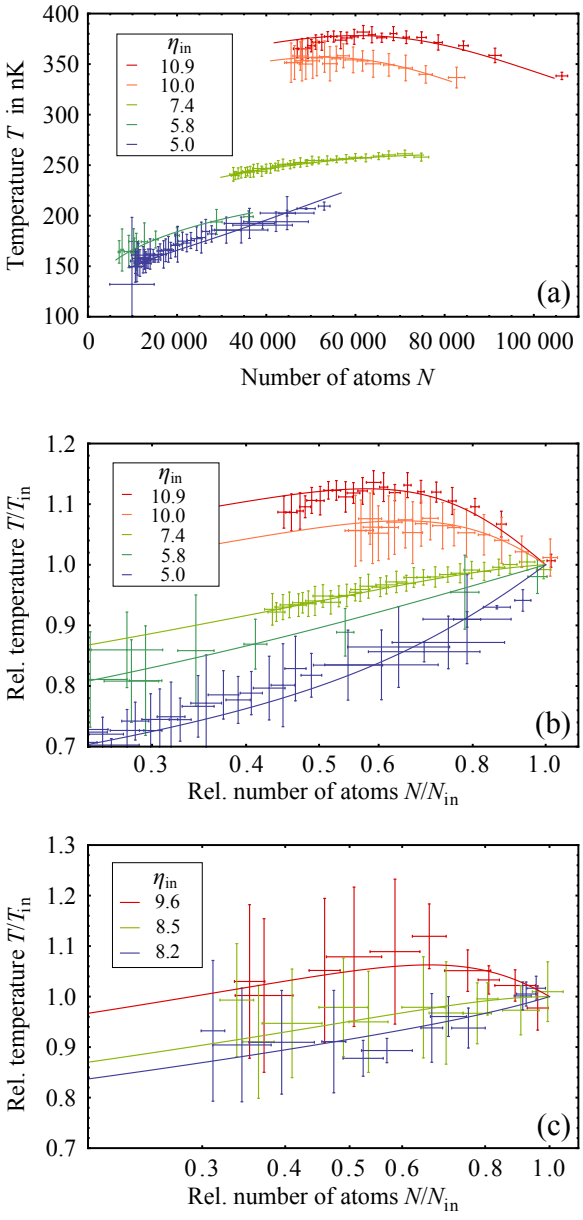

FIG. 3: (Color online) Evolution of the unitary ^{133}Cs gas in (a) absolute and (b) relative numbers. The solid lines are fits of the data using the theory presented here, and the fitted initial relative trap depth $\eta_{\rm in} = U/k_{\rm B}T_{\rm in}$ is given in the legend. Error bars are statistical. The condition for $({\rm d}T/{\rm d}N)|_{t=0}$ is expected for $\eta_{\rm in} \approx \eta_{\rm m} \approx 8.2$, very close to the measured data for $\eta_{\rm in} = 7.4$ (green lines in a) and b)). (c) Evolution of the unitary ^{7}Li gas. The solid lines are fits of the data using our 2D evaporation model, and the fitted initial relative trap depth $\eta_{\rm in} = U/k_{\rm B}T_{\rm in}$ is given in the legend. Error bars are statistical. In 2D evaporation, $\eta_{\rm in} \approx \eta_{\rm m}^{\rm eff} = \eta_{\rm m} + 1 = 8.5$ is required to meet the $({\rm d}T/{\rm d}N)|_{t=0}$ condition, and is found in excellent agreement with the measured value 8.5 (green line in c)), see text.

C. Universality of the three-body loss

As the last application we now show the validity of the $L_3 \propto T^{-2}$ law for the tree-body loss of unitary ^{7}Li and ^{133}Cs Bose gases. Because both species are situated at the extreme ends of the (stable) alkaline group, they have a large mass ratio of $133/7 = 19$ and the temperature range is varied over two orders of magnitude from 0.1 μK to 10 μK. We determine the three-body loss coefficients λ_3 from fits to decay curves such as shown in Fig.3. We present in Fig. 4 the results for the rate coefficient L_3, which varies over approximately two orders of magnitude for both species. In order to emphasize universality, the loss data is plotted as a function of $(m/m_{\rm H})^3 T_{\rm in}^2$, where $m_{\rm H}$ is the hydrogen mass. In this representation, the unitary limit for any species collapses to a single universal line (dotted line in Fig. 4, cf. Eq. (3)).

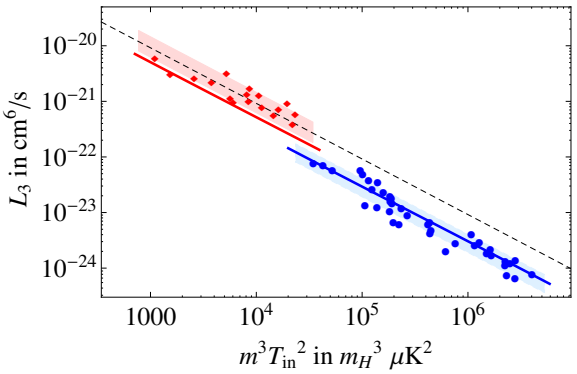

FIG. 4: (Color online) The magnitude of three-body loss rate at unitarity for ^{7}Li (red) and ^{133}Cs (blue) with the respective ±1 standard deviation (shaded areas). On the horizontal axis, masses are scaled to the hydrogen atom mass $m_{\rm H}$. The dashed line represents the unitary limit (Eq. (3) with $\eta_* \to \infty$). Solid lines are predictions of universal theory [15] with $\eta_* = 0.21$ for ^{7}Li and $\eta_* = 0.098(7)$ for ^{133}Cs, see text. The data confirms the universality of the $L_3 \propto T^{-2}$ law.

For ^{7}Li, we cover the 1-10 μK temperature range. We find for the temperature-independent loss coefficient $\lambda_3 = 3.0(3) \times 10^{-20}\,\mathrm{cm^6 \mu K^2 s^{-1}}$, very close to the unitary limit $\lambda_3^{\max} \approx 2.7 \times 10^{-20}\,\mathrm{cm^6 \mu K^2 s^{-1}}$. It is also close to the value $\lambda_3 = 2.5(3) \times 10^{-20}\,\mathrm{cm^6 \mu K^2 s^{-1}}$ found in [15] with a restricted set of data, and to the predicion from Eq. (2) with $\eta_* = 0.21$ from [28] (red solid line in Fig. 4). We cannot measure η_* here because the ^{7}Li data coincides with the unitary limit.

Furthermore the quality of the ^{133}Cs temperature and atom number data enables us to directly measure the previously unknown η_* parameter of the 47.8-G Feshbach resonance. The standard technique for obtaining η_* is measuring the three-body loss rate $L_3(a, T \to 0)$ as a function of scattering length in the zero-temperature limit, and subsequent fitting of the resulting spectrum to universal theory. However, for a given experimental magnetic field stability, this method becomes hard to put into practice for narrow resonances like the 47.8-G resonance in ^{133}Cs. Instead, we use the fits to our theory model in order to obtain η_* from λ_3. We cover the 0.1-1 μK range and find $\lambda_3 = 1.27(7) \times 10^{-24}\,\mathrm{cm^6 \mu K^2 s^{-1}}$. Plugging this number into Eq. (3), we deduce a value for the Efimov inelasticity parameter $\eta_* = 0.098(7)$. The corresponding curve is the blue line in Fig. 4 and is significantly below the unitary line because of the smallness of η_*. This new value is comparable to the Efimov inelasticity parameter found for other resonances in ^{133}Cs, in the range 0.06...0.19 [29, 30].

The plot of the full theoretical expression Eq. (2) for $L_3(m^3T^2)$ in Fig. 4 (full lines) requires an additional parameter describing three-body scattering around this Feshbach resonance, the so-called three-body parameter. It can be represented by the location of the first Efimov resonance position $a_-^{(1)}$ [31]. Because of the lack of experimental knowledge for the 47.8-G resonance, we take the quasi-universal value $a_-^{(1)} = -9.73(3) r_{\rm vdW}$, $r_{\rm vdW}$ being the van-der-Waals radius, for which theoretical explanations have been given recently [31–33]. The theory curve then displays log-periodic oscillations with a temperature period set by the Efimov state energy spacing of $\exp(2\pi/s_0) \approx 515$, where $s_0 = 1.00624$, and with a phase given by $a_-^{(1)}$. The relative peak-to-peak amplitude is 7% for ^{133}Cs. As seen in Fig. 4, such oscillations cannot be resolved in the experimental data because of limited signal-to-noise and the limited range of temperature. The predicted contrast of these oscillations for ^{7}Li is even smaller (∼ 6%). This is a general property of the system of three identical bosons due to the smallness of $|s_{11}|$ [15].

IV. CONCLUSIONS

In this article, we developed a general theoretical model for the coupled time dynamics of atom number and temperature of the 3D harmonically trapped unitary Bose gas in the non-degenerate regime. The theory takes full account of evaporative loss and the related cooling mechanism, as well as of the universal three-body loss and heating. It is furthermore extended to the special case of 2D evaporation. We predict and experimentally verify the existence of a "magic" trap depth, where the time derivative of temperature vanishes both in 3D and 2D evaporation.

We compare our model to two different set of experiments with lithium and cesium with vastly different mass and temperature ranges. The data illustrates the universal T^{-2} scaling over 2 orders of magnitude in temperature, and we obtain an experimental value of the Efimov inelasticity parameter for the 47.8-G resonance in ^{133}Cs. The theory further enables an independent determination of the trap depth. The agreement found here

with standard methods shows that it can be used in more complex trap geometries (crossed dipole traps, or hybrid magnetic-optical traps) where the actual trap depth is often not easy to measure.

In future work it would be highly interesting to probe the discrete symmetry of the unitary Bose gas by revealing the 7% log-periodic modulation of the three-body loss coefficient expected over a factor 515 energy range.

Acknowledgments

We would like to thank the Institut de France (Louis D. award), the region Ile de France DIM nanoK/IFRAF (ATOMIX project), and the European Research Council ERC (ThermoDynaMix grant) for support. We acknowledge support from the NSF-MRSEC program, NSF Grant No. PHY-1206095, and Army Research Office Multidisciplinary University Research Initiative (ARO-MURI) Grant No. W911NF-14-1-0003. L.-C. H. is supported by the Grainger Fellowship and the Taiwan Government Scholarship. We also acknowledge the support from the France-Chicago Center.

[1] Y.-W. Lee and Y.-L. Lee. Quantum phase transition in an atomic bose gas near a feshbach resonance. *Phys. Rev. B*, 70:224506, 2004.

[2] M. W. .J. Romans, R. A. Duine, S. Sashdev, and H. T. C. Stoof. Quantum phase transition in an atomic bose gas with a feshbach resonance. *Phys. Rev. Lett.*, 93:020405, 2004.

[3] L. Radzihovsky, P. B. Weichmann, and J. I. Park. Superfluidity and phase transitions in a resonant bose gas. *Annals of Physics*, 323:2376, 2008.

[4] A. Koetsier, P. Massignan, R. A. Duine, and H. T. C. Stoof. Strongly interacting bose gas: Nosiéres and schmitt-rink theory and beyond. *Phys. Rev. A*, 79:063609, 2009.

[5] F. Cooper, C.-C. Chien, B. Mihaila, J. F. Dawson, and E. Timmermans. Non-perturbative predictions for cold atom bose gases with tunable interactions. *Phys. Rev. Lett.*, 105:240402, 2010.

[6] S. Cowell, H. Heiselberg, I. E. Mazets, J. Morales, V. R. Pandharipande, and C. J. Pethick. Cold bose gases with large scattering length. *Phys. Rev. Lett.*, 88:210403, 2002.

[7] J. L. Song and F. Zhou. Ground state properties of cold bosonic atoms at large scattering lengths. *Phys. Rev. Lett.*, 103:025302, 2009.

[8] Y.-L. Lee and Y.-W. Lee. Universality and stability for a dilute bose gas with a feshbach resonance. *Phys. Rev. A*, 81:063613, 2010.

[9] J. M. Diederix, T. C. F van Heijst, and H. T. C Stoof. Ground state of a resonantly interacting bose gas. *Phys. Rev. A*, 84:033618, 2011.

[10] Weiran Li and Tin-Lun Ho. Bose gases near unitarity. *Phys. Rev. Lett.*, 108:195301, May 2012.

[11] Swann Piatecki and Werner Krauth. Efimov-driven phase transitions of the unitary bose gas. *Nat. Commun.*, 5:3503, 2014.

[12] S.B. Papp, J. M. Pino, R. J. Wild, S. Ronen, C.E. Wiemann, D. S. Jin, and E. A. Cornell. Bragg spectroscopy of a strongly interacting ^{85}rb bose-einstein condensate. *Phys. Rev. Lett.*, 101:135301, 2008.

[13] N. Navon, S. Piatecki, K. Günter, B. Rem, T. C. Nguyen, F. Chevy, W. Krauth, and C. Salomon. Dynamics and thermodynamics of the low-temperature strongly interacting bose gas. *Phys. Rev. Lett.*, 107:135301, 2011.

[14] Li-Chung Ha, Chen-Lung Hung, Xibo Zhang, Ulrich Eismann, Shih-Kuang Tung, and Cheng Chin. Strongly interacting two-dimensional bose gases. *Phys. Rev. Lett.*, 110:145302, Apr 2013.

[15] B. Rem, A. T. Grier, I. Ferrier-Barbut, U. Eismann, T. Langen, N. Navon, L. Khaykovich, F. Werner, D. S. Petrov, F. Chevy, and C. Salomon. Lifetime of the bose gas with resonant interactions. *Phys. Rev. Lett.*, 110:163202, 2013.

[16] R. J. Fletcher, A. L. Gaunt, N. Navon, R. P. Smith, and Z. Hadzibabic. Stability of a unitary bose gas. *Phys. Rev. Lett.*, 111:125303, 2013.

[17] P. Makotyn, C. E. Klauss, D. L. Goldberg, E. A. Cornell, and D. S. Jin. Universal dynamics of a degenerate unitary bose gas. *Nat. Physics*, 10:116, 2014.

[18] T. Weber, J. Herbig, M. Mark, H.-C. Nägerl, and R. Grimm. Three-body recombination at large scattering lengths in an ultracold atomic gas. *Phys. Rev. Lett.*, 91:123201, 2003.

[19] V. Efimov. Energy levels arising from resonant two-body forces in a three-body system. *Physics Letters B*, 33(8):563–564, 1970.

[20] S.-K. Tung, K. Jiménez-García, J. Johansen, C. V. Parker, and C. Chin. *Phys. Rev. Lett.*, 113:240402, 2014.

[21] O. J. Luiten, M. W. Reynolds, and J. T. M. Walraven. Kinetic theory of the evaporative cooling of a trapped gas. *Phys. Rev. A*, 53:381, 1996.

[22] L. Luo, B. Clancy, J. Joseph, J. Kinast, A. Turlapov, and J. E. Thomas. *New J. Phys.*, 8:213, 2006.

[23] E. L. Surkov, J. T. M. Walraven, and G. V. Shlyapnikov. Collisionless motion and evaporative cooling of atoms in magnetic traps. *Phys. Rev. A*, 53:3403, 1996.

[24] P. W. H. Pinkse, A. Mosk, M. Weidemüller, M. W. Reynolds, T. W. Hijmans, and J. T. M. Walraven. One-dimensional evaporative cooling of magnetically trapped atomic hydrogen. *Phys. Rev. A*, 57:4747, 1998.

[25] E. Mandonnet, A. Minguzzi, R. Dum, I. Carusotto, Y. Castin, and J. Dalibard. Evaporative cooling of an atomic beam. *Eur. Phys. J D*, 10:9, 2000.

[26] A. D. Lange, K. Pilch, A. Prantner, F. Ferlaino, B. Engeser, H.-C. Nägerl, R. Grimm, and C. Chin. Determination of atomic scattering lengths from measurements of molecular binding energies near feshbach resonances. *Phys. Rev. A*, 79:013622, Jan 2009.

[27] C. Chin, R. Grimm, P. Julienne, and E. Tiesinga. *Rev. Mod. Phys.*, 82:1225, 2010.

[28] N. Gross, Z. Shotan, S.J.J.M.F. Kokkelmans, and L. Khaykovich. *Phys. Rev. Lett.*, 105:103203, 2010.
[29] T. Kraemer, M. Mark, P. Waldburger, J.G. Danzl, C. Chin, B. Engeser, A.D. Lange, K. Pilch, A. Jaakkola, H.-C. Nägerl, and R. Grimm. *Nature*, 440:315–318, 2006.
[30] M. Berninger, A. Zenesini, B. Huang, W. Harm, H.-C. Nägerl, F. Ferlaino, R. Grimm, P.S. Julienne, and J.M. Hutson. *Phys. Rev. Lett.*, 107:120401, 2011.
[31] Cheng Chin. Universal scaling of efimov resonance positions in cold atom systems. *arXiv preprint arXiv:1111.1484*, 2011.
[32] Jia Wang, J. P. D'Incao, B. D. Esry, and Chris H. Greene. Origin of the three-body parameter universality in efimov physics. *Phys. Rev. Lett.*, 108:263001, Jun 2012.
[33] Pascal Naidon, Shimpei Endo, and Masahito Ueda. Microscopic origin and universality classes of the efimov three-body parameter. *Phys. Rev. Lett.*, 112:105301, Mar 2014.
[34] Chen-Lung Hung, Xibo Zhang, Nathan Gemelke, and Cheng Chin. Accelerating evaporative cooling of atoms into Bose-Einstein condensation in optical traps. *Phys Rev A*, 78(1):011604, July 2008.
[35] Chen-Lung Hung. private communication. 2013.
[36] Chen-Lung Hung, Xibo Zhang, Li-Chung Ha, Shih-Kuang Tung, Nathan Gemelke, and Cheng Chin. Extracting density–density correlations from in situ images of atomic quantum gases. *New Journal of Physics*, 13(7):075019, 2011.

Bibliography

[Abad *et al.*, 2015] M. Abad, A. Recati, S. Stringari and F. Chevy. "Counter-flow instability of a quantum mixture of two superfluids". *The European Physical Journal D*, **vol. 69**, no. 5, 126 (2015) (cited pages 7, 54)

[Abo-Shaeer *et al.*, 2001] J. R. Abo-Shaeer, C. Raman, J. M. Vogels and W. Ketterle. "Observation of Vortex Lattices in Bose-Einstein Condensates". *Science*, **vol. 292**, no. 5516, pp. 476–479 (2001) (cited pages 2, 13, 21)

[Aidelsburger *et al.*, 2011] M. Aidelsburger, M. Atala, S. Nascimbène, S. Trotzky, Y.-A. Chen and I. Bloch. "Experimental Realization of Strong Effective Magnetic Fields in an Optical Lattice". *Phys. Rev. Lett.*, **vol. 107**, p. 255301 (2011) (cited page 3)

[Aidelsburger *et al.*, 2013] M. Aidelsburger, M. Atala, M. Lohse, J. T. Barreiro, B. Paredes and I. Bloch. "Realization of the Hofstadter Hamiltonian with Ultracold Atoms in Optical Lattices". *Phys. Rev. Lett.*, **vol. 111**, p. 185301 (2013) (cited page 3)

[Allen and Jones, 1938] J. F. Allen and H. Jones. "New Phenomena Connected with Heat Flow in Helium II". *Nature*, **vol. 141**, pp. 243–244 (1938) (cited page 54)

[Allen and Misener, 1938] J. F. Allen and A. D. Misener. "Flow of Liquid Helium II". *Nature*, **vol. 141**, pp. 75–75 (1938) (cited pages 1, 11, 53)

[Altmeyer *et al.*, 2007] A. Altmeyer, S. Riedl, C. Kohstall, M. Wright, R. Geursen, M. Bartenstein, C. Chin, J. Hecker-Denschlag and R. Grimm. "Precision Measurements of Collective Oscillations in the BEC-BCS Crossover". *Phys. Rev. Lett.*, **vol. 98**, no. 4, 040401 (2007) (cited page 88)

[Amo *et al.*, 2009] A. Amo, J. Lefrère, S. Pigeon, C. Adrados, C. Ciuti, I. Carusotto, R. Houdré, E. Giacobino and A. Bramati. "Superfluidity of polaritons in semiconductor microcavities". *Nature Physics*, **vol. 5**, no. 11, pp. 805–810 (2009) (cited page 2)

[Amoruso *et al.*, 1998] M. Amoruso, A. Minguzzi, S. Stringari, M. Tosi and L. Vichi. "Temperature-dependent density profiles of trapped boson-fermion mixtures". *The European Physical Journal D-Atomic, Molecular, Optical and Plasma Physics*, **vol. 4**, no. 3, pp. 261–265 (1998) (cited page 98)

[Amoruso *et al.*, 1999] M. Amoruso, I. Meccoli, A. Minguzzi and M. Tosi. "Collective excitations of a degenerate Fermi vapour in a magnetic trap". *The European Physical Journal D-Atomic, Molecular, Optical and Plasma Physics*, **vol. 7**, no. 3, pp. 441–447 (1999) (cited page 88)

[Anderson *et al.*, 1995] M. H. Anderson, J. R. Ensher, M. R. Matthews, C. E. Wieman and E. A. Cornell. "Observation of Bose-Einstein Condensation in a Dilute Atomic Vapor". *Science*, **vol. 269**, no. 5221, pp. 198–201 (1995) (cited pages 2, 12, 39, 40, 54)

[Andrews *et al.*, 1997a] M. R. Andrews, D. M. Kurn, H.-J. Miesner, D. S. Durfee, C. G. Townsend, S. Inouye and W. Ketterle. "Propagation of Sound in a Bose-Einstein Condensate". *Phys. Rev. Lett.*, **vol. 79**, pp. 553–556 (1997) (cited pages 13, 82)

[Andrews *et al.*, 1997b] M. R. Andrews, C. G. Townsend, H.-J. Miesner, D. S. Durfee, D. M. Kurn and W. Ketterle. "Observation of Interference Between Two Bose Condensates". *Science*, **vol. 275**, no. 5300, pp. 637–641 (1997) (cited pages 13, 54)

[Armijo *et al.*, 2011] J. Armijo, T. Jacqmin, K. Kheruntsyan and I. Bouchoule. "Mapping out the quasicondensate transition through the dimensional crossover from one to three dimensions". *Phys. Rev. A*, **vol. 83**, p. 021605 (2011) (cited page 4)

[Aspect *et al.*, 1988] A. Aspect, E. Arimondo, R. Kaiser, N. Vansteenkiste and C. Cohen-Tannoudji. "Laser Cooling below the One-Photon Recoil Energy by Velocity-Selective Coherent Population Trapping". *Phys. Rev. Lett.*, **vol. 61**, pp. 826–829 (1988) (cited page 134)

[Aspuru-Guzik and Walther, 2012] A. Aspuru-Guzik and P. Walther. "Photonic quantum simulators". *Nature Physics*, **vol. 8**, no. 4, pp. 285–291 (2012) (cited page 1)

[Astrakharchik, 2014] G. Astrakharchik. *Quantum Monte Carlo study of ultracold gases*. Ph.D. thesis, University of Trento (2014) (cited page 72)

[Astrakharchik *et al.*, 2004] G. E. Astrakharchik, J. Boronat, J. Casulleras and S. Giorgini. "Equation of State of a Fermi Gas in the BEC-BCS Crossover: A Quantum Monte Carlo Study". *Phys. Rev. Lett.*, **vol. 93**, p. 200404 (2004) (cited page 61)

[Astrakharchik *et al.*, 2005] G. E. Astrakharchik, R. Combescot, X. Leyronas and S. Stringari. "Equation of State and Collective Frequencies of a Trapped Fermi Gas Along the BEC-Unitarity Crossover". *Phys. Rev. Lett.*, **vol. 95**, p. 030404 (2005) (cited page 88)

[Bakr *et al.*, 2009] W. S. Bakr, J. I. Gillen, A. Peng, S. Folling and M. Greiner. "A quantum gas microscope for detecting single atoms in a Hubbard-regime optical lattice". *Nature*, **vol. 462**, no. 7269, pp. 74–77 (2009) (cited page 2)

[Balili *et al.*, 2007] R. Balili, V. Hartwell, D. Snoke, L. Pfeiffer and K. West. "Bose-Einstein Condensation of Microcavity Polaritons in a Trap". *Science*, **vol. 316**, no. 5827, pp. 1007–1010 (2007) (cited page 2)

[Banerjee, 2007] A. Banerjee. "Collective oscillations of a Bose-Fermi mixture: Effect of unequal masses of Bose and Fermi particles". *Phys. Rev. A*, **vol. 76**, p. 023611 (2007) (cited page 61)

[Bardeen *et al.*, 1957] J. Bardeen, L. Cooper and J. Schrieffer. "Theory of superconductivity". *Phys. Rev.*, **vol. 108**, pp. 1175–1204 (1957) (cited page 1)

[Bartenstein *et al.*, 2004a] M. Bartenstein, A. Altmeyer, S. Riedl, S. Jochim, C. Chin, J. H. Denschlag and R. Grimm. "Collective Excitations of a Degenerate Gas at the BEC-BCS Crossover". *Phys. Rev. Lett.*, **vol. 92**, p. 203201 (2004) (cited page 88)

[Bartenstein *et al.*, 2004b] M. Bartenstein, A. Altmeyer, S. Riedl, S. Jochim, C. Chin, J. Hecker Denschlag and R. Grimm. "Crossover from a Molecular Bose-Einstein Condensate to a Degenerate Fermi Gas". *Phys. Rev. Lett.*, **vol. 92**, no. 12, p. 120401 (2004) (cited page 88)

[Baur *et al.*, 2009] S. K. Baur, S. Basu, T. N. De Silva and E. J. Mueller. "Theory of the normal-superfluid interface in population-imbalanced Fermi gases". *Phys. Rev. A*, **vol. 79**, p. 063628 (2009) (cited page 95)

[Bausmerth *et al.*, 2009] I. Bausmerth, A. Recati and S. Stringari. "Chandrasekhar-Clogston limit and phase separation in Fermi mixtures at unitarity". *Phys. Rev. A*, **vol. 79**, p. 043622 (2009) (cited page 4)

[Beattie *et al.*, 2013] S. Beattie, S. Moulder, R. J. Fletcher and Z. Hadzibabic. "Persistent Currents in Spinor Condensates". *Phys. Rev. Lett.*, **vol. 110**, p. 025301 (2013) (cited page 151)

[Ben Dahan *et al.*, 1996] M. Ben Dahan, E. Peik, J. Reichel, Y. Castin and C. Salomon. "Bloch Oscillations of Atoms in an Optical Potential". *Phys. Rev. Lett.*, **vol. 76**, pp. 4508–4511 (1996) (cited page 3)

[Berninger *et al.*, 2011] M. Berninger, A. Zenesini, B. Huang, W. Harm, H.-C. Nägerl, F. Ferlaino, R. Grimm, P. S. Julienne and J. M. Hutson. "Universality of the Three-Body Parameter for Efimov States in Ultracold Cesium". *Phys. Rev. Lett.*, **vol. 107**, p. 120401 (2011) (cited page 19)

[Bianchi *et al.*, 2003] A. Bianchi, R. Movshovich, C. Capan, P. G. Pagliuso and J. L. Sarrao. "Possible Fulde-Ferrell-Larkin-Ovchinnikov Superconducting State in $CeCoIn_5$". *Phys. Rev. Lett.*, **vol. 91**, p. 187004 (2003) (cited page 5)

[Billy *et al.*, 2008] J. Billy, V. Josse, Z. Zuo, A. Bernard, B. Hambrecht, P. Lugan, D. Clement, L. Sanchez-Palencia, P. Bouyer and A. Aspect. "Direct observation of Anderson localization of matter waves in a controlled disorder". *Nature*, **vol. 453**, no. 7197, pp. 891–894 (2008) (cited page 3)

[Blatt and Roos, 2012] R. Blatt and C. F. Roos. "Quantum simulations with trapped ions". *Nature Physics*, **vol. 8**, no. 4, pp. 277–284 (2012) (cited page 1)

[Bloch *et al.*, 2000] I. Bloch, T. W. Hansch and T. Esslinger. "Measurement of the spatial coherence of a trapped Bose gas at the phase transition". *Nature*, **vol. 403**, no. 6766, p. 166 (2000) (cited pages 2, 13, 54)

[Bloch *et al.*, 2008] I. Bloch, J. Dalibard and W. Zwerger. "Many-body physics with ultracold gases". *Rev. Mod. Phys.*, **vol. 80**, pp. 885–964 (2008) (cited pages 1, 3)

[Bloch *et al.*, 2012] I. Bloch, J. Dalibard and S. Nascimbène. "Quantum Simulations with ultracold quantum gases". *Nature Physics*, **vol. 8**, no. 4, pp. 267–276 (2012) (cited pages 1, 22)

[Boada *et al.*, 2012] O. Boada, A. Celi, J. I. Latorre and M. Lewenstein. "Quantum Simulation of an Extra Dimension". *Phys. Rev. Lett.*, **vol. 108**, p. 133001 (2012) (cited page 4)

[Boettcher *et al.*, 2016] I. Boettcher, L. Bayha, D. Kedar, P. A. Murthy, M. Neidig, M. G. Ries, A. N. Wenz, G. Zürn, S. Jochim and T. Enss. "Equation of State of Ultracold Fermions in the 2D BEC-BCS Crossover Region". *Phys. Rev. Lett.*, **vol. 116**, p. 045303 (2016) (cited page 4)

[Bogoliubov, 1947] N. Bogoliubov. "On the Theory of Superfluidity". *Journal of Physics (USSR)*, **vol. 11**, no. 1, pp. 23–32 (1947) (cited page 21)

[Boiron *et al.*, 1995] D. Boiron, C. Triché, D. R. Meacher, P. Verkerk and G. Grynberg. "Three-dimensional cooling of cesium atoms in four-beam gray optical molasses". *Phys. Rev. A*, **vol. 52**, pp. R3425–R3428 (1995) (cited page 134)

[Boiron *et al.*, 1998] D. Boiron, A. Michaud, J. M. Fournier, L. Simard, M. Sprenger, G. Grynberg and C. Salomon. "Cold and dense cesium clouds in far-detuned dipole traps". *Phys. Rev. A*, **vol. 57**, pp. R4106–R4109 (1998) (cited page 134)

[Bourdel *et al.*, 2004] T. Bourdel, L. Khaykovich, J. Cubizolles, J. Zhang, F. Chevy, M. Teichmann, L. Tarruell, S. J. J. M. F. Kokkelmans and C. Salomon. "Experimental Study of the BEC-BCS Crossover Region in Lithium 6". *Phys. Rev. Lett.*, **vol. 93**, p. 050401 (2004) (cited page 92)

[Bradley *et al.*, 1997] C. C. Bradley, C. A. Sackett and R. G. Hulet. "Bose-Einstein Condensation of Lithium: Observation of Limited Condensate Number". *Phys. Rev. Lett.*, **vol. 78**, pp. 985–989 (1997) (cited pages 19, 21)

[Brantut *et al.*, 2012] J.-P. Brantut, J. Meineke, D. Stadler, S. Krinner and T. Esslinger. "Conduction of Ultracold Fermions Through a Mesoscopic Channel". *Science*, **vol. 337**, no. 6098, pp. 1069–1071 (2012) (cited page 3)

[Brantut *et al.*, 2013] J.-P. Brantut, C. Grenier, J. Meineke, D. Stadler, S. Krinner, C. Kollath, T. Esslinger and A. Georges. "A Thermoelectric Heat Engine with Ultracold Atoms". *Science*, **vol. 342**, no. 6159, pp. 713–715 (2013) (cited page 13)

[Breit and Rabi, 1931] G. Breit and I. I. Rabi. "Measurement of Nuclear Spin". *Phys. Rev.*, **vol. 38**, pp. 2082–2083 (1931) (cited page 28)

[Brey *et al.*, 1989] L. Brey, N. F. Johnson and B. I. Halperin. "Optical and magneto-optical absorption in parabolic quantum wells". *Phys. Rev. B*, **vol. 40**, pp. 10647–10649 (1989) (cited page 58)

[Bulgac and Forbes, 2007] A. Bulgac and M. M. Forbes. "Zero-temperature thermodynamics of asymmetric Fermi gases at unitarity". *Phys. Rev. A*, **vol. 75**, p. 031605 (2007) (cited pages 4, 114)

[Bulgac and Forbes, 2008] A. Bulgac and M. Forbes. "Unitary Fermi Supersolid: The Larkin-Ovchinnikov Phase". *Physical Review Letters*, **vol. 101**, p. 215301 (2008) (cited pages 5, 108)

[Burchianti *et al.*, 2014] A. Burchianti, G. Valtolina, J. A. Seman, E. Pace, M. De Pas, M. Inguscio, M. Zaccanti and G. Roati. "Efficient all-optical production of large ^{6}Li quantum gases using D_1 gray-molasses cooling". *Phys. Rev. A*, **vol. 90**, p. 043408 (2014) (cited page 135)

[Caldeira and Leggett, 1983] A. O. Caldeira and A. J. Leggett. "Path integral approach to quantum Brownian motion". *Physica A: Statistical Mechanics and its Applications*, **vol. 121**, no. 3, pp. 587 – 616 (1983) (cited page 82)

[Capuzzi *et al.*, 2006] P. Capuzzi, P. Vignolo, F. Federici and M. P. Tosi. "Sound propagation in elongated superfluid fermionic clouds". *Phys. Rev. A*, **vol. 73**, p. 021603 (2006) (cited pages 72, 73)

[Carlson *et al.*, 2003] J. Carlson, S.-Y. Chang, V. R. Pandharipande and K. E. Schmidt. "Superfluid Fermi Gases with Large Scattering Length". *Phys. Rev. Lett.*, **vol. 91**, p. 050401 (2003) (cited page 61)

[Castin and Dum, 1996] Y. Castin and R. Dum. "Bose-Einstein Condensates in Time Dependent Traps". *Phys. Rev. Lett.*, **vol. 77**, pp. 5315–5319 (1996) (cited page 111)

[Castin *et al.*, 2015] Y. Castin, I. Ferrier-Barbut and C. Salomon. "La vitesse critique de Landau d'une particule dans un superfluide de fermions". *Comptes Rendus Physique*, **vol. 16**, no. 2, pp. 241–253 (2015) (cited pages 7, 54, 55, 68, 73, 151)

[Casula *et al.*, 2008] M. Casula, D. M. Ceperley and E. J. Mueller. "Quantum Monte Carlo study of one-dimensional trapped fermions with attractive contact interactions". *Phys. Rev. A*, **vol. 78**, p. 033607 (2008) (cited page 5)

[Celi *et al.*, 2014] A. Celi, P. Massignan, J. Ruseckas, N. Goldman, I. B. Spielman, G. Juzeliūnas and M. Lewenstein. "Synthetic Gauge Fields in Synthetic Dimensions". *Phys. Rev. Lett.*, **vol. 112**, p. 043001 (2014) (cited page 4)

[Chandrasekhar, 1962] B. Chandrasekhar. "A note on the maximum critical field of high-field superconductors". *App. Phys. Lett.*, **vol. 1**, no. 1, pp. 7–8 (1962) (cited pages 4, 92)

[Cheng and Yip, 2007] C.-H. Cheng and S.-K. Yip. "Trapped resonant fermions above the superfluid transition temperature". *Phys. Rev. B*, **vol. 75**, p. 014526 (2007) (cited page 115)

[Cheuk *et al.*, 2012] L. W. Cheuk, A. T. Sommer, Z. Hadzibabic, T. Yefsah, W. S. Bakr and M. W. Zwierlein. "Spin-Injection Spectroscopy of a Spin-Orbit Coupled Fermi Gas". *Phys. Rev. Lett.*, **vol. 109**, p. 095302 (2012) (cited page 3)

[Chevy, 2006] F. Chevy. "Universal phase diagram of a strongly interacting Fermi gas with unbalanced spin populations". *Phys. Rev. A*, **vol. 74**, p. 063628 (2006) (cited pages 4, 94, 99)

[Chevy, 2015] F. Chevy. "Counterflow in a doubly superfluid mixture of bosons and fermions". *Phys. Rev. A*, **vol. 91**, p. 063606 (2015) (cited pages 7, 54)

[Chikkatur *et al.*, 2000] A. P. Chikkatur, A. Görlitz, D. M. Stamper-Kurn, S. Inouye, S. Gupta and W. Ketterle. "Suppression and Enhancement of Impurity Scattering in a Bose-Einstein Condensate". *Phys. Rev. Lett.*, **vol. 85**, pp. 483–486 (2000) (cited page 54)

[Chin *et al.*, 2010] C. Chin, R. Grimm, P. Julienne and E. Tiesinga. "Feshbach resonances in ultracold gases". *Rev. Mod. Phys.*, **vol. 82**, pp. 1225–1286 (2010) (cited page 33)

[Chomaz *et al.*, 2014] L. Chomaz, L. Corman, T. Bienaimé, R. Desbuquois, C. Weitenberg, S. Nascimbène, J. Beugnon and J. Dalibard. "Emergence of coherence via transverse condensation in a uniform quasi-two-dimensional Bose gas". *Nature Communications*, **vol. 6**, no. 6162 (2014) (cited page 6)

[Chou *et al.*, 2008] C.-H. Chou, T. Yu and B. L. Hu. "Exact master equation and quantum decoherence of two coupled harmonic oscillators in a general environment". *Phys. Rev. E*, **vol. 77**, p. 011112 (2008) (cited page 82)

[Chu, 1991] S. Chu. "Laser Manipulation of Atoms and Particles". *Science*, **vol. 253**, no. 5022, pp. 861–866 (1991) (cited page 134)

[Chu *et al.*, 1985] S. Chu, L. Hollberg, J. E. Bjorkholm, A. Cable and A. Ashkin. "Three-dimensional viscous confinement and cooling of atoms by resonance radiation pressure". *Phys. Rev. Lett.*, **vol. 55**, pp. 48–51 (1985) (cited page 133)

[Chu *et al.*, 1986] S. Chu, J. E. Bjorkholm, A. Ashkin and A. Cable. "Experimental Observation of Optically Trapped Atoms". *Phys. Rev. Lett.*, **vol. 57**, pp. 314–317 (1986) (cited page 133)

[Clogston, 1962] A. M. Clogston. "Upper Limit for the Critical Field in Hard Superconductors". *Phys. Rev. Lett.*, **vol. 9**, pp. 266–267 (1962) (cited pages 4, 92)

[Combescot and Giraud, 2008] R. Combescot and S. Giraud. "Normal state of highly polarized Fermi gases: full many-body treatment." *Physical Review Letters*, **vol. 101**, p. 050404 (2008) (cited page 94)

[Combescot *et al.*, 2006] R. Combescot, M. Y. Kagan and S. Stringari. "Collective mode of homogeneous superfluid Fermi gases in the BEC-BCS crossover". *Physical Review A*, **vol. 74**, p. 042717 (2006) (cited pages 69, 88)

[Corman *et al.*, 2014] L. Corman, L. Chomaz, T. Bienaimé, R. Desbuquois, C. Weitenberg, S. Nascimbène, J. Dalibard and J. Beugnon. "Quench-Induced Supercurrents in an Annular Bose Gas". *Phys. Rev. Lett.*, **vol. 113**, p. 135302 (2014) (cited pages 5, 7, 95, 136)

[Dalibard and Cohen-Tannoudji, 1989] J. Dalibard and C. Cohen-Tannoudji. "Laser cooling below the Doppler limit by polarization gradients: simple theoretical models". *J. Opt. Soc. Am. B*, **vol. 6**, no. 11, pp. 2023–2045 (1989) (cited page 133)

[Dalibard, 1999] J. Dalibard. "Collisional dynamics of ultra-cold atomic gases". In M Inguscio, S Stringari and C Wieman, editors, "Proceedings of the International School of Physics "Enrico Fermi", 1998, Bose-Einstein Condensation in Atomic Gases", Course CXL, pp. 321–349. Società Italiana di Fisica, IOS Press (1999) (cited page 30)

[Dalibard *et al.*, 2011] J. Dalibard, F. Gerbier, G. Juzeliūnas and P. Öhberg. "*Colloquium* : Artificial gauge potentials for neutral atoms". *Rev. Mod. Phys.*, **vol. 83**, pp. 1523–1543 (2011) (cited page 3)

[Davis *et al.*, 1995a] K. B. Davis, M. O. Mewes, M. R. Andrews, N. J. van Druten, D. S. Durfee, D. M. Kurn and W. Ketterle. "Bose-Einstein Condensation in a Gas of Sodium Atoms". *Phys. Rev. Lett.*, **vol. 75**, pp. 3969–3973 (1995) (cited pages 2, 12, 39, 40, 54)

[Davis *et al.*, 1995b] K. B. Davis, M.-O. Mewes, M. A. Joffe, M. R. Andrews and W. Ketterle. "Evaporative Cooling of Sodium Atoms". *Phys. Rev. Lett.*, **vol. 74**, pp. 5202–5205 (1995) (cited page 40)

[De Silva and Mueller, 2006a] T. N. De Silva and E. J. Mueller. "Profiles of near-resonant population-imbalanced trapped Fermi gases". *Phys. Rev. A*, **vol. 73**, p. 051602 (2006) (cited page 115)

[De Silva and Mueller, 2006b] T. N. De Silva and E. J. Mueller. "Surface Tension in Unitary Fermi Gases with Population Imbalance". *Phys. Rev. Lett.*, **vol. 97**, p. 070402 (2006) (cited page 95)

[Deh *et al.*, 2008] B. Deh, C. Marzok, C. Zimmermann and P. W. Courteille. "Feshbach resonances in mixtures of ultracold ^{6}Li and ^{87}Rb gases". *Phys. Rev. A*, **vol. 77**, p. 010701 (2008) (cited page 6)

[Deh *et al.*, 2010] B. Deh, W. Gunton, B. G. Klappauf, Z. Li, M. Semczuk, J. Van Dongen and K. W. Madison. "Giant Feshbach resonances in ^{6}Li-^{85}Rb mixtures". *Phys. Rev. A*, **vol. 82**, p. 020701 (2010) (cited page 6)

[Delehaye *et al.*, 2015] M. Delehaye, S. Laurent, I. Ferrier-Barbut, S. Jin, F. Chevy and C. Salomon. "Critical Velocity and Dissipation of an Ultracold Bose-Fermi Counterflow". *Phys. Rev. Lett.*, **vol. 115**, p. 265303 (2015) (cited pages 2, 7, 23)

[DeMarco and Jin, 1999] B. DeMarco and D. S. Jin. "Onset of Fermi Degeneracy in a Trapped Atomic Gas". *Science*, **vol. 285**, no. 5434, pp. 1703–1706 (1999) (cited pages 2, 22, 54)

[Demokritov *et al.*, 2006] S. Demokritov, V. Demidov, O. Dzyapko, G. Melkov, A. Serga, B. Hillebrands and A. Slavin. "Bose–Einstein condensation of quasi-equilibrium magnons at room temperature under pumping". *Nature*, **vol. 443**, no. 7110, pp. 430–433 (2006) (cited page 2)

[Desbuquois, 2013] R. Desbuquois. *Thermal and superfluid properties of the two–dimensional Bose gas*. Ph.D. thesis, Université Paris IV (2013) (cited page 85)

[Desbuquois *et al.*, 2012] R. Desbuquois, L. Chomaz, T. Yefsah, J. Léonard, J. Beugnon, C. Weitenberg and J. Dalibard. "Superfluid behaviour of a two-dimensional Bose gas". *Nature Physics*, **vol. 8**, no. 9, pp. 645–648 (2012) (cited page 54)

[Dieckmann *et al.*, 1998] K. Dieckmann, R. J. C. Spreeuw, M. Weidemüller and J. T. M. Walraven. "Two-dimensional magneto-optical trap as a source of slow atoms". *Phys. Rev. A*, **vol. 58**, pp. 3891–3895 (1998) (cited page 33)

[Dobson, 1994] J. F. Dobson. "Harmonic-Potential Theorem: Implications for Approximate Many-Body Theories". *Phys. Rev. Lett.*, **vol. 73**, pp. 2244–2247 (1994) (cited page 58)

[Donley *et al.*, 2001] E. A. Donley, N. R. Claussen, S. L. Cornish, J. L. Roberts, E. A. Cornell and C. E. Wieman. "Dynamics of collapsing and exploding Bose-Einstein condensates". *Nature*, **vol. 412**, no. 6844, pp. 295–299 (2001) (cited pages 19, 21)

[Duarte *et al.*, 2011] P. M. Duarte, R. A. Hart, J. M. Hitchcock, T. A. Corcovilos, T.-L. Yang, A. Reed and R. G. Hulet. "All-optical production of a lithium quantum gas using narrow-line laser cooling". *Phys. Rev. A*, **vol. 84**, p. 061406 (2011) (cited pages 28, 135)

[Dubessy *et al.*, 2014] R. Dubessy, C. D. Rossi, T. Badr, L. Longchambon and H. Perrin. "Imaging the collective excitations of an ultracold gas using statistical correlations". *New Journal of Physics*, **vol. 16**, no. 12, p. 122001 (2014) (cited page 83)

[Edge and Cooper, 2009] J. M. Edge and N. R. Cooper. "Signature of the Fulde-Ferrell-Larkin-Ovchinnikov Phase in the Collective Modes of a Trapped Ultracold Fermi Gas". *Phys. Rev. Lett.*, **vol. 103**, p. 065301 (2009) (cited page 5)

[Efimov, 1970] V. Efimov. "Energy levels arising from resonant two-body forces in a three-body system". *Physics Letters B*, **vol. 33**, no. 8, pp. 563–564 (1970) (cited page 19)

[Eismann *et al.*, 2012] U. Eismann, F. Gerbier, C. Canalias, A. Zukauskas, G. Trénec, J. Vigué, F. Chevy and C. Salomon. "An all-solid-state laser source at 671 nm for cold-atom experiments with lithium". *Applied Physics B*, **vol. 106**, no. 1, pp. 25–36 (2012) (cited page 140)

[Eismann *et al.*, 2013] U. Eismann, A. Bergschneider, F. Sievers, N. Kretzschmar, C. Salomon and F. Chevy. "2.1-watts intracavity-frequency-doubled all-solid-state light source at 671 nm for laser cooling of lithium". *Opt. Express*, **vol. 21**, no. 7, pp. 9091–9102 (2013) (cited page 144)

[Eismann *et al.*, 2015] U. Eismann, L. Khaykovich, S. Laurent, I. Ferrier-Barbut, B. S. Rem, A. T. Grier, M. Delehaye, F. Chevy, C. Salomon, L.-C. Ha and C. Chin. "Universal Loss Dynamics in a Unitary Bose Gas". *Submitted to PRX* (2015) (cited pages 7, 19, 32)

[Endres *et al.*, 2012] M. Endres, T. Fukuhara, D. Pekker, M. Cheneau, P. Schauss, C. Gross, E. Demler, S. Kuhr and I. Bloch. "The 'Higgs' amplitude mode at the two-dimensional superfluid/Mott insulator transition". *Nature*, **vol. 487**, no. 7408, pp. 454–458 (2012) (cited page 1)

[Ensher *et al.*, 1996] J. R. Ensher, D. S. Jin, M. R. Matthews, C. E. Wieman and E. A. Cornell. "Bose-Einstein Condensation in a Dilute Gas: Measurement of Energy and Ground-State Occupation". *Phys. Rev. Lett.*, **vol. 77**, pp. 4984–4987 (1996) (cited page 4)

[Fedichev and Shlyapnikov, 2001] P. Fedichev and G. Shlyapnikov. "Critical velocity in cylindrical Bose-Einstein condensates". *Physical Review A*, **vol. 63**, p. 045601 (2001) (cited pages 2, 72)

[Feiguin and Heidrich-Meisner, 2007] A. E. Feiguin and F. Heidrich-Meisner. "Pairing states of a polarized Fermi gas trapped in a one-dimensional optical lattice". *Phys. Rev. B*, **vol. 76**, p. 220508 (2007) (cited page 5)

[Fenech *et al.*, 2016] K. Fenech, P. Dyke, T. Peppler, M. G. Lingham, S. Hoinka, H. Hu and C. J. Vale. "Thermodynamics of an Attractive 2D Fermi Gas". *Phys. Rev. Lett.*, **vol. 116**, p. 045302 (2016) (cited page 4)

[Fernandes *et al.*, 2012] D. R. Fernandes, F. Sievers, N. Kretzschmar, S. Wu, C. Salomon and F. Chevy. "Sub-Doppler laser cooling of fermionic ^{40}K atoms in three-dimensional gray optical molasses". *EPL (Europhysics Letters)*, **vol. 100**, no. 6, p. 63001 (2012) (cited page 134)

[Ferrier-Barbut, 2014] I. Ferrier-Barbut. *Mixtures of Bose and Fermi Superfluids*. Ph.D. thesis, École Normale Supérieure (2014) (cited pages 45, 87, 102)

[Ferrier-Barbut *et al.*, 2014] I. Ferrier-Barbut, M. Delehaye, S. Laurent, A. T. Grier, M. Pierce, B. S. Rem, F. Chevy and C. Salomon. "A mixture of Bose and Fermi superfluids". *Science*, **vol. 345**, no. 6200, pp. 1035–1038 (2014) (cited pages 7, 23, 65)

[Ferrier-Barbut *et al.*, 2016] I. Ferrier-Barbut, H. Kadau, M. Schmitt, M. Wenzel and T. Pfau. "Observation of quantum droplets in a strongly dipolar Bose gas". *arXiv:1601.03318* (2016) (cited page 4)

[Feshbach, 1958] H. Feshbach. "Unified theory of nuclear reactions". *Annals of Physics*, **vol. 5**, no. 4, pp. 357 – 390 (1958) (cited page 31)

[Feynman, 1953] R. P. Feynman. "Atomic Theory of the λ Transition in Helium". *Phys. Rev.*, **vol. 91**, pp. 1291–1301 (1953) (cited page 13)

[Feynman, 1954] R. P. Feynman. "Atomic Theory of the Two-Fluid Model of Liquid Helium". *Phys. Rev.*, **vol. 94**, pp. 262–277 (1954) (cited page 13)

[Feynman, 1982] R. P. Feynman. "Simulating physics with computers". *International Journal of Theoretical Physics*, **vol. 21**, no. 6, pp. 467–488 (1982) (cited page 1)

[Fisher *et al.*, 1989] M. P. A. Fisher, P. B. Weichman, G. Grinstein and D. S. Fisher. "Boson localization and the superfluid-insulator transition". *Phys. Rev. B*, **vol. 40**, pp. 546–570 (1989) (cited page 2)

[Fuchs *et al.*, 2003] J. N. Fuchs, X. Leyronas and R. Combescot. "Hydrodynamic modes of a one-dimensional trapped Bose gas". *Phys. Rev. A*, **vol. 68**, p. 043610 (2003) (cited page 115)

[Fuchs *et al.*, 2007] J. Fuchs, G. J. Duffy, G. Veeravalli, P. Dyke, M. Bartenstein, C. J. Vale, P. Hannaford and W. J. Rowlands. "Molecular Bose–Einstein condensation in a versatile low power crossed dipole trap". *Journal of Physics B: Atomic, Molecular and Optical Physics*, **vol. 40**, no. 20, p. 4109 (2007) (cited page 133)

[Fulde and Ferrell, 1964] P. Fulde and R. Ferrell. "Superconductivity in a strong spin-exchange field". *Phys. Rev*, **vol. 135**, p. A550 (1964) (cited page 4)

[Gaunt *et al.*, 2013] A. L. Gaunt, T. F. Schmidutz, I. Gotlibovych, R. P. Smith and Z. Hadzibabic. "Bose-Einstein Condensation of Atoms in a Uniform Potential". *Phys. Rev. Lett.*, **vol. 110**, p. 200406 (2013) (cited pages 5, 7, 95, 136)

[Gehm, 2003] M. E. Gehm. "Properties of ^{6}Li". *Unpublished* (2003) (cited page 26)

[Gerbier *et al.*, 2004a] F. Gerbier, J. H. Thywissen, S. Richard, M. Hugbart, P. Bouyer and A. Aspect. "Critical Temperature of a Trapped, Weakly Interacting Bose Gas". *Phys. Rev. Lett.*, **vol. 92**, p. 030405 (2004) (cited page 4)

[Gerbier *et al.*, 2004b] F. Gerbier, J. H. Thywissen, S. Richard, M. Hugbart, P. Bouyer and A. Aspect. "Experimental study of the thermodynamics of an interacting trapped Bose-Einstein condensed gas". *Phys. Rev. A*, **vol. 70**, p. 013607 (2004) (cited page 4)

[Gerton *et al.*, 2000] J. M. Gerton, D. Strekalov, I. Prodan and R. G. Hulet. "Direct observation of growth and collapse of a Bose-Einstein condensate with attractive interactions". *Nature*, **vol. 408**, no. 6813, pp. 692–695 (2000) (cited pages 19, 21)

[Gezerlis and Carlson, 2008] A. Gezerlis and J. Carlson. "Strongly paired fermions: Cold atoms and neutron matter". *Phys. Rev. C*, **vol. 77**, p. 032801 (2008) (cited page 4)

[Goldman *et al.*, 2014] N. Goldman, G. Juzeliunas, P. Öhberg and I. B. Spielman. "Light-induced gauge fields for ultracold atoms". *Reports on Progress in Physics*, **vol. 77**, no. 12, p. 126401 (2014) (cited page 3)

[Greif *et al.*, 2015] D. Greif, G. Jotzu, M. Messer, R. Desbuquois and T. Esslinger. "Formation and Dynamics of Antiferromagnetic Correlations in Tunable Optical Lattices". *Phys. Rev. Lett.*, **vol. 115**, p. 260401 (2015) (cited page 4)

[Greiner *et al.*, 2002] M. Greiner, O. Mandel, T. Esslinger, T. Hänsch and I. Bloch. "Quantum phase transition from a superfluid to a Mott insulator in a gas of ultracold atoms". *Nature*, **vol. 415**, no. 6867, pp. 39–44 (2002) (cited page 2)

[Greiner *et al.*, 2003] M. Greiner, C. Regal and D. Jin. "Emergence of a molecular Bose-Einstein condensate from a Fermi gas". *Nature*, **vol. 426**, no. 6966, pp. 537–540 (2003) (cited page 92)

[Grier *et al.*, 2013] A. T. Grier, I. Ferrier-Barbut, B. S. Rem, M. Delehaye, L. Khaykovich, F. Chevy and C. Salomon. "Λ-enhanced sub-Doppler cooling of lithium atoms in D_1 gray molasses". *Phys. Rev. A*, **vol. 87**, p. 063411 (2013) (cited pages 7, 135, 140)

[Grynberg and Courtois, 1994] G. Grynberg and J. Courtois. "Proposal for a magneto-optical lattice for trapping atoms in nearly-dark states". *EPL (Europhysics Letters)*, **vol. 27**, no. 1, p. 41 (1994) (cited page 134)

[Guan *et al.*, 2007] X. W. Guan, M. T. Batchelor, C. Lee and M. Bortz. "Phase transitions and pairing signature in strongly attractive Fermi atomic gases". *Phys. Rev. B*, **vol. 76**, p. 085120 (2007) (cited page 5)

[Guéry-Odelin and Stringari, 1999] D. Guéry-Odelin and S. Stringari. "Scissors Mode and Superfluidity of a Trapped Bose-Einstein Condensed Gas". *Phys. Rev. Lett.*, **vol. 83**, pp. 4452–4455 (1999) (cited page 88)

[Guéry-Odelin and Trizac, 2015] D. Guéry-Odelin and E. Trizac. "Ultracold atoms: Boltzmann avenged". *Nature Physics*, **vol. 11**, no. 12, pp. 988–988 (2015) (cited page 88)

[Guéry-Odelin *et al.*, 1999] D. Guéry-Odelin, F. Zambelli, J. Dalibard and S. Stringari. "Collective oscillations of a classical gas confined in harmonic traps". *Phys. Rev. A*, **vol. 60**, pp. 4851–4856 (1999) (cited page 88)

[Günter *et al.*, 2006] K. Günter, T. Stöferle, H. Moritz, M. Köhl and T. Esslinger. "Bose-Fermi Mixtures in a Three-Dimensional Optical Lattice". *Phys. Rev. Lett.*, **vol. 96**, p. 180402 (2006) (cited page 2)

[Gurarie *et al.*, 2009] V. Gurarie, L. Pollet, N. V. Prokof'ev, B. V. Svistunov and M. Troyer. "Phase diagram of the disordered Bose-Hubbard model". *Phys. Rev. B*, **vol. 80**, p. 214519 (2009) (cited page 3)

[Hadzibabic *et al.*, 2002] Z. Hadzibabic, C. A. Stan, K. Dieckmann, S. Gupta, M. W. Zwierlein, A. Görlitz and W. Ketterle. "Two-Species Mixture of Quantum Degenerate Bose and Fermi Gases". *Phys. Rev. Lett.*, **vol. 88**, p. 160401 (2002) (cited page 6)

[Hall and Vinen, 1956a] H. E. Hall and W. F. Vinen. "The Rotation of Liquid Helium II. II. The Theory of Mutual Friction in Uniformly Rotating Helium II". *Proceedings of the Royal Society of London A: Mathematical, Physical and Engineering Sciences*, **vol. 238**, no. 1213, pp. 215–234 (1956) (cited page 13)

[Hall and Vinen, 1956b] H. E. Hall and W. F. Vinen. "The Rotation of Liquid Helium II. II. The Theory of Mutual Friction in Uniformly Rotating Helium II". *Proceedings of the Royal Society of London Series A*, **vol. 238**, pp. 215–234 (1956) (cited page 54)

[Hall *et al.*, 1998] D. S. Hall, M. R. Matthews, J. R. Ensher, C. E. Wieman and E. A. Cornell. "Dynamics of Component Separation in a Binary Mixture of Bose-Einstein Condensates". *Phys. Rev. Lett.*, **vol. 81**, pp. 1539–1542 (1998) (cited page 54)

[Hamilton *et al.*, 2014] P. Hamilton, G. Kim, T. Joshi, B. Mukherjee, D. Tiarks and H. Müller. "Sisyphus cooling of lithium". *Phys. Rev. A*, **vol. 89**, p. 023409 (2014) (cited page 135)

[Hansen *et al.*, 2011] A. H. Hansen, A. Khramov, W. H. Dowd, A. O. Jamison, V. V. Ivanov and S. Gupta. "Quantum degenerate mixture of ytterbium and lithium atoms". *Phys. Rev. A*, **vol. 84**, p. 011606 (2011) (cited page 6)

[Hara *et al.*, 2011] H. Hara, Y. Takasu, Y. Yamaoka, J. M. Doyle and Y. Takahashi. "Quantum Degenerate Mixtures of Alkali and Alkaline-Earth-Like Atoms". *Phys. Rev. Lett.*, **vol. 106**, p. 205304 (2011) (cited page 6)

[Haussmann *et al.*, 2007] R. Haussmann, W. Rantner, S. Cerrito and W. Zwerger. "Thermodynamics of the BCS-BEC crossover". *Phys. Rev. A*, **vol. 75**, p. 023610 (2007) (cited page 23)

[Heiselberg, 2001] H. Heiselberg. "Fermi systems with long scattering lengths". *Phys. Rev. A*, **vol. 63**, p. 043606 (2001) (cited page 93)

[Henriet and Hur, 2015] L. Henriet and K. L. Hur. "Quantum sweeps, synchronization, and Kibble-Zurek physics in dissipative quantum spin systems". *ArXiv e-prints*, , no. arXiv:1502.06863 (2015) (cited page 82)

[Hess, 1986] H. F. Hess. "Evaporative cooling of magnetically trapped and compressed spin-polarized hydrogen". *Phys. Rev. B*, **vol. 34**, pp. 3476–3479 (1986) (cited page 40)

[Ho and Shenoy, 1996] T.-L. Ho and V. B. Shenoy. "Binary Mixtures of Bose Condensates of Alkali Atoms". *Phys. Rev. Lett.*, **vol. 77**, pp. 3276–3279 (1996) (cited page 152)

[Ho and Zhou, 2009] T. Ho and Q. Zhou. "Obtaining phase diagram and thermodynamic quantities of bulk systems from the densities of trapped gases". *Nature Physics*, **vol. 6**, no. 2, pp. 131–134 (2009) (cited page 115)

[Ho, 2004] T.-L. Ho. "Universal Thermodynamics of Degenerate Quantum Gases in the Unitarity Limit". *Phys. Rev. Lett.*, **vol. 92**, p. 090402 (2004) (cited page 4)

[Horikoshi *et al.*, 2010] M. Horikoshi, S. Nakajima, M. Ueda and T. Mukaiyama. "Measurement of Universal Thermodynamic Functions for a Unitary Fermi Gas". *Science*, **vol. 327**, no. 5964, pp. 442–445 (2010) (cited pages 4, 114)

[Hou *et al.*, 2013] Y.-H. Hou, L. P. Pitaevskii and S. Stringari. "First and second sound in a highly elongated Fermi gas at unitarity". *Phys. Rev. A*, **vol. 88**, p. 043630 (2013) (cited page 13)

[Hu and Liu, 2006] H. Hu and X. Liu. "Mean-field phase diagrams of imbalanced Fermi gases near a Feshbach resonance". *Physical Review A*, **vol. 73**, p. 051603 (2006) (cited page 108)

[Huang *et al.*, 2014] B. Huang, L. A. Sidorenkov, R. Grimm and J. M. Hutson. "Observation of the Second Triatomic Resonance in Efimov's Scenario". *Phys. Rev. Lett.*, **vol. 112**, p. 190401 (2014) (cited page 19)

[Hu *et al.*, 2004] H. Hu, A. Minguzzi, X.-J. Liu and M. P. Tosi. "Collective Modes and Ballistic Expansion of a Fermi Gas in the BCS-BEC Crossover". *Phys. Rev. Lett.*, **vol. 93**, p. 190403 (2004) (cited page 88)

[Hu *et al.*, 2007] H. Hu, X.-J. Liu and P. D. Drummond. "Phase Diagram of a Strongly Interacting Polarized Fermi Gas in One Dimension". *Phys. Rev. Lett.*, **vol. 98**, p. 070403 (2007) (cited page 5)

[Hung *et al.*, 2011] C.-L. Hung, X. Zhang, N. Gemelke and C. Chin. "Observation of scale invariance and universality in two-dimensional Bose gases". *Nature*, **vol. 470**, no. 7333, pp. 236–239 (2011) (cited page 4)

[Jaksch and Zoller, 2005] D. Jaksch and P. Zoller. "The cold atom Hubbard toolbox". *Annals of Physics*, **vol. 315**, no. 1, pp. 52 – 79 (2005). Special Issue (cited page 2)

[Jaksch *et al.*, 1998] D. Jaksch, C. Bruder, J. I. Cirac, C. W. Gardiner and P. Zoller. "Cold Bosonic Atoms in Optical Lattices". *Phys. Rev. Lett.*, **vol. 81**, no. 15, pp. 3108–3111 (1998) (cited page 2)

[Jezek *et al.*, 2004] D. M. Jezek, M. Barranco, M. Guilleumas, R. Mayol and M. Pi. "K-Rb Fermi-Bose mixtures: Vortex states and sag". *Phys. Rev. A*, **vol. 70**, p. 043630 (2004) (cited page 152)

[Jin *et al.*, 1996] D. S. Jin, J. R. Ensher, M. R. Matthews, C. E. Wieman and E. A. Cornell. "Collective Excitations of a Bose-Einstein Condensate in a Dilute Gas". *Phys. Rev. Lett.*, **vol. 77**, pp. 420–423 (1996) (cited page 3)

[Jochim *et al.*, 2003] S. Jochim, M. Bartenstein, A. Altmeyer, G. Hendl, S. Riedl, C. Chin, J. Hecker Denschlag and R. Grimm. "Bose-Einstein condensation of molecules". *Science*, **vol. 302**, no. 5653, p. 2101 (2003) (cited page 92)

[Jordens *et al.*, 2008] R. Jordens, N. Strohmaier, K. Gunter, H. Moritz and T. Esslinger. "A Mott insulator of fermionic atoms in an optical lattice". *Nature*, **vol. 455**, no. 7210, pp. 204–207 (2008) (cited page 2)

[Joseph *et al.*, 2007] J. Joseph, B. Clancy, L. Luo, J. Kinast, A. Turlapov and J. E. Thomas. "Measurement of Sound Velocity in a Fermi Gas near a Feshbach Resonance". *Phys. Rev. Lett.*, **vol. 98**, p. 170401 (2007) (cited page 72)

[Kadau *et al.*, 2016] H. Kadau, M. Schmitt, M. Wenzel, C. Wink, T. Maier, I. Ferrier-Barbut and T. Pfau. "Observing the Rosensweig instability of a quantum ferrofluid". *Nature* (2016) (cited page 4)

[Kakashvili and Bolech, 2009] P. Kakashvili and C. J. Bolech. "Paired states in spin-imbalanced atomic Fermi gases in one dimension". *Phys. Rev. A*, **vol. 79**, p. 041603 (2009) (cited page 5)

[Kapitza, 1938] P. Kapitza. "Viscosity of Liquid Helium below the λ-Point". *Nature*, **vol. 141**, p. 74 (1938) (cited pages 1, 11, 53)

[Ketterle and Druten, 1996] W. Ketterle and N. V. Druten. "Evaporative Cooling of Trapped Atoms". vol. 37 of *Advances In Atomic, Molecular, and Optical Physics*, pp. 181 – 236. Academic Press (1996) (cited page 40)

[Kinnunen *et al.*, 2006] J. Kinnunen, L. M. Jensen and P. Törmä. "Strongly Interacting Fermi Gases with Density Imbalance". *Phys. Rev. Lett.*, **vol. 96**, p. 110403 (2006) (cited page 5)

[Köhl *et al.*, 2005] M. Köhl, H. Moritz, T. Stöferle, K. Günter and T. Esslinger. "Fermionic Atoms in a Three Dimensional Optical Lattice: Observing Fermi Surfaces, Dynamics, and Interactions". *Phys. Rev. Lett.*, **vol. 94**, p. 080403 (2005) (cited page 2)

[Kohn, 1961] W. Kohn. "Cyclotron Resonance and de Haas-van Alphen Oscillations of an Interacting Electron Gas". *Phys. Rev.*, **vol. 123**, pp. 1242–1244 (1961) (cited page 58)

[Kondov *et al.*, 2011] S. S. Kondov, W. R. McGehee, J. J. Zirbel and B. DeMarco. "Three-Dimensional Anderson Localization of Ultracold Matter". *Science*, **vol. 334**, no. 6052, pp. 66–68 (2011) (cited page 3)

[Kontos *et al.*, 2001] T. Kontos, M. Aprili, J. Lesueur and X. Grison. "Inhomogeneous Superconductivity Induced in a Ferromagnet by Proximity Effect". *Phys. Rev. Lett.*, **vol. 86**, pp. 304–307 (2001) (cited page 5)

[Kraemer *et al.*, 2006] T. Kraemer, M. Mark, P. Waldburger, J. G. Danzl, C. Chin, B. Engeser, A. D. Lange, K. Pilch, A. Jaakkola, H.-C. Nägerl and R. Grimm. "Evidence for Efimov quantum states in an ultracold gas of caesium atoms". *Nature*, **vol. 440**, no. 7082, pp. 315–318 (2006) (cited page 19)

[Kretschmar *et al.*, 2016] N. Kretschmar, U. Eismann, F. Sievers, F. Chevy and C. Salomon. "Multiwatt-level second harmonic generation in ppZn:LN ridge waveguide". *in preparation* (2016) (cited page 144)

[Ku *et al.*, 2012] M. J. H. Ku, A. T. Sommer, L. W. Cheuk and M. W. Zwierlein. "Revealing the Superfluid Lambda Transition in the Universal Thermodynamics of a Unitary Fermi Gas". *Science*, **vol. 335**, no. 6068, pp. 563–567 (2012) (cited pages 4, 62, 93)

[Kuopanportti *et al.*, 2012] P. Kuopanportti, J. A. M. Huhtamäki and M. Möttönen. "Exotic vortex lattices in two-species Bose-Einstein condensates". *Phys. Rev. A*, **vol. 85**, p. 043613 (2012) (cited page 152)

[Ladd *et al.*, 2010] T. D. Ladd, F. Jelezko, R. Laflamme, Y. Nakamura, C. Monroe and J. L. O/'Brien. "Quantum Computers". *Nature*, **vol. 464**, no. 7285, pp. 45–53 (2010) (cited page 1)

[Lahaye *et al.*, 2007] T. Lahaye, T. Koch, B. Frohlich, M. Fattori, J. Metz, A. Griesmaier, S. Giovanazzi and T. Pfau. "Strong dipolar effects in a quantum ferrofluid". *Nature*, **vol. 448**, no. 7154, pp. 672–675 (2007) (cited page 4)

[Lahaye *et al.*, 2008] T. Lahaye, J. Metz, B. Fröhlich, T. Koch, M. Meister, A. Griesmaier, T. Pfau, H. Saito, Y. Kawaguchi and M. Ueda. "*d*-Wave Collapse and Explosion of a Dipolar Bose-Einstein Condensate". *Phys. Rev. Lett.*, **vol. 101**, p. 080401 (2008) (cited page 4)

[Lahaye *et al.*, 2009] T. Lahaye, C. Menotti, L. Santos, M. Lewenstein and T. Pfau. "The physics of dipolar bosonic quantum gases". *Reports on Progress in Physics*, **vol. 72**, no. 12, p. 126401 (2009) (cited page 4)

[Landau, 1941] L. Landau. "Theory of the Superfluidity of Helium II". *Phys. Rev.*, **vol. 60**, pp. 356–358 (1941) (cited pages 1, 12)

[Landau, 1957] L. Landau. "The theory of a Fermi liquid". *Sov. Phys. JETP*, **vol. 3**, no. 6, pp. 920–925 (1957) (cited pages 54, 55)

[Larkin and Ovchinnikov, 1964] A. Larkin and Y. Ovchinnikov. "Nonuniform state of superconductors". *Zh. Eksp. Teor. Fiz*, **vol. 47**, p. 1136 (1964) (cited page 4)

[Leggett, 1975] A. J. Leggett. "A theoretical description of the new phases of liquid ^{3}He". *Rev. Mod. Phys.*, **vol. 47**, pp. 331–414 (1975) (cited pages 2, 12)

[Léonard *et al.*, 2014] J. Léonard, M. Lee, A. Morales, T. M. Karg, T. Esslinger and T. Donner. "Optical transport and manipulation of an ultracold atomic cloud using focus-tunable lenses". *New Journal of Physics*, **vol. 16**, no. 9, p. 093028 (2014) (cited pages 136, 138)

[Lett *et al.*, 1988] P. D. Lett, R. N. Watts, C. I. Westbrook, W. D. Phillips, P. L. Gould and H. J. Metcalf. "Observation of Atoms Laser Cooled below the Doppler Limit". *Phys. Rev. Lett.*, **vol. 61**, pp. 169–172 (1988) (cited page 133)

[Liao *et al.*, 2010] Y. Liao, A. Rittner, T. Paprotta, W. Li, G. Partridge, R. Hulet, S. Baur and E. Mueller. "Spin-Imbalance in a One-Dimensional Fermi Gas". *Nature*, **vol. 467**, no. 7315, pp. 567–569 (2010) (cited page 5)

[Lin *et al.*, 2009] Y.-J. Lin, R. L. Compton, K. Jimenez-Garcia, J. V. Porto and I. B. Spielman. "Synthetic magnetic fields for ultracold neutral atoms". *Nature*, **vol. 462**, no. 7273, pp. 628–632 (2009) (cited page 3)

[Liu and Wilczek, 2003] W. V. Liu and F. Wilczek. "Interior Gap Superfluidity". *Phys. Rev. Lett.*, **vol. 90**, p. 047002 (2003) (cited page 92)

[Liu *et al.*, 2014] C.-F. Liu, H. Fan, S.-C. Gou and W.-M. Liu. "Crystallized and amorphous vortices in rotating atomic-molecular Bose-Einstein condensates". *Scientific Reports*, **vol. 4**, no. 4224 (2014) (cited page 152)

[Lloyd, 1996] S. Lloyd. "Universal Quantum Simulators". *Science*, **vol. 273**, no. 5278, pp. 1073–1078 (1996) (cited page 1)

[Lobo *et al.*, 2006] C. Lobo, A. Recati, S. Giorgini and S. Stringari. "Normal state of a polarized Fermi gas at unitarity". *Phys. Rev. Lett.*, **vol. 97**, p. 200403 (2006) (cited pages 4, 60, 94, 95, 99)

[London, 1938] F. London. "The λ-Phenomenon of Liquid Helium and the Bose-Einstein Degeneracy". *Nature*, **vol. 141**, pp. 643–644 (1938) (cited pages 1, 12)

[Lu *et al.*, 2012] M. Lu, N. Q. Burdick and B. L. Lev. "Quantum Degenerate Dipolar Fermi Gas". *Phys. Rev. Lett.*, **vol. 108**, p. 215301 (2012) (cited page 6)

[Luo *et al.*, 2007] L. Luo, B. Clancy, J. Joseph, J. Kinast and J. Thomas. "Measurement of the entropy and critical temperature of a strongly interacting Fermi gas". *Physical Review Letters*, **vol. 98**, p. 080402 (2007) (cited pages 4, 72)

[Madison *et al.*, 2000] K. Madison, F. Chevy, W. Wohlleben and J. Dalibard. "Vortex formation in a stirred Bose-Einstein condensate". *Physical Review Letters*, **vol. 84**, pp. 806–809 (2000) (cited pages 2, 3, 13, 21, 54)

[Masuhara *et al.*, 1988] N. Masuhara, J. M. Doyle, J. C. Sandberg, D. Kleppner, T. J. Greytak, H. F. Hess and G. P. Kochanski. "Evaporative Cooling of Spin-Polarized Atomic Hydrogen". *Phys. Rev. Lett.*, **vol. 61**, pp. 935–938 (1988) (cited page 40)

[Mathey *et al.*, 2014] A. C. Mathey, C. W. Clark and L. Mathey. "Decay of a superfluid current of ultracold atoms in a toroidal trap". *Phys. Rev. A*, **vol. 90**, p. 023604 (2014) (cited page 151)

[Matthews *et al.*, 1999] M. R. Matthews, B. P. Anderson, P. C. Haljan, D. S. Hall, C. E. Wieman and E. A. Cornell. "Vortices in a Bose-Einstein Condensate". *Phys. Rev. Lett.*, **vol. 83**, pp. 2498–2501 (1999) (cited pages 2, 13, 21)

[McNamara *et al.*, 2006] J. M. McNamara, T. Jeltes, A. S. Tychkov, W. Hogervorst and W. Vassen. "Degenerate Bose-Fermi Mixture of Metastable Atoms". *Phys. Rev. Lett.*, **vol. 97**, p. 080404 (2006) (cited page 6)

[Meyrath *et al.*, 2005] T. P. Meyrath, F. Schreck, J. L. Hanssen, C.-S. Chuu and M. G. Raizen. "Bose-Einstein condensate in a box". *Phys. Rev. A*, **vol. 71**, p. 041604 (2005) (cited pages 5, 7)

[Miller *et al.*, 2007] D. E. Miller, J. K. Chin, C. A. Stan, Y. Liu, W. Setiawan, C. Sanner and W. Ketterle. "Critical Velocity for Superfluid Flow across the BEC-BCS Crossover". *Physical Review Letters*, **vol. 99**, p. 070402 (2007) (cited pages 2, 23, 54, 55, 70, 74, 89, 151)

[Minguzzi *et al.*, 2001] A. Minguzzi, G. Ferrari and Y. Castin. "Dynamic structure factor of a superfluid Fermi gas". *The European Physical Journal D-Atomic, Molecular, Optical and Plasma Physics*, **vol. 17**, no. 1, pp. 49–55 (2001) (cited page 69)

[Miyakawa *et al.*, 2000] T. Miyakawa, T. Suzuki and H. Yabu. "Sum-rule approach to collective oscillations of a boson-fermion mixed condensate of alkali-metal atoms". *Phys. Rev. A*, **vol. 62**, p. 063613 (2000) (cited page 61)

[Miyake *et al.*, 2013] H. Miyake, G. A. Siviloglou, C. J. Kennedy, W. C. Burton and W. Ketterle. "Realizing the Harper Hamiltonian with Laser-Assisted Tunneling in Optical Lattices". *Phys. Rev. Lett.*, **vol. 111**, p. 185302 (2013) (cited page 3)

[Mizushima *et al.*, 2005] T. Mizushima, K. Machida and M. Ichioka. "Direct Imaging of Spatially Modulated Superfluid Phases in Atomic Fermion Systems". *Phys. Rev. Lett.*, **vol. 94**, p. 060404 (2005) (cited page 5)

[Mølmer, 1998] K. Mølmer. "Bose Condensates and Fermi Gases at Zero Temperature". *Phys. Rev. Lett.*, **vol. 80**, pp. 1804–1807 (1998) (cited page 98)

[Mora and Chevy, 2010] C. Mora and F. Chevy. "Normal Phase of an Imbalanced Fermi Gas". *Phys. Rev. Lett.*, **vol. 104**, no. 23, p. 230402 (2010) (cited page 94)

[Müther and Sedrakian, 2002] H. Müther and A. Sedrakian. "Spontaneous Breaking of Rotational Symmetry in Superconductors". *Phys. Rev. Lett.*, **vol. 88**, p. 252503 (2002) (cited page 93)

[Nascimbène, 2010] S. Nascimbène. *Thermodynamics of ultracold Fermi gases*. Ph.D. thesis, University Pierre et Marie Curie, Paris VI (2010) (cited pages 26, 115)

[Nascimbène *et al.*, 2009] S. Nascimbène, N. Navon, K. Jiang, L. Tarruell, M. Teichmann, J. McKeever, F. Chevy and C. Salomon. "Collective Oscillations of an Imbalanced Fermi Gas: Axial Compression Modes and Polaron Effective Mass". *Physical Review Letters*, **vol. 103**, p. 170402 (2009) (cited page 96)

[Nascimbène *et al.*, 2010] S. Nascimbène, N. Navon, K. Jiang, F. Chevy and C. Salomon. "Exploring the Thermodynamics of a Universal Fermi Gas". *Nature*, **vol. 463**, no. 7284, pp. 1057–1060 (2010) (cited pages 4, 6, 22, 60, 83, 115)

[Nath *et al.*, 2013] D. Nath, R. K. Easwaran, G. Rajalakshmi and C. S. Unnikrishnan. "Quantum-interference-enhanced deep sub-Doppler cooling of ^{39}K atoms in gray molasses". *Phys. Rev. A*, **vol. 88**, p. 053407 (2013) (cited page 135)

[Navon *et al.*, 2010] N. Navon, S. Nascimbène, F. Chevy and C. Salomon. "The Equation of State of a Low-Temperature Fermi Gas with Tunable Interactions". *Science*, **vol. 328**, no. 5979, pp. 729–732 (2010) (cited pages 4, 32, 60, 61, 62, 72, 93, 94, 95, 115)

[Navon *et al.*, 2015] N. Navon, A. L. Gaunt, R. P. Smith and Z. Hadzibabic. "Critical dynamics of spontaneous symmetry breaking in a homogeneous Bose gas". *Science*, **vol. 347**, no. 6218, pp. 167–170 (2015) (cited page 6)

[Nikuni *et al.*, 2000] T. Nikuni, M. Oshikawa, A. Oosawa and H. Tanaka. "Bose-Einstein Condensation of Dilute Magnons in tlcucl$_3$". *Phys. Rev. Lett.*, **vol. 84**, pp. 5868–5871 (2000) (cited page 2)

[Onofrio and Sundaram, 2015] R. Onofrio and B. Sundaram. "Effective microscopic models for sympathetic cooling of atomic gases". *Phys. Rev. A*, **vol. 92**, p. 033422 (2015) (cited page 82)

[Onofrio *et al.*, 2000] R. Onofrio, C. Raman, J. M. Vogels, J. R. Abo-Shaeer, A. P. Chikkatur and W. Ketterle. "Observation of Superfluid Flow in a Bose-Einstein Condensed Gas". *Phys. Rev. Lett.*, **vol. 85**, pp. 2228–2231 (2000) (cited pages 2, 12, 21)

[Onsager, 1949] L. Onsager. "Statistical hydrodynamics". *Il Nuovo Cimento (1943-1954)*, **vol. 6**, no. 2, pp. 279–287 (1949) (cited page 13)

[Orso, 2007] G. Orso. "Attractive Fermi Gases with Unequal Spin Populations in Highly Elongated Traps". *Phys. Rev. Lett.*, **vol. 98**, p. 070402 (2007) (cited page 5)

[Orth *et al.*, 2010] P. P. Orth, D. Roosen, W. Hofstetter and K. Le Hur. "Dynamics, synchronization, and quantum phase transitions of two dissipative spins". *Phys. Rev. B*, **vol. 82**, p. 144423 (2010) (cited page 82)

[Osheroff *et al.*, 1972a] D. D. Osheroff, W. J. Gully, R. C. Richardson and D. M. Lee. "New Magnetic Phenomena in Liquid he^3 below 3 mK". *Phys. Rev. Lett.*, **vol. 29**, pp. 920–923 (1972) (cited pages 2, 12, 54)

[Osheroff *et al.*, 1972b] D. D. Osheroff, R. C. Richardson and D. M. Lee. "Evidence for a New Phase of Solid he^3". *Phys. Rev. Lett.*, **vol. 28**, pp. 885–888 (1972) (cited pages 2, 12, 54)

[Ospelkaus *et al.*, 2006] S. Ospelkaus, C. Ospelkaus, O. Wille, M. Succo, P. Ernst, K. Sengstock and K. Bongs. "Localization of Bosonic Atoms by Fermionic Impurities in a Three-Dimensional Optical Lattice". *Phys. Rev. Lett.*, **vol. 96**, p. 180403 (2006) (cited page 2)

[Ott *et al.*, 2004] H. Ott, E. de Mirandes, F. Ferlaino, G. Roati, G. Modugno and M. Inguscio. "Collisionally Induced Transport in Periodic Potentials". *Phys. Rev. Lett.*, **vol. 92**, p. 160601 (2004) (cited page 3)

[Ottenstein *et al.*, 2008] T. B. Ottenstein, T. Lompe, M. Kohnen, A. N. Wenz and S. Jochim. "Collisional Stability of a Three-Component Degenerate Fermi Gas". *Phys. Rev. Lett.*, **vol. 101**, p. 203202 (2008) (cited page 136)

[Ozawa *et al.*, 2014] T. Ozawa, A. Recati, M. Delehaye, F. Chevy and S. Stringari. "Chandrasekhar-Clogston limit and critical polarization in a Fermi-Bose superfluid mixture". *Phys. Rev. A*, **vol. 90**, p. 043608 (2014) (cited pages 103, 121)

[Parish *et al.*, 2007a] M. M. Parish, S. K. Baur, E. J. Mueller and D. A. Huse. "Quasi-One-Dimensional Polarized Fermi Superfluids". *Phys. Rev. Lett.*, **vol. 99**, p. 250403 (2007) (cited page 5)

[Parish *et al.*, 2007b] M. M. Parish, F. M. Marchetti, A. Lamacraft and B. D. Simons. "Finite-temperature phase diagram of a polarized Fermi condensate". *Nature Physics*, **vol. 3**, no. 2, pp. 124–128 (2007) (cited pages 5, 108)

[Park *et al.*, 2012] J. W. Park, C.-H. Wu, I. Santiago, T. G. Tiecke, S. Will, P. Ahmadi and M. W. Zwierlein. "Quantum degenerate Bose-Fermi mixture of chemically different atomic species with widely tunable interactions". *Phys. Rev. A*, **vol. 85**, p. 051602 (2012) (cited page 6)

[Partridge *et al.*, 2006a] G. B. Partridge, W. Li, R. I. Kamar, Y.-a. Liao and R. G. Hulet. "Pairing and Phase Separation in a Polarized Fermi Gas". *Science*, **vol. 311**, no. 5760, pp. 503–505 (2006) (cited pages 92, 95)

[Partridge *et al.*, 2006b] G. B. Partridge, W. Li, Y. A. Liao, R. G. Hulet, M. Haque and H. T. C. Stoof. "Deformation of a Trapped Fermi Gas with Unequal Spin Populations". *Phys. Rev. Lett.*, **vol. 97**, p. 190407 (2006) (cited pages 92, 95)

[Petrich *et al.*, 1995] W. Petrich, M. H. Anderson, J. R. Ensher and E. A. Cornell. "Stable, Tightly Confining Magnetic Trap for Evaporative Cooling of Neutral Atoms". *Phys. Rev. Lett.*, **vol. 74**, pp. 3352–3355 (1995) (cited page 39)

[Pilati and Giorgini, 2008] S. Pilati and S. Giorgini. "Phase Separation in a Polarized Fermi Gas at Zero Temperature". *Phys. Rev. Lett.*, **vol. 100**, p. 030401 (2008) (cited page 94)

[Pires *et al.*, 2014] R. Pires, J. Ulmanis, S. Häfner, M. Repp, A. Arias, E. D. Kuhnle and M. Weidemüller. "Observation of Efimov Resonances in a Mixture with Extreme Mass Imbalance". *Phys. Rev. Lett.*, **vol. 112**, p. 250404 (2014) (cited page 19)

[Pitaevskii and Stringari, 2003] L. Pitaevskii and S. Stringari. *Bose-Einstein Condensation*. Clarendon Press (2003) (cited page 56)

[Pohl *et al.*, 2010] T. Pohl, E. Demler and M. D. Lukin. "Dynamical Crystallization in the Dipole Blockade of Ultracold Atoms". *Phys. Rev. Lett.*, **vol. 104**, p. 043002 (2010) (cited page 3)

[Price *et al.*, 2015] H. M. Price, O. Zilberberg, T. Ozawa, I. Carusotto and N. Goldman. "Four-Dimensional Quantum Hall Effect with Ultracold Atoms". *Phys. Rev. Lett.*, **vol. 115**, p. 195303 (2015) (cited page 4)

[Pritchard, 1983] D. E. Pritchard. "Cooling Neutral Atoms in a Magnetic Trap for Precision Spectroscopy". *Phys. Rev. Lett.*, **vol. 51**, pp. 1336–1339 (1983) (cited page 39)

[Pritchard *et al.*, 1989] D. Pritchard, K. Helmerson and A. Martin. "About RF evaporation". Atomic physics, p. 179. World Scientific (1989) (cited page 40)

[Prokof'ev and Svistunov, 2008] N. Prokof'ev and B. Svistunov. "Fermi-polaron problem: Diagrammatic Monte Carlo method for divergent sign-alternating series". *Phys. Rev. B*, **vol. 77**, no. 2, 020408 (2008) (cited page 94)

[Radzihovsky and Sheehy, 2010] L. Radzihovsky and D. E. Sheehy. "Imbalanced Feshbach-resonant Fermi gases". *Reports on Progress in Physics*, **vol. 73**, no. 7, p. 076501 (2010) (cited pages 5, 108, 127)

[Ramanathan *et al.*, 2011] A. Ramanathan, K. C. Wright, S. R. Muniz, M. Zelan, W. T. Hill, C. J. Lobb, K. Helmerson, W. D. Phillips and G. K. Campbell. "Superflow in a Toroidal Bose-Einstein Condensate: An Atom Circuit with a Tunable Weak Link". *Phys. Rev. Lett.*, **vol. 106**, p. 130401 (2011) (cited page 151)

[Raman *et al.*, 1999] C. Raman, M. Köhl, R. Onofrio, D. S. Durfee, C. E. Kuklewicz, Z. Hadzibabic and W. Ketterle. "Evidence for a Critical Velocity in a Bose-Einstein Condensed Gas". *Phys. Rev. Lett.*, **vol. 83**, pp. 2502–2505 (1999) (cited pages 2, 12, 21, 54)

[Rath *et al.*, 2010] S. P. Rath, T. Yefsah, K. J. Günter, M. Cheneau, R. Desbuquois, M. Holzmann, W. Krauth and J. Dalibard. "Equilibrium state of a trapped two-dimensional Bose gas". *Phys. Rev. A*, **vol. 82**, p. 013609 (2010) (cited page 4)

[Rayfield and Reif, 1964] G. W. Rayfield and F. Reif. "Quantized Vortex Rings in Superfluid Helium". *Phys. Rev.*, **vol. 136**, pp. A1194–A1208 (1964) (cited page 13)

[Recati *et al.*, 2008] A. Recati, C. Lobo and S. Stringari. "Role of interactions in spin-polarized atomic Fermi gases at unitarity". *Phys. Rev. A*, **vol. 78**, p. 023633 (2008) (cited pages 94, 95)

[Regal *et al.*, 2004a] C. A. Regal, M. Greiner and D. S. Jin. "Lifetime of Molecule-Atom Mixtures near a Feshbach Resonance in^{40} K". *Phys. Rev. Lett.*, **vol. 92**, p. 083201 (2004) (cited page 74)

[Regal *et al.*, 2004b] C. A. Regal, M. Greiner and D. S. Jin. "Observation of Resonance Condensation of Fermionic Atom Pairs". *Phys. Rev. Lett.*, **vol. 92**, p. 040403 (2004) (cited pages 22, 54)

[Reinaudi *et al.*, 2007] G. Reinaudi, T. Lahaye, Z. Wang and D. Guéry-Odelin. "Strong saturation absorption imaging of dense clouds of ultracold atoms". *Opt. Lett.*, **vol. 32**, no. 21, pp. 3143–3145 (2007) (cited page 45)

[Rem, 2013] B. S. Rem. *The Road to the Unitary Bose Gas*. Ph.D. thesis, École Normale Supérieure (2013) (cited pages 17, 19)

[Rem *et al.*, 2013] B. S. Rem, A. T. Grier, I. Ferrier-Barbut, U. Eismann, T. Langen, N. Navon, L. Khaykovich, F. Werner, D. S. Petrov, F. Chevy and C. Salomon. "Lifetime of the Bose Gas with Resonant Interactions". *Phys. Rev. Lett.*, **vol. 110**, p. 163202 (2013) (cited pages 7, 19, 32)

[Repp *et al.*, 2013] M. Repp, R. Pires, J. Ulmanis, R. Heck, E. D. Kuhnle, M. Weidemüller and E. Tiemann. "Observation of interspecies ^{6}Li-^{133}Cs Feshbach resonances". *Phys. Rev. A*, **vol. 87**, p. 010701 (2013) (cited page 6)

[Roati *et al.*, 2002] G. Roati, F. Riboli, G. Modugno and M. Inguscio. "Fermi-Bose Quantum Degenerate ^{40}K-^{87}Rb Mixture with Attractive Interaction". *Phys. Rev. Lett.*, **vol. 89**, p. 150403 (2002) (cited page 6)

[Roati *et al.*, 2008] G. Roati, C. D/'Errico, L. Fallani, M. Fattori, C. Fort, M. Zaccanti, G. Modugno, M. Modugno and M. Inguscio. "Anderson localization of a non-interacting Bose-Einstein condensate". *Nature*, **vol. 453**, no. 7197, pp. 895–898 (2008) (cited page 3)

[Roberts *et al.*, 2001] J. L. Roberts, N. R. Claussen, S. L. Cornish, E. A. Donley, E. A. Cornell and C. E. Wieman. "Controlled Collapse of a Bose-Einstein Condensate". *Phys. Rev. Lett.*, **vol. 86**, pp. 4211–4214 (2001) (cited pages 19, 21)

[Rysti, 2013] J. Rysti. *Microscopic and Macroscopic Studies of Liquid and Solid Helium Mixtures*. Ph.D. thesis, Aalto University (2013) (cited page 17)

[Rysti *et al.*, 2012] J. Rysti, J. Tuoriniemi and A. Salmela. "Effective ^{3}He interactions in dilute ^{3}He-^{4}He mixtures". *Phys. Rev. B*, **vol. 85**, p. 134529 (2012) (cited pages 6, 16)

[Sackett *et al.*, 1999] C. A. Sackett, J. M. Gerton, M. Welling and R. G. Hulet. "Measurements of Collective Collapse in a Bose-Einstein Condensate with Attractive Interactions". *Phys. Rev. Lett.*, **vol. 82**, pp. 876–879 (1999) (cited pages 19, 21)

[Salomon *et al.*, 2013] G. Salomon, L. Fouché, P. Wang, A. Aspect, P. Bouyer and T. Bourdel. "Gray-molasses cooling of ^{39}K to a high phase-space density". *EPL (Europhysics Letters)*, **vol. 104**, no. 6, p. 63002 (2013) (cited page 135)

[Sansonetti *et al.*, 2011] C. J. Sansonetti, C. E. Simien, J. D. Gillaspy, J. N. Tan, S. M. Brewer, R. C. Brown, S. Wu and J. V. Porto. "Absolute Transition Frequencies and Quantum Interference in a Frequency Comb Based Measurement of the ^{6,7}Li *D* Lines". *Phys. Rev. Lett.*, **vol. 107**, p. 023001 (2011) (cited page 139)

[Schauß *et al.*, 2012] P. Schauß, M. Cheneau, M. Endres, T. Fukuhara, S. Hild, A. Omran, T. Pohl, C. Gross, S. Kuhr and I. Bloch. "Observation of spatially ordered structures in a two-dimensional Rydberg gas". *Nature*, **vol. 491**, no. 7422, pp. 87–91 (2012) (cited page 3)

[Schneider *et al.*, 2008] U. Schneider, L. Hackermüller, S. Will, T. Best, I. Bloch, T. A. Costi, R. W. Helmes, D. Rasch and A. Rosch. "Metallic and Insulating Phases of Repulsively Interacting Fermions in a 3D Optical Lattice". *Science*, **vol. 322**, no. 5907, pp. 1520–1525 (2008) (cited page 2)

[Schneider *et al.*, 2012] U. Schneider, L. Hackermuller, J. P. Ronzheimer, S. Will, S. Braun, T. Best, I. Bloch, S. Demler, Eugeneand Mandt, D. Rasch and A. Rosch. "Fermionic transport and out-of-equilibrium dynamics in a homogeneous Hubbard model with ultracold atoms". *Nature Physics*, **vol. 8**, no. 3, pp. 213–218 (2012) (cited page 3)

[Schreck, 2002] F. Schreck. *Mixtures of ultracold gases: Fermi sea and Bose-Einstein condensate of Lithium isotopes*. Ph.D. thesis, University Pierre et Marie Curie, Paris VI (2002) (cited pages 7, 26)

[Schreck *et al.*, 2001a] F. Schreck, G. Ferrari, K. L. Corwin, J. Cubizolles, L. Khaykovich, M.-O. Mewes and C. Salomon. "Sympathetic cooling of bosonic and fermionic lithium gases towards quantum degeneracy". *Phys. Rev. A*, **vol. 64**, p. 011402 (2001) (cited page 40)

[Schreck *et al.*, 2001b] F. Schreck, L. Khaykovich, K. L. Corwin, G. Ferrari, T. Bourdel, J. Cubizolles and C. Salomon. "Quasipure Bose-Einstein Condensate Immersed in a Fermi Sea". *Phys. Rev. Lett.*, **vol. 87**, p. 080403 (2001) (cited pages 6, 22)

[Schreiber *et al.*, 2015] M. Schreiber, S. S. Hodgman, P. Bordia, H. P. Lüschen, M. H. Fischer, R. Vosk, E. Altman, U. Schneider and I. Bloch. "Observation of many-body localization of interacting fermions in a quasirandom optical lattice". *Science*, **vol. 349**, no. 6250, pp. 842–845 (2015) (cited page 3)

[Sheehy and Radzihovsky, 2007] D. E. Sheehy and L. Radzihovsky. "BEC–BCS crossover, phase transitions and phase separation in polarized resonantly-paired superfluids". *Annals of Physics*, **vol. 322**, no. 8, pp. 1790 – 1924 (2007) (cited page 5)

[Shen and Zheng, 2015] H. Shen and W. Zheng. "Landau damping in a mixture of Bose and Fermi superfluids". *Phys. Rev. A*, **vol. 92**, p. 033620 (2015) (cited pages 7, 54)

[Shin, 2008] Y.-i. Shin. "Determination of the equation of state of a polarized Fermi gas at unitarity". *Phys. Rev. A*, **vol. 77**, p. 041603 (2008) (cited pages 4, 92, 114)

[Shin *et al.*, 2006] Y. Shin, M. Zwierlein, C. Schunck, A. Schirotzek and W. Ketterle. "Observation of phase separation in a strongly interacting imbalanced Fermi gas". *Physical Review Letters*, **vol. 97**, p. 030401 (2006) (cited pages 92, 95, 96)

[Shin *et al.*, 2008] Y. Shin, C. Schunck, A. Schirotzek and W. Ketterle. "Phase diagram of a two-component Fermi gas with resonant interactions". *Nature*, **vol. 451**, no. 7179, pp. 689–693 (2008) (cited pages 92, 114)

[Shotan *et al.*, 2014] Z. Shotan, O. Machtey, S. Kokkelmans and L. Khaykovich. "Three-Body Recombination at Vanishing Scattering Lengths in an Ultracold Bose Gas". *Phys. Rev. Lett.*, **vol. 113**, p. 053202 (2014) (cited page 102)

[Sidorenkov *et al.*, 2013] L. A. Sidorenkov, M. K. Tey, R. Grimm, Y.-H. Hou, L. Pitaevskii and S. Stringari. "Second sound and the superfluid fraction in a Fermi gas with resonant interactions". *Nature*, **vol. 498**, no. 7452, pp. 78–81 (2013) (cited pages 13, 54)

[Sievers *et al.*, 2015] F. Sievers, N. Kretzschmar, D. R. Fernandes, D. Suchet, M. Rabinovic, S. Wu, C. V. Parker, L. Khaykovich, C. Salomon and F. Chevy. "Simultaneous sub-Doppler laser cooling of fermionic ^{6}Li and ^{40}K on the D_1 line: Theory and experiment". *Phys. Rev. A*, **vol. 91**, p. 023426 (2015) (cited page 135)

[Silber *et al.*, 2005] C. Silber, S. Günther, C. Marzok, B. Deh, P. W. Courteille and C. Zimmermann. "Quantum-Degenerate Mixture of Fermionic Lithium and Bosonic Rubidium Gases". *Phys. Rev. Lett.*, **vol. 95**, p. 170408 (2005) (cited page 6)

[Simon *et al.*, 2011] J. Simon, W. S. Bakr, R. Ma, M. E. Tai, P. M. Preiss and M. Greiner. "Quantum simulation of antiferromagnetic spin chains in an optical lattice". *Nature*, **vol. 472**, no. 7343, pp. 307–312 (2011) (cited page 4)

[Singh *et al.*, 2015] V. P. Singh, W. Weimer, K. Morgener, J. Siegl, K. Hueck, N. Luick, H. Moritz and L. Mathey. "Probing superfluidity of Bose-Einstein condensates via laser stirring". *arXiv preprint arXiv:1509.02168* (2015) (cited page 74)

[Sommer *et al.*, 2011] A. Sommer, M. Ku, G. Roati and M. W. Zwierlein. "Universal spin transport in a strongly interacting Fermi gas". *Nature*, **vol. 472**, no. 7342, pp. 201–204 (2011) (cited page 3)

[Stadler *et al.*, 2012] D. Stadler, S. Krinner, J. Meineke, J.-P. Brantut and T. Esslinger. "Observing the drop of resistance in the flow of a superfluid Fermi gas". *Nature*, **vol. 491**, no. 7426, pp. 736–739 (2012) (cited page 12)

[Stamper-Kurn *et al.*, 1998] D. M. Stamper-Kurn, H.-J. Miesner, S. Inouye, M. R. Andrews and W. Ketterle. "Collisionless and Hydrodynamic Excitations of a Bose-Einstein Condensate". *Phys. Rev. Lett.*, **vol. 81**, pp. 500–503 (1998) (cited pages 13, 82)

[Stellmer *et al.*, 2013] S. Stellmer, R. Grimm and F. Schreck. "Production of quantum-degenerate strontium gases". *Phys. Rev. A*, **vol. 87**, p. 013611 (2013) (cited page 6)

[Stewart *et al.*, 2006] J. T. Stewart, J. P. Gaebler, C. A. Regal and D. S. Jin. "Potential Energy of a ^{40}K Fermi Gas in the BCS-BEC Crossover". *Phys. Rev. Lett.*, **vol. 97**, p. 220406 (2006) (cited page 4)

[Stringari, 1998] S. Stringari. "Dynamics of Bose-Einstein condensed gases in highly deformed traps". *Physical Review A*, **vol. 58**, pp. 2385–2388 (1998) (cited page 72)

[Stringari, 2004] S. Stringari. "Sum rules and the collective oscillations of a quantum gas". *J. Phys. IV France*, **vol. 116**, pp. 47–66 (2004) (cited page 61)

[Stringari, 2007] S. Stringari. "Dynamics and Superfluidity of an ultracold Fermi gas". In "Ultra-cold Fermi gases", (2007) (cited page 88)

[Strohmaier *et al.*, 2007] N. Strohmaier, Y. Takasu, K. Günter, R. Jördens, M. Köhl, H. Moritz and T. Esslinger. "Interaction-Controlled Transport of an Ultracold Fermi Gas". *Phys. Rev. Lett.*, **vol. 99**, p. 220601 (2007) (cited page 2)

[Struck *et al.*, 2013] J. Struck, M. Weinberg, C. Olschlager, P. Windpassinger, J. Simonet, K. Sengstock, R. Hoppner, P. Hauke, A. Eckardt, M. Lewenstein and L. Mathey. "Engineering Ising-XY spin-models in a triangular lattice using tunable artificial gauge fields". *Nature Physics*, **vol. 9**, no. 11, pp. 738–743 (2013) (cited page 3)

[Suchet *et al.*, 2015] D. Suchet, M. Rabinovic, T. Reimann, N. Kretschmar, F. Sievers, C. Salomon, J. Lau, O. Goulko, C. Lobo and F. Chevy. "Quasi-thermalization of non-interacting particles in a quadrupole potential: Analog simulation of Weyl fermions". *ArXiv e-prints* (2015) (cited pages 1, 39)

[Sugawa *et al.*, 2011] S. Sugawa, K. Inaba, S. Taie, R. Yamazaki, M. Yamashita and Y. Takahashi. "Interaction and filling-induced quantum phases of dual Mott insulators of bosons and fermions". *Nature Physics*, **vol. 7**, no. 8, pp. 642–648 (2011) (cited page 6)

[Taglieber *et al.*, 2008] M. Taglieber, A. Voigt, T. Aoki, T. Hänsch and K. Dieckmann. "Quantum degenerate two-species Fermi-Fermi mixture coexisting with a Bose-Einstein condensate". *Phys. Rev. Lett.*, **vol. 100**, p. 010401 (2008) (cited page 6)

[Tarruell, 2008] L. Tarruell. *Superfluidity in an ultracold Fermi gas.* Ph.D. thesis, University Pierre et Marie Curie, Paris VI (2008) (cited pages 7, 26, 150)

[Tey *et al.*, 2010] M. K. Tey, S. Stellmer, R. Grimm and F. Schreck. "Double-degenerate Bose-Fermi mixture of strontium". *Phys. Rev. A*, **vol. 82**, p. 011608 (2010) (cited page 6)

[Tey *et al.*, 2013] M. K. Tey, L. A. Sidorenkov, E. R. S. Guajardo, R. Grimm, M. J. H. Ku, M. W. Zwierlein, Y.-H. Hou, L. Pitaevskii and S. Stringari. "Collective Modes in a Unitary Fermi Gas across the Superfluid Phase Transition". *Phys. Rev. Lett.*, **vol. 110**, p. 055303 (2013) (cited page 61)

[Thomas *et al.*, 2005] J. E. Thomas, J. Kinast and A. Turlapov. "Virial Theorem and Universality in a Unitary Fermi Gas". *Phys. Rev. Lett.*, **vol. 95**, p. 120402 (2005) (cited page 4)

[Tiecke *et al.*, 2009] T. G. Tiecke, S. D. Gensemer, A. Ludewig and J. T. M. Walraven. "High-flux two-dimensional magneto-optical-trap source for cold lithium atoms". *Phys. Rev. A*, **vol. 80**, p. 013409 (2009) (cited page 34)

[Tisza, 1938] L. Tisza. "Transport Phenomena in Helium II". *Nature*, **vol. 141**, pp. 913–913 (1938) (cited pages 1, 12)

[Tisza, 1947] L. Tisza. "The Theory of Liquid Helium". *Phys. Rev.*, **vol. 72**, pp. 838–854 (1947) (cited pages 1, 12)

[Truscott *et al.*, 2001] A. G. Truscott, K. E. Strecker, W. I. McAlexander, G. B. Partridge and R. G. Hulet. "Observation of Fermi pressure in a gas of trapped atoms". *Science*, **vol. 291**, no. 5513, pp. 2570–2572 (2001) (cited page 6)

[Tung *et al.*, 2014] S.-K. Tung, K. Jiménez-García, J. Johansen, C. V. Parker and C. Chin. "Geometric Scaling of Efimov States in a ^{6}Li-^{133}Cs Mixture". *Phys. Rev. Lett.*, **vol. 113**, p. 240402 (2014) (cited page 19)

[Tuoriniemi *et al.*, 2002] J. Tuoriniemi, J. Martikainen, E. Pentti, A. Sebedash, S. Boldarev and G. Pickett. "Towards Superfluidity of ^{3}He Diluted by ^{4}He". *Journal of Low Temperature Physics*, **vol. 129**, no. 5-6, pp. 531–545 (2002) (cited pages 6, 16)

[Ungar *et al.*, 1989] P. J. Ungar, D. S. Weiss, E. Riis and S. Chu. "Optical molasses and multilevel atoms: theory". *J. Opt. Soc. Am. B*, **vol. 6**, no. 11, pp. 2058–2071 (1989) (cited page 133)

[van Amerongen *et al.*, 2008] A. H. van Amerongen, J. J. P. van Es, P. Wicke, K. V. Kheruntsyan and N. J. van Druten. "Yang-Yang Thermodynamics on an Atom Chip". *Phys. Rev. Lett.*, **vol. 100**, p. 090402 (2008) (cited page 4)

[Van Houcke *et al.*, 2012] K. Van Houcke, F. Werner, E. Kozik, N. Prokofíev, B. Svistunov, M. Ku, A. Sommer, L. Cheuk, A. Schirotzek and M. Zwierlein. "Feynman diagrams versus Fermi-gas Feynman emulator". *Nature Physics*, **vol. 8**, no. 5, pp. 366–370 (2012) (cited page 114)

[Veeravalli *et al.*, 2008] G. Veeravalli, E. Kuhnle, P. Dyke and C. J. Vale. "Bragg Spectroscopy of a Strongly Interacting Fermi Gas". *Phys. Rev. Lett.*, **vol. 101**, p. 250403 (2008) (cited page 23)

[Vichi and Stringari, 1999] L. Vichi and S. Stringari. "Collective oscillations of an interacting trapped Fermi gas". *Phys. Rev. A*, **vol. 60**, no. 6, pp. 4734–4737 (1999) (cited page 88)

[Viverit *et al.*, 2000] L. Viverit, C. J. Pethick and H. Smith. "Zero-temperature phase diagram of binary boson-fermion mixtures". *Phys. Rev. A*, **vol. 61**, p. 053605 (2000) (cited page 101)

[Volovik *et al.*, 1975] G. Volovik, V. Mineev and I. Khalatnikov. "Theory of solutions of a superfluid Fermi liquid in a superfluid Bose liquid". *Zh. Eksp. Teor. Fiz*, **vol. 69**, pp. 675–687 (1975) (cited page 89)

[Walraven, 2012] J. T. M. Walraven. "Elements of quantum gases: collisions and statistics". In "Les Houches School", (2012) (cited pages 17, 30)

[Wang *et al.*, 2012] P. Wang, Z.-Q. Yu, Z. Fu, J. Miao, L. Huang, S. Chai, H. Zhai and J. Zhang. "Spin-Orbit Coupled Degenerate Fermi Gases". *Phys. Rev. Lett.*, **vol. 109**, p. 095301 (2012) (cited page 3)

[Weidemüller *et al.*, 1994] M. Weidemüller, T. Esslinger, M. A. Ol'shanii, A. Hemmerich and T. W. Hänsch. "A Novel Scheme for Efficient Cooling below the Photon Recoil Limit". *EPL (Europhysics Letters)*, **vol. 27**, no. 2, p. 109 (1994) (cited page 134)

[Weimer *et al.*, 2008] H. Weimer, R. Löw, T. Pfau and H. P. Büchler. "Quantum Critical Behavior in Strongly Interacting Rydberg Gases". *Phys. Rev. Lett.*, **vol. 101**, p. 250601 (2008) (cited page 3)

[Weimer *et al.*, 2015] W. Weimer, K. Morgener, V. P. Singh, J. Siegl, K. Hueck, N. Luick, L. Mathey and H. Moritz. "Critical Velocity in the BEC-BCS Crossover". *Phys. Rev. Lett.*, **vol. 114**, p. 095301 (2015) (cited pages 2, 23, 54, 55, 70, 74, 89, 151)

[Wen and Li, 2014] L. Wen and J. Li. "Structure and dynamics of a rotating superfluid Bose-Fermi mixture". *Physical Review A*, **vol. 90**, p. 053621 (2014) (cited pages 7, 54)

[Wilks and Betts, 1987] J. Wilks and D. Betts. *An introduction to liquid helium*. Oxford science publications. Clarendon Press (1987). ISBN 9780198514718 (cited pages 12, 54)

[Will *et al.*, 2010] S. Will, T. Best, U. Schneider, L. Hackermuller, D.-S. Luhmann and I. Bloch. "Time-resolved observation of coherent multi-body interactions in quantum phase revivals". *Nature*, **vol. 465**, no. 7295, pp. 197–201 (2010) (cited page 2)

[Wright *et al.*, 2013a] K. C. Wright, R. B. Blakestad, C. J. Lobb, W. D. Phillips and G. K. Campbell. "Driving Phase Slips in a Superfluid Atom Circuit with a Rotating Weak Link". *Phys. Rev. Lett.*, **vol. 110**, p. 025302 (2013) (cited page 151)

[Wright *et al.*, 2013b] K. C. Wright, R. B. Blakestad, C. J. Lobb, W. D. Phillips and G. K. Campbell. "Threshold for creating excitations in a stirred superfluid ring". *Phys. Rev. A*, **vol. 88**, p. 063633 (2013) (cited page 151)

[Wu *et al.*, 2011] C.-H. Wu, I. Santiago, J. W. Park, P. Ahmadi and M. W. Zwierlein. "Strongly Interacting Isotopic Bose-Fermi Mixture Immersed in a Fermi Sea". *Phys. Rev. A*, **vol. 84**, p. 011601 (2011) (cited page 6)

[Yakimenko *et al.*, 2015] A. I. Yakimenko, K. O. Isaieva, S. I. Vilchinskii and E. A. Ostrovskaya. "Vortex excitation in a stirred toroidal Bose-Einstein condensate". *Phys. Rev. A*, **vol. 91**, p. 023607 (2015) (cited page 151)

[Yefsah *et al.*, 2011] T. Yefsah, R. Desbuquois, L. Chomaz, K. J. Günter and J. Dalibard. "Exploring the Thermodynamics of a Two-Dimensional Bose Gas". *Phys. Rev. Lett.*, **vol. 107**, p. 130401 (2011) (cited page 4)

[Zeng *et al.*, 2015] T.-S. Zeng, C. Wang and H. Zhai. "Charge Pumping of Interacting Fermion Atoms in the Synthetic Dimension". *Phys. Rev. Lett.*, **vol. 115**, p. 095302 (2015) (cited page 4)

[Zhang *et al.*, 2014] R. Zhang, W. Zhang, H. Zhai and P. Zhang. "Calibration of the interaction energy between Bose and Fermi superfluids". *Phys. Rev. A*, **vol. 90**, p. 063614 (2014) (cited page 99)

[Zheng and Zhai, 2014] W. Zheng and H. Zhai. "Quasiparticle Lifetime in a Mixture of Bose and Fermi Superfluids". *Physical Review Letters*, **vol. 113**, p. 265304 (2014) (cited pages 7, 54)

[Zürcher and Talkner, 1990] U. Zürcher and P. Talkner. "Quantum-mechanical harmonic chain attached to heat baths. I. Equilibrium properties". *Phys. Rev. A*, **vol. 42**, pp. 3267–3277 (1990) (cited page 82)

[Zürn *et al.*, 2013] G. Zürn, T. Lompe, A. N. Wenz, S. Jochim, P. S. Julienne and J. M. Hutson. "Precise Characterization of ^{6}Li Feshbach Resonances Using Trap-Sideband-Resolved RF Spectroscopy of Weakly Bound Molecules". *Phys. Rev. Lett.*, **vol. 110**, p. 135301 (2013) (cited page 93)

[Zwerger, 2012] W. Zwerger, editor. *The BCS-BEC Crossover and the Unitary Fermi Gas*, vol. 836 of *Lecture Notes in Physics*. Springer, Berlin (2012) (cited page 93)

[Zwierlein *et al.*, 2003] M. Zwierlein, C. Stan, C. Schunck, S. Raupach, S. Gupta, Z. Hadzibabic and W. Ketterle. "Observation of Bose-Einstein Condensation of Molecules". *Phys. Rev. Lett.*, **vol. 91**, no. 25, p. 250401 (2003) (cited pages 22, 92)

[Zwierlein *et al.*, 2004] M. W. Zwierlein, C. A. Stan, C. H. Schunck, S. M. F. Raupach, A. J. Kerman and W. Ketterle. "Condensation of Pairs of Fermionic Atoms near a Feshbach Resonance". *Phys. Rev. Lett.*, **vol. 92**, p. 120403 (2004) (cited page 22)

[Zwierlein *et al.*, 2005] M. W. Zwierlein, J. R. Abo-Shaeer, A. Schirotzek, C. H. Schunck and W. Ketterle. "Vortices and superfluidity in a strongly interacting Fermi gas". *Nature*, **vol. 435**, no. 7045, pp. 1047–1051 (2005) (cited pages 2, 13, 23, 54)

[Zwierlein *et al.*, 2006a] M. Zwierlein, A. Schirotzek, C. Schunck and W. Ketterle. "Fermionic superfluidity with imbalanced spin populations". *Science*, **vol. 311**, no. 5760, pp. 492–496 (2006) (cited pages 2, 4, 92, 95, 96, 97)

[Zwierlein *et al.*, 2006b] M. Zwierlein, C. Schunck, A. Schirotzek and W. Ketterle. "Direct observation of the superfluid phase transition in ultracold Fermi gases". *Nature*, **vol. 442**, no. 7098, pp. 54–58 (2006) (cited page 92)

Résumé

Les atomes froids sont des outils uniques pour sonder la physique de la matière quantique. Hautement contrôlables, les gaz de Bose et de Fermi ultrafroids sont des systèmes idéaux pour la simulation quantique et pour explorer des manifestations spectaculaires des effets quantiques, comme la superfluidité.
Avec des gaz froids de ^{6}Li et de ^{7}Li, nous avons produit le premier mélange de superfluides bosonique-fermionique, et étudié ses propriétés en initiant un contre-flot entre les nuages de Bose et de Fermi (mode dipolaire). La vitesse critique de superfluidité a été mesurée dans le crossover BEC-BCS et elle est trouvée proche de la vitesse du son dans le gaz de Fermi. Nous comparons nos mesures avec des prédictions théoriques récentes. En élevant la température du mélange, nous avons aussi observé une synchronisation inattendue entre les mouvements des deux nuages, interprétée comme un effet Zénon induit par la dissipation.
Finalement, ce mélange de bosons et de fermions offre la possibilité unique de créer un piège homogène pour le gaz de Fermi. En ajustant finement les interactions, nous proposons d'utiliser la répulsion entre les bosons et les fermions pour compenser la courbure du piège harmonique pour les fermions. Pour des fermions présentant une polarisation de spin, nous prédisons théoriquement l'existence d'un superfluide avec une structure en "coquille" et fournissons les premières indications expérimentales de l'observation de ce superfluide topologiquement original.

Mots Clés

gaz quantiques, condensats de Bose-Einstein, superfluides de Fermi, mélanges Bose-Fermi, vitesse critique, piège uniforme

Abstract

Ultracold atoms are unique tools to probe the physics of quantum matter. Indeed, the high degree of tunability of ultracold Bose and Fermi gases makes them ideal systems for quantum simulation and for exploring macroscopic manifestations of quantum effects, such as superfluidity.
In this work, we have realized the first Bose-Fermi superfluid mixture, with ultracold gases of ^{6}Li and ^{7}Li. The properties of the mixture are investigated by initiating a Bose-Fermi counterflow through their dipole modes. The superfluid critical velocity is measured in the BEC-BCS crossover, and is found close to the sound velocity of the Fermi gas near unitarity. We compare our findings to recent theoretical predictions. Raising the temperature of the mixture, we observe an unexpected synchronization of the motion of the two clouds, interpreted with a Zeno-like model induced by dissipation.
Finally, this Bose-Fermi mixture offers the unique possibility to create a homogeneous trap for the Fermi gas. By a fine tuning of the interactions, we propose to use the Bose-Fermi repulsion to compensate the curvature of the harmonic trap for fermions. For a spin-polarized Fermi gas in such a trap, we theoretically predict the existence of a superfluid with a shell structure and we provide first experimental evidence for this topologically new superfluid.

Keywords

quantum gases, Bose-Einstein condensates, Fermi superfluids, Bose-Fermi mixtures, critical velocity, uniform trap

Numéro national de thèse:
181666

Marion Delehaye **8 Avril 2016**

Sujet : Mélanges de superfluides

Résumé : Les atomes froids sont des outils uniques pour sonder la physique de la matière quantique. Hautement contrôlables, les gaz de Bose et de Fermi ultrafroids sont des systèmes idéaux pour la simulation quantique et pour explorer des manifestations spectaculaires des effets quantiques, comme la superfluidité. Avec des gaz froids de ^{6}Li et de ^{7}Li, nous avons produit le premier mélange de superfluides bosonique-fermionique, et étudié ses propriétés en initiant un contre-flot entre les nuages de Bose et de Fermi (mode dipolaire). La vitesse critique de superfluidité a été mesurée dans le crossover BEC-BCS et elle est trouvée proche de la vitesse du son dans le gaz de Fermi. Nous comparons nos mesures avec des prédictions théoriques récentes. En élevant la température du mélange, nous avons aussi observé une synchronisation inattendue entre les mouvements des deux nuages, interprétée comme un effet Zénon induit par la dissipation. Finalement, ce mélange de bosons et de fermions offre la possibilité unique de créer un piège homogène pour le gaz de Fermi. En ajustant finement les interactions, nous proposons d'utiliser la répulsion entre les bosons et les fermions pour compenser la courbure du piège harmonique pour les fermions. Pour des fermions présentant une polarisation de spin, nous prédisons théoriquement l'existence d'un superfluide avec une structure en "coquille" et fournissons les premières indications expérimentales de l'observation de ce superfluide topologiquement original.

Cette thèse est rédigée en langue anglaise.

Mots clés : gaz quantiques, condensats de Bose-Einstein, superfluides de Fermi, mélanges Bose-Fermi, vitesse critique, piège uniforme

Subject : Mixtures of superfluids

Abstract : Ultracold atoms are unique tools to probe the physics of quantum matter. Indeed, the high degree of tunability of ultracold Bose and Fermi gases makes them ideal systems for quantum simulation and for exploring macroscopic manifestations of quantum effects, such as superfluidity. In this work, we have realized the first Bose-Fermi superfluid mixture, with ultracold gases of ^{6}Li and ^{7}Li. The properties of the mixture are investigated by initiating a Bose-Fermi counterflow through their dipole modes. The superfluid critical velocity is measured in the BEC-BCS crossover, and is found close to the sound velocity of the Fermi gas near unitarity. We compare our findings to recent theoretical predictions. Raising the temperature of the mixture, we observe an unexpected synchronization of the motion of the two clouds, interpreted with a Zeno-like model induced by dissipation. Finally, this Bose-Fermi mixture offers the unique possibility to create a homogeneous trap for the Fermi gas. By a fine tuning of the interactions, we propose to use the Bose-Fermi repulsion to compensate the curvature of the harmonic trap for fermions. For a spin-polarized Fermi gas in such a trap, we theoretically predict the existence of a superfluid with a shell structure and we provide first experimental evidence for this topologically new superfluid.

This thesis is written in English.

Keywords : quantum gases, Bose-Einstein condensates, Fermi superfluids, Bose-Fermi mixtures, critical velocity, uniform trap